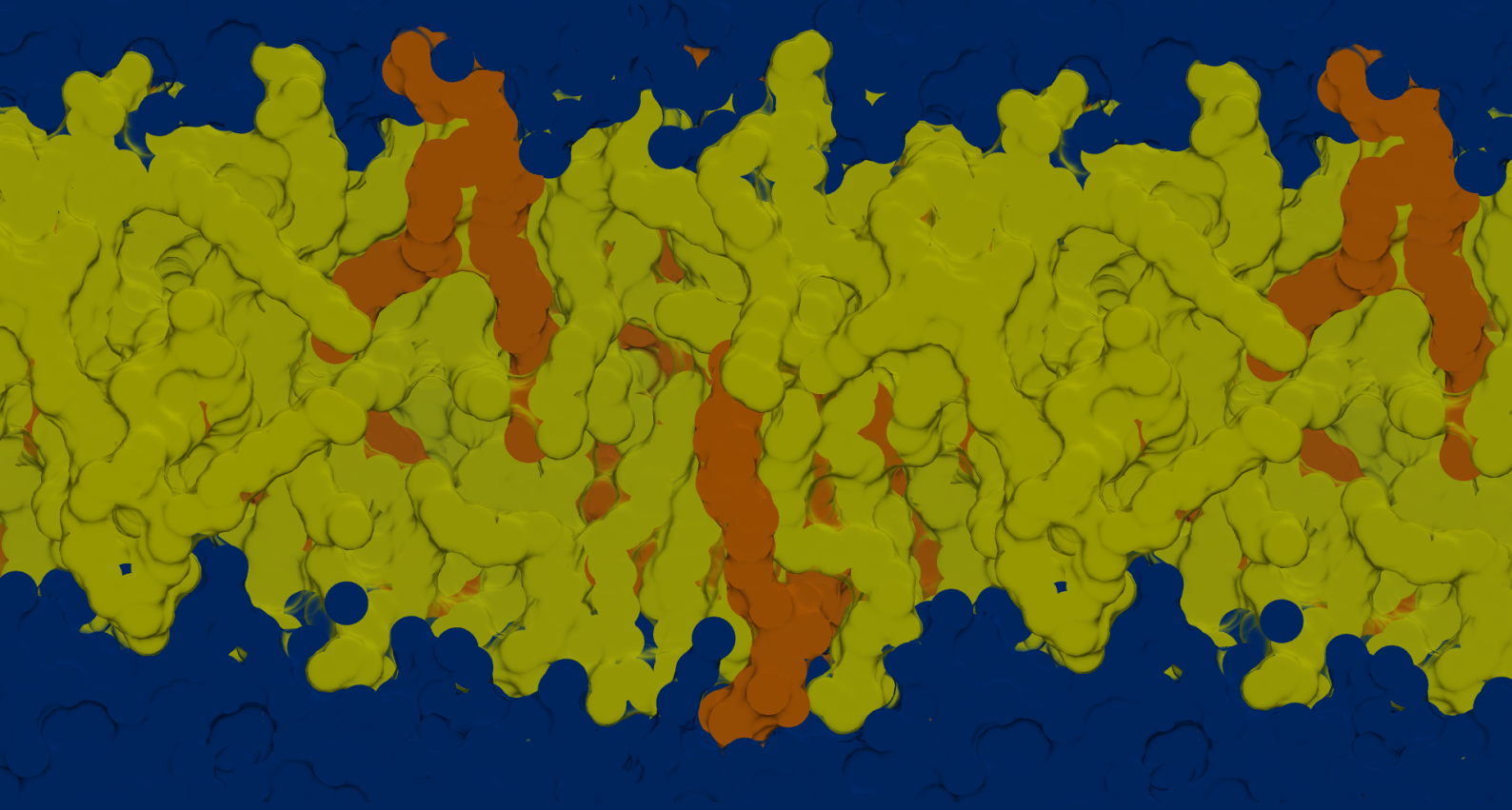

MICHAIL PALAIOKOSTAS-AVRAMIDIS

Molecular Dynamics Simulations of Small Molecule Permeation Through Lipid Membranes

Queen Mary University of London

School of Engineering and Materials Science

Doctoral College

Queen Mary
University of London

Molecular dynamics simulations of small molecule permeation through lipid membranes

by

Michail Palaiokostas-Avramidis

A thesis submitted to the

School of Engineering and Materials Science

in partial fulfilment of the requirements of the

Degree of Doctor of Philosophy

Supervisors:
Dr. Mario Orsi
Dr. Lorenzo Botto

London, July 2017

You'll come to learn a great deal if you study the Insignificant in depth

---

Odysseas Elytis

How simple and frugal a thing is happiness: a glass of wine, a roast chestnut, a wretched little brazier, the sound of the sea... All that is required to feel that here and now is happiness is a simple, frugal heart. [...] The highest point a man can obtain is not Knowledge, or Virtue, or Goodness, or Victory, but something even greater, more heroic and more despairing: Sacred Awe!

Zorba the Greek
Nikos Kazantzakis

The darkest hour is just before the dawn

Thomas Fuller

Acknowledgements

Since the beginning of my undergraduate studies I was charmed by the challenge, mystery and excitement that lies in the path of scientific method and research. Only now, that this first journey comes to an end, am I able to understand the extreme difficulty, but also the importance and responsibility that comes with creating new knowledge. Because of this, I could not have asked for a better PhD supervisor than Dr. Mario Orsi, to whom I am truly grateful for all his guidance, support and patience. During this time, Mario was not just a supervisor, but also a good friend and mentor to look upon for encouragement and scientific excellence.

I would also, like to thank the other two members of "Orsi group", Wei Ding and Ganesh Shahane, for sharing the moments of epiphany, the frustrations due to software bugs, the relief of good results and the excitement for conference travels.

I feel very lucky for all the great people that I have met in SEMS during the last four years and have had the pleasure of enjoying their company everyday. Special thanks to Pelin Yilmaz, William Megone, Matthew Dibble, Kathrin Preuß, David Stratford Devalba, Oliver Brookes, Emma Butterworth, Servann Herou, Luis Flore, Isil Top, Francesca Carleo, Dexu Kong, Halimat Reji, Daniel Arancibia, Burcu Colak, Marta Godinho and Andrew Heffron for all the social events we shared, the lunches, the luncheons, the demonstrations, the Friday nights at the Half Moon pub and the raids on SEMS seminars for leftover cookies & coffee.

Meeting Matteo Orlando and Alice Marini, my first friends and flatmates in London helped me retain my sanity during the first year in the adventurous accommodation of Floyer House. An acknowledgement is also due to Tom Teschner and Felipe Portela for the great BBQs, as well as for sharing the experiences of their PhDs.

Also, many thanks to my Greek friends, Haris Malamidis, Nikos Peitzikas, Giorgos Mousmoulis, Tommy Thomopoulos, Spyros Kontogiannis, Manos Fragkakis, Anna Dimitriadou, Filoklis Pileidis and Chara Simitzi for being there every time I was feeling nostalgic, for being understanding to my unbearable Greek nagging, for reminding me that life should be enjoyed and most of all for their help, especially during the last months.

What made this journey unforgettable was meeting, in chronological order, Stephania di Cio, Sahand Mozafari and Anuroopa Kalyan. Thank you for all the memories, the craziness, the laughs and the love. I have a special place in my heart for you guys.

Finally, this PhD would never have finished without the unconditional love and support of my family, which was always on the other side of the video-call to listen and comfort me; my "always-positive" mother Olga, my "always-cool" father Yiannis, my "little" sister Katerina and also Vicky, Fotis and Julian. Most of all, I want to express my gratitude to Artemis, my best friend and life companion, because she was always there for the few ups and the many downs, for pulling me to the surface when I was drowning, and for giving me hope when I was desperate. I love you and this dissertation is dedicated to you.

Queen Mary University of London
School of Engineering and Materials Science

Degree of Doctor of Philosophy

STATEMENT OF ORIGINALITY

Molecular dynamics simulations of small molecule permeation through lipid membranes

by Michail Palaiokostas-Avramidis

I, Michail Palaiokostas-Avramidis, confirm that the research included within this thesis is my own work or that where it has been carried out in collaboration with, or supported by others, that this is duly acknowledged below and my contribution indicated. Previously published material is also acknowledged below.

I attest that I have exercised reasonable care to ensure that the work is original, and does not to the best of my knowledge break any UK law, infringe any third party's copyright or other Intellectual Property Right, or contain any confidential material.

I accept that the College has the right to use plagiarism detection software to check the electronic version of the thesis.

I confirm that this thesis has not been previously submitted for the award of a degree by this or any other university.

Signature: Michail Palaiokostas-Avramidis
Date: July 14, 2017

Details of collaboration and publications:
Dr. Wei Ding has provided the coordinate files of the bilayers used in this dissertation.

Queen Mary University of London
School of Engineering and Materials Science

Degree of Doctor of Philosophy

ABSTRACT

Molecular dynamics simulations of small molecule permeation through lipid membranes

by Michail Palaiokostas-Avramidis

Passive permeation through biological membranes is an important mechanism for transporting molecules and regulating the cellular content. Studying and understanding passive permeation is also extremely relevant to many industrial applications, including drug design and nanotechnology. *In vivo* membranes typically consist of mixtures of lamellar and nonlamellar lipids. Lamellar lipids are characterised by their tendency to form lamellar bilayer phases, which are predominant in biology. Nonlamellar lipids, when isolated, instead form non-bilayer structures such as inverse hexagonal phases. While mixed lamellar/nonlamellar lipid membranes tend to adopt the ubiquitous bilayer structure, the presence of nonlamellar lipids is known to have profound effects on key membrane properties, such as internal distributions of stress and elastic properties. This dissertation examines permeation through lamellar and nonlamellar lipid membranes by utilising atomistic molecular dynamics simulations in conjunction with two different methods, the z-constraint and the z-restraint, in order to obtain transfer free energy profiles, diffusion profiles and permeation coefficients. An assessment of these methods is performed in search for the optimal, with the goal to create an automated, accurate and robust permeation study framework. Part of the dissertation involves the creation of the corresponding software. Furthermore, this work examines the effect of changing the lamellar vs. nonlamellar lipid composition on the passive permeation mechanism of a series of 13 small molecules and drugs. These nonlamellar lipids are known to affect the lateral pressure distribution inside the membranes. This work investigates the hypothesis that the differences in lateral pressure should increase the resistance to permeation. The results indicate that, upon addition of nonlamellar lipids, permeation is hindered for small molecules but is facilitated for the largest. All results are in agreement with previous experimental and computational studies. This work represents an advancement towards the development of more realistic *in silico* permeability assays, which may have a substantial future impact in the area of rational drug design.

Table of Contents

List of Figures

List of Tables

Nomenclature

Physical constants

ϵ_0	Vacuum permittivity	$8.854\,187\,82 \times 10^{-12}\,\mathrm{F\,m^{-1}}$
π		3.14159
e		2.71828
k_B	Boltzmann constant	$1.380\,648\,52 \times 10^{-23}\,\mathrm{J\,K^{-1}}$
N_A	Avogadro's number	$6.022\,140\,857 \times 10^{23}\,\mathrm{mol^{-1}}$
R	Universal gas constant	$8.314\,459\,8\,\mathrm{J\,mol^{-1}\,K^{-1}}$

Latin symbols

A_L	Area per lipid
b	Bond length
C	Concentration
c_0	Monolayer spontaneous curvature
C_V	Heat capacity
d_{HH}	Headgroup-headgroup bilayer distance
E	Energy
F	Force
f_c	Constraint force
f_{X-X}	Fraction of lipid type X
G	Gibbs free-energy
H	Enthalpy
h	Thickness
H_{II}	Inverse hexagonal phase
K	Kinetic energy

k	Force constant
$K(z)$	Lipid/water partition coefficient
L_c	Solid crystalline phase
L_α	Liquid-disordered phase
$L_{\beta'}$	Gel phase with tilted lipid chains
m	Mass
P	Permeation coefficient
$p(x)$	Probability density
$P_{\beta'}$	Rippled gel phase
$P_{o/w}$	Octanol/water partition coefficient
q	Partial charge of a particle
r	Position
$R(z)$	Permeation resistance
r_{ij}	Lennard-Jones radius
S	Entropy
S_{CD}	Deuterium order parameters
T	Temperature
t	Time
u	Velocity
V	Volume
V_i	Potential energy
V_L	Volume per lipid
z	Permeant position along the bilayer
P	Pressure
R	Radius

Greek symbols

α	Acceleration
β	Isothermal compressibility
δ	Dihedral phase shift
ϵ	Dielectric constant

κ_b Elastic bending modulus

κ_G Gaussian bending modulus

Φ Protein backbone dihedral angle

ϕ Dihedral angle

Π Lateral pressure

Ψ Protein backbone dihedral angle

τ Characteristic time of an autocorrelation function

τ_i Coupling time constant

θ Bond angle

ε_{ij} Lennard-Jones well-depth

Lipid molecules abbreviations

DLPC 1,2-dilinoleoyl-*sn*-glycero-3-phosphocholine

DMPC 1,2-dimyristoyl-*sn*-glycero-3-phosphocholine

DMPE 1,2-dimyristoyl-*sn*-glycero-3-phosphoethanolamine

DOPC 1,2-dioleoyl-*sn*-glycero-3-phosphocholine

DOPE 1,2-dioleoyl-*sn*-glycero-3-phosphoethanolamine

DPhPC 1,2-diphytanoyl-*sn*-glycero-3-phosphocholine

DPPC 1,2-dipalmitoyl-*sn*-glycero-3-phosphocholine

DPPE 1,2-dipalmitoyl-*sn*-glycero-3-phosphoethanolamine

DSPC 1,2-distearoyl-*sn*-glycero-3-phosphocholine

EPC Egg phosphocholine

FFA Free fatty acids

PC Phosphatidylcholine

PE Phosphatidylethanoloamine

POPC 1-palmitoyl-2-oleoyl-*sn*-glycero-3-phosphocholine

POPE 1-palmitoyl-2-oleoyl-*sn*-glycero-3-phosphoethanolamine

SC *Stratum corneum*

SOPC 1-stearoyl-2-oleoyl-*sn*-glycero-3-phosphocholine

Other abbreviations

ACF Autocorrelation function

ADME Absorption, distribution, metabolism and excretion

BLM Black lipid membranes

EDP Electron density profile

FF Force field

HB Hydrogen bonds

HPC High performance computing

HTS High throughput screening

LPP Lateral pressure profile

MC Monte Carlo

MD Molecular dynamics

MSD Mean square displacement

MW Molecular weight

NCE New chemical entities

NMR Nuclear magnetic resonance

NPT Isothermal-isobaric ensemble

NVE Micro-canonical ensemble

NVT Canonical ensemble

PAMPA Parallel artificial membrane permeability assay

PBC Periodic boundary conditions

PME Particle-mesh Ewald

PMF Potential of mean force

QSAR Quantitative structure activity relationship

SPME Smooth particle-mesh Ewald

TPSA Topological polar surface area

UHTS Ultra-high throughput screening

VdW Van der Waals

WHAM Weighted histogram analysis method

Chapter 1

Introduction

1.1 Motivation

Drug development is a resource-intensive and time-consuming process with a very high risk of failure. New chemical entities (NCEs) are typically studied for a decade or more before they reach the general population. During this long period of time, a potential drug candidate has to successfully pass both pre-clinical and clinical tests, that further involve many phases[1]. This rigorous process screens an initial compound library of several millions NCEs to just a few potential candidates that can be further examined during the clinical trials[2]. On average, the cost of research and development for each drug can reach $802 million[3].

The pre-clinical work, also known as the drug discovery cycle, can be distinguished into three stages[2]; target selection, lead identification and lead optimisation. Initially, research focuses on a particular disease and the corresponding interaction targets or processes, that a drug could affect within the body. The next step is to identify chemical entities that could potentially affect the previously found target. During that stage, by using high and ultra-high throughput screening techniques (HTS/UHTS)[4], researchers screen an initial set of a few million substances to about 10-15, while at the same time obtain initial information regarding pharmacokinetic properties including absorption, distribution, metabolism and excretion (ADME)[5,6]. Finally, during the lead optimisation stage, by performing detailed research for 2 to 3 years, the potential candidates are reduced further to just a few, which can then proceed for clinical trials.

All the aforementioned stages are research-intensive and time-consuming processes that involve *in vitro*, *in vivo* and *in silico* techniques. In particular the latter, with the exponential growth of the available computational power during the last four decades, has provided new perspectives in the drug discovery process[7–9]. Figure 1.1 shows the possible areas

than *in silico* techniques could be used depending on the scale of the problem (figure 1.2). Commonly used methods include:

- molecular docking, which is usually utilised to study the binding of ligands in targets (e.g., protein receptors)[10,11],
- quantitative structure activity relationship (QSAR), which correlates the structural properties of compounds to their biological activity,
- Monte Carlo (MC) and molecular dynamics (MD) simulations, which provide a perspective of the conformational changes (MC & MD) and time evolution (MD) of biological systems on the nanometre scale.

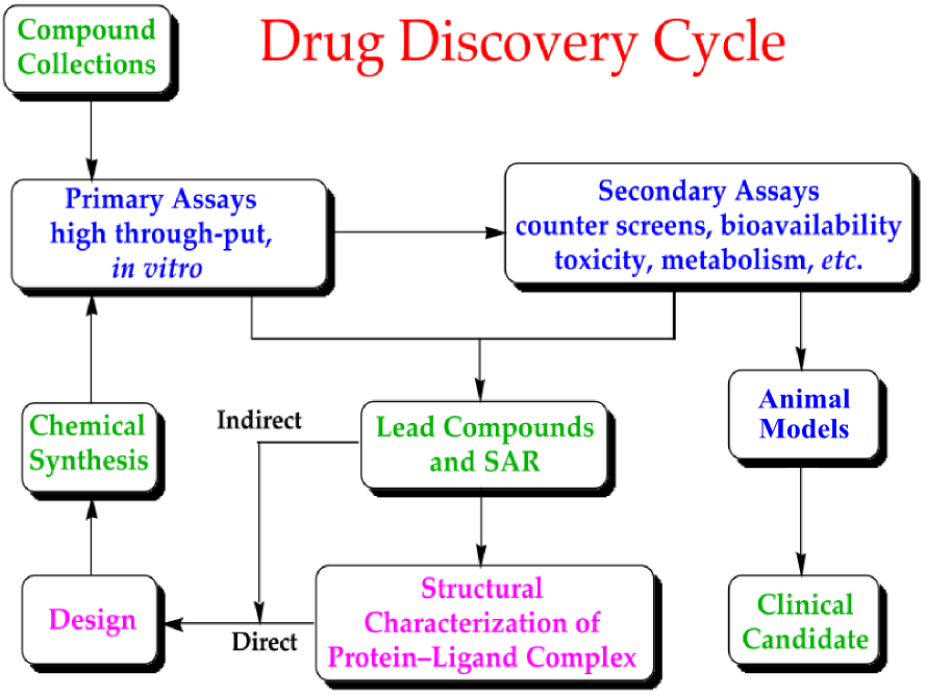

Figure 1.1: Contribution areas of *in silico* methods in modern drug discovery cycle. Modified version of reference[12]

MD is an essential technique for the design of new drugs and in the past, research has focused on the study of proteins and interactions of proteins with ligands (proteomics). It allows the prediction of thousands of different molecular conformations based on structural data obtained with experiments or quantum mechanics simulations[13]. It also allows a visual and dynamo-kinetic representation of the binding of potential drugs to biological targets[14,15]. Another emerging field that utilises MD extensively, is the study of lipid membranes or the identification of the role of lipids in important biological processes. Lipid molecules exist predominantly in biological interfaces e.g., cell membranes; thus the majority of research on the topic concentrates on the individual or collective properties of lipids, as well as their interactions with other micro- and macro- molecules[16].

Cell membranes are the predominant structures of biological systems and are vital for the

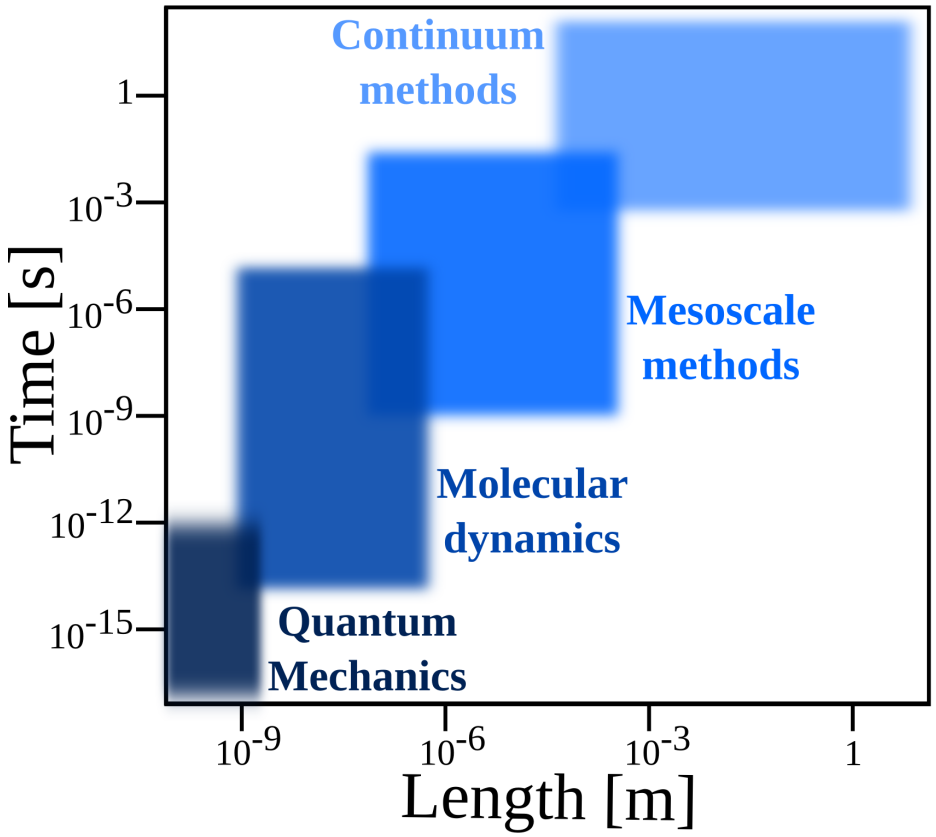

Figure 1.2: Time and spatial scales accessible by simulation methods

existence of life[17]. The plasma membrane is a thin cell-surface membrane that encapsulates the contents of the cell and exists in both prokaryotic and eukariotic cells. However, the latter have extra internal cell membranes that allow for the compartmentalisation of different biological processes. Plasma membranes comprise mainly lipid molecules and proteins, as well as a small percentage of carbohydrates (figure 1.3). Lipids found in plasma membranes are typically phospholipids or glycolipids, which have an amphiphatic nature[18]. This molecular structure leads to the so-called "hydrophobic effect", in which the hydrophobic part tends to minimise its contact with the aqueous environment, while the hydrophilic part tends to maximise it. The shape of the plasma membrane is a result of the hydrophobic effect, where lipid molecules self-assemble in a bilayer structure, with the hydrophobic parts protected in the centre and the hydrophilic parts exposed to the aqueous environment.

One of the most fundamental functions of the cell membrane is the regulation of molecules transportation, which is of immense importance in the drug discovery cycle. The majority of neutral-charged, hydrophobic, small molecules and drugs, permeate lipid membranes spontaneously via a process called passive permeation, which occurs due to the compound concentration gradient along the membrane and no carrier proteins or extra energy are required. Many parameters affect passive permeation and the identification of individual contributions (e.g., from lipid properties, membrane properties or permeant properties) is an active research field. Molecular dynamics as a technique, provides a sub-nanometre magnifying glass that allows a detailed examination of the complicated transport phenom-

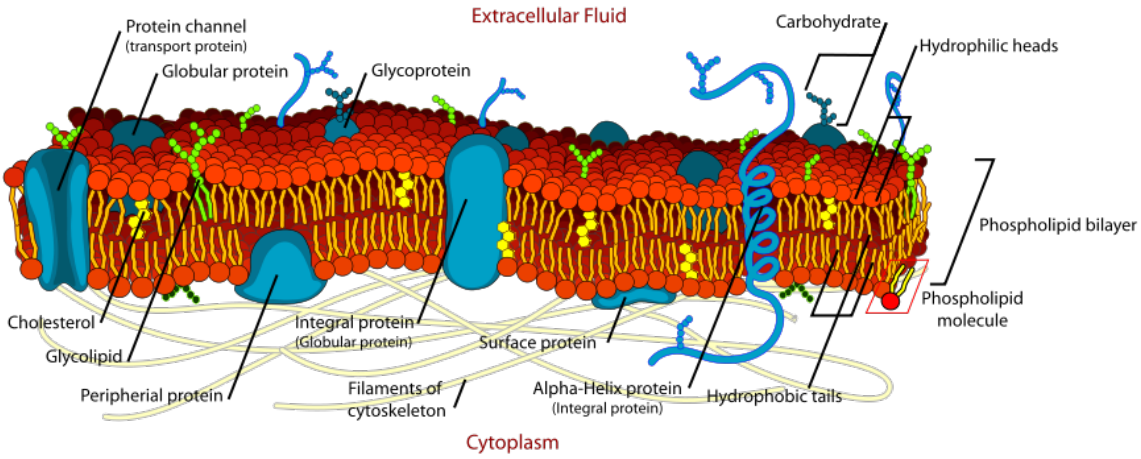

Figure 1.3: An artistic representation of the plasma membrane[19].

ena which cannot be currently probed by experiments due to the small thickness of the membrane[20].

Cell membranes are composed by hundreds of different types of lipid molecules and different lipid compositions induce different phase formations and structure properties[17]. In the past, studies of passive permeation focused on single lipid-type systems, however, recent findings indicate a strong dependence of key lipid bilayer properties on lipid composition[21,22]. These properties have the potential to affect significantly, among other processes, the passive permeation of molecules through the membrane. Considering that MD can provide a detailed atomistic perspective on biological phenomena, in this work, MD simulations are utilised in order to study the possible effect of lipid composition on the passive permeation of small molecules and drugs and the prospective consequences in the drug discovery cycle.

1.2 Hypothesis and aims

Previous studies have shown that the lateral pressure profile of a membrane changes significantly when lipid molecules that form nonlamellar structures are mixed with lipid molecules that form lamellar structures[21,22]. In particular, they observed an increase of repulsive forces in the hydrophobic part of the bilayer when nonlamellar lipids were added. In this work it was hypothesised that this increase in repulsive forces should lead to an increase in the resistance to permeation trough the membrane.

The first aim of the present study was to investigate and quantify the effect of combining nonlamellar and lamellar lipids, on passive permeation of small molecules and drugs. Specifically it investigated whether this increase of repulsive forces had the potential to alter the passive permeation of molecules through the membrane. The examined model membranes consisted of the lamellar DOPC and the nonlamellar DOPE lipids while 13 permeants of biological relevance were selected based on a broad range of physical proper-

ties.

The second aim was to assess which of the two most commonly biased molecular dynamics methods for permeation studies provided the optimal combination of speed, accuracy and robustness. Also, part of this aim was to produce a pre-processing and post-processing software toolbox that would allow the automation of building, managing and analysing permeation simulations. Overall, the project aimed to build a methodological framework for permeation studies that appeals both to the academic and non-academic communities.

1.3 Statement of novelty

Several novel contributions are made in this dissertation that originate from the study of passive permeation of small molecules and drugs through lamellar/nonlamellar DOPC:DOPE mixtures. Although previous studies have examined the permeation through either pure DOPC or pure DOPE membranes and a few have also measured permeation through a mixture of both, this is the first study that examines the effect of DOPE for a large set of molecules and attempts a connection to key membrane properties, such as the lateral pressure profile. Furthermore, this is the first time that certain parameters of the methods used to measure permeation are thoroughly investigated. The novelty claims of this study are as follows:

- The z-restraint and the z-constraint methods were compared for their accuracy, robustness, convergence speed and computational efficiency in order to find the optimal solution for an automated permeation study framework.
- Two methods to measure local diffusion coefficients were compared, the Hummer method[23] and the Zhu and Hummer[24] method. For the latter, four different techniques were used to compute the integral of the autocorrelation function of the z-restraint position and assessed against the previously used fitting of a double exponential function. With regards to the Zhu and Hummer method, it is the first time that is reported in a permeation study after its publication.
- A software toolbox was built in order to perform the pre-processing, simulation management and analysis of results, with minimum effort from the user.
- Comparison between DOPC and DOPC:DOPE(1:3) membranes was made for Gibbs free-energy, local diffusion and local resistance profiles, as well as permeation coefficients in order identify the effect of DOPE on permeation. The calculation of hydrogen bond formations indicated that the lateral pressure profile is probably the main source of permeation differences between the membranes. Also, the permeation coefficients and their logarithm to base 10 were correlated to 5 physicochemical properties of the permeants.

1.4 Dissertation outline

The current chapter gave a short introduction to the motivation behind this dissertation as well as the open scientific question, the project hypothesis and the general aims of the work. The rest of the chapters are divided as follows:

- **Chapter 2: Theoretical Background.** This chapter begins with a review of key concepts of molecular dynamics simulations, such as the potential function, temperature and pressure control and periodic boundary conditions. It continues with an introduction to lipid molecules, lipid membranes and their fundamental properties. Then, the theoretical background of spontaneous passive permeation is presented along with the most common experimental and computational methods to study it. The chapter ends with a two-fold literature review; firstly it reports previous studies that examined the effect of nonlamellar lipids on mechanical membrane properties and then it reports studies that focused on permeation through various mixed-composition membranes.

- **Chapter 3: Materials and Methods.** In this chapter the 2 lipid molecules and 13 permeants are presented and their properties are discussed in detail. Also, the simulation protocols for the reproduction of this dissertation results are provided.

- **Chapter 4: MDrug: A preparation, analysis and HPC management toolbox**. This chapter describes the features of the MDrug software toolbox for the three main operations of a permeation study; the pre-processing, the post-processing and the simulation management.

- **Chapter 5: Results and discussion.** Chapter 5 presents the results of this dissertation and their discussion. The chapter begins with the outcomes of the methodological issues examined and their parametric studies. Then it presents the free-energy profiles, the local diffusion profiles, the local resistance profiles and the permeation coefficients in regards to the z-constraint and z-restraint methods and as a comparison between the DOPC and DOPC:DOPE membranes. Further analysis of the z-restraint results includes the hydrogen bond formation, correlation and regression analyses and lateral mobility plots. The chapter ends with the discussion on the two aims of the project, the effect of nonlamellar lipids on permeation and the best methodology for automated studies.

In the final chapter, the key findings and conclusions of this work are summarised and based on that, perspectives for future research are given.

Chapter 2

Theoretical background

2.1 Molecular dynamics

2.1.1 Equation of motion

Molecular transport through the cell membrane is a microscopic phenomenon, taking place over nanometre length scales. To identify permeation rates, experimental techniques measure the concentration difference of chemical compounds over a specific time duration. In order to explore the biophysical mechanisms of permeation in the nano- and sub-nano-scales, one can utilise atomistic simulations, where electrons are ignored and individual atomic nuclei are approximated as spherical particles. The aim of such simulations is to obtain a sufficiently large number of phase space samples, so that, through the ergodic hypothesis, reliable macroscopic thermodynamic properties can be extracted.

The molecular dynamics method simulates the time evolution of a small number of classical particles by solving Newton's second law of motion, $\boldsymbol{F} = m\boldsymbol{a}$. Assuming a system of N interacting particles, the equation can be expressed as:

$$\boldsymbol{F}_i = m_i \frac{\partial^2 \boldsymbol{r}_i}{\partial t^2} \ , \ i = 1 \dots N \tag{2.1}$$

where $\boldsymbol{F}$ is the force on each particle i, m is its mass, $\boldsymbol{r}$ is its position vector (contains the Cartesian coordinates) and t is the time variable. The forces of the system can be computed as the negative spatial derivative of the potential energy function $V(\boldsymbol{r}_1, \dots, \boldsymbol{r}_N)$:

$$\boldsymbol{F}_i = -\frac{\partial V}{\partial \boldsymbol{r}_i} \ , \ i = 1 \dots N. \tag{2.2}$$

Therefore, equation 2.1 can be rewritten as:

$$m_i \frac{\partial^2 \boldsymbol{r}_i}{\partial t^2} = -\frac{\partial V}{\partial \boldsymbol{r}_i} \ , \ i = 1 \dots N. \tag{2.3}$$

The solution of equation 2.3 is found numerically with small increments of the time variable, also known as timestep δt, by following the procedure that is shown on figure 2.1. In order for the simulation to begin, the starting positions $\boldsymbol{r}$ and velocities $\boldsymbol{v}$ have to be given. Afterwards and for the rest of the simulation, each timestep is separated to three distinct sub-steps. Initially, the forces on each atom of the system are calculated based on the potential function (equation 2.2). Then, the positions of the particles are updated based on the numerical solution of equation 2.1 and finally, if necessary, important properties of the system are saved (e.g., temperature, pressure, positions etc.). All the aforementioned steps, as well as the algorithms used for this work, are explained in detail on the following sections.

2.1.2 Potential energy functions

The total potential energy V of the system is the summation of all the interactions that the particles of the system experience. Molecular dynamics simulations are possible because of two important assumptions. The first is the Born-Oppenheimer approximation that separates the fast electronic motions from the slow nuclear motions, allowing the former to be averaged out. The second is the assumption that nuclei are heavy enough so that quantum effects are negligible. Based on these two assumptions, the potential energy of each interaction can be expressed according to classical mechanics and a set of interaction parameters, namely, the force field (FF).

The force field refers to the combination of parametric potential energy functions and parameter sets that relate chemical structure and conformation to energy, usually produced by fitting the functions to available experimental data and thus termed empirical force fields. Although there are currently many different force fields available and several variations of their functional forms, in general, they commonly separate contributions into bonded and non-bonded. The former, refer to covalent bond stretching, angle bending and torsion due to bond rotation (dihedral angles), while the latter refer to van der Waals and electrostatic forces. A generic expression of the functional form is:

$$\begin{aligned} V_{total} &= V_{bonded} + V_{nonbonded} \\ &= \left(V_{bond} + V_{angle} + V_{dihedral}\right) + \left(V_{van\ der\ Waals} + V_{electrostatic}\right) \end{aligned} \tag{2.4}$$

however different force fields might add extra contributions and terms.

THE GLOBAL MD ALGORITHM

1. Input initial conditions

Potential interaction V as a function of atom positions
Positions $\boldsymbol{r}$ of all atoms in the system
Velocities $\boldsymbol{v}$ of all atoms in the system
$\Downarrow$

repeat 2,3,4 for the required number of steps:

2. Compute forces

The force on any atom

$$\boldsymbol{F}_i = -\frac{\partial V}{\partial \boldsymbol{r}_i}$$

is computed by calculating the force between non-bonded atom pairs:

$\boldsymbol{F}_i = \sum_j \boldsymbol{F}_{ij}$

plus the forces due to bonded interactions (which may depend on 1, 2, 3, or 4 atoms), plus restraining and/or external forces.
The potential and kinetic energies and the pressure tensor may be computed.
$\Downarrow$

3. Update configuration

The movement of the atoms is simulated by numerically solving Newton's equations of motion

$$\frac{\mathrm{d}^2\boldsymbol{r}_i}{\mathrm{d}t^2} = \frac{\boldsymbol{F}_i}{m_i}$$

or

$$\frac{\mathrm{d}\boldsymbol{r}_i}{\mathrm{d}t} = \boldsymbol{v}_i; \quad \frac{\mathrm{d}\boldsymbol{v}_i}{\mathrm{d}t} = \frac{\boldsymbol{F}_i}{m_i}$$

$\Downarrow$

4. if required: **Output step**
write positions, velocities, energies, temperature, pressure, etc.

Figure 2.1: Molecular dynamics algorithm[25]

2.1.2.1 The CHARMM force field

In this dissertation, one of the most commonly used force fields for simulations of biological molecules was chosen, the "Chemistry at HARvard Molecular Mechanics" (CHARMM)[26]. The potential energy function defined by CHARMM has the generic bonded and nonbonded terms of equation 2.4, as well as a few extra bonded:

$$V_{\text{bonded}} = V_{\text{bond}} + V_{\text{angle}} + V_{\text{Urey-Bradley}} + V_{\text{dihedral}} + V_{\text{improper}} + V_{\text{CMAP}} \tag{2.5}$$

with the extra terms $V_{Urey-Bradley}$, $V_{improper}$ and V_{CMAP} representing angle bending due to nonbonded van der Waals interactions between atoms 1 and 3, out-of-plane bending and corrections for protein backbone dihedral angles, respectively. Overall, the potentials used for the total expression of the CHARMM potential energy are harmonic, periodic, Lennard-Jones and Coulomb and they are all presented in table 2.1. The total potential energy function can be written as:

$$\begin{aligned} V_{total} = & \sum_{\text{bonds}} k_b \left(b - b^0\right)^2 \\ & + \sum_{\text{angles}} k_\theta \left(\theta - \theta^0\right)^2 \\ & + \sum_{\text{Urey-Bradley}} k_{UB} \left(b^{1-3} - b^{1-3,0}\right)^2 \\ & + \sum_{\text{dihedrals}} k_\varphi \left(1 + \cos\left(n\varphi - \delta\right)\right) \\ & + \sum_{\text{impropers}} k_\omega \left(\omega - \omega^0\right)^2 \\ & + \sum_{\text{residues}} V_{\text{CMAP}}(\Phi, \Psi) \\ & + \sum_{\text{nonbonded pairs}} \varepsilon_{ij} \left[\left(\frac{r_{ij}^{min}}{r_{ij}}\right)^{12} - 2\left(\frac{r_{ij}^{min}}{r_{ij}}\right)^{6}\right] + \frac{q_i q_j}{4\pi\epsilon_0 r_{ij}} \end{aligned} \tag{2.6}$$

where the superscript naught symbol $\left(^0\right)$ indicates equilibrium terms, k terms indicate force constants, n is the multiplicity of the dihedral function, ϕ is the dihedral angle, δ is dihedral phase shift, Φ and Ψ are the protein backbone dihedral angles, ε_{ij} and r_{ij} are the geometric mean $\left(\varepsilon_{ij} = \sqrt{\varepsilon_i \varepsilon_j}\right)$ and arithmetic mean $\left(r_{ij} = \left(r_i + r_j\right)/2\right)$ of the Lennard-Jones parameters of particles i and j, respectively, $q_i q_j$ are the partial charges of the particles and ϵ_0 is the vacuum permittivity.

2.1.2.2 Cut-off radius and long-range interactions

Calculation of nonbonded interactions such as van der Waals and electrostatics is the most computationally demanding part of an MD simulation. The reason is that, in principle, both of these interactions exist between all particles. One approximation that helps with the large amount of calculations is to consider only pairs of particles (pairwise interactions)

Table 2.1: Particle interactions and potential functions.

Interactions	Type	Potential	Function
Bond stretching	Bonded	Harmonic	$k_b\left(b-b^0\right)^2$
Angle bending	Bonded	Harmonic	$k_\theta\left(\theta-\theta^0\right)^2$
Urey-Bradley	Bonded	Harmonic	$k_{UB}\left(b^{1-3}-b^{1-3,0}\right)^2$
Dihedral	Bonded	Periodic	$k_\varphi\left(1+\cos\left(n\varphi-\delta\right)\right)$
Improper	Bonded	Harmonic	$k_\omega\left(\omega-\omega^0\right)^2$
CMAP	Bonded	-	Correction terms for Φ and Ψ
van der Waals	Nonbonded	Lennard-Jones	$\varepsilon_{ij}\left[\left(\frac{r_{ij}^{min}}{r_{ij}}\right)^{12}-2\left(\frac{r_{ij}^{min}}{r_{ij}}\right)^{6}\right]$
Electrostatic	Nonbonded	Coulomb	$\left(q_iq_j\right)\left(4\pi\epsilon_0 r_{ij}\right)^{-1}$

Equilibrium terms. b^0:bonds, θ^0:angles, $b^{1-3,0}$:Urey-Bradley, n:dihedral multiplicity, δ:dihedral phase, ω^0:impropers
Force constants. k_b:bonds, k_θ:angles, k_{UB}:Urey-Bradley, k_φ:dihedrals, k_ω:impropers
Other terms. ε_{ij}:Lennard-Jones well-depth, r_{ij}:Lennard-Jones radius, ϵ_0:vacuum permittivity

and thus for N particles, NxN calculations are required. However, this is still a considerably large amount of computations. Therefore, a second approximation is the construction of a neighbour list around each particle and the use of a cut-off radius, beyond which interactions are not computed.

To construct the neighbour list, all particles within a specific radius of each particle (the neighbour list cut-off), must be found. Then, the particles that have exclusively bonded interaction are discarded. In the end, the neighbour list includes only pairs of particles with nonbonded interactions. To enhance computational efficiency, many MD solvers (e.g., GROMACS), do not update the neighbour list every timestep but every 20, 40 or even more, depending on the simulated system.

The application of a cut-off radius for van der Waals forces (and the respective Lennard-Jones potential) is a reasonable approximation because they decay rapidly as the distance grows (figure 2.2). However, the approximation is not valid for electrostatics, which decay much slower and have a longer effective range. To alleviate the problem, electrostatics are divided in short-range and long-range. The former are computed based on a cut-off radius similar to the one used for van der Waals forces. For the latter, when periodic boundary conditions are used (see section 2.1.5), a special technique called Ewald summation[27] can be utilised. With this technique, the long-range electrostatics are represented by a finite

Fourier series which is solved in the reciprocal space. Most modern MD solvers use the Particle Mesh Ewald (PME) algorithm[28] that uses fast Fourier transformations and distributes system partial charges into a grid.

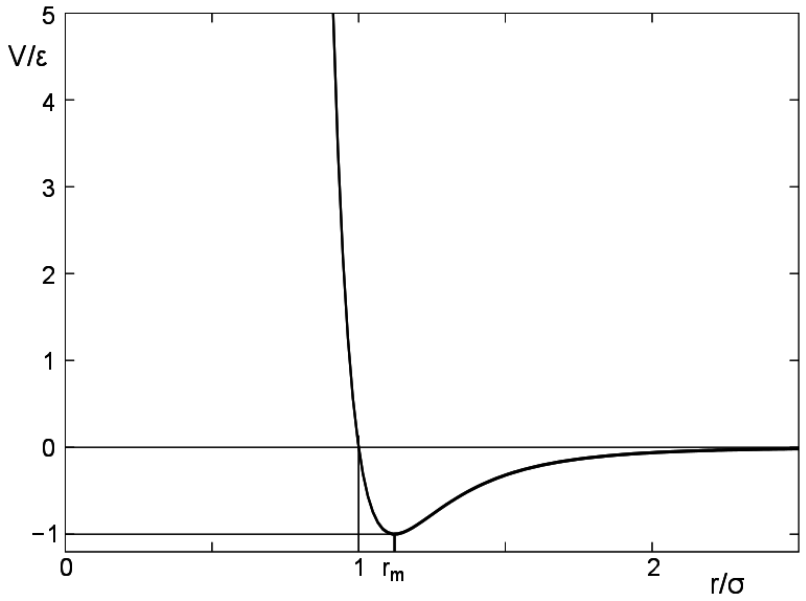

Figure 2.2: The Lennard-Jones potential energy function[29]

The use of cut-offs introduces a significant issue on the limits of the cut-off radii. Particles close to them, by moving inside or outside over simulation steps, introduce discontinuities in the potential energy function which affect the stability of the simulation. To prevent these abrupt changes in the potential energy, it is customary for force fields to alter their functional forms either by using a switching or shifting function. In the first case, two cut-offs are used; until the inner cut-off the functional form is the original, while between the inner and outer cut-offs, a sigmoidal function "switches" the potential energy to zero (in CHARMM FF, typically the two cut-offs are 1.0 nm and 1.2 nm). In the second case, the functional form is altered entirely in order to decay continuously to zero in the cut-off radius.

2.1.3 Energy minimisation and initial conditions

Usually, before a molecular dynamics simulation, all particles undergo a process called energy minimisation, where, the starting configuration, according to a minimal energy criterion, is rearranged so that the potential energy function finds a local minimum. This process increases the stability of the upcoming MD simulation, especially in the initial phase, when particle overlaps and far-from-equilibrium bonds, angles or dihedrals could result in extreme forces that the integrator could not handle. A popular algorithm for energy minimisation is the steepest descent[25]; in every iteration of the minimisation, a step is taken towards the negative gradient of the potential (the direction of the total force), until a local minimum is reached.

In order for a simulation to begin, several parameters should be defined, such as, the size of simulation box, as well as, the initial coordinates and velocities of the particles. The initial velocities, if unknown, can be generated according to the Maxwell-Boltzmann distribution (figure 2.3) for any temperature T:

$$p(u_i) = \sqrt{\frac{m_i}{2\pi k_B T}} \exp\left[-\frac{m_i u_i^2}{2k_B T}\right] \tag{2.7}$$

where $p(u_i)$ is the probability density as a function of speed u of any particle i, m_i is the particle mass and k_B is Boltzmann's constant.

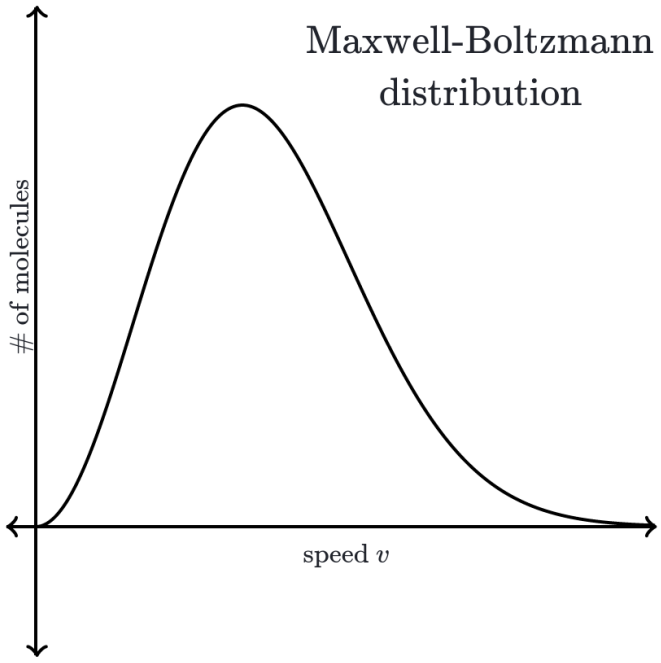

Figure 2.3: Maxwell-Boltzmann velocity distribution[30]. The symbol # stands for "Number of".

2.1.4 Numerical solution

In every timestep, once the total force on each particle is computed according to equation 2.2, the MD integrator transforms the forces into conformational changes according to equation 2.1 via numerical integration. In order to solve the differential equations numerically, the finite difference method is used. Several algorithms have been proposed as integrators[31–34]. One of the most commonly used algorithms is the Verlet[34]; considering that the positions $\boldsymbol{r}$, velocities $\boldsymbol{v}$ and accelerations $\boldsymbol{a}$ are known in a particular time t, the positions in the next timestep $t + \delta t$ can be computed by a Taylor's expansion as:

$$\boldsymbol{r}(t + \delta t) = \boldsymbol{r}(t) + \boldsymbol{v}(t)\delta t + \frac{1}{2}\boldsymbol{a}(t)(\delta t)^2 + \frac{1}{6}\boldsymbol{b}(t)(\delta t)^3 + \ldots \tag{2.8}$$

while the positions $\boldsymbol{r}$ for the previous timestep can be expressed as:

$$\boldsymbol{r}(t-\delta t) = \boldsymbol{r}(t) - \boldsymbol{v}(t)\delta t + \frac{1}{2}\boldsymbol{a}(t)(\delta t)^2 - \frac{1}{6}\boldsymbol{b}(t)(\delta t)^3 + \dots \tag{2.9}$$

Addition of equations 2.8 and 2.9 gives:

$$\boldsymbol{r}(t+\delta t) = 2\boldsymbol{r}(t) - \boldsymbol{r}(t-\delta t) + \boldsymbol{a}(t)(\delta t)^2 \tag{2.10}$$

where $\boldsymbol{a}$ can be computed from the potential energy based on equation 2.3 and only for the initial timestep, the $\boldsymbol{r}(t-\delta t)$ term can be approximated as:

$$\boldsymbol{r}(-\delta t) = \boldsymbol{r}(0) - \boldsymbol{v}(0)\delta t \tag{2.11}$$

The main disadvantage of the Verlet algorithm is that velocities do not explicitly appear in the equation and thus direct control of the temperature of the particles is impossible. To circumvent this issue, many MD integrators (such as GROMACS) use the leap-frog algorithm[35], where the positions in the next timestep can be computed by the velocity at half timestep:

$$\boldsymbol{r}(t+\delta t) = \boldsymbol{r}(t) + \boldsymbol{v}(t+\frac{\delta t}{2})\delta t \tag{2.12}$$

$$\boldsymbol{v}(t+\frac{\delta t}{2}) = \boldsymbol{v}(t-\frac{\delta t}{2}) + \boldsymbol{a}(t)\delta t \tag{2.13}$$

Then at each full timestep δt, the velocity is calculated as:

$$\boldsymbol{v}(t) = \frac{1}{2}(\boldsymbol{v}(t+\frac{1}{2}\delta t) + \boldsymbol{v}(t-\frac{1}{2}\delta t)) \tag{2.14}$$

Although the leap frog algorithm introduces the velocity component in the numerical equation of motion, it is still out-of sync and an extra calculation of higher order error is required on each timestep (eq. 2.14). To further tackle this issue, the velocity-Verlet algorithm[36] is used which allows a synchronised time progression of all properties $(\boldsymbol{r}, \boldsymbol{v}, \boldsymbol{a})$ by first computing the new position $\boldsymbol{r}(t+\delta t)$ as:

$$\boldsymbol{r}(t+\delta t) = \boldsymbol{r}(t) + \boldsymbol{v}(t)\delta t + \frac{1}{2}\boldsymbol{a}(t)(\delta t)^2 \tag{2.15}$$

then the new acceleration is computed based on equation 2.3 for $t+\delta t$ as:

$$\boldsymbol{a}(t+\delta t) = -\frac{1}{m}\frac{\partial V}{\partial \boldsymbol{r}(t+\delta t)} \tag{2.16}$$

and finally:

$$\boldsymbol{v}(t+\delta t) = \boldsymbol{v}(t) + \frac{1}{2}\left(\boldsymbol{a}(t) + \boldsymbol{a}(t+\delta t)\right)\delta t. \tag{2.17}$$

Timestep δt is one of the most important parameters of the simulation protocol as it affects the accuracy of the results, as well as the robustness of the simulation. The criterion

for its selection is related to the fastest processes of the examined system. These are typically the stretching vibrations of covalent bonds with hydrogen atoms[37], which however, have a small effect on the calculated properties of the system. Therefore, their length is usually constrained to their equilibrium distance during the simulation, allowing for larger timesteps and thus simulations of larger timescales for the same computational cost. constraint algorithms work by evaluating the proper length of bonds after unrestrained movements. Three commonly used constraint algorithms are the SHAKE[38], RATTLE[39] and LINCS[40,41], with the first two using an iterative process to determine the correct constraint forces for Verlet and velocity Verlet integrators respectively, while LINCS only has two iterations, is faster and more robust, but has more limitations in comparison to the other two[25].

2.1.5 Boundary conditions

Due to the small number of particles utilised in a molecular dynamics simulation (compared to Avogadro's number), boundary conditions of solid walls can introduce significant surface effects that will not represent correctly bulk thermodynamic properties. Therefore, it is necessary in many MD simulations to use periodic boundary conditions (PBC), whereby an infinite number of replicas surround the original system. Figure 2.4 shows a 2D representation of periodic boundary conditions, with the original system being in the centre. Each particle has infinite surrounding copies and when it moves out of the simulation domain from one side, its copy moves in from the opposite side.

As it was mentioned in section 2.1.2, the computation of the potential energy for all particles is a prerequisite for the prediction of system's evolution. Furthermore, calculating nonbonded interactions is the most computationally demanding part of MD. Since infinite copies of particles exist, in theory, infinite interactions should be taken into account. This is practically impossible and thus the minimum image convention is used, in which, each particle interacts only with the nearest image of any other particle (figure 2.4). However, even with this convention, the number of pairwise interactions is very high, therefore the cut-off radius is further introduced to increase computational efficiency with minimum effect on physical properties calculation (see figure 2.4 and also section 2.1.2.2).

2.1.6 Temperature and pressure control

2.1.6.1 Ensembles

Molecular dynamics simulations generate ensembles of constant number of particles N, volume V and energy E (NVE) with fluctuating temperature T and pressure P. Most experiments, however, are performed under controlled temperature and/or pressure, therefore it is important to be able to reproduce the respective ensembles, canonical (NVT) or isothermal-isobaric (NPT). In order to achieve this, the velocities or the positions of the particles are

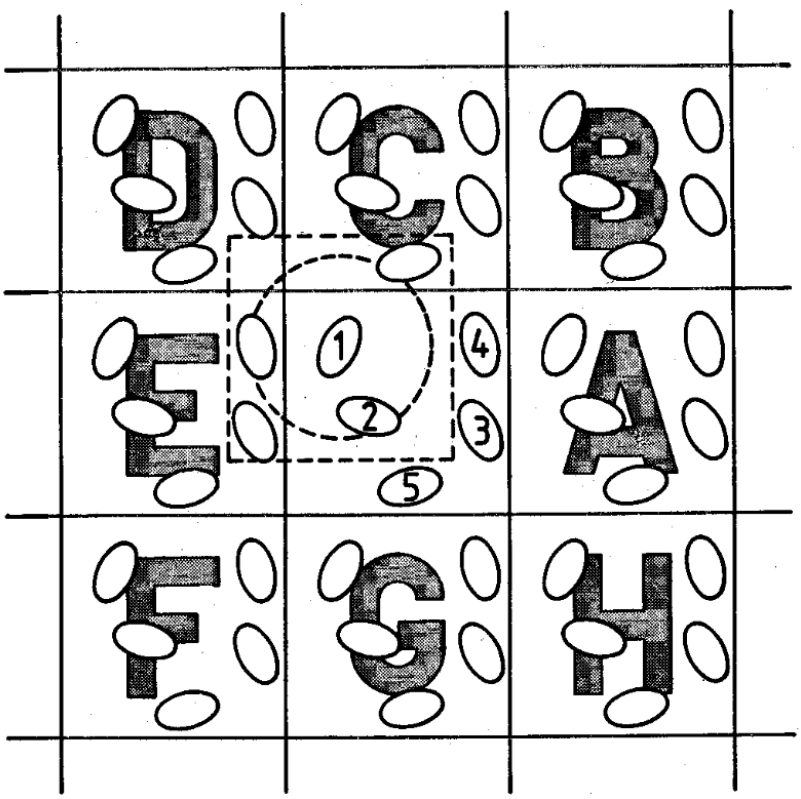

Figure 2.4: Periodic boundary conditions of the central square, the minimum image convention (the square around particle 1, dashed line) and the potential energy cut-off radius (the circle around particle 1, dashed line), for a 2D system[35].

modified by thermostats and/or barostats. The aforementioned ensembles are presented in figure 2.5

2.1.6.2 Thermostats

The temperature of the system is directly related to its total kinetic energy, thus in order to control it during an MD simulation, it is necessary to couple it to an external "heat bath" of fixed temperature T_0.

2.1.6.2.1 Berendsen thermostat

The Berendsen[42] is one of the most commonly used thermostats, due to its efficiency. It allows the weak coupling of the heat bath to the system through first-order kinetics by correcting every deviation of the system from the target temperature according to[25]:

$$\frac{dT}{dt} = \frac{T_0 - T}{\tau} \tag{2.18}$$

where τ is a time constant equal to:

$$\tau = \frac{2C_V\tau_T}{N_{df}k_B} \tag{2.19}$$

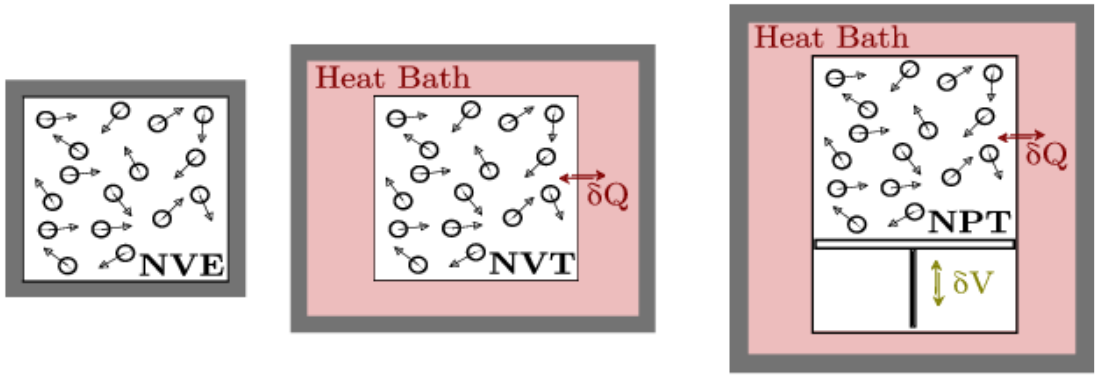

Figure 2.5: Thermodynamic ensembles commonly produced by MD simulations. The isolated constant-energy NVE, the constant volume and temperature NVT and the constant pressure and temperature NPT.

with C_V being the total heat capacity of the system, τ_T the temperature coupling time constant, N_{df} are the number of degrees of freedom of the system and k_B is Boltzmann's constant. In general, if τ_T is taken larger than 0.5 ps, the dynamics of the system are not significantly affected by the coupling and the temperature decays exponentially to the reference value. However, because the kinetic energy fluctuations are suppressed, the Berendsen thermostat cannot produce the correct canonical ensemble.

2.1.6.2.2 Nosè-Hoover thermostat

To circumvent the inability of the Berendsen thermostat to produce the canonical ensemble, the extended-ensemble approach was proposed by Nosè[43] and Hoover[44], by introducing in the equations of motion a term representing a "thermal reservoir", as well as a frictional term ξ[25]:

$$\frac{d^2\boldsymbol{r}_i}{dt^2} = \frac{\boldsymbol{F}_i}{m_i} - \frac{p_\xi}{Q}\frac{d\boldsymbol{r}_i}{dt} \tag{2.20}$$

with ξ being a quantity with its own momentum p_ξ and equation of motion. The time derivative of p_ξ is computed from the difference between current temperature T and the reference temperature T_0:

$$\frac{dp_\xi}{dt} = T - T_0 \tag{2.21}$$

where Q is the mass parameter of the thermal reservoir and together with T_0 define the strength of the coupling (similar to τ in the Berendsen). Although Nosè-Hoover thermostat enables canonical ensemble simulations, the relaxation of the temperature takes much longer and has an oscillatory behaviour.

2.1.6.2.3 Stochastic velocity rescaling thermostat

Another weak coupling thermostat, based on the Berendsen, is the stochastic velocity rescaling proposed by Bussi et al.[45], where the addition of a stochastic term gives a correct kinetic energy distribution. The correction term of the kinetic energy distribution is:

$$dK = (K_0 - K)\frac{\delta t}{\tau_T} + 2\sqrt{\frac{KK_0}{N_f}}\frac{dW}{\sqrt{\tau_T}} \tag{2.22}$$

where K is the kinetic energy, τ_T the temperature coupling time constant defined in equation 2.19, N_{df} are the number of degrees of freedom of the system, δt is the timestep and dW is a Wiener process. The great advantage of this method is that it exponentially dampens temperature deviations, without the oscillations of the Nose-Hoover method and also, produces the correct canonical ensemble.

2.1.6.3 Barostats

Similar to thermostats, techniques that couple the system to a "pressure bath" have also been developed.

2.1.6.3.1 Berendsen barostat

Berendsen barostat[42] has a similar formulation to the thermostat. Instant pressure $\mathbf{P}$ is weakly coupled to the reference pressure $\mathbf{P}_0$ with first order kinetics by rescaling the coordinates and box vectors every n_{pc} steps, according to a scaling matrix $\boldsymbol{\mu}$:

$$\frac{d\mathbf{P}}{dt} = \frac{\mathbf{P}_0 - \mathbf{P}}{\tau_p} \tag{2.23}$$

$$\mu_{ij} = \delta_{ij} - \frac{n_{pc}\delta t}{3\tau_p}\beta_{ij}\left\{\mathrm{P}_{0ij} - \mathrm{P}_{ij}(t)\right\} \tag{2.24}$$

where δ_{ij} is Dirac's delta and β_{ij} is the isothermal compressibility of the system (for water at 1 atm and 300 K, β=4.6 $\times$ 10^{-10} Pa^{-1}). The main disadvantage of the Berendsen barostat is that it does not reproduce correctly the isothermal-isobaric NPT ensemble.

2.1.6.3.2 Parrinello-Rahman barostat

This technique was developed by Parrinello and Rahman[46] and is the pressure analogous of Nosè-Hoover thermostat. The equation of motion changes similarly:

$$\frac{d^2\boldsymbol{r}_i}{dt^2} = \frac{\boldsymbol{F}_i}{m_i} - \boldsymbol{M}\frac{d\boldsymbol{r}_i}{dt} \tag{2.25}$$

where $\boldsymbol{M}$ is:

$$\boldsymbol{M} = \boldsymbol{b}^{-1}\left[\boldsymbol{b}\frac{d\boldsymbol{b}'}{dt} + \frac{d\boldsymbol{b}}{dt}\right]\boldsymbol{b}'^{-1}. \tag{2.26}$$

The quantity $\boldsymbol{b}$ is a matrix representing the simulation box vectors and can be computed according to:

$$\frac{d^2\boldsymbol{b}}{dt^2} = V\boldsymbol{W}^{-1}\boldsymbol{b}'^{-1}\left(\mathbf{P} - \mathbf{P}_{\boldsymbol{ref}}\right) \tag{2.27}$$

where V is the volume of the box, $\boldsymbol{W}$ is a matrix parameter that determines coupling strength and $\mathbf{P}$ and $\mathbf{P}_{\boldsymbol{ref}}$ refer to the instant and reference pressure matrices, respectively. The prime notation indicates extended system variables. In the molecular dynamics software GROMACS, the inverse of $\boldsymbol{W}$ is defined as:

$$\left(\boldsymbol{W}^{-\mathbf{1}}\right)_{ij} = \frac{4\pi^2\beta_{ij}}{3\tau_p^2 L} \tag{2.28}$$

where β is the isothermal compressibility, τ_p is the pressure time constant and L is the largest box matrix element. The Parrinello-Rahman barostat has the advantage of returning the correct NPT ensemble, however, it takes much longer to reach the reference pressure and in case that the system is too far from equilibrium, it might lead to oscillatory behaviour.

2.2 Biological membranes

2.2.1 Lipid molecules

All living organisms are composed of cells, which are complex structures composed of four different organic macromolecules: polysaccharides, proteins, nucleic acids and lipids[17]. Cells are encapsulated by thin membranes, also known as plasma membranes, which among other functions, act as barriers and regulators of molecules' transportation between the cell and its environment. The backbone of the plasma membrane is the lipid bilayer, which is composed of hundreds of different lipid molecules that can be categorised primarily in three types; phospholipids, glycolipids and cholesterol, all characterised by an amphiphatic nature due to a polar and a non polar part. Cholesterol is a steroid and therefore structurally different from phospholipids and glycolipids. It has the four carbon rings of a steroid structure, as well as an extra short hydrocarbon chain and a hydroxylic group. It exists in all plasma membranes in various concentrations and its biological importance is paramount; cholesterol induces lipid domains[47], increases the thickness of lipid bilayers[48] and stabilises their structure ensuring a liquid-ordered phase[49].

Glycolipids are molecules that have a carbohydrate attached in the polar part, which protrudes outside the cell, in the aqueous environment[18]. Glycolipids are important for maintaining membrane stability, as well as for providing recognition sites for chemicals[50].

Phospholipids are the most common lipid molecules in biological membranes[18] and take their name from a phosphate group (figure 2.6a) linked to the backbone, either a sphingosine or glycerol, as a phosphate ester. Glycerophospholipids are the main components of lipid bilayers and the focus of this work. The phosphate group forms another phosphate ester link with an amino alcohol, comprising an amine and a hydroxyl group. There are several types of amino alcohols and in this work we examine the most commonly encountered, choline and ethanolamine. They both have a similar chemical structure but the former has methyl groups linked to the amine group instead of simple hydrogens like the latter (figures 2.6b and 2.6c). The amino alcohol in conjunction with the phosphate group form the polar part of the lipid molecule.

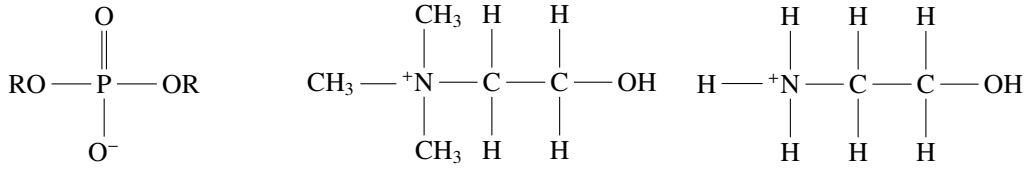

(a) Phosphate group (b) Choline (c) Ethanolamine

Figure 2.6: Commonly found moieties of the polar part of phospholipids in the plasma membrane.

The glycerol backbone, apart from the phosphate ester link, has two more ester links with fatty acids, comprising the non polar part of glycerophospholipids (figure 2.7). The fatty

acids are long hydrocarbons composed of many methanediyl groups ($-CH_2-$), a methyl group ($-CH_3$) attached in one end and a carboxylic acid ($-COOH$) attached to other. They can can have a large variety of lengths, typically between 14 to 22 carbon atoms and one or more double bonds. Fatty acids with no double bonds are called saturated, while with one or more double bond are called unsaturated. The double bond can be *cis* or *trans* depending on whether it creates a kink in the hydrocarbon chain or not, respectively.

(a) Glycerol

(b) Fatty acid structure with N number of carbon atoms

Figure 2.7: The backbone and non polar part of glycerophospholipids in the plasma membrane.

Based on the above, a phospholipid will have a structure similar to the one depicted in figure 2.8. Due to this polar/apolar coexistence, when phospholipids are found in an aqueous environment, they do not dissolve but instead self-assemble into lipid aggregates. This phenomenon is called the hydrophobic effect which is apparent in all mixtures of water and oils and is driven by entropy. Water molecules can form up to 4 hydrogen bonds with neighbouring water molecules, resulting in a highly dynamic, loose network of hydrogen bonds that is stabilised by maximum system* entropy[17]. Oils are mainly composed of hydrocarbon chains, which despite the fact that they can have dipole-dipole interactions with water molecules, they are incapable of forming hydrogen bonds. Therefore, when a non polar molecule is dispersed into water molecules, the latter reorient themselves around it, in a structured solvation shell, in order to maintain as much as possible, the previous dynamic hydrogen bond network. Also, the mobility of the surrounding water molecules is restricted and the entropy of the system is reduced, making the whole process unfavourable, as it can also be seen by Gibbs free-energy $\Delta G = \Delta H - T\Delta S$, where H is the enthalpy, T is the temperature and S is the entropy. Therefore, in order to minimise this disruptive behaviour, the non polar molecules aggregate and reduce the available surface that is in contact with water[51].

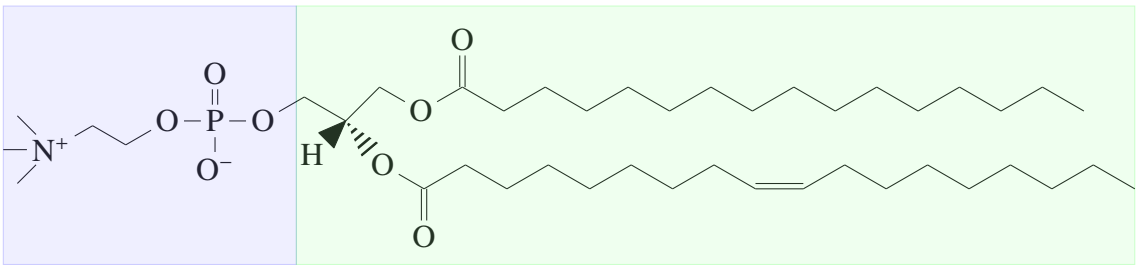

Figure 2.8: The polar(blue)/apolar(green) structure of a typical phospholipid, the 1-palmitoyl-2-oleoyl-sn-glycero-3-phosphocholine (POPC).

*System refers to the cooperative hydrogen bonds network of all water molecules

As it was mentioned already, lipid molecules vary widely in terms of size, chemical structure or polarity. Due to many possible corresponding compositional differences, lipid assemblies can display a variety of different physical properties and structures[17] (figure 2.9). One of the driving factors governing the form of the lipid aggregate is the lipid molecule shape[17,52], defined according to a packing parameter $\mathcal{P}$:

$$\mathcal{P} = \frac{v}{al} \tag{2.29}$$

where a is the cross-sectional area of the polar region and v and l are the volume and length of the non polar region. For cylindrically-shaped lipids, where $P \approx 1$, lipids typically self-assemble into lamellar bilayer structures, where the hydrophilic heads are submerged into the aqueous environment and the hydrophobic tails are isolated in the centre (figure 2.9d). Under standard thermodynamic conditions, as lipids' shapes deviate from the cylindrical, they tend to form non lamellar phases such as the conically shaped lipids (smaller polar than apolar part), which form inverse hexagonal structures with long lipid tubes filled with water molecules[53] (figure 2.9b). The lamellar bilayer form is the most commonly found in biological systems and is the predominant form of the plasma membrane.

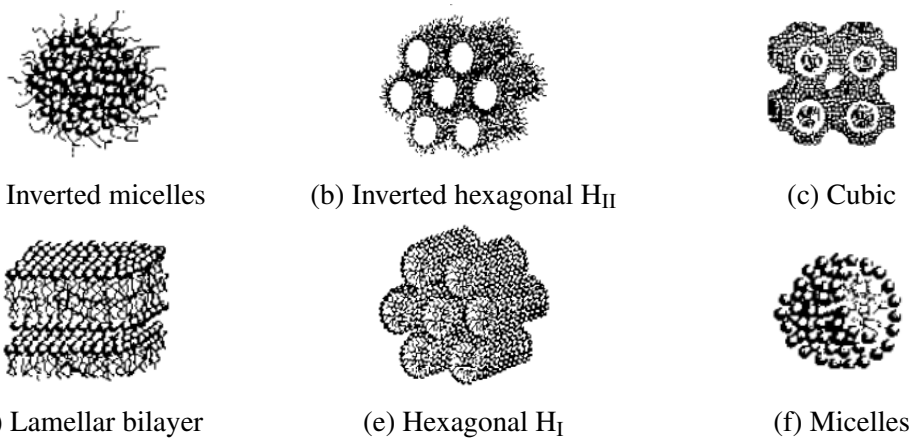

(a) Inverted micelles (b) Inverted hexagonal H_{II} (c) Cubic

(d) Lamellar bilayer (e) Hexagonal H_I (f) Micelles

Figure 2.9: Various lipid aggregates forms in aqueous environment[17]. Top left refers to lipids of packing parameter $P > 1$, the lamellar bilayer has $P \approx 1$ and the bottom right micelle refers to $P < 1/3$.

2.2.2 Lipid bilayers

2.2.2.1 Phase behaviour

When lipid molecules self-assemble into aggregates of any form, they can undergo two different kinds of phase transitions. The first type of transition is related to the aggregate morphology, in which by changing various parameters such as the lipid hydration, aggregates can transform between the structures presented in figure 2.9. The second transition type is internal for each different form, in which properties change between the solid crystalline, the ordered liquid-crystalline (gel) phase, the disordered liquid-crystalline (smectic) phase and liquid phase. In the smectic liquid-crystalline phase, which is the form lipid bi-

layers adopt in biological applications under physiological conditions, lipid molecules are ordered in separate planes similar to solid crystals and also retain an orientation. However, within each plane they are disordered and monolayers exhibit liquid phase characteristics (figure 2.10b).

Different lipids undergo all or parts of the aforementioned transitions. On one hand, medium-chainlength phosphatidylcholines experience transitions in consecutive lamellar phases by increasing the temperature[54]:

$$L_c \longrightarrow L_{\beta'} \longrightarrow P_{\beta'} \longrightarrow L_\alpha \tag{2.30}$$

where L_c is the solid crystalline phase (figure 2.10a), $L_{\beta'}$ is the gel phase with tilted lipid chains, $P_{\beta'}$ is the rippled gel phase and finally L_α is the liquid-disordered phase (figure 2.10b). On the other hand, phosphatidylethanolamines do not display a rippled gel phase and their gel phase L_β does not have tilted chains:

$$L_c \longrightarrow L_\beta \longrightarrow L_\alpha. \tag{2.31}$$

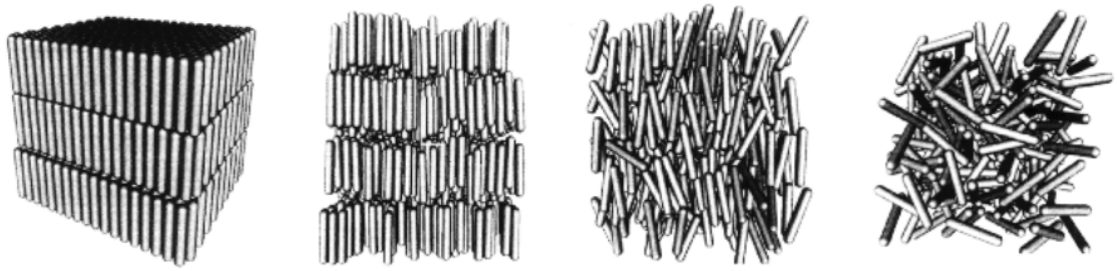

(a) Crystalline (b) Smectic l.c. (c) Nematic l.c. (d) Liquid

Figure 2.10: Different phases of elongated model molecule aggregates[17]. Lipid bilayers of biologically relevant systems, exist in a smectic liquid crystalline meso-phase.

2.2.2.2 Structure

The structure of the plasma membrane has been interpreted and revised numerous times during the 20th century; from the simple lipid bilayer of Gorter and Grendel[55] in 1925 to the popular fluid mosaic model of Singer and Nicolson[56] in 1972, to more modern complex and sophisticated models[57–59]. Despite the plethora of interpretations, the key building block of the membrane remains the lipid bilayer.

The actual characterisation of the real structure of the lipid bilayer in non trivial, as in the biologically relevant L_a phase, the hydrocarbon chains are conformationally disordered. Consequently, there is not a single representative correct atomic description of the structure but rather a statistical distribution function that incorporates the fluctuations of fully hydrated liquid-disordered bilayers[60]. Experiments, such as X-ray diffraction are usually done on multilamellar arrays of lipid bilayers (figure 2.11) and can yield density profiles

which show the probability distribution of different chemical moieties along the bilayer thickness (figure 2.12b). Similar density profiles can also be produced with molecular dynamics simulations which also provide an atomistic representation of the bilayer. When the two density profiles are qualitatively and quantitatively similar, an accurate depiction of the bilayer structure can be obtained (figure 2.12a).

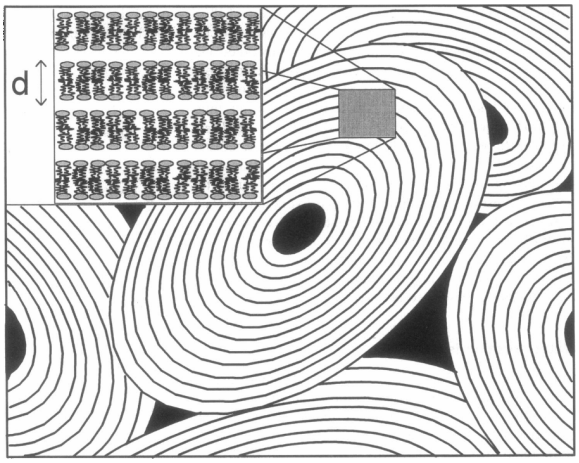

Figure 2.11: Multilamellar lipid membrane stacks of thickness d, commonly used in experimental studies[61].

From figure 2.12 it is clear that lipid membranes are heterogeneous structures that can be separated in a few different distinct regions according to the density of water and the chemical moieties of lipid molecules[60,62–64]. The first region comprises the lipid headgroups and the water molecules that hydrate them. The second region is the polar/apolar interface where the polar water molecules come into contact with the apolar lipid chains and due to the hydrophobic effect, give rise to the minimisation of surface and the forming of the interface. Also this is the region where the headgroups are predominantly positioned. Finally, the third region includes the lipid chains which can be separated in the high order part, close to the interface and the low-order part close to the bilayer centre.

Apart from the electron density profile presented above, there are several other physical properties that allow the quantitative definition of a lipid bilayer structure. Using the density profile one can identify the bilayer thickness as the distance between the two phosphate group peaks, namely the head-head thickness d_{HH} obtained both experimentally and computationally. More details on the available techniques for the measurement of d_{HH}, as well as the challenges on the agreement of results between them are presented on a recent review written by Nagle in 2013[64].

The average area and volume per lipid are also commonly used properties for the understanding of the bilayer structure. In simulations, their computation is trivial and is based on readily available variables of the simulation box[22,65]. In particular, the average area per lipid A_L can be computed as

$$A_L = \frac{A_{xy}}{N_L} \tag{2.32}$$

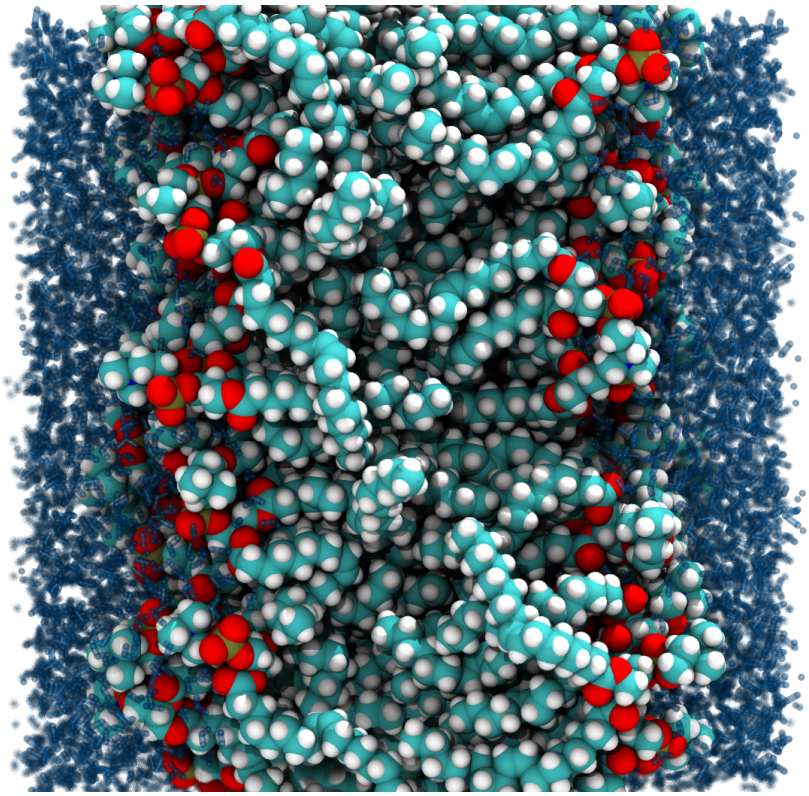

(a) DOPC bilayer

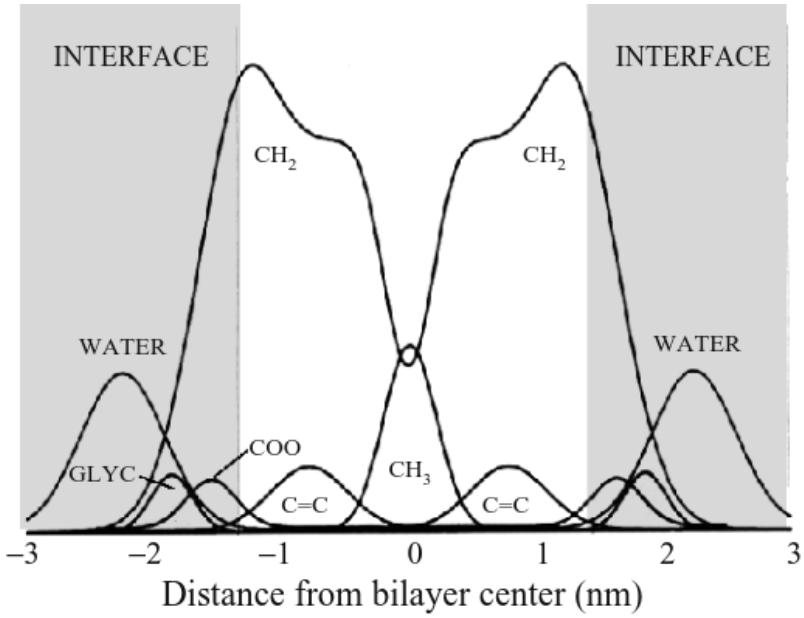

(b) The density profile of the chemical components of DOPC

Figure 2.12: Atomistic representation of a 1,2-dioleoyl-sn-glycero-3-phosphocholine (DOPC) bilayer from a molecular dynamics simulation and a density profile of DOPC obtained from experiments[17]. Water molecules are represented with transparent dark blue, carbon atoms with cyan, oxygen atoms with red, phosphorus atoms with gold and nitrogen atoms with blue.

where A_{xy} is the total area of the simulation box on the xy plane (parallel to the polar/apolar interface) and N_L is the number of lipid molecules per leaflet. While this method has been found to underestimate the real area per lipid because of undulations, in practice the calculated error is negligible for less than 1000 lipid molecules per bilayer[66,67]. The average volume per lipid V_L is similarly computed as:

$$V_L = \frac{V_{box} - V_{water}}{N_L} \tag{2.33}$$

where V_{box} is the volume of the simulation box and V_{water} is the total volume of water molecules. Experimentally, both A_L and V_L require more sophisticated processes to be measured and several techniques have been developed, presented in detail in a review by Nagle and Tristam-Nagle[60].

Furthermore, examination of the acyl chains can also provide valuable insight on the structure of the bilayer core. One commonly used method involves the measurement of the average orientation of the carbon-deuterium bonds, namely deuterium order parameter S_{CD}, which indicates the overall anisotropy of lipid chains. It can be measured both experimentally through nuclear magnetic resonance[60,61,63] (NMR) or through MD simulations[25,68], as:

$$S_{CD} = \frac{1}{2}\langle 3\cos^2\theta_i - 1\rangle \tag{2.34}$$

where θ_i is the angle between the C-D vector and axis normal to bilayer surface. The angular brackets represent an ensemble average.

Finally, an important open question regarding the structure of bilayers is the formation of domains of same lipids[69,70]. Experimentally, identifying any lateral organisation that would indicate the existence of a domain has been a challenging task with controversial results until very recently[71]. Computationally, this can be done with a nearest neighbour analysis[65,68] where the fraction f_{X-X} of each lipid type X can be computed by:

$$f_{X-X} = \frac{N_X}{N} \tag{2.35}$$

where N_X is the number of nearest lipid type X neighbours and N is the total number of nearest neighbours (suggested as 4 by de Vries et al.[68]).

2.2.2.3 Lateral pressure profile

Lamellar lipid bilayers in mechanical equilibrium are by definition, stress free. However, internally are very inhomogeneous structures with an anisotropic distribution of stresses that vary as a function of depth within the membrane but also compensate each other in magnitude (figure 2.13). If the interactions between the individual monolayers' terminal methyl groups are neglected as relatively small, the rest of the stresses can be decomposed to three different force contributions, a repulsive, an attractive and a mixed repul-

sive/attractive (depending on the lipids) (figure 2.13a). Repulsive forces produce positive lateral pressure contributions, while attractive forces produce negative (figure 2.13b).

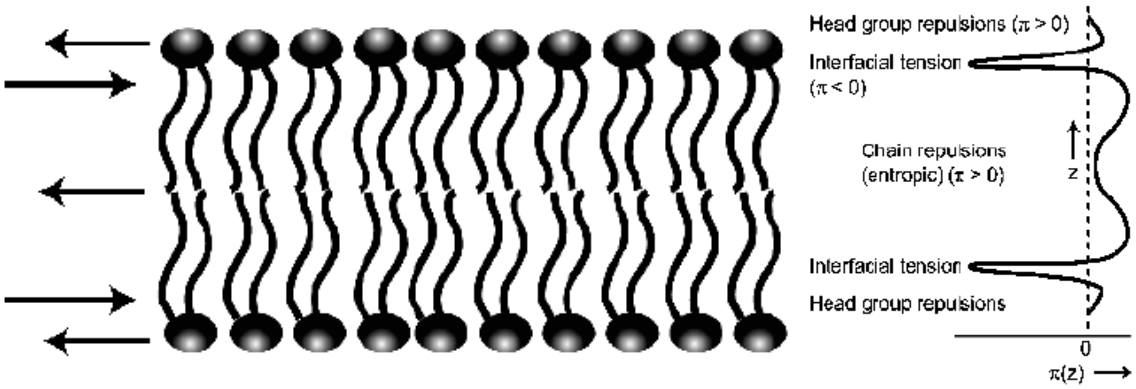

(a) Pressure contributors (b) Pressure profile

Figure 2.13: The lateral pressure profile of a lipid membrane[17]. On the left are shown the forces that contribute on the pressure profile and on the right are shown the positive and negative lateral stresses π_n as a function of bilayer depth z.

In the polar part of the bilayer, depending on the lipid headgroups, there can be repulsive forces due to charges or steric and hydrational effects or attractive forces due to enhanced hydrogen bonds formation between them[72]. In the hydrophobic/hydrophilic interface, there are strong attractive forces, induced by the hydrophobic effect, where the system entropy drives a minimisation of the interface area. Finally, along the hydrophobic region of the bilayer, there are more repulsive forces due to the thermal fluctuations and the conformational entropy of the hydrocarbon chains. Overall, the tension-free bilayer has a mechanical equilibrium expressed as[73]:

$$\pi_{\text{hydrophobic effect}} = \pi_{\text{steric}}\left(A_L^0\right) + \pi_{\text{hydration}}\left(A_L^0\right) \tag{2.36}$$

where A_L^0 is the equilibrium area per lipid and π_i are the lateral pressure contributions due to the hydrophobic effect $\pi_{\text{hydrophobic effect}}$, the inter- and intra- molecular interactions π_{steric} and the headgroup hydration interactions $\pi_{\text{hydration}}$.

The lateral pressure profile $\Pi(z)$ incorporates all the interactions that exist in the membrane and thus has been described as the most fundamental membrane property[17]. It is affected by the lipid composition[22,74–79] or alcohols in large concentrations[80–82] and can have a significant impact on phase transition[83,84], water penetration[85] and drug transport[86,87], anaesthesia[88–91] and functioning of proteins[92–98].

Quantitative measurements of the lateral pressure profile have been very difficult to perform experimentally, because the probing of such a thin, flexible structure introduces stresses that make measurements void. In the past, pyrene enriched PC lipids such as dipyrenylphosphatidylcholine (dipyPC) have been used to obtain qualitative lateral pressure profiles by relating the excimer/monomer fluorescence ratio to the localised pressure of the pyrene

moieties[72,85,99]. However, a more recent molecular dynamics study by Fraňová et al.[100] indicated that the lateral pressure profile was not the dominant factor of the fluorescence ratio. Therefore, at the moment, quantitative lateral pressure profiles can be obtained only by analytical models[101] or molecular dynamics simulations[22]. For the latter, the simulation region is separated along the z direction in different slabs that are parallel to the bilayer surface. The lateral pressure profile can be then defined as[102]:

$$\Pi(z) = \frac{\mathrm{P}_{xx}(z) + \mathrm{P}_{yy}(z)}{2} - \mathrm{P}_{zz}(z) \tag{2.37}$$

where P_{xx}, P_{yy} and P_{zz} are the diagonal elements of the pressure tensor in each slab. Typically, lipid bilayers are simulated with planar symmetry for pressure and thus $\mathrm{P}_{xx}(z) = \mathrm{P}_{yy}(z)$, while P_{zz} is always constant for all slabs and equal to the external pressure imposed to the system. Therefore, to compute the pressure profile only the pressure contributions in one of the lateral directions are needed. There are two commonly used methods for the calculation of the pressure contributions per slab, the Irving-Kirkwood[103] and the Harasima[104], that are explained in detail by Ollila and Vattualainen[102].

2.2.2.4 Elastic properties

Biologically relevant lipid membranes are fluid and are susceptible to two elastic deformations, stretching and bending[17] (figure 2.14). The stretching deformation can be defined by the energy that is required to stretch a surface of area A_0 in order to produce an area change ΔA, according to:

$$E_{\text{stretch}} = \frac{1}{2}\kappa_A \left(\frac{\Delta A}{A_0}\right)^2 \tag{2.38}$$

where κ_A is the area compressibility modulus.

(a) Stretching (b) Bending

Figure 2.14: Elastic deformations of fluid membranes[17].

The elastic bending of a generic surface with zero thickness can be defined by the energy per unit area that is required to bend an element of area dA, as[105]:

$$dE_{\text{bending}} = \left[\frac{1}{2}\kappa_b H_c^2 + \kappa_G G\right] dA \tag{2.39}$$

where κ_b and κ_G are the bending modulus and Gaussian curvature modulus, respectively.

The term H_c is the mean curvature of the surface defined as:

$$H_c = \frac{c_1 + c_2}{2} \tag{2.40}$$

and the term G_c is the Gaussian curvature of the surface defined as:

$$G_c = c_1\, c_2 \tag{2.41}$$

where $c_1 = 1/\mathrm{R}_1$ and $c_2 = 1/\mathrm{R}_2$ are the surface principal curvatures of radii R_1 and R_2, respectively.

Equation 2.39 refers to a surface of zero thickness. However, lipid bilayers comprise two monolayers which have a spontaneous curvature depending on the lipids' shape (section 2.2.1), which in turn is an indication of where the interfacial tension balances, the headgroups or the chains[106]. In most physiological conditions, monolayers have a spontaneous curvature which leads to a bilayer with an intrinsic tendency to deform even when no external force is applied. In order to accommodate this extra curvature term, the bending energy per area of the monolayer becomes:

$$dE_{\text{bending}} = \left[\frac{1}{2}\kappa_b\,(c_1 + c_2 - 2c_0)^2 + \kappa_G\, c_{,}c_2\right] dA \tag{2.42}$$

where c_0 is the spontaneous curvature of the monolayer. By convention spontaneous curvature is negative when the membrane bends towards the exterior and positive when it bends towards the interior (figure 2.15).

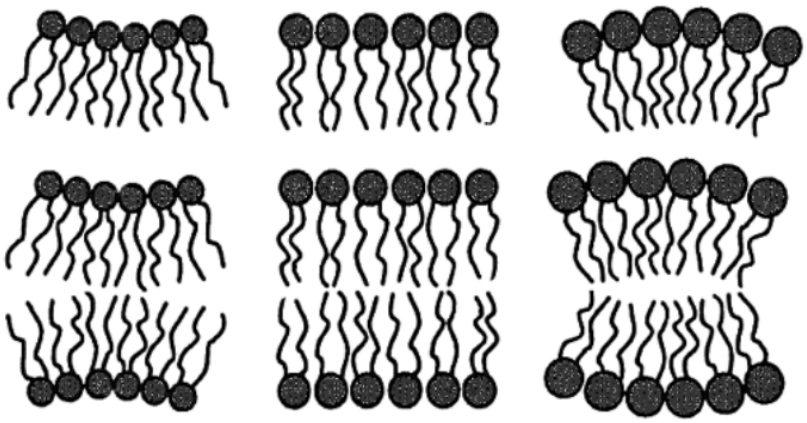

Figure 2.15: Spontaneous curvature of monolayers and bilayers. From left to right: negative, zero and positive curvature[17].

It is clear that when a monolayer has an intrinsic curvature but is forced to stay flat inside the bilayer, there is a stored elastic energy in the system equal to $2\kappa_b c_0^2$ which is the case for the lamellar lipid bilayers of biological importance[72]. This stored elastic energy creates a lateral torque tension τ_L in the monolayer that can be computed by the first moment of the lateral pressure profile $\Pi(z)$ and can be directly related to the product of bending modulus

and spontaneous curvature [106]:

$$\tau_L = \int z\,\Pi(z)dz = -\kappa_b c_0. \tag{2.43}$$

If both the monolayers are symmetrical in the bilayer, the torque tension will be zero. The second moment of the lateral pressure profile, however, will not necessarily be zero and will equal to the Gaussian modulus:

$$\kappa_G = \int z^2\,\Pi(z)dz. \tag{2.44}$$

2.3 Spontaneous passive permeation

2.3.1 Physical model of passive permeation

Permeation phenomena are crucial for the existence of life. Cells during their lifetime depend on the external and internal membranes, to compartmentalise biological components and processes. There are three main mechanisms of molecule transportation through membranes; passive, facilitated and active. Passive permeation is the dominant mechanism for the majority of neutral small molecules or drugs [107] and is driven by the concentration gradient of the substance across the membrane (figure 2.16). Facilitated permeation is also driven by the concentration gradient but it also requires a carrier protein to occur. Both passive and facilitated permeation do not require energy. Finally, active permeation, requires not only a carrier protein but also energy because it occurs against the concentration gradient.

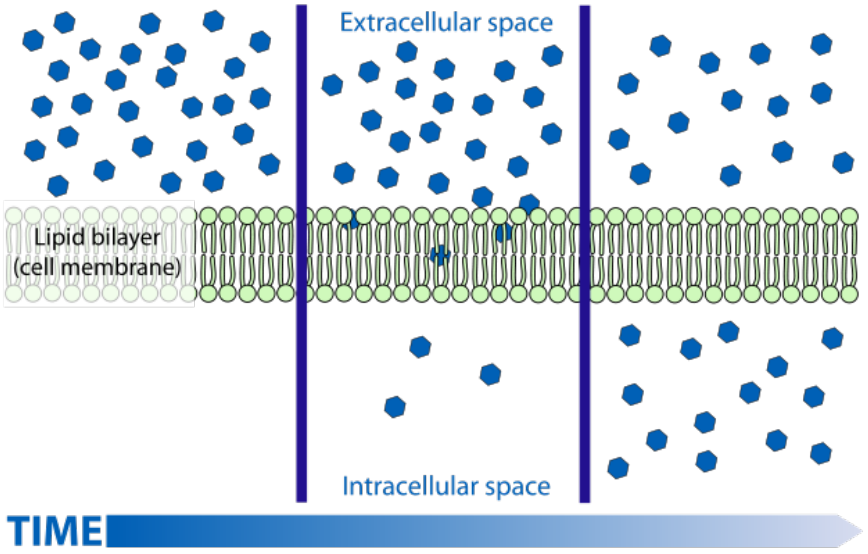

Figure 2.16: Passive permeation of a substance over time [108].

This project focuses on passive permeation since it is the predominant transportation mechanism for small molecules and drugs [109]. Fick's law of diffusion predicts the transport of a substance along a concentration gradient of a membrane as [110]:

$$J = PA\,(C_{in} - C_{out}) \tag{2.45}$$

where J is the transport flux ($\mathrm{mol\,s^{-1}}$), $(C_{in} - C_{out})$ is the concentration gradient across the membrane, A is the total surface of the membrane ($\mathrm{cm^2}$) and P is the permeability coefficient ($\mathrm{cm\,s^{-1}}$).

Meyer and Overton [111,112] correlated the permeability of a molecule through a lipid bilayer to its octanol-water partition coefficient $\log P_{\mathrm{oct/water}}$. The latter is an indication of the solubility preference of the solute between a phase of octanol and a phase of water and it is defined as

the ratio of concentrations between the two phases. Based on this observation by Meyer and Overton, the bulk solubility-diffusion model of permeability was proposed[113], in which the membrane was considered a homogeneous "oily" bulk body. The permeability P through that bulk body could then be predicted by:

$$P = \frac{K\,D}{h} \tag{2.46}$$

where K is the bulk oil/water partition coefficient and D is the diffusion coefficient of the solute, inside the membrane of thickness h.

The idea of a homogeneous hydrophobic bulk phase however was not an adequate representation of a complex mixture of molecules that comprise both polar and apolar moieties, as well as other unique structural characteristics. Therefore, the inhomogeneous solubility-diffusion model was proposed by Diamond et al.[114], according to which the permeation P of a solute through a membrane can be predicted from:

$$\frac{1}{P} = \int_{z1}^{z2} R(z)dz = \int_{z1}^{z2} \frac{1}{K(z)D(z)}dz \tag{2.47}$$

where z is the position normal to the bilayer surface with $z1$ and $z2$ representing the bulk water regions on the two sides of the membrane. Also, $R(z)$ is the local resistance to permeation, $D(z)$ is the local diffusion coefficient of the solute and $K(z)$ is the partition coefficient between the water phase and the position z inside the membrane.

2.3.2 Experimental methods to compute permeation coefficients

As it can be seen from equation 2.47, permeation is a property that depends on the solute partitioning and the diffusion of the solute inside the membrane. Experimentally there are no methods to measure the two components explicitly. In particular, experiments can only measure the partition coefficients for the most favourable partition positions of a solute inside the membrane. Also, it is close to impossible to isolate the diffusion coefficient component for the normal to bilayer surface direction[110].

Despite the aforementioned limitations, experiments allow the measurement of the overall permeation coefficient through the application of Fick's law (equation 2.45). The reported experimental measurements however, can often vary by orders of magnitude for the same permeant, depending on the conditions, instruments and methods used by each laboratory[115,116]. It it therefore common to rely on the relative permeation predictions between solutes rather than the absolute values[20].

2.3.2.1 Black lipid membranes - BLM

One of the first experimental methods used to measure permeability was the "painted" lipid bilayers, also known as the black lipid membranes[113,117–119] (BLM). In this method, a hydrophobic material, usually Teflon, is used to partition a chamber filled with a solvent. A sub-millimetre diameter aperture is opened in the Teflon sheet, which is coated with a mixture of decane and squalene. Then it is further coated with lipid molecules, forming a lipid bilayer in the middle of the hole (figure 2.17). One part of the chamber is then injected with the molecule to be examined and after an incubation time, the concentration difference between the donor and acceptor chamber is measured.

The apparent permeation coefficient is computed according to[117]:

$$P = \frac{dC_{\text{receiver}}}{dt} \cdot \frac{V_{\text{chamber}}}{A\, C_{\text{donor}}} \tag{2.48}$$

where V_{chamber} is the volume of water in each chamber, C_{receiver} is the concentration of the molecule in the receiver chamber, C_{donor} is the concentration of the molecule in the donor chamber and A is the average bilayer surface. This method has several disadvantages such as residual apolar solvent trapped between the two bilayer leaflets, reduced stability and limited lifetime.

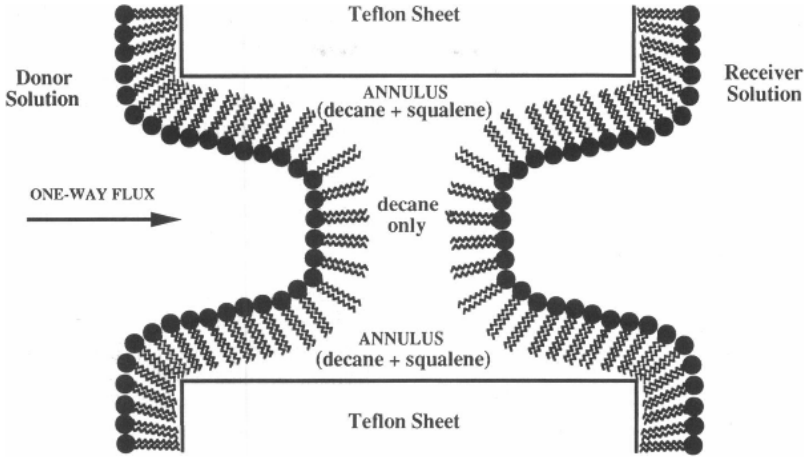

Figure 2.17: Schematic of a typical black lipid membrane apparatus[117].

2.3.2.2 Lipid vesicles

An alternative technique which was less popular than BLM, involved the measurement of molecular concentrations across large unilamellar lipid vesicles[115,120,121]. The vesicles were lipid bilayers that formed a spherical shell, trapping a small amount of water inside, allowing for a concentration gradient to be created between the two bilayer leaflets. For permeation studies, this method, as well as BLM, have been mostly succeeded by other, more robust, simple and accurate techniques (described in the following sections).

2.3.2.3 Caco-2 cell monolayers

The Caco-2 cell monolayers are heterogeneous cell lines of human colorectal adenocarcinoma cells which are cultured under specific conditions to approximate the morphology and function of intestinal epithelium cells. The monolayer is supported by a permeable filter which divides two stacked microwell plates (figure 2.18) in one of which the examined molecules are injected. The concentration in the two plates is then measured and the apparent permeability coefficient P_{app} is computed according to[122]:

$$P_{app} = \frac{dQ/dt}{C_0 A} \tag{2.49}$$

where dQ/dt is the rate of permeation of the molecule, C_0 is the initial concentration of the molecule in the donor plate and A is the area of the cell monolayer surface.

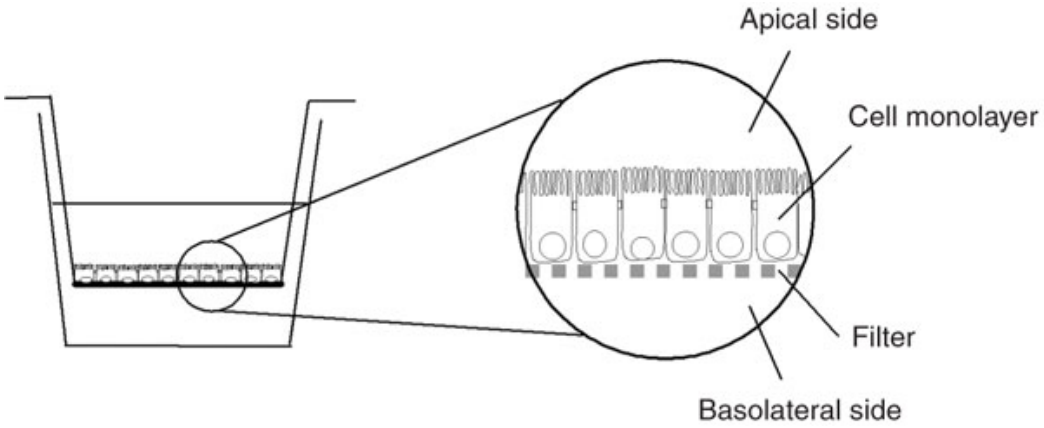

Figure 2.18: Schematic of a Caco-2 monolayer permeability assay, in which the monolayer is supported by a permeable filter[123].

Caco-2 cell monolayers is an *in vitro* permeability assay based on the pioneering work of Fogh and Trempe[124] that begun developing in the early 90s and soon was widely accepted by the pharmaceutical industry as the "gold-standard" method, due to the good correlation of measured Caco-2 apparent permeability and orally administered drug absorption[125].

This method, however, is characterised by certain disadvantages. Firstly, since the monolayers are composed of cells, all possible membrane transportation mechanisms are taking place in the permeation which makes hard the identification of particular contributions (e.g., passive vs. active). Furthermore, depending on the initial cells and culture techniques, the cell monolayers might vary in consistency, creating a discrepancy between different studies and laboratories[126]. Finally, experimental assays with Caco-2 cells usually require a long time to be completed due to the long culture times which can take up to 20 days[126].

2.3.2.4 PAMPA

In the late 90s another *in vitro* permeability assay was developed by Kansy et al.[127]. The parallel artificial membrane permeability assay (PAMPA) comprises a similar, "sandwich" setup as Caco-2 assays, in which a donor compartment at the bottom and an acceptor compartment at the top, are separated by an artificial membrane infused with several lipid bilayers (figure 2.19). The molecule to be examined is injected in the donor compartment and after a certain incubation time, the concentration in the two compartments is measured to compute permeation.

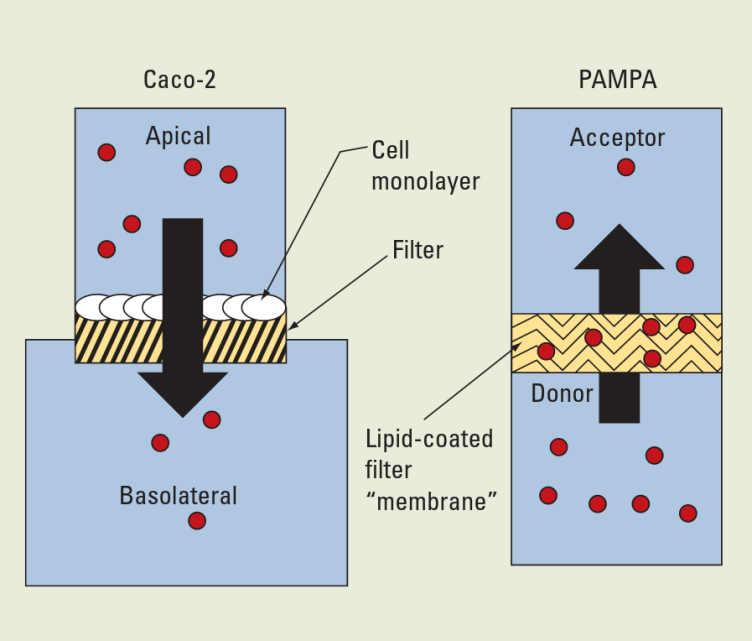

Figure 2.19: Comparison schematic between Caco-2 assays and PAMPA[126].

In contrast to Caco-2 assays, PAMPA allows for better control over the membrane consistency and is able to reproduce more and different cellular environments such as Caco-2[128,129] or the blood-brain barrier[130]. Another important advantage is that the only transportation mechanism examined through the artificial membrane is passive permeation, leading to more consistent results between experiments and more reliable drug screening. Finally, the only required time for PAMPA is the incubation time which can be from a few minutes to a day[20], which is much faster than Caco-2, resulting in a reduction in the overall cost of the process.

2.3.3 *In silico* methods to compute permeation coefficients

Although experimental methods cannot provide details on the separate components of the passive permeation mechanism such as the partitioning and the diffusion, several *in silico* methods have been developed to try and predict the underlying physical phenomena such as molecular dynamics or quantitative structure–activity relationship models (QSAR).

Molecular dynamics techniques has been a particularly popular choice, because they offer

quantitative examination of the interactions of the permeant with the membrane[110]. Over the years several permeation-specific techniques have been developed, and a few of them have become especially popular, with the z-constraint and the z-restraint methods being the most prominent. In the following sections the most commonly used methods will be presented together with their limitations and strengths.

2.3.3.1 Unbiased MD simulations

One of the simplest techniques to obtain permeation coefficients is to perform unconstrained molecular dynamics simulations and measure the mean residence time of the permeant at a certain position z. In particular, the partition coefficient $K(z)$ of equation 2.47 can be computed as:

$$K(z) = \frac{t_z}{t_w} \tag{2.50}$$

where t_z is the the total time the permeant spends at a given position $z \pm \Delta z$, and t_w is the total time it spends in the neighbouring water region.

The major drawback of this method is that there is no robust way to compute local diffusion coefficients and thus compute reliable permeation coefficients. Furthermore, obtaining converged results requires very long simulation times in order to allow sufficient sampling of unfavourable partitioning positions. This is especially needed in cases where the permeants are either very hydrophillic or very hydrophobic and thus might not even visit certain membrane regions[131]. Finally, although increased number of permeants generally increase the sampling frequency and thus the computational efficiency, a high concentration of permeants might disrupt certain physical properties of the membrane[132,133].

2.3.3.2 Biased MD simulations

Due to the aforementioned limitations of unconstrained simulations, the majority of permeation studies are performed with biased molecular dynamics, where an artificial potential/force is applied to the permeant in order to sample unfavourable partitioning regions. Berendsen and Marrink[62,134] in 1993 and 1994 extended the inhomogeneous solubility-diffusion model to relate the properties of equation 2.47 to properties that can be obtained directly from biased molecular dynamics simulations. In particular, the partition coefficient is calculated as:

$$\frac{1}{K(z)} = \exp\left[\frac{\Delta G(z)}{RT}\right] \tag{2.51}$$

where T is the simulation temperature, R is the universal gas constant (which is equal to the product of Boltzmann's constant k_B with Avogadro's number N_A, $R = k_B \cdot N_A$) and $\Delta G(z)$ is the free-energy difference between the thermodynamic states of the permeant at bulk water and position z. Specifically, the free-energy difference represents the thermodynamic forces (entropic and enthalpic)[135] that drive the process of permeation, quantifying its spontaneity

and preferred partitioning position. Equation 2.47 then becomes:

$$\frac{1}{P} = \int_{z_1}^{z_2} \exp\left[\frac{\Delta G(z)}{RT}\right] \frac{1}{D(z)} dz \tag{2.52}$$

which relates the permeability coefficient to the free-energy difference $\Delta G(z)$ and the local diffusion coefficients $D(z)$, which both vary along the permeation direction. In order to obtain $\Delta G(z)$ and $D(z)$, several enhanced sampling methods have been developed, such as the z-constraint or the z-restraint which are further discussed in the following sections. More details on the different simulation techniques can be found in several excellent publications on the topic [136–138].

2.3.3.2.1 The z-constraint method

In the z-constraint method [62,134], the permeant is placed in selected z positions along the bilayer (the direction normal to the bilayer surface) and is allowed to move freely on the xy plane while its movement on the z direction is constrained. The free energy difference is obtained by the potential of mean force according to:

$$\Delta G(z) = -\int_{\text{water}}^{z} \langle f_c(z') \rangle dz' \tag{2.53}$$

where f_c is the force applied to the centre-of-mass of the permeant to constrain its z-direction movement and $\langle \cdots \rangle$ indicates an ensemble average over the simulation time.

Local diffusion coefficients along the z-direction can also be calculated by the constraint force according to:

$$D(z) = \frac{(RT)^2}{\int_0^\infty \langle \delta f_c(z,t) \delta f_c(z,0) \rangle dt} \tag{2.54}$$

where the denominator is the characteristic time of the unnormalised form of the autocorrelation function of the constraint force. According to its definition $\delta z(t) = z(t) - \langle z \rangle$ is the deviation of the instantaneous force from the average force acting on the permeant.

The main disadvantage of the method is that it is not directly implemented in most of the available molecular dynamics software and requires custom MD codes [139] or special usage of modular codes, such as LAMMPS. Also, the instant force is a widely fluctuating property and requires frequent sampling to ensure reliable uncertainty prediction for both the free-energy differences and diffusion coefficients.

2.3.3.2.2 The z-restraint method

The z-restraint method is not a single methodology proposed by one research group or paper, but rather a combination of methods that can be combined, proposed over the last

two decades and from several groups. With this method, the free-energy difference can be obtained by using the umbrella sampling method[140], where a potential is used (typically a harmonic) to restrain the movement of the permeant in a small "window" around each position along the z-direction (the reaction coordinate path) (figure 2.20). The free-energy difference is then calculated based on:

$$\Delta G(z) = -RT\ lnP_b(z) + V_b(z) \tag{2.55}$$

where $V_b(z)$ is the biasing potential and $P_b(z)$ is the permeant's spatial distribution along z positions. Usually umbrella windows have to overlap in order to ensure a smooth sampling distribution. Finally, in order to obtain the unbiased potential of mean force (PMF) and thus the free-energy difference ΔG, the weighted histogram analysis method (WHAM) is used[141,142].

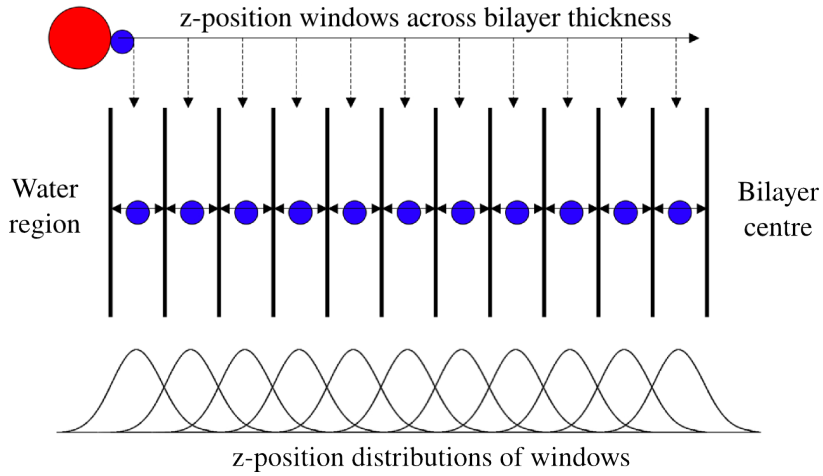

Figure 2.20: Schematic of the umbrella sampling method[143]. The red circle is the permeant and the blue circles are the different positions along the z-direction, in which the permeant is restrained in a small "window".

Computing reliable local diffusion coefficients $D(z)$ from restrained simulations is still a very active research field. At the moment, the most popular method is the one introduced by Hummer[23] in 2005, based on the previous works of Berne et al.[144] and Woolf and Roux[145]. In this method, when umbrella sampling simulations are performed with a harmonic bias along a reaction coordinate, such as the z-direction normal to bilayer surface, the diffusion can be computed as:

$$D(z\ =\ \langle z\rangle) = \frac{\mathrm{var}(z)}{\tau} \tag{2.56}$$

where $\langle z\rangle$ is the average of the z distance between the centres-of-mass of the permeant and membrane, $\mathrm{var}(z) = \langle z^2\rangle - \langle z\rangle^2$ is its variance and τ is the characteristic time of its autocorrelation function:

$$\tau = \int_0^\infty \frac{\langle \delta z(t)\delta z(0)\rangle}{\mathrm{var}(z)} dt \tag{2.57}$$

where according to the definition of the autocorrelation function $\delta z(t) = z(t) - \langle z\rangle$.

In 2012, Zhu and Hummer[24] further simplified the calculation of local diffusion coefficients for simulations of continuous trajectories that do not undergo replica exchange. In particular, instead of computing the characteristic time of the autocorrelation function (equation 2.57), they approximate it according to:

$$\tau \approx \left[\frac{n \, \mathrm{var}(\bar{z})}{\mathrm{var}(z)} - 1 \right] \frac{\Delta t}{2} \tag{2.58}$$

where n is the number of sample points of the z-distance timeseries and $\mathrm{var}(\bar{z})$ is the variance of the mean that can be estimated with block averaging[146,147]. The main advantage of the z-restraint method is that the umbrella sampling methodology is implemented in all major molecular dynamics codes, enabling in this way a much easier and robust calculation of the free-energy differences. However, recent studies indicated possible convergence issues that could potentially require μs long trajectories for medium/large permeants[148–150], as well as several other sampling errors[151]. Furthermore, the methods introduced by Hummer and Zhu are fairly recent and there are still no widely accepted and tested analysis tools. Specifically, for the Zhu and Hummer method no published results exist apart from the original article.

2.3.3.3 QSAR

An alternative to the complex and computationally expensive molecular dynamics simulations, is the use of quantitative structure-activity relation (QSAR) models. These are theoretical models that relate structural properties of the permeants to several activities, such as the permeation through a membrane. In fact, Mayer and Overton's[111,112] discovery of the correlation between the potency of anaesthetics and their octanol/water partition coefficient can be considered a precursor of QSAR models. Apart from the octanol/water partition coefficient[152], modern QSAR permeation studies examine permeation correlations to the molecular weight, the number of hydrogen bond acceptors and donors and the total polar surface area (TPSA) of the molecule[153]. This is a commonly used method in the pharmaceutical industry due to its simplicity, ready-made tools and the high throughput screening of molecules. Usually a database of molecules can scan hundreds of thousands of combinations in a day. However, the accuracy and validity of the results depend heavily on the initial training set of the model. Due to this, QSAR results are typically good only for a specific set of training properties/descriptors that the model has been built for and fail in a diverse set of permeants[154].

2.3.3.4 Enhanced physical model of permeation

An enhanced physical model of permeation has been proposed recently by Leung et al.[155,156] as a middle ground between the highly-accurate MD simulations and high-throughput QSAR calculations. The idea behind the model is that the permeation coefficient not only depends on the transfer free-energy (ΔG) but also on the deionisation/tautomerisation energy penalty ($\Delta G_{\mathrm{state}}$) and the conformational penalty for the permeant to adopt its membranephilic con-

formation (ΔG_{cf}). The method is based on computationally cheap calculations of the aforementioned properties that are allowed due to simplistic approximations, e.g., membranes are considered homogeneous and diffusion calculations consider permeants as spherical particles. The advantage of the method is the computational efficiency, its scalabitity and its modular accuracy. The latter can be improved by the fine-tuning of individual components of the calculations depending on the requirements. Overall, the reported permeation coefficients have generally sufficient correlation to experimental data and can provide a useful insight especially for comparing relative permeation performance between solutes.

2.4 Lamellar-nonlamellar membranes

2.4.1 Importance of lamellar-nonlamellar membranes

Physiologically relevant membranes predominantly exist in a lamellar phase (figure 2.9d). They are mainly composed by phosphatidylcholine (PC) lipids that form lamellar phases in excess water and physiological condition and phosphatidylethanoloamine (PE) lipids that form hexagonal H_{II} phases under the same conditions, when they have unsaturated chains. One could then wonder what is the role of these nonlamellar lipids in the complex lipid matrix of the lamellar structure. Researchers for many years considered lipid bilayers simply as "filler or passive solvent" for membrane-embedded proteins[157].

During the last thirty years, however, with the progress in the study and characterisation of lipids, a growing amount of evidence indicates that membranes with lamellar-nonlamellar compositions and cholesterol affect the modulation of protein function[78,158–163]. This mechanism can provide an explanation for general anaesthesia where ion channels activate and deactivate according to the concentration of nonlamellar lipids[88,96,164] or the concentration of solutes that alter membrane properties[82,90,98,165–168] e.g., ethanol[80,81,169–174]. Finally, lamellar-nonlamellar mixtures might be necessary for membrane processes such as fission, fusion and pore formation[83,93,175]. The aforementioned observations have initiated a very active research field that is aiming to identify the membrane property that is affected by the lamellar-nonlamellar compositional changes[106] and regulates the underlying mechanisms of such phenomena.

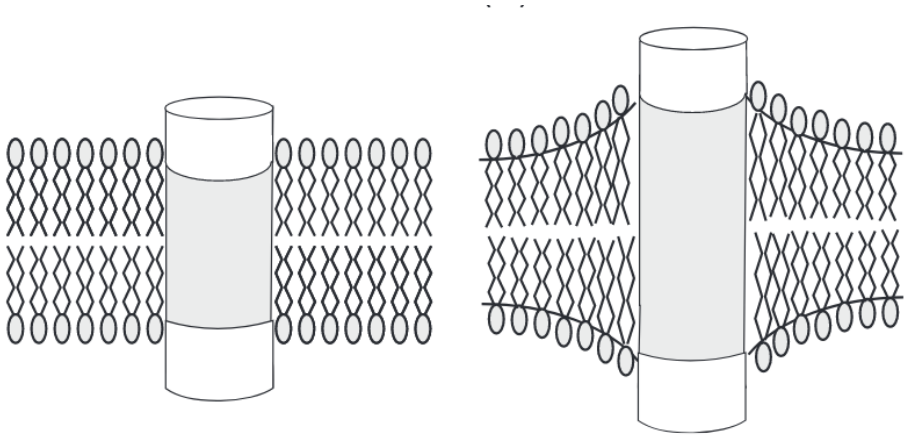

Figure 2.21: Protein conformational changes due to spontaneous curvature. When the spontaneous curvature is negative, the protein will adopt a conformation (right schematic) of larger hydrophobic matching (grey area)[176].

In particular for the membrane-protein interactions, two approaches have been formulated to connect it to a known membrane property; the first is based on the spontaneous curvature frustration[84,157,177–182] and the second is based on the lateral pressure profile[78,87,92,96,97,183–185]. According to the former, the stored elastic energy of a bilayer can facilitate one conformational change of a protein over another, depending on whether the protein change will

release the curvature frustration. As it can be seen from figure 2.21, membranes with negative spontaneous curvature will promote a protein conformation with larger hydrophobic matching. According to the latter approach, differences in the lateral pressure profile might induce localised changes in the protein lateral area and consequently alter its conformation and affect its functionality (figure 2.22). It has been shown that both of these approaches are equivalent (they predict the same shape alterations) and they are presented in detail in several recent review articles[93,186,187]. This is not surprising given the close analytical relation between the pressure profile and the spontaneous curvature through the first integral moment (equation 2.43).

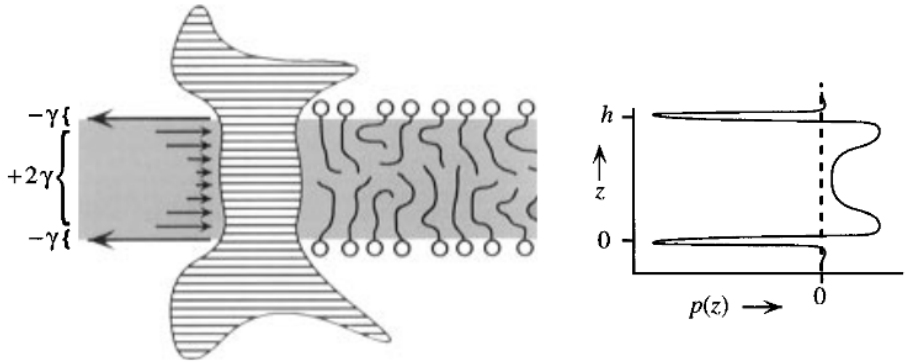

Figure 2.22: Schematic of membrane-protein interactions and the corresponding lateral pressure distribution[92].

2.4.2 Properties of lamellar-nonlamellar membranes

From the previous section it is clear that lamellar-nonlamellar mixtures have an important role on numerous biological processes. A lot of attention has been given in the past on the phase formation of H_{II} hexagonal phases and the energetic costs of bending and hydrating such bilayer mixtures[188–191]. In the following section past studies that specifically examined the mechanical and dynamical properties of such mixtures will be presented, in order to provide a solid perspective on the effect of nonlamellar lipids. Table 2.2 summarises the most important findings of these studies. As it can be observed, most of the research was done with dioleoylphosphatidylcholine (DOPC) and dioleoylphosphatidylethanolamine (DOPE) lipids, although some had a variety of acyl chains including the palmitoyloleoylphosphatidylcholine (POPC) and palmitoyloleoylphosphatidylethanolamine (POPE).

Templer et al.[72] have utilised pyrene probes attached to PC lipids, in order to probe the lateral pressure distribution inside the core of DOPC:DOPE bilayers of varying relative composition. Although their method only allowed probing of limited positions and later came under critique by Fraňová et al.[100], they saw an increase of pressure in the chain regions with the addition of PE lipids.

Cantor[184] performed statistical thermodynamic calculations to estimate the lateral pressure

profile, the thickness and the area per lipid of symmetrical lipid bilayers for a wide range of compositions. His results for a theoretical model of a POPC:POPE mixture predicted that an increase on the POPE content led to a decrease in the area per lipid and an increase in the thickness. He also saw a significant redistribution of pressures from the headgroup region of the bilayer towards the centre without disrupting, however, an overall decreasing behaviour from the outwards to the centre.

De Vries et al.[68] utilised atomistic molecular dynamics simulations with DOPC:DOPE bilayers of varying content. They observed that properties did not change linearly and a saturation behaviour was found for the PC:PE 1:3 composition. Increase in DOPE led to a decrease in the area and volume per lipid and an increase in the thickness of the bilayer. Also an increase in the hydration of the PC headgroups was observed. Finally, in their simulations no domains between lipids were formed.

Lu and Voth[192] developed a solvent-free coarse-grained model for a 1:1 DOPC:DOPE mixture. Their simulations focused on the dynamic properties such as the mean square displacement of the lipids and domain formation. In regards to the latter, they observed small clusters of the same lipids although these two lipids have been reported to be well mixed in previous experiments[193,194].

Orsi and Essex[65] simulated mixed DOPC:DOPE bilayers in various concentrations with their own coarse-grained model[195–197]. They examined the lateral organisation and did not observe any lipid domains. Furthermore, they calculated the area per lipid which decreased with increased PE content while the electron density profile had a marginal change. Also, they provided, for the first time, a quantitative characterisation of the lateral pressure profile in which the addition of PE lipids increased the positive pressure in the headgroups and chains regions and also increased the magnitude of the negative pressure in the polar/apolar interface. Finally, the spontaneous curvature decreased with higher PE composition.

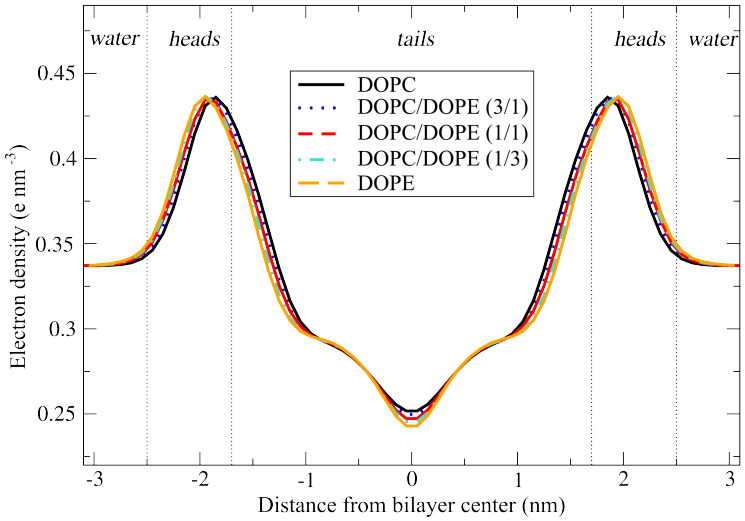

Figure 2.23: Electron density profile for various DOPC/DOPE compositions[22].

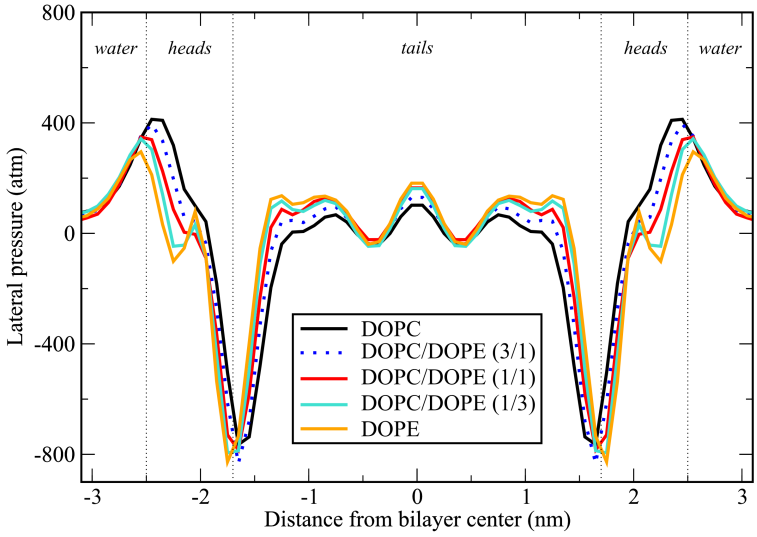

Figure 2.24: Lateral pressure profile for various DOPC/DOPE compositions[22].

Perin et al.[21] performed atomistic molecular dynamics simulations on various mixtures including a 1:1 POPE:POPG(palmitoyloleoylphosphatidylglycerol). While they reported the lateral pressure profile, they did not systematically examined compositional changes and thus no clear conclusions on the results could be made in regards to the effect of PE.

Ding et al.[22] is the first atomistic MD systematic study of lamellar-nonlamellar bilayers that reports the lateral pressure profile. They observed a decrease of 6% and 3.5% for area and volume per lipid, respectively, and an increase of 4% in the thickness, with increased PE content. The changes in electron density profile were also marginal (figure 2.23). The lateral pressure profile changed considerably with the addition of PE (figure 2.24). The headgroup peaks and interface troughs were shifted slightly outwards. The magnitude of the former reduced and of the latter increased. All across the chain region, the pressure increased.

Finally, membranes are greatly affected by chains' unsaturation and length. An increase in the number of carbon atoms in the chains, naturally, increases the thickness of the membrane. Also, unsaturation was found to decrease the sensitivity of membranes to temperature and phase changes[79]. An increase in unsaturation affected the lateral pressure profile by redistributing stresses from the interior towards the lipid-water interface[76]. Finally, membrane behaviour is affected by cholesterol. Several studies[77,94,102,198] have shown that it alters the pressure profile and thus its elasticity to more rigid or elastic, depending on the rest of the lipids saturation.

Table 2.2: Previous studies on the effect of lamellar/nonlamellar compositions on membrane mechanical properties.Numbers in parentheses indicate molar fractions.

Authors	**Year**	**Membranes**	**Properties**	**Methods**	**Effect of adding PE**
Templer et al.[72]	1998	DOPC, DOPE 0 mol%-80 mol% PE	Qualitative Π	Exp., Pyrene probes	Increase of pressure in the chain region
Cantor[184]	1999	POPC, POPE Various mixtures	d_{HH}, A_L, $\Pi(z)$	Theoretical predictions	Increase on d_{HH} Decrease on A_L Increase of $\Pi(z)$ in the headgr. Decrease of $\Pi(z)$ in the chains
De Vries et al.[68]	2004	DOPC, DOPE (1:0, 3:1, 1:1, 1:3, 1:7, 0:1)	d_{HH}, A_L, V_L, MSD, f_{X-X}	MD, 303 K	Nonlinear reduction on A_L, V_L Increase on d_{HH} Increase on hydration No formation of domains
Lu & Voth[192]	2009	DOPC:DOPE (1:1)	MSD, domains	MD CG, 310 K	Small clusters formation
Orsi & Essex[65]	2013	DOPC, DOPE (1:0, 3:1, 1:1, 1:3, 0:1)	A_L, f_{X-X}, EDP(z), $\Pi(z)$, c_0	MD CG, 303 K	No domains observed Decrease on A_L Minor change on EDP Amplified $\Pi(z)$ max. and min. Decrease of c_0
Ding et al.[22]	2015	DOPC, DOPE (1:0, 3:1, 1:1, 1:3, 0:1)	d_{HH}, A_L, V_L, $\Pi(z)$, EDP(z)	MD, 300 K	Increase of d_{HH} & decrease of A_L, V_L Marginal change on EDP Decrease of $\Pi(z)$ in headgroups Increase of $\Pi(z)$ in tails

d_{HH}: Bilayer thickness, A_L: Area per lipid, V_L: Volume per lipid, f_{X-X}: Lipid type fraction (see equation 2.35)
$\Pi(z)$: Lateral pressure profile, EDP(z): Electron density profile, c_0: Spontaneous curvature, MSD: Mean square displacement
Exp.: Experimental, MD: Molecular dynamics, CG: Coarse-grained

2.4.3 Permeation through pure and mixed membranes

Lipid composition clearly affects the mechanical properties of the membranes which in turn affect, through the lateral pressure profile and the spontaneous curvature frustration, crucial biological functions such as interactions with proteins and membrane fusion. Another important property of the membrane is to act as a regulator of permeation for the cell, as it was discussed in section 2.3. The combination of the above gave rise to a relatively new field of research that attempts to study membrane-solute interactions[199]. Previous studies on passive permeation through biological membranes can be categorised in two main groups, those that examined the permeation from the perspective of the permeants such as the molecular weight, the size and the chemical moieties, and those that examined it from the perspective of the lipid bilayers. This section will focus on studies from both groups that involved permeation studies through mixtures or varying lipid compositions.

Since water is the predominant biological solvent, its penetration through lipid bilayers has been of particular interest to researchers, especially in regards to the permeation pathway[200]. However, while the majority of permeation studies in the past focused on water, other small molecules and drugs have been under investigation. For most small non-electrolytes, penetration is generally accepted to take place without the assistance of special proteins[201] and the permeation rate changes have been correlated to various alterations of the lipid amalgam. Table 2.3 summarises all the studies that will be discussed in the following paragraphs and have focused on lamellar-nonlamellar compositions.

One of the first lipid characteristics that has been examined is the length of the lipid chains and consequently the bilayer thickness[202]. In the study of Jansen and Blume[203], where DMPC, DPPC and DSPC were examined, no direct conclusion was established between permeation and thickness. However, Paula et al.[121] observed a fivefold linear decrease of permeability with an increase of PC bilayer thickness, as a result of longer lipid chains. An MD study on several small molecules by Sugii et al.[204] was in agreement with Paula et al. as they estimated a considerable decrease in permeation for increased chain lengths (DMPC, DPPC, DLPC). Furthermore, Lee et al.[205] have examined model stratum corneum (SC) membranes composed of ceramide, cholesterol and a mix of free fatty acids (FFA) of varying length but did not measure a significant change in permeation due to the length difference. Arouri et al.[75] studied the effect of free fatty acids in the permeability barrier of DPPC liposomes and MCF-7 cell lines. For the DPPC liposomes, they observed a linear relationship between reduced permeability rates and increase of fatty acid lengths which was however, not observable in the more realistic model of living cells (MCF-7 cell lines).

Another important parameter is the unsaturation of lipid chains. It has been observed both experimentally[115] and via MD simulations[206] a clear increase on permeation with increased chain unsaturation, which can be attributed to looser packing and greater area per lipid, or increased free volume in the bilayer centre that can locally facilitate permeation[207]. In a sys-

tematic study of structural properties of membranes on permeation, Mathai et al.[208] have only found a clear correlation of permeation to area per lipid while the results for thickness, bending and area compressibility modulii did not indicate an obvious relationship (figure 2.25). In conclusion, the results from various studies regarding the thickness are contradictory, however area per lipid seems to produce more obvious correlations (membranes of high A_L tend to have higher P).

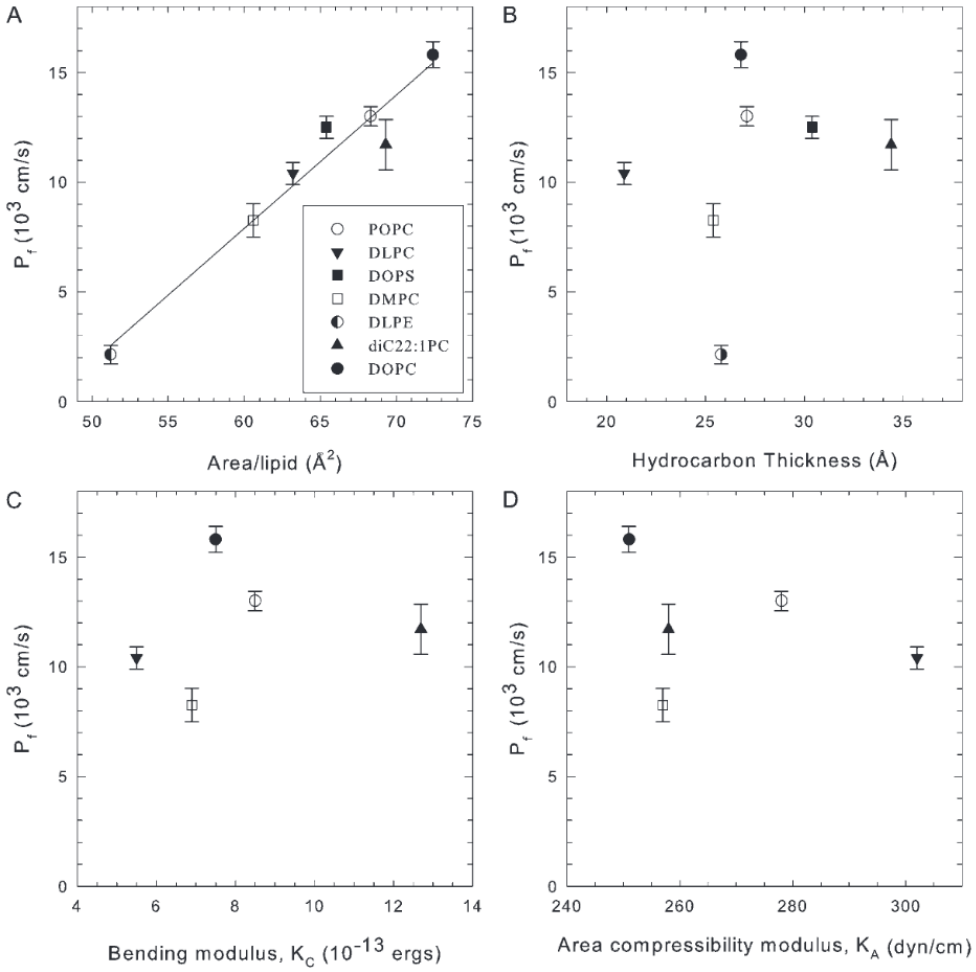

Figure 2.25: Correlation of water permeability to structural properties of different membranes[208].

Lipid headgroups play also an important role on the permeability of molecules through the bilayer. Jansen and Blume[203] measured water permeability for pure lipid vesicles comprising different headgroups. They observed an almost twofold increase in permeation for pure DMPE compared to pure DMPC and a marginal decrease for DPPE compared to pure DPPC. They attributed these differences to increased intra-molecular hydrogen bonding of PE lipids but did not explain the discrepancy between them. Similarly, Johansson and Lindahl[209] have computed the solvation free-energy of 8 amino acids in 2 regions of several membranes. They found that for all amino acids, the absolute free-energy is higher for PE bilayers, due to their higher propensity for inter-lipid hydrogen bonding, which reduces bonding with polar solutes and makes the bilayer more hydrophobic, enhancing the solvation of nonpolar solutes. Also, Hub et al.[210] observed an order of magnitude decrease in

permeation of ammonia between a pure POPC and pure POPE bilayer.

In regards to lamellar-nonlamellar mixtures, Huster et al.[115] have observed that the addition of nonlamellar DOPE lipids reduced the permeation of water by 40 % in comparison to a pure DOPC bilayer and by 18 %, within statistical error, when mixed on a pure polyunsaturated 18:1-22:6 PC bilayer. The results were explained based on the lipid order increase, which is more prominent in saturated and monounsaturated lipids, and which led to tighter packing and smaller area per lipid. Purushothaman et al.[211] very recently examined the permeation of the antibiotic norfloxacin through pure and mixed DOPC, DOPE and DOPG bilayers. As it can be seen from figure 2.26, the addition of PE lipids generally reduced the permeation coefficient, although the reduction was higher for smaller concentrations of PE. The authors attributed this either to the higher intrinsic curvature which might assist the solubility or to low accuracy of their measurements.

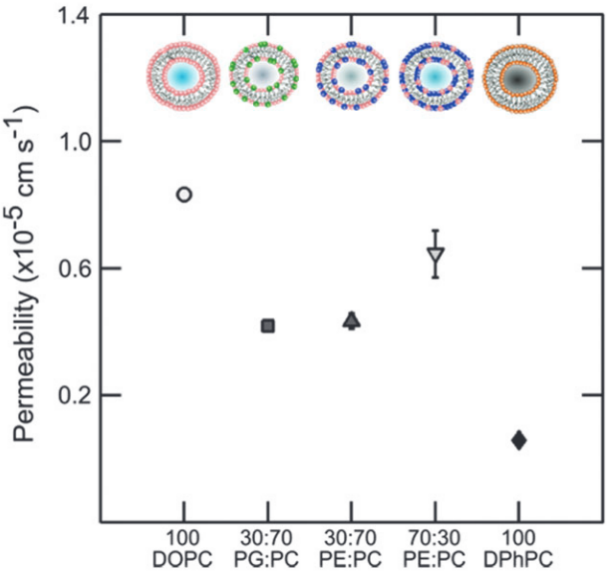

Figure 2.26: Permeation of the antibiotic norfloxacin through lamellar-nonlamellar membranes[211].

Finally, although in this dissertation the effect of cholesterol on passive permeation is not examined, it is noteworthy that there have been many past studies indicating that by increasing membrane rigidity[212], cholesterol also affects permeation. In particular, the addition of cholesterol decreases water[48,213] and oxygen[214–216] permeability substantially, while other small molecules are affected according to their polarity[210,217,218] and size[219].

Table 2.3: Previous studies on the effect of lamellar/nonlamellar compositions on the permeation through membranes. Numbers in parentheses indicate molar fractions.

Authors	**Year**	**Membranes**	**Permeants**	**Methods**	**Effect of PE**
Jansen & Blume[203]	1995	DMPC, DMPE, DPPC, DPPE (1:0)	Water	Exp.	DMPC/PE: Increase of P DPPC/PE: Small decrease of P
Huster et al.[115]	1997	DOPC, DOPE, 18:1-22:6 PC (1:1)	Water	Exp.	Decrease of P Smaller effect in polyunsaturated
Seo et al.[220]	2006	DOPC, DOPE, 18:2-18:2 PC,PE (1:0, 0:1)	Metoprolol, mannitol, benzoic acid, sucrose, taurocholic acid	Exp.	DOPC/PE: Increased P 18:2-18:2 PC/PE: Increased P
Johansson & Lindahl[209]	2009	POPC, POPE (1:0)	8 amino acid analogs	MD	Absolute solvation ΔG increased Extra HB. increased hydrophobicity
Hub et al.[210]	2010	POPC, POPE (1:0, 1:1, 0:1)	Carbon dioxide, ammonia	MD	Decrease of P
Wennberg et al.[219]	2012	POPC, POPE (1:0, 0:1)	Ammonia, ethanol, nitric oxide, benzene, propane, neopentane	MD	Transfer ΔG increased for all solutes
Zocher et al.[218]	2013	DOPC, DOPE (1:0, 0:1)	Ammonia, triethylamine	MD	Decrease of P
Purushothaman et al.[211]	2016	DOPC, DOPE (1:0, 3:1, 1:3)	Norfloxacin	Exp.	Decrease of P

P: Permeability coefficient, HB.: Hydrogen bonds, ΔG: Free-energy difference
Exp.: Experimental, MD: Molecular dynamics, CG: Coarse-grained

Chapter 3

Materials and methods

3.1 Materials

3.1.1 Phospholipids and bilayer compositions

Molecular dynamics simulations were performed on two different glycerophospholipid bilayer systems. The first comprised only DOPC (1,2-dioleoyl-*sn*-glycero- 3-phosphocholine) lipids and the second was a mixture of 1 DOPC to 3 DOPE (1,2-dioleoyl-*sn*-glycero-3-phosphoethanolamine) lipids. The chemical structure of the two different lipids is presented in figure 3.1 and the details of the bilayer systems examined are shown on table 3.1. Each system comprised 4300 water molecules, 128 lipid molecules (64 per leaflet) and 1 permeating molecule. Both the pure DOPC and the DOPC:DOPE(1:3) membrane systems were taken pre-equilibrated (1 μs) from a recent published study[22]. Also, both membranes were fully hydrated; PC bilayers require 23 waters per lipid while PE bilayers require 10[221].

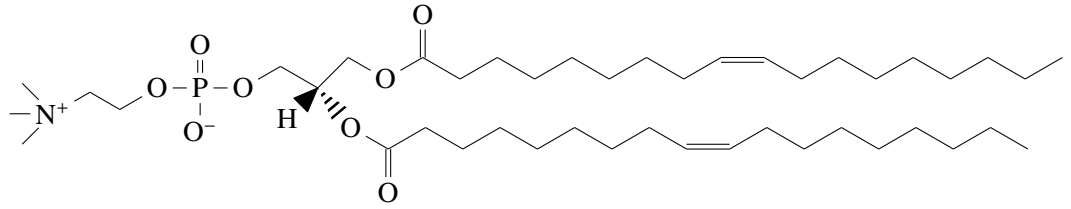

(a) 1,2-dioleoyl-sn-glycero-3-phosphocholine (DOPC)

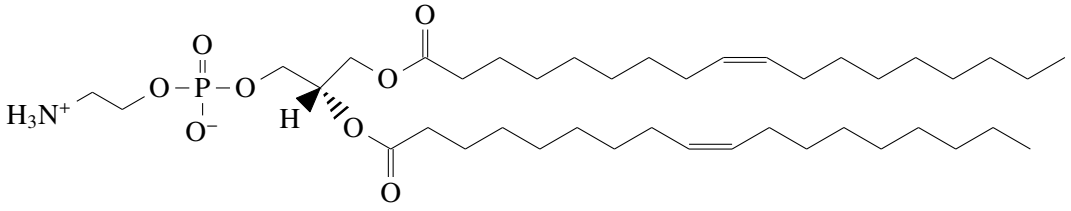

(b) 1,2-dioleoyl-sn-glycero-3-phosphoethanolamine (DOPE)

Figure 3.1: Skeletal chemical structure of the simulated phospholipids

DOPC (figure 3.1a) is a typical representative of the lipids that form lamellar structures and

Table 3.1: Lipid composition of simulated membranes. N refers to the number of each component.

System	N_{DOPC}	N_{DOPE}	N_{water}
DOPC	128	0	4300
1 DOPC : 3 DOPE	32	96	4300

are predominant in biological membranes. Its chemical structure comprises a polar headgroup region where a choline is linked to the phosphate group, and an apolar hydrocarbon region with two monounsaturated oleic fatty acids of 18 carbons, ester linked to the first two hydroxyls of the glycerol backbone. Both monounsaturated DOPC chains kink due to the *cis* double bond.

DOPE (figure 3.1b) is also a good representative of another type of lipids found in biological membranes, those that have a propensity to form nonlamellar inverted hexagonal H_{II} structures (figure 2.9b), depending on the temperature and number of hydrating water molecules[53,189,198,222,223]. DOPE differs from DOPC on the amino alcohol of the headgroup region, where instead of a choline, it has the substantially smaller ethanolamine linked to the phosphate group. Both of these phospholipids are well studied molecules and have been used in the past in several molecular dynamics permeation studies as components of model biological membranes[136].

3.1.2 Permeating solutes

To examine the permeation process, 13 small molecules and drugs were selected as solutes; 10 with molecular weight lower than 100 g mol^{-1} and 3 with higher. The selection of the molecules was based on several factors so that a diverse set of physical properties would be examined in the permeation study. Table 3.2 presents the chosen solutes as well as their molecular weight, hydrogen bonds donors and acceptors, the topological polar surface area (TPSA) which is the sum of the surface over all polar atoms and their hydrogens, the number of heavy (non-hydrogen) atoms, QSAR computed logarithm of octanol/water partition coefficients $\log P_{o/w}$ and finally, where available, the experimental $\log P_{o/w}$.

Table 3.2: Physical properties of the permeating molecules

Molecule		**MW** [g/mol]	**HB Dn**‡	**HB Ac**‡	**TPSA** [Å^2]	**HA**	**Exp LogP$_{o/w}$**	**CAx LogP$_{o/w}$**
Ammonia	NH_3	17.03	1	1	13.6	1		-0.98
Water	H_2O	18.02	1	1	25.3	1	-1.38†	-0.65
Fluoromethane	CH_3F	34.03	0	1	0	2	0.51*	0.37
Carbon dioxide	CO_2	44.01	0	2	34.1	3	0.83†	-0.28
Propane	C_3H_8	44.10	0	0	0	3	2.36†	1.8
Ethanol	C_2H_6O	46.07	1	1	20.2	3	-0.30*	-0.16
Urea	CH_4N_2O	60.06	2	1	69.1	4	-2.11†	-1.36
Isopropanol	C_3H_8O	60.10	1	1	20.2	4	0.05*	0.25
Glycine	$C_2H_5NO_2$	75.07	2	3	63.3	5	-3.21†	-3.41
Phenol	C_6H_6O	94.11	1	1	20.2	7	1.50*	1.67
Benzoic Acid	$C_7H_6O_2$	122.12	1	2	37.3	9	1.87*	1.63
Coumarin	$C_9H_6O_2$	146.15	0	1	26.3	11	1.39†	1.78
Paracetamol	$C_8H_9NO_2$	151.17	2	2	49.3	11		0.91

MW: Molecular weight
HB Dn: The sum of the atoms in the molecule which have the hydrogen donor property
HB Ac: The sum of the acceptor atoms. An acceptor atom always has a lone electron pair/lone electron pairs that is capable of establishing a hydrogen bond
TPSA: Topological polar surface area
HA: Number of heavy atoms (non-hydrogen)
Exp LogP$_{o/w}$: Experimental logarithm of octanol/water partition coefficients
CAx LogP$_{o/w}$: Computed octanol/water partition coefficient with the ChemAxon logP[152] QSAR online tool "Chemicalize" (`http://chemicalize.com`)
$*$: Reference[224]
† : Reference[225]
‡ : Computed with the online tool "Chemicalize" (`http://chemicalize.com`)

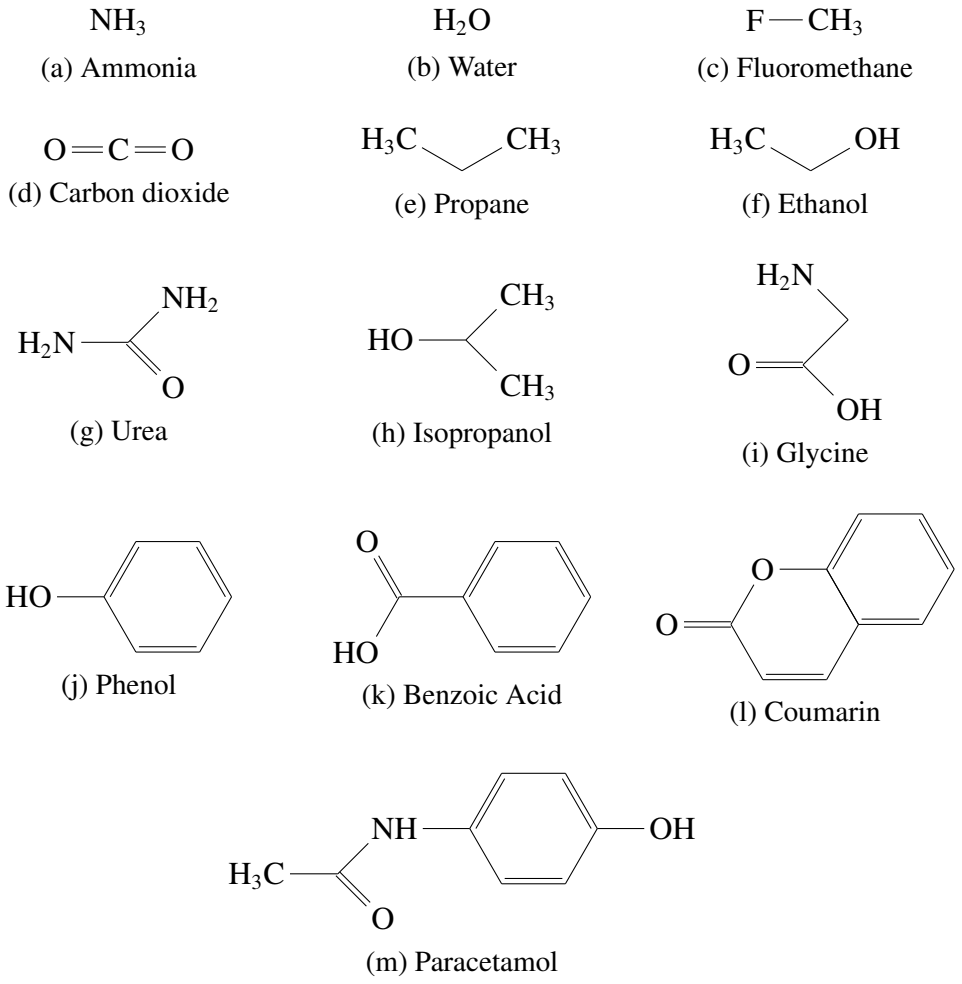

Figure 3.2: Skeletal chemical structure of the simulated permeants

3.2 Simulation protocols

3.2.1 The z-constraint method

For the z-constraint method, only ammonia, water, fluoromethane and carbon dioxide (table 3.2 and figure 3.2) were simulated through the pure DOPC and mixed DOPC:DOPE membrane. Each permeant was placed in 30 different positions along the bilayer, from the water region to the membrane centre. The simulations were performed only on the upper half monolayer and then due to the bilayer symmetry, the results were mirrored in the opposite direction.

The LAMMPS[226] (version October 2014) molecular dynamics software was used to perform the simulations. The non-bonded and bonded pairwise interactions for lipid and water molecules were modelled with the CHARMM36 (version August 2014) force field (FF) parameters[227,228], while permeant molecules were represented by compatible CGenFF[229,230] parameters. When interactions between particles were not explicitly defined, the arithmetic mixing rules of LAMMPS were used. Non-bonded Van der Waals interactions were approximated with a Lennard-Jones potential with an energy switching function, in order to be compatible with the CHARMM FF. The inner cutoff was taken at 1 nm and the external cutoff at 1.2 nm. The short range electrostatics were computed analytically from a Coulomb potential with a cutoff at 1.2 nm and the long range electrostatics were computed in reciprocal space with the particle-particle particle-mesh solver[231,232] which is similar to the PME[28] technique presented in section 2.1.2.2.

The equations of motion were integrated with the velocity-Verlet algorithm and all simulations were performed with a 2 fs timestep by constraining the hydrogen covalent bonds with the LAMMPS implementation of the SHAKE algorithm[38,39]. The temperature and pressure of the systems were kept at 300 K and 1 bar with the Berendsen[42] thermostat and barostat respectively, with a coupling time of 2 ps. The pressure was applied to the system semi-isotropically, having the same magnitude on the x and y directions but different on the z. The momentum of the whole system was removed every 100 timesteps to keep the total centre-of-mass still. Finally, the trajectory and the constraint force applied on the permeant, computed with 3 different methods (see appendix A), was sampled every 10 ps. The simulation process following the creation of each system consisted of 4 steps:

1. **Relaxation.** A small 10 ps relaxation simulation was executed with an imposed 0.1 Å limit in the distance each atom can move per timestep. This technique was used as an alternative to an energy minimisation simulation, in order to fix any overlapping particles and extreme forces due to steric effects, without crashing. The disadvantage with the energy minimisation in the z-constraint method is that the permeant could potentially move along the z-direction and thus the constraint simulation would continue in the wrong z position.

2. **Equilibration.** The system was equilibrated for 500 ps and then the first production simulation started.

3. **Production.** Production simulations ran in separate 10 ns sets for a total of 100 ns.

4. **Pre-analysis.** For the analysis of the results, depending on the convergence, the first sets of the production simulations were discarded as further equilibration.

The first part of the z-constraint results analysis examined how the sampling of the constraint force affected the free-energy difference profile. Furthermore different convergence methods were tested and then the free-energy difference, the local diffusion coefficients and the permeation coefficients were computed for all permeants and the DOPC and DOPC:DOPE membranes.

3.2.2 The z-restraint method

With the z-restraint method, all the molecules presented in table 3.2 and figure 3.2 were examined with the DOPC and DOPC:DOPE(1:3) membranes. In order to perform the simulations, the GROMACS 5.1.1[233–238] molecular dynamics software was used. The equation of motion was integrated with the leap-frog algorithm (section 2.1.4). Van der Waals forces between atoms were approximated with a Lennard-Jones potential with a switching cutoff from 1 nm to 1.2 nm, short range electrostatics were approximated with a Coulomb potential with a cutoff at 1.2 nm and finally for long range electrostatics the Smooth Particle-Mesh Ewald (SPME)[239] method was used. Lipid molecules were represented by the CHARMM36 (August 2015 version) force field[227,228], permeant molecules were represented by CHARMM36 or compatible CGenFF[229,230] parameters and water molecules were represented by the CHARMM implementation of TIP3P[240]. Permeants were inserted manually in 28 positions along the depth of the upper lipid leaflet, from the water region to the bilayer centre.

Initially, an energy minimisation was performed to correct any potential overlaps and then a short constant temperature and pressure (NPT) 100 ps equilibration was ran. Both during the minimisation and the equilibration, the distance between the centres of mass of the membrane and the permeant was constrained, in order to ensure the correct distance between them in the beginning of the production simulation. Overall 28 z-positions were examined for each permeant-membrane combination and for each, a 100 ns NPT production simulation was performed, totalling 2.8 μs simulation time for each system.

For temperature coupling during the equilibration and production simulations, the velocity rescale algorithm[45] was used. All the systems were kept at 300 K and the coupling time constant was set at 1 ps. Pressure was kept at 1 bar with the Berendsen[42] and Parrinello-Rahman[46,241,242] barostats during equilibration and production simulations, respectively. For both, the coupling time constant was 5 ps and for pressure the coupling type was semi-

isotropic; isotropic for x and y directions but independent from the z direction. In order to utilise a 2 fs timestep, covalent bonds with hydrogen atoms were constrained; the SETTLE algorithm[243] was used for water molecules and the LINCS algorithm[40,41] was used for the rest.

The restraining forces and z-axis fluctuations of the permeant were sampled every 1 ps resulting in two timeseries of 100 000 points each. The first 30 ns (30 000 points) were discarded as extra equilibration time and all final results were produced using the last 70 ns. Standard errors for the calculated properties were computed with the block averaging method[146,147] (section 4.3), where the 70 ns timeseries were separated in 7 blocks of 10 ns.

The analysis of the results of the z-restraint method began with a convergence study to identify when free-energy profiles were approximately stable. Then the free-energy profiles $\Delta G(z)$ were computed with the umbrella sampling method and the GROMACS implementation[244] of the weighted histogram analysis method (WHAM)[142,245]. The permeant was restrained by a virtual spring with a harmonic force constant of 1000 kJ mol^{-1} nm^{-2} along the z-axis, every 0.1 nm from the water slab to the bilayer core.

Local diffusion coefficients $D(z)$ were computed with two different methods, the one developed by Hummer[23] (equations 2.56 and 2.57) and the one simplified by Zhu and Hummer[24]. A comparative analysis between the two methods was performed to identify the best. Other elements of the diffusion calculation, such as the numerical integration of the autocorrelation function or the handling of oscillatory profiles with the application of filters, were further examined.

The resistance profiles and the permeability coefficients were computed by direct substitution of $\Delta G(z)$ and $D(z)$ on equation 2.52. In order to increase the computational efficiency and since the monolayers' composition was the same for each examined membrane, the simulations covered only one leaflet of the bilayer, similar to the z-constraint method. Afterwards, the position-dependent results were treated as symmetrical to cover the entire z-dimension of the bilayer. The statistical significance of the differences between the permeations of the pure and mixed membranes was also checked.

Furthermore, the hydrogen bond formations between the permeants and the lipid-water molecules were computed to examine any possible effect on the permeation. Also, a correlation and regression analysis was performed for the computed permeation values in relation to several physical properties (table 3.2) of the permeants. Finally, the proper dynamics of the bilayer systems was ensured by visualising the lateral mobility of the permeant and computing the lateral diffusion coefficients of the DOPC and DOPE lipid molecules.

Chapter 4

MDrug: A preparation, analysis and HPC management toolbox

One of the main challenges in passive permeation studies is the preparation, management and analysis of hundreds or even thousands of simulations. While several research groups have performed similar studies, there is not at the moment a widely accepted, universal, reliable set of tools to assist the researcher throughout the whole process. In the best cases, individual tools are provided by MD software packages, but even then, they lack interconnectivity or features. In order to perform the z-constraint and z-restraint permeation studies presented in this dissertation, more than 3100 production systems were created*, simulated and analysed, not including energy minimisation, equilibration, benchmarks and testing simulations. Therefore, one of the most prominent tasks of this work was the creation of a reliable toolbox to allow and automate the aforementioned process.

The created toolbox, namely MDrug, can be separated in three distinct categories, the pre-processor, the HPC simulation-manager and the post-processor. In the following section, the philosophy of operations will be presented for each part, along with their respective algorithms/techniques. All of these tools are publicly available in a GitHub repository† under an LGPLv3 license.

4.1 Pre-processing of the systems

The pre-processing tools include all those operations that are necessary to gather components, organise them and prepare the production system. The prerequisites (input) for running a permeation study are:

*__z-constraint:__ 8 permeants − membranes × 30 positions × 10 sets of 10 ns = 2400 simulations;
__z-restraint:__ 26 permeants − membranes × 28 positions = 728 simulations

†`https://github.com/mpalaiokostas/MDrug`

1. an MD program selection (currently LAMMPS or GROMACS)
2. a method selection (z-constraint (only available with LAMMPS) or z-restraint (only available with GROMACS))
3. a .pdb file of a properly equilibrated membrane
4. a .pdb file of a permeant that is compatible with the CHARMM36 force field
5. an initial and final z position, as well as the z interval
6. a high performance computer HPC server to upload the created test case

The main advantage of MDrug is the automated handling of hundreds of files without the necessity of user intervention. All the aforementioned operations create a lot of files but with MDrug, the user just decides on the 6 input parameters and with the ease of pressing a button, a complete permeation study case (a membrane-permeant combination) is automatically prepared and uploaded, ready to be simulated. A permeation-case generally consists of 4 main directories that allow each user to supervise the whole process from the beginning to the end (figure 4.1).

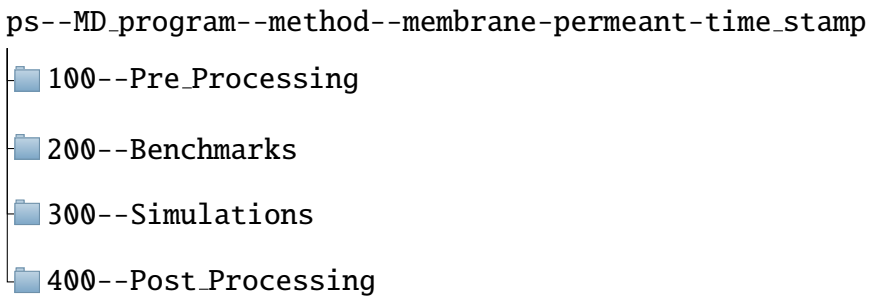

Figure 4.1: MDrug produced directory tree. This structure allows the user to check each step of the permeation study clearly and in detail.

Figure 4.2 shows the operational flow chart based on the input. At the moment MDrug supports two MD programs, LAMMPS and GROMACS and two permeation methods, z-constraint and z-restraint, respectively. In theory, both LAMMPS and GROMACS allow both methods, however in practice there are severe issues on performance or compatibility and thus only two combinations are supported. The pre-processing software is based on the 3.4 version of the Python programming language which performs all the file/directories manipulations, invokes external software for system creations and short simulations and connects/uploads the complete test case to any HPC securely (key-based SSH connections). For system creation, a TCL script is used in conjunction with the visual molecular dynamics (VMD) application to merge the permeant and membrane structures and also move the permeant to the correct position. Then in the case of GROMACS/z-restraint, MDrug invokes certain GROMACS-suite tools through compatible scripts to perform an energy minimisation and a small equilibration for each z-position.

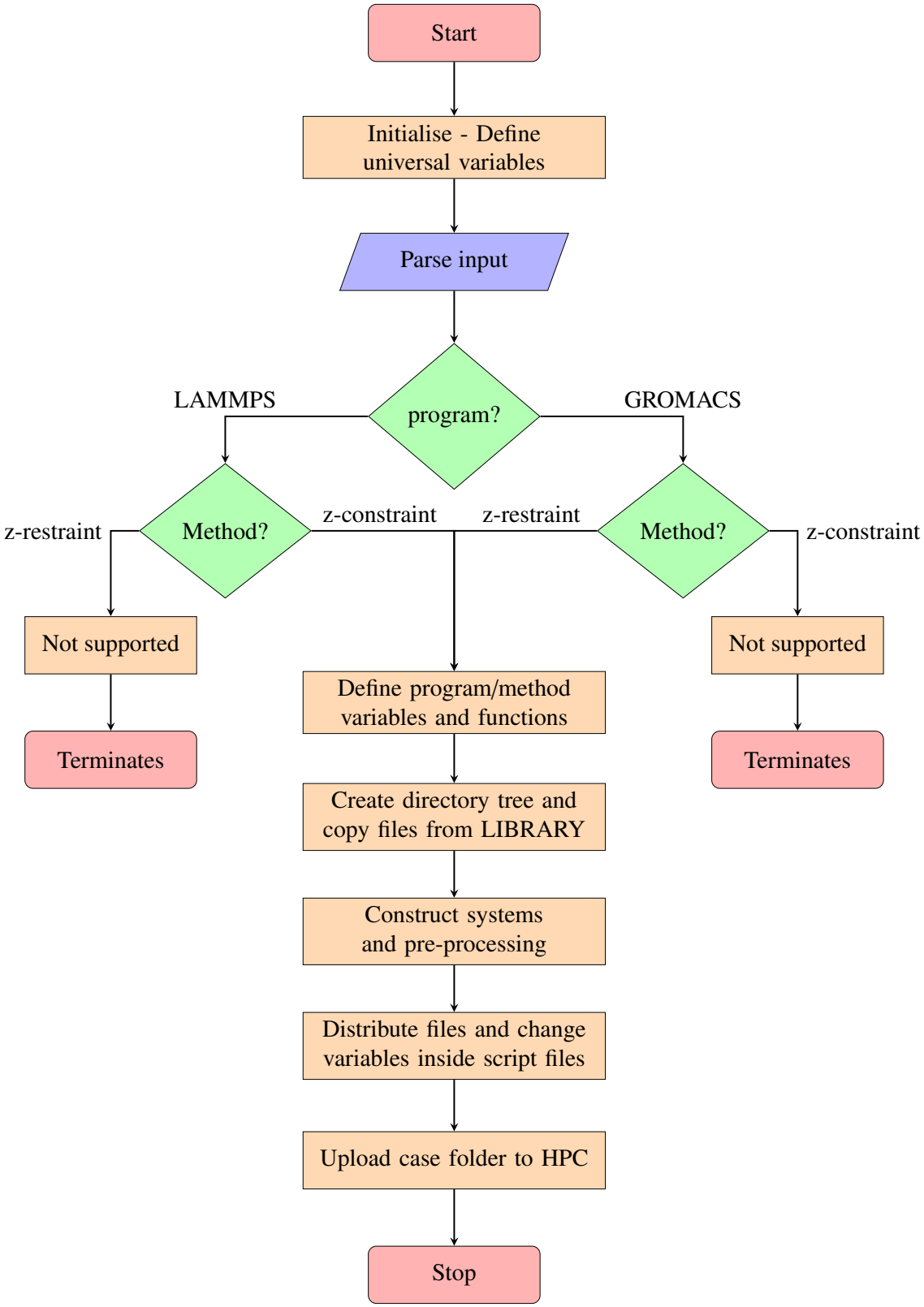

Figure 4.2: Flow chart of the pre-processing operations of MDrug.

4.2 HPC simulation management

Once permeation cases are uploaded to an HPC, the MDrug simulation management toolbox is responsible for submitting and monitoring simulations. The toolbox is especially useful in cases where there are more than 2 permeation cases uploaded in the HPC and there is a limit in the number of jobs that can be submitted in the queue and running. For instance, the UK national supercomputer, ARCHER, allows up to 16 submitted jobs in the queue and up to 8 running at the same time. Considering that each permeation study comprises 28 to 30 positions, normally, the user would have to manually check the queue and submit new jobs all the time. Instead, the MDrug toolbox allows:

- the monitoring of the HPC user queue
- the automatic submission of jobs depending on the available slots
- the monitoring of the status of each job (waiting, started, crashed, completed)
- the creation of local log files based on the monitor operations

The flowchart of the aforementioned processes is presented in figure 4.4. The key advantage of the toolbox is that it allows the user to easily know the progress of each permeation case by simply looking at a specially formatted log file (figure 4.3). Also, it saves a lot of time and utilises the HPC budget in the most efficient way. The monitoring toolbox is entirely written in the BASH scripting language and requires a Linux environment with the Crontab scheduling manager in order to perform connections to the server hourly.

```
#CASE: ps--gmx--umb--dopc32_dope96-h2o--20160801112223 | HPC: Archer
#FOLDER: 330-Restart_Simulation-01 | SIM.No: 01
#POS|ID         |DT_SUBM |TM_SUBM |NAME  |STS|DT_START   |TM_START|TM_ELAPS|DT_COMP |TM_COMP |
#---|-----------|--------|--------|------|---|-----------|--------|--------|--------|--------|
00  |3851791.sdb|01-08-16|13:34:18|Z0    |C  |2-Aug-2016 |17:34:29|15:04:32|03-08-16|08:39:01|
01  |3851792.sdb|01-08-16|13:34:18|Z1    |C  |2-Aug-2016 |17:52:37|18:29:41|03-08-16|12:22:18|
02  |3851793.sdb|01-08-16|13:34:18|Z2    |C  |2-Aug-2016 |18:12:57|21:14:41|03-08-16|15:27:38|
03  |3851794.sdb|01-08-16|13:34:19|Z3    |C  |2-Aug-2016 |18:24:16|14:46:06|03-08-16|09:10:22|
04  |3851795.sdb|01-08-16|13:34:19|Z4    |C  |2-Aug-2016 |18:57:43|19:13:51|03-08-16|14:11:34|
05  |3851796.sdb|01-08-16|13:34:19|Z5    |C  |2-Aug-2016 |18:59:59|14:20:41|03-08-16|09:20:40|
06  |3851797.sdb|01-08-16|13:34:19|Z6    |C  |2-Aug-2016 |19:27:13|15:35:47|03-08-16|11:03:00|
07  |3851798.sdb|01-08-16|13:34:19|Z7    |C  |2-Aug-2016 |19:37:58|15:46:56|03-08-16|11:24:54|
08  |3851799.sdb|01-08-16|13:34:20|Z8    |C  |2-Aug-2016 |20:04:54|14:20:27|03-08-16|10:25:21|
09  |3851800.sdb|01-08-16|13:34:20|Z9    |C  |2-Aug-2016 |20:16:31|14:28:50|03-08-16|10:45:21|
10  |3851801.sdb|01-08-16|13:34:20|Z10   |C  |2-Aug-2016 |20:56:05|14:12:12|03-08-16|11:08:17|
11  |3851802.sdb|01-08-16|13:34:21|Z11   |C  |2-Aug-2016 |21:02:24|14:25:14|03-08-16|11:27:38|
12  |3851803.sdb|01-08-16|13:34:21|Z12   |C  |2-Aug-2016 |21:43:38|14:14:58|03-08-16|11:58:36|
13  |3851804.sdb|01-08-16|13:34:21|Z13   |C  |2-Aug-2016 |21:43:39|14:21:22|03-08-16|12:05:00|
14  |3851805.sdb|01-08-16|13:34:21|Z14   |C  |2-Aug-2016 |21:52:46|14:24:02|03-08-16|12:16:48|
15  |3851806.sdb|01-08-16|13:34:22|Z15   |C  |2-Aug-2016 |21:53:44|14:00:47|03-08-16|11:54:31|
16  |3855145.sdb|03-08-16|09:34:28|Z16   |C  |3-Aug-2016 |21:51:49|23:08:55|04-08-16|21:00:44|
17  |3855146.sdb|03-08-16|09:34:28|Z17   |C  |3-Aug-2016 |22:50:45|23:53:47|04-08-16|22:44:32|
18  |3855147.sdb|03-08-16|09:34:28|Z18   |C  |3-Aug-2016 |23:03:10|14:55:19|04-08-16|13:58:29|
19  |3855286.sdb|03-08-16|10:34:29|Z19   |C  |4-Aug-2016 |00:41:22|21:08:03|04-08-16|21:49:25|
20  |3855502.sdb|03-08-16|11:34:28|Z20   |C  |4-Aug-2016 |01:35:27|19:53:56|04-08-16|21:29:23|
21  |3855503.sdb|03-08-16|11:34:29|Z21   |C  |4-Aug-2016 |01:45:28|16:35:02|04-08-16|18:20:30|
22  |3855504.sdb|03-08-16|11:34:29|Z22   |C  |4-Aug-2016 |02:31:46|19:25:36|04-08-16|21:57:22|
23  |3855507.sdb|03-08-16|11:34:30|Z23   |C  |4-Aug-2016 |02:53:30|20:13:59|04-08-16|23:07:28|
24  |3855509.sdb|03-08-16|11:34:30|Z24   |C  |4-Aug-2016 |02:55:07|21:05:33|05-08-16|00:00:40|
25  |3855667.sdb|03-08-16|12:34:29|Z25   |C  |4-Aug-2016 |03:01:57|22:54:40|05-08-16|01:56:37|
26  |3855668.sdb|03-08-16|12:34:30|Z26   |C  |4-Aug-2016 |04:42:58|14:53:07|04-08-16|19:36:05|
27  |3855669.sdb|03-08-16|12:34:30|Z27   |C  |4-Aug-2016 |04:45:20|14:28:25|04-08-16|19:13:45|
28  |3855670.sdb|03-08-16|12:34:30|Z28   |C  |4-Aug-2016 |05:17:21|23:19:12|05-08-16|04:36:32|
29  |3855671.sdb|03-08-16|12:34:31|Z29   |C  |4-Aug-2016 |05:51:51|15:23:48|04-08-16|21:15:39|
30  |3855970.sdb|03-08-16|14:34:33|Z30   |C  |4-Aug-2016 |06:36:35|16:32:57|04-08-16|23:09:31|
```

Figure 4.3: Example monitor log file for the mixed membrane and water permeant.

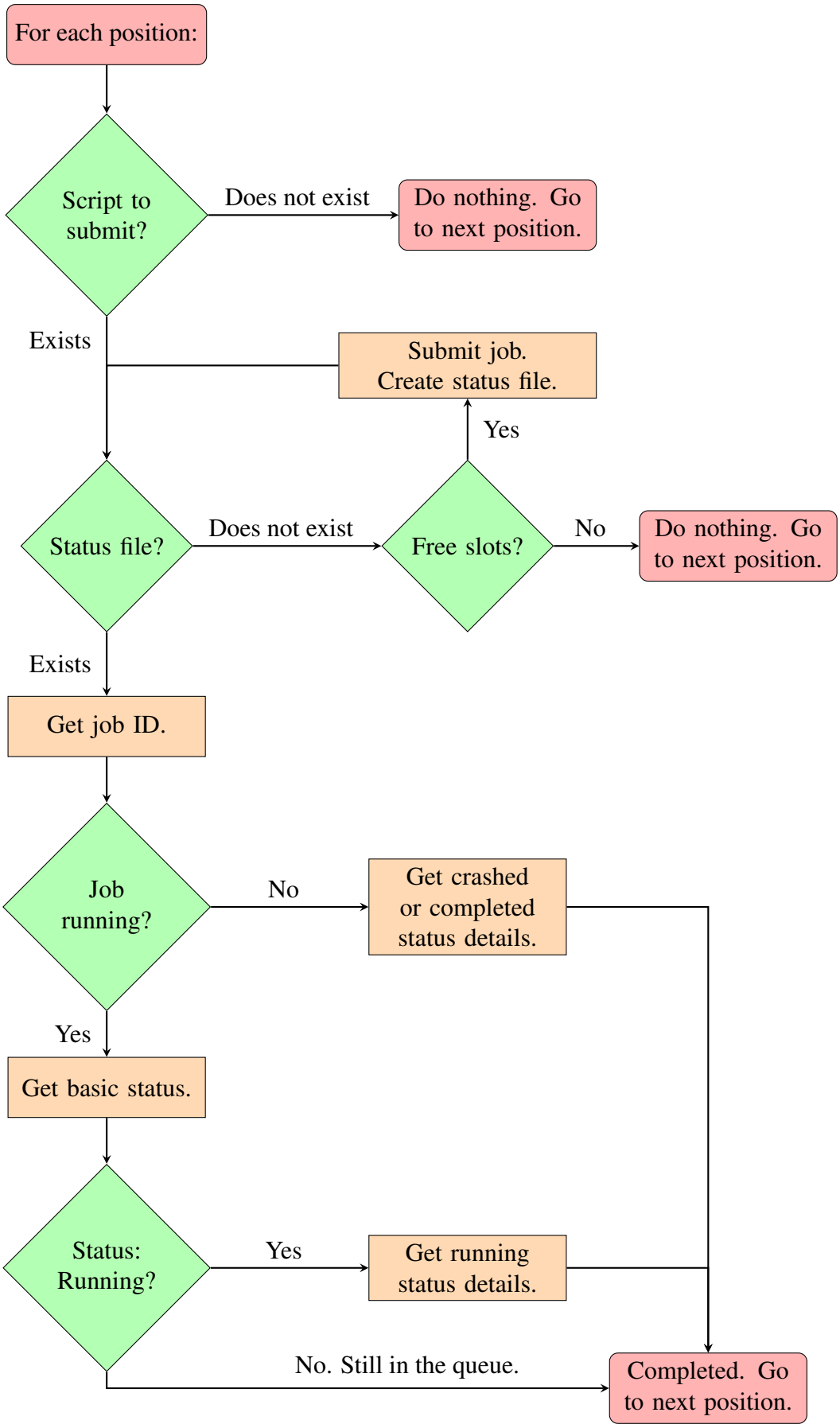

Figure 4.4: Flow chart of the HPC monitoring operations of MDrug.

4.3 Post-processing of the systems

The third set of tools of MDrug is dedicated to the visualisation and analysis of the simulation trajectories and output. This part was also developed with the end-user in mind, so that it performs complex analyses or sophisticated visualisation with minimal effort. The tools can be categorised as follows:

- checking completion and merging of multi-part trajectories
- visualisation of trajectories
- computing permeation properties by using simulation output
- performing convergence studies
- extracting centre-of-mass translation on the z direction
- performing block-averaging and bootstrapping analysis to compute statistics
- computing lateral mean-square-displacement (MSD) to ensure proper dynamics
- performing hydrogen bonds analysis
- produce publication-quality plots, automatically, for all the above

```
Simulation in position 0 completed successfully!
Simulation in position 1 completed successfully!
Simulation in position 2 killed at t= 96.005ns
Simulation in position 3 completed successfully!
Simulation in position 4 killed at t= 90.254ns
Simulation in position 5 completed successfully!
Simulation in position 6 completed successfully!
Simulation in position 7 completed successfully!
Simulation in position 8 killed at t= 91.767ns
Simulation in position 9 completed successfully!
Simulation in position 10 killed at t= 96.665ns
Simulation in position 11 completed successfully!
Simulation in position 12 completed successfully!
Simulation in position 13 killed at t= 92.894ns
Simulation in position 14 completed successfully!
Simulation in position 15 completed successfully!
Simulation in position 16 completed successfully!
Simulation in position 17 killed at t= 97.237ns
Simulation in position 18 completed successfully!
Simulation in position 19 completed successfully!
Simulation in position 20 killed at t= 96.358ns
Simulation in position 21 completed successfully!
Simulation in position 22 completed successfully!
Simulation in position 23 completed successfully!
Simulation in position 24 completed successfully!
Simulation in position 25 completed successfully!
Simulation in position 26 completed successfully!
Simulation in position 27 completed successfully!
Simulation in position 28 completed successfully!
```

(a) Log file before extended simulation

```
Simulation in position 0 completed successfully!
Simulation in position 1 completed successfully!
Simulation in position 2 completed successfully!
Simulation in position 3 completed successfully!
Simulation in position 4 completed successfully!
Simulation in position 5 completed successfully!
Simulation in position 6 completed successfully!
Simulation in position 7 completed successfully!
Simulation in position 8 completed successfully!
Simulation in position 9 completed successfully!
Simulation in position 10 completed successfully!
Simulation in position 11 completed successfully!
Simulation in position 12 completed successfully!
Simulation in position 13 completed successfully!
Simulation in position 14 completed successfully!
Simulation in position 15 completed successfully!
Simulation in position 16 completed successfully!
Simulation in position 17 completed successfully!
Simulation in position 18 completed successfully!
Simulation in position 19 completed successfully!
Simulation in position 20 completed successfully!
Simulation in position 21 completed successfully!
Simulation in position 22 completed successfully!
Simulation in position 23 completed successfully!
Simulation in position 24 completed successfully!
Simulation in position 25 completed successfully!
Simulation in position 26 completed successfully!
Simulation in position 27 completed successfully!
Simulation in position 28 completed successfully!
```

(b) Log file after extended simulation

Figure 4.5: Examples of log files that are produced by the MDrug completion check tool before and after the extension of simulations.

In some occasions the available computational time on an HPC is not enough to allow the completion of the required simulation time and thus it is common for the HPC to kill these overextended jobs. This however creates an issue for the researcher as it is very difficult to distinguish the simulations that are completed successfully from those that are killed, especially for the thousands of simulations that are involved in a permeation study. MDrug provides a Python script that allows the researcher to quickly check which simulations have this problem (figure 4.5). Then it automatically creates all the necessary files to extend the

simulations that were killed, which can be easily uploaded back to the HPC to continue. Once they are completed, MDrug allows an easy and safe merging of all the trajectories and output files from the different folders into one.

Regarding the visualisation, the VMD software is used in conjunction with a TCL script that has instructions regarding the permeation location, colouring and material selections, lighting and rendering options. Therefore, the visualisation of 30 systems is fast and reliable allowing quick inspection of important simulation phases (system creation, minimisation, equilibration etc.). The visualisation of systems after their creation is extremely important to ensure that permeants with complicated structures or aromatic rings are properly introduced in the membrane; in some occasions entanglement of lipid chains by aromatic rings is possible and thus MDrug allows the researcher to quickly fix it and avoid problematic simulations (figure 4.6).

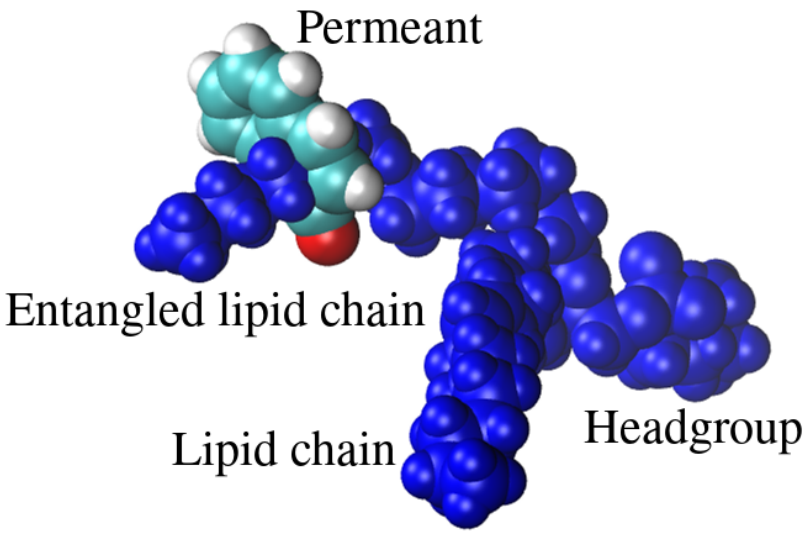

Figure 4.6: MDrug system visualisation allows early error detection. In this case, a permeant with aromatic rings, unnaturally entangles a lipid chain, just after system creation.

An important criterion for the evaluation of simulation results is their convergence over time. MDrug allows the researcher to run 2 different convergence techniques for each position and examine whether important properties like the free-energy difference, diffusion or permeation stabilises over time. The convergence techniques are examined in detail in section 5.1.2.1 where the results of this project are presented.

The main functionality of the post-processing toolset is the computation of the free-energy difference profile, the local diffusion coefficients profile and naturally the permeation coefficients for each permeant through each membrane. All the computations, as all the rest of MDrug features, are computed with the press of a button regardless of the number of positions examined. For permeation studies with LAMMPS as the selected program, a Python code is used to compute all properties according to equations 2.53 and 2.54. For studies performed with GROMACS, the free-energy difference is computed by the GROMACS

tool “gmx wham” and the local diffusion coefficients can be computed with two different methods shown in section 2.3.3.2.2. The differences in the results between the two methods are presented in section 5.3.2.

The centre-of-mass, lateral MSD and hydrogen bonds analyses are performed with TCL scripts and VMD and a Python script is utilised to manage the files and output results for all positions. Lateral diffusion can be alternatively computed with the GROMACS msd tool if this is the selected program.

The statistics for all properties and for each position are computed with the block averaging method introduced theoretically by Flyvbjerg and Petersen[146]. The code used in MDrug is a modified version of the Python implementation by Berendsen[147].

Finally, all the aforementioned results can be easily visualised either in a per-case or in a case-comparison way, with high quality plots produced by the Python library matplotlib, and a general management Python script.

Overall, the complete set of features provided with MDrug is expected to enhance considerably the productivity of any researcher performing permeation studies, whether in a local computer or in a remote HPC. All the results presented in this dissertation were produced with MDrug.

Chapter 5

Results and discussion

The results presented in the following sections are ordered as follows. In the first section (5.1) all the methodological issues of both the z-constraint and z-restraint methods are examined and addressed. The main results of this study start from section 5.2 where both the z-constraint and the z-restraint findings are presented in a way to cover the two corresponding aims of this dissertation:

- assessing the optimal method for automated, fast and robust permeation studies
- isolating the effect of the nonlamellar DOPE lipids on permeation.

5.1 Methodological issues

5.1.1 Computational efficiency

All the results presented in the following sections were produced with MD simulations that were run in the ARCHER UK national supercomputer located in the University of Edinburgh. One of the most surprising observations was the difference in the computational efficiency between the two methodologies and chosen MD software.

The combination of the z-constraint methodology and LAMMPS produced approximately 10 ns of trajectory per system per day. Each system consisted of 1 z-position, a membrane and a permeant. In total ARCHER allowed only 8 systems to run at the same time therefore in 24 h, a total of 80 ns could be completed. The z-restraint methodology and GROMACS was substantially faster, as it produced 100 ns of trajectory per system per day and 800 ns per day, in total. Due to a technical problem in its code*, the theoretically available z-constraint method could not be tested with GROMACS. Due to this big difference in

* www.mail-archive.com/gromacs.org_gmx-users@maillist.sys.kth.se/msg16753.html
www.mail-archive.com/gromacs.org_gmx-users@maillist.sys.kth.se/msg17177.html

the computational efficiency, the examination of 4 permeants with the z-constraint method required a year to complete. On the contrary, the examination of 13 permeants with the z-restraint method required less than 6 months. Table 5.1 summarises all the observations.

The reason behind this huge difference in computational efficiency lies in two factors that are more related to the software rather than the methods. Firstly, GROMACS is heavily optimised to simulate biological systems in comparison to LAMMPS that is more versatile, modular but also less biology-oriented. Secondly, it was noticed that LAMMPS updates the neighbour list in every timestep in comparison to GROMACS that by default it updates it every 40 and this could play a role in the slowdown of calculations. Overall, in terms of computational efficiency, GROMACS was found to be much better for permeation simulations with a 10× speed-up. The real bottleneck for the permeation study with GROMACS was the limit of 8 running jobs on ARCHER per day.

Table 5.1: Comparison of performance between LAMMPS and GROMACS and the respective MD software. All simulations ran on the ARCHER UK national supercomputer.

Method	Simulation time per system per day	Total simulation time per day	Number of permeants	Physical time for simulating the complete set
z-constraint	10 ns	80 ns	4	1 year
z-restraint	100 ns	800 ns	13	6 months

5.1.2 Convergence of simulations

5.1.2.1 Establishing a convergence evaluation technique

According to equation 2.52, the exponential of the free-energy difference is the dominant factor in the computation of the permeation coefficient and as such, it was chosen as the key property to examine simulation convergence. However, the constraint/restraint force and the derived potential of mean force are dynamic properties that fluctuate during the simulation. In fact, statistically, due to the nature of MD simulations, these properties can never be considered absolutely converged due to the fact that ergodicity is an assumption and the complete exploration of phase space is impractical or impossible[246]. Therefore, special techniques have been used in the past but also devised in this dissertation in order to establish a measure of relative convergence.

Before examining the convergence for all permeants, a case with the DOPC membrane and the water molecule was tested with two different techniques, in order to examine which is the best in identifying convergence. In the first technique, the constraint force timeseries was separated in ten different 10 ns parts and the free energy profile was created for each part. As it can be seen in figure 5.2a, the free-energy profile qualitatively obtains its form from the first 10 ns, however, quantitatively it fluctuates over 2 to 3 kcal mol^{-1} in both the

head group and bilayer centre regions. Therefore, an obvious convergence time limit could not be identified.

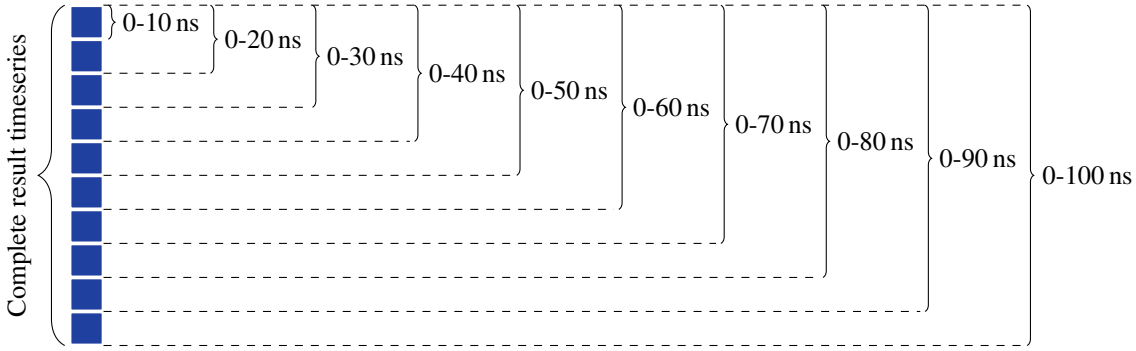

Figure 5.1: Schematic of the convergence study technique with cumulative sets of the time-series.

In the second technique, the constraint force timeseries was separated in 10 consecutive cumulative parts starting from the beginning of the timeseries and then each consecutive part was added in the timeseries used to produce the free-energy profile. Figure 5.1 visualises how this approach works. Furthermore, the results produced with this technique are shown in figure 5.2b and in contrast to the previous one, both quantitative and qualitative convergence was revealed clearly after the first 3 cumulative sets, making it a better and more robust way to identify convergence.

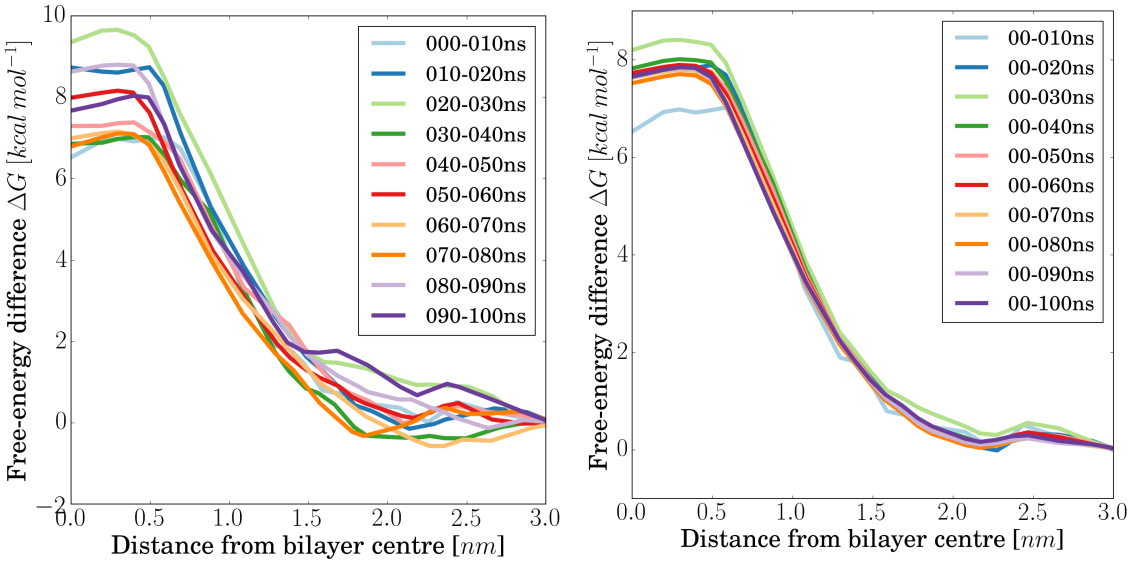

(a) Method 1: Independent sets.

(b) Method 2: Cumulative sets.

Figure 5.2: Comparison of convergence study methods for the DOPC membrane and a water permeant

Similar methodologies have been used in previous studies. Bemporad et al.[247–250] have examined the behaviour of the constraint-force timeseries to ensure its convergence to a particular value. Neale et al.[149] have used the block averaging[146] method to identify the equilibration time based on the initial systematic errors. In the same article, they propose the definition of a key observable, such as the binding free-energy, and the estimation of

convergence based on its behaviour as a function of simulation time. Nitschke et al[251] defined as the key observable in their study of ammonia and ibuprofen, the PMF barrier and minimum respectively.

Paloncỳovà et al.[252] used a contour plot showcasing the time evolution of the energy minima and barriers with their respective positions. Carpenter et al.[253] used a variation of the moving-average method to examine the convergence of free-energy profiles. Finally, Lee et al.[254] observed that simulation over the whole range of the bilayer thickness instead of half, even for shorter time, generally improved convergence speed. They also recommended a 50 to 100 ns equilibration for each window. It is clear from the aforementioned studies that there is no established methodology in the literature regarding the convergence of permeation studies. Therefore, the results of the approach introduced in this dissertation can provide researchers with an extra insight on this crucial parameter.

5.1.2.2 Convergence with the z-constraint

Applying the cumulative sets method to the four permeants examined with the z-constraint method and both membranes produced the results of figure 5.3. The cumulative sets vary in size based on the total simulation time. In all cases, curves converged qualitatively within the first 3 cumulative sets. Quantitatively results vary depending on the system; ammonia converged during the first 50 ns for both membranes, water converged faster for DOPC ($\approx$ 40 ns) than DOPC:DOPE ($\approx$ 70 ns), fluoromethane converged faster for the mixture ($\approx$ 60 ns) than for DOPC ($\approx$ 80 ns) and finally, carbon dioxide converged for both systems at around 30 ns.

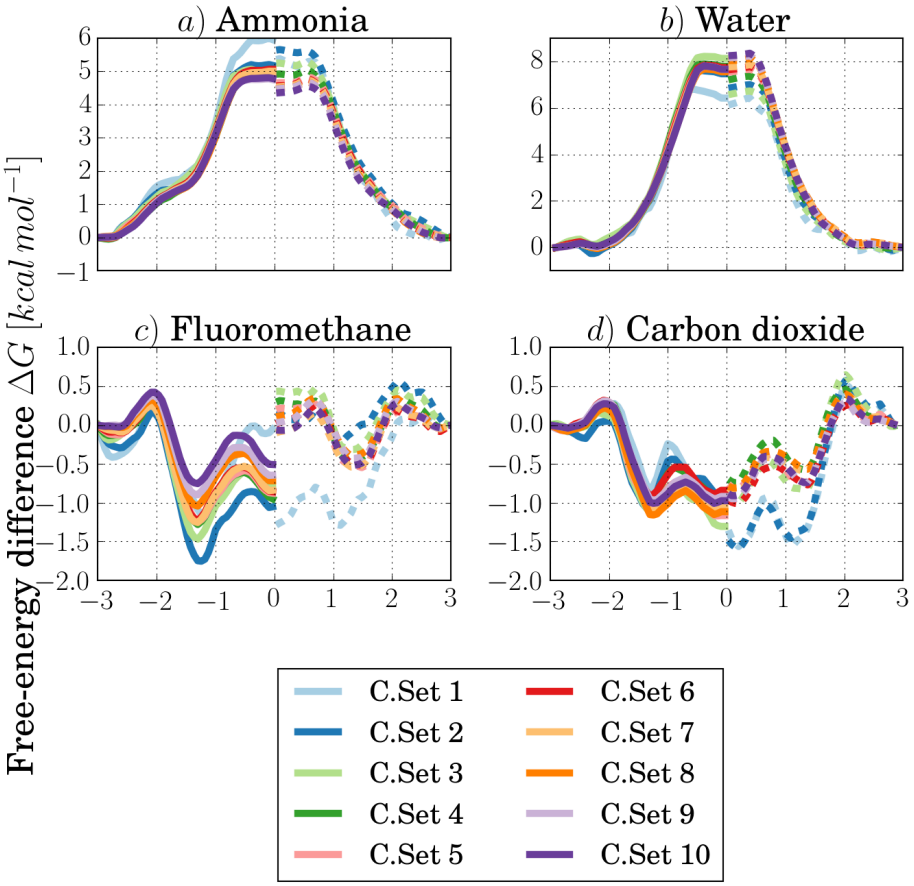

Figure 5.3: Convergence of ΔG profiles for all permeants and both membranes. Each diagram shows two halves of the bilayer with the solid lines representing the pure DOPC systems and the dashed lines representing the DOPC:DOPE systems. C.Set stands for cumulative set and the larger the number the larger the cumulative set e.g., for the water-DOPC system, C.Set 2 stands for the 0-20 ns set and C.Set 3 stands for the 0-30 ns set.

5.1.2.3 Convergence with the z-restraint

Figures 5.4 and 5.5 show the evolution of the free-energy profile of the DOPC and DOPC:DOPE (1:3) membranes and all permeants, for the z-restraint method. Generally profiles stabilise between the 0-30 ns and 0-40 ns blocks. Initial blocks fluctuate more because the permeant-membrane complex relaxes to accommodate the new restraint behaviour of the permeant. Also, they are relatively more noisy than the latter blocks because the number of sampled points is smaller. Nevertheless, even in the worst case of urea and the DOPC membrane, the maximum ΔG fluctuation between the initial block of 0-10 ns and the stable block of 0-40 ns is $\approx$3 kcal mol^{-1} and localised only on the bilayer centre.

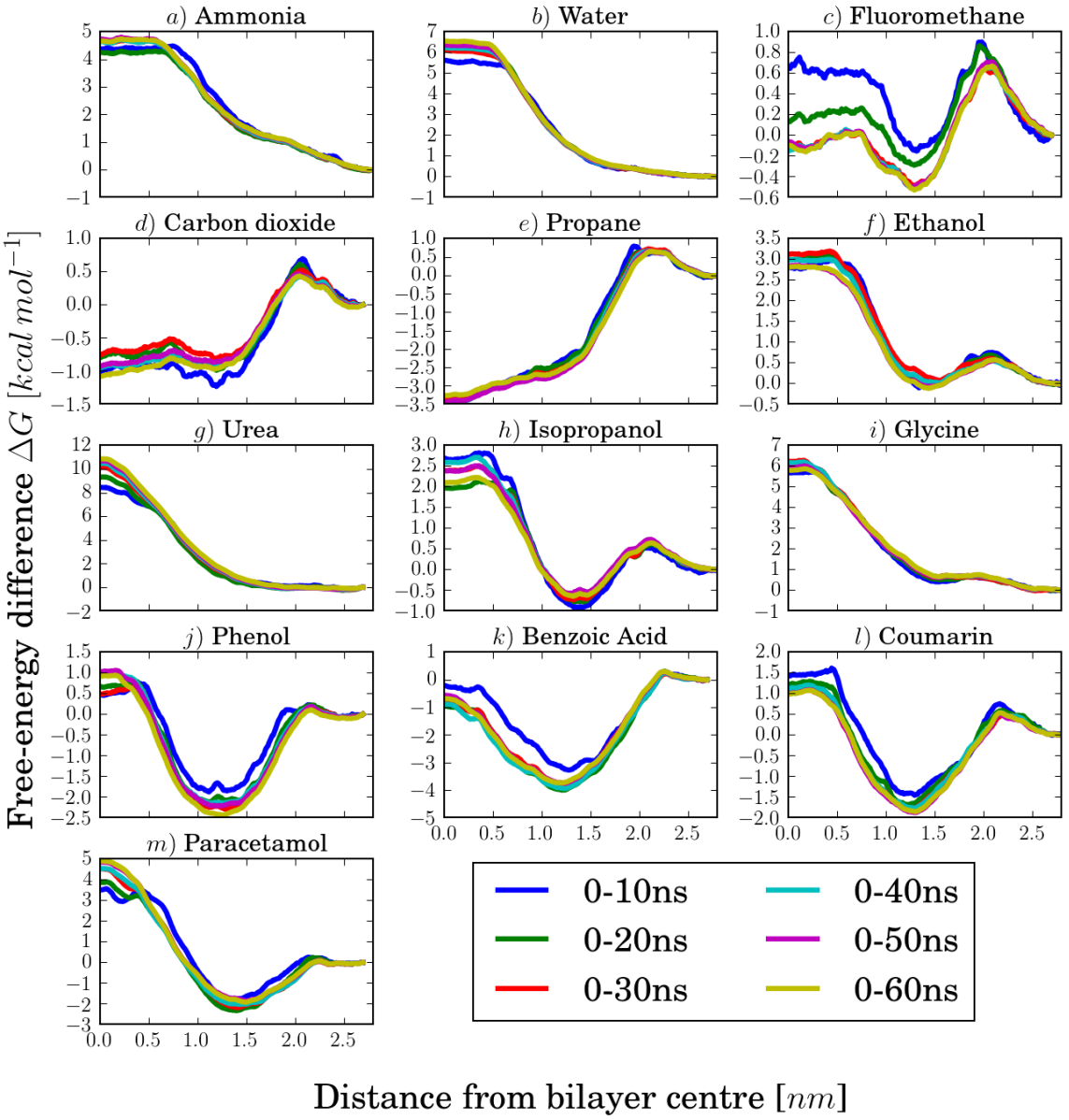

Figure 5.4: Convergence of ΔG for all permeants and the DOPC membrane

Qualitatively, profile fluctuations are more prominent in fluoromethane or carbon dioxide but this is due to the small scale of the y-axis which amplifies the differences. Based on the above, the first 30 ns of the production trajectories and outputs were discarded as further

equilibration and the rest of the results presented in the following sections correspond to the last 70 ns.

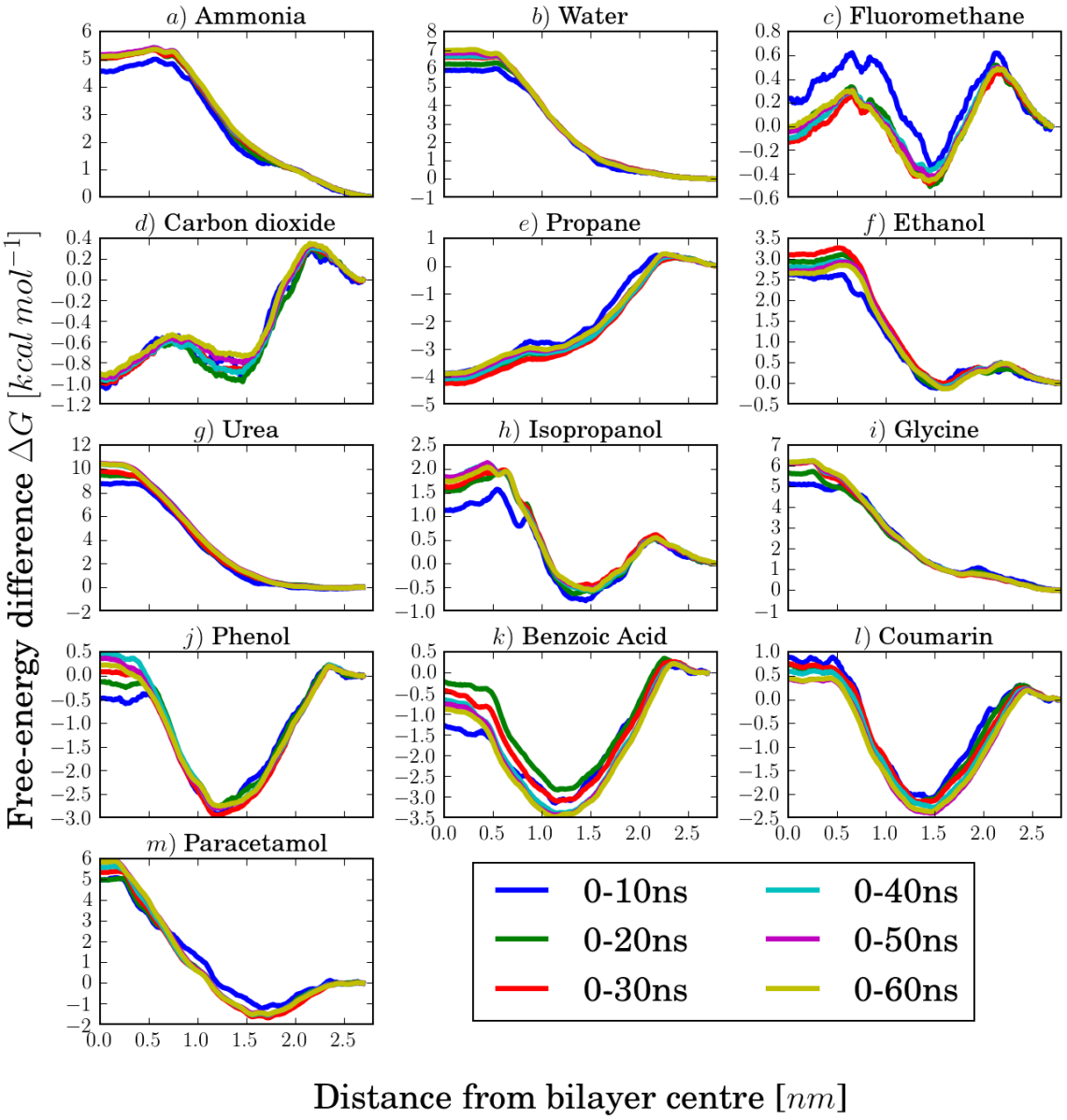

Figure 5.5: Convergence of ΔG for all permeants and the DOPC:DOPE(1:3) membrane

For most permeants the convergence was 10 to 15 ns faster through the pure DOPC than through the mixture and the difference was particularly evident for the largest permeants, phenol, benzoic acid, coumarin and paracetamol. However, the same or slower convergence for the permeation through DOPC was observed for fluoromethane, carbon dioxide and isopropanol. Slower convergence for bilayers of mixed composition has also been observed in a study of Hong et al.[255] where they examined the total time for complete mixing of various lipids in symmetrical bilayers. They saw that the radial pair distribution function of PE:PG and PC:cholesterol membranes was slower to converge than that of pure POPC.

5.1.2.4 Effect of method on convergence speed

Comparison between the results of the two methods shows that generally the umbrella sampling simulations converged faster than the z-constraint simulations. It is not possible to conclude whether this is due to the faster GROMACS software or due to the difference between constraining and restraining. The faster convergence of PMFs with the z-restraint is in contrast to the findings of Paloncỳovà et al.[252] who have observed a faster convergence with the z-constraint method, especially when starting positions were obtained by unbiased permeation simulations. However, in their work, the z-restraint positions were initiated by a preceding pulling simulation, which for polar molecules like coumarin might carry along a hydration shell of water molecules introducing bilayer deformations. This disadvantage of initial steered MD has also been reported by Lee et al.[138] who recommended building the membrane around the permeant or insert the permeant in a perturbative fashion. The method followed in this work was a combination of the latter recommendations in which the permeants were inserted in each position directly followed by a minimisation/relaxation of the whole structure, avoiding in this way violent membrane disruptions or unwanted shell hydrations due to pulling.

The equilibration/convergence timings chosen in this dissertation (+30 ns) are among the highest reported in the literature. It is noteworthy however, that Neale et al.[149,150] have discovered that umbrella sampling simulations suffer from systematic sampling errors risen from previously unconsidered slow-converging degrees of freedom (DOF), orthogonal to the typically chosen reaction coordinate (the distance between centres of masses). These slower DOFs might involve, among others, the lateral organisation of the lipids and permeants' conformational changes, especially when intramolecular hydrogen bonds can be formed[110,250,256]. Regarding the former, the membranes used in this work were taken pre-equilibrated for 1 μs ensuring converged dynamics. Regarding the latter, the extra 30 ns equilibration per window is considered sufficient for the exploration of the examined small molecules conformational changes. Finally, while urea, glycine, benzoic acid and paracetamol can form internal hydrogen bonds, it is not possible to estimate if there is an underlying DOF delaying true convergence as the presented results in figures 5.4 and 5.5 quickly stabilise for both membranes.

5.1.3 Establishing a diffusion calculation technique for the z-restraint method

In order to evaluate the best method for the calculation of the local diffusion coefficients for the z-restraint method, a test case of the DOPC membrane and the water molecule was examined with both the Hummer[23] (equations 2.56 and 2.57) and the Zhu and Hummer[24] (equations 2.56 and 2.58) methods.

5.1.3.1 Hummer method

The method proposed by Hummer requires the calculation of the integrated autocorrelation function τ of the z-axis distance between the permeant and the membrane's centre of mass, for each 10 ns part of the z-position timeseries (7 in total from 30 ns to 100 ns). While the computation of the autocorrelation function is trivial due to pre-existing numerical libraries, the calculation of the integral poses a challenge. A practice that has been used previously[247,253] involves the fitting of a double exponential function to the autocorrelation of the z-axis distance. Unfortunately, when it was attempted to fit a double exponential function to different 10 ns autocorrelation values of the z-axis distance, the fitting failed partially or completely (figures 5.6a, 5.6b and 5.6c). Reduction of the autocorrelation datasets from 10 000 to 1000 did not improve the overall poor performance of the fitting (figures 5.6d, 5.6e and 5.6f).

O'Neill et al.[257] have examined an alternative technique for the calculation of the autocorrelation function integral. Instead of fitting, they used 4 different cut-offs in order to decide the integration domain (the length of the autocorrelation dataset), which was then integrated numerically with the trapezoidal rule. In the first cut-off, the entire autocorrelation dataset was considered for the integral, the second included the values until the global minimum of the negative values, the third included the values until the first time that autocorrelation became zero and finally the fourth took into account all values until when autocorrelation became smaller than 1/e. Table 5.2 presents the results for the DOPC-water system, for 4 different distances from the bilayer core and for the 4 different techniques.

When considering the whole extend of the autocorrelation (9999 points for a 10 ns timeseries) the calculated diffusion coefficients were nonphysical, due to the long oscillatory behaviour of the decay tail. The fourth method overestimated diffusion coefficients especially in the hydrophobic region of the bilayer, that for water are usually much smaller[249,258] than 1 cm s^{-2}. Also, for fast decaying autocorrelations, the 1/e criterion was very high and was a potential source of error. Finally, the other 2 methods produced similar, physically plausible values, however, in cases where the autocorrelation never becomes negative or it has multiple minima, the ACF = ACF_{min} criterion becomes problematic.

In order to examine whether the fitting performance would be better for a smaller autocorre-

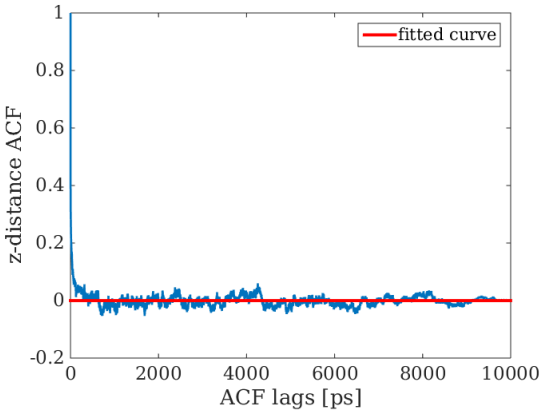

(a) 10 ns. Complete failure.

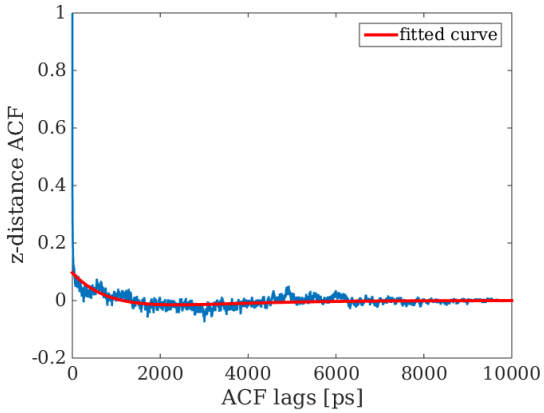

(b) 10 ns. Missed initial part.

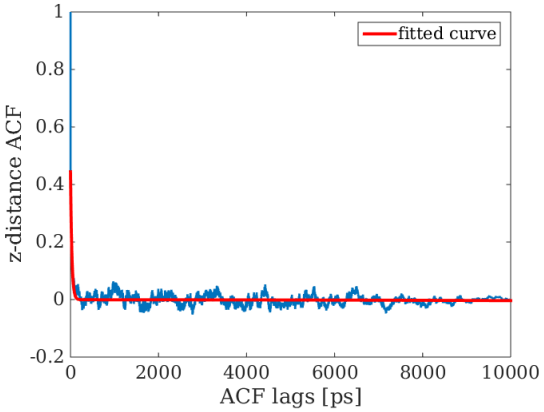

(c) 10 ns. Partial fit through initial part.

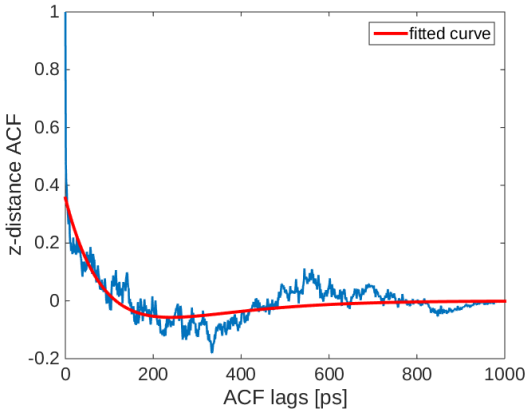

(d) 1 ns. Partial fit through initial part.

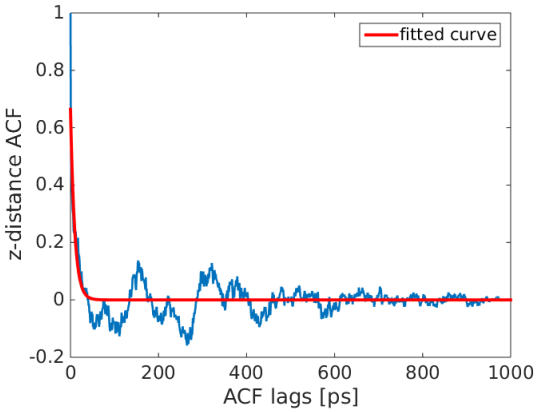

(e) 1 ns. Negative-positive fluctuation.

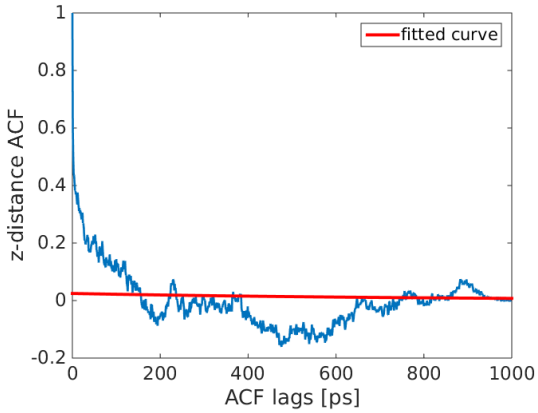

(f) 1 ns. Complete failure.

Figure 5.6: Common problems encountered when attempting to fit a double exponential function to a 10 ns or a 1 ns part of the clean z-distance autocorrelation. The system is the DOPC-water and the autocorrelation is between 90 ns to 100 ns.

Table 5.2: Evaluation of the integral domain for the Hummer method based on the work of O'Neill et al.[257].

	D [x10^{-5} cm^2/s]			
Integration domain	z=0.1 nm	z=1 nm	z=2 nm	2.8 nm
x = xmax	237305	504341	-198962	151866
x at ACF = ACF_{min}	2.06	0.15	0.8	4.26
x at ACF = 0	1.48	0.13	0.53	3.38
x at ACF = 1/e	3.98	1.63	2.31	4.59

lation dataset, the x at ACF = 0 criterion was used in conjunction with a double exponential fitting. Figure 5.7 shows that with a smaller number of points, the fitting behaviour improved, however, the computed diffusion coefficients were orders of magnitude lower than expected.

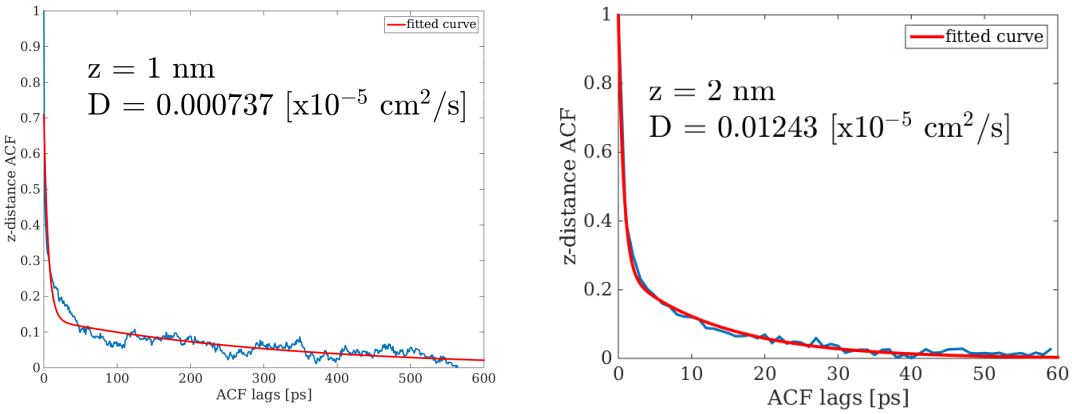

(a) 1 nm. Lost initial part.

(b) 2 nm. Good fit. Wrong D.

Figure 5.7: Fitting of a double exponential function to a filtered z-distance autocorrelation. The system is the DOPC-water and the ACF is from 90 ns to 100 ns

In conclusion, regarding the Hummer method for the calculation of diffusion coefficients, the integral domain for x at ACF = 0, with no fitting, is preferred for its robustness and general applicability independent of the ACF behaviour.

5.1.3.2 Zhu and Hummer method

The method from Zhu and Hummer[24] was used in conjunction with the block averaging method[146] for each 10 ns part of the z-position timeseries, in order to compute the variance of the mean as the square of the standard deviation. Figure 5.8a is a typical example of the aforementioned behaviour; it shows how the standard deviation of the mean z position reaches the plateau at 0.0014 nm, for the DOPC-water system, z=2 nm and the 40 ns to 50 ns part of the z-position timeseries.

It can be observed that the larger the block size, the larger the uncertainty of the standard deviation. This is expected because as the block size increases, less blocked points will

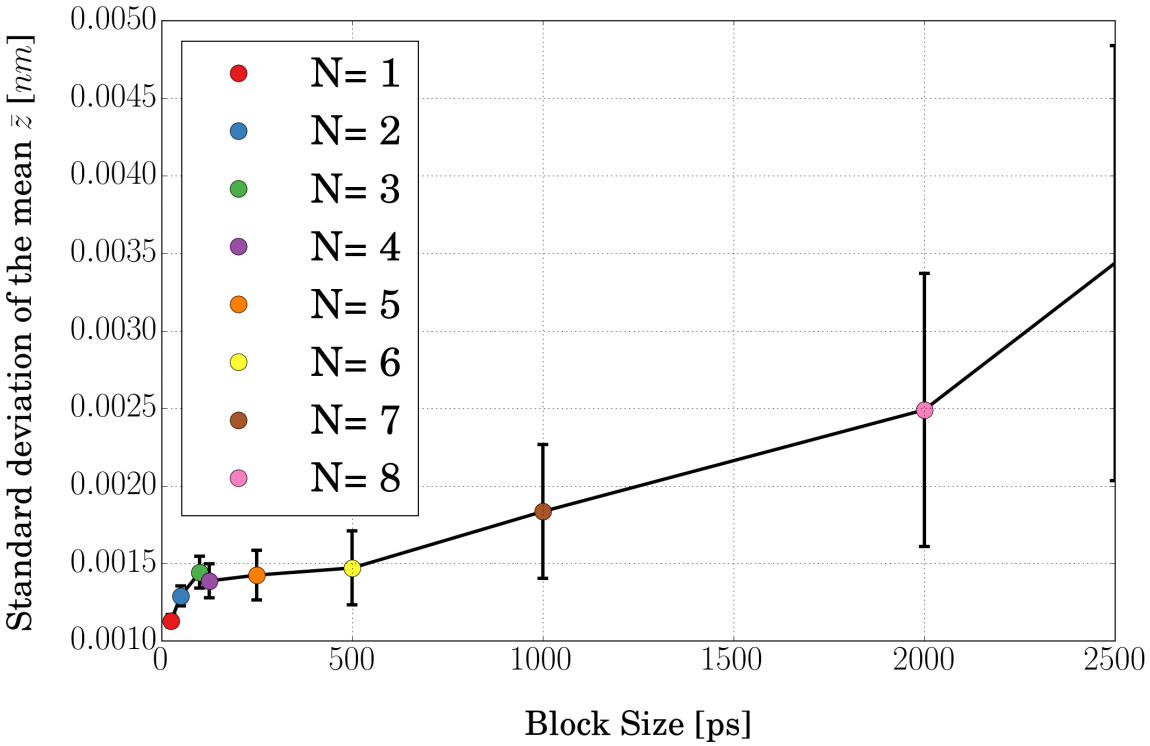

(a) The standard deviation of the mean for the 2 nm z position, between 40 ns to 50 ns, that is calculated by block averaging. Each point refers to the respective set of points in figures 5.8b and 5.8c.

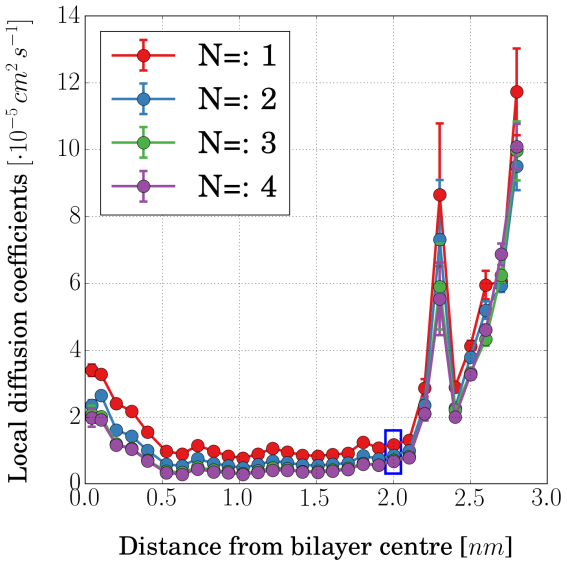

(b) Local diffusion coefficient from smaller block sizes.

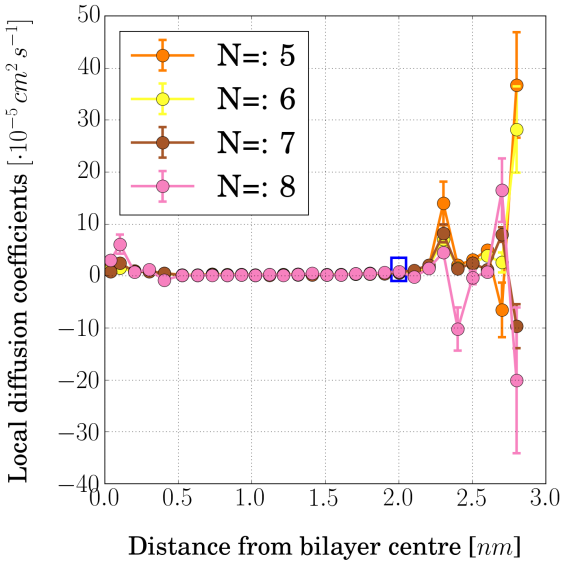

(c) Local diffusion coefficient from larger block sizes

Figure 5.8: The effect of the block size in the robustness of the Zhu and Hummer method. The results presented here are for the DOPC membrane and the water molecule. The blue rectangle in figures 5.8b and 5.8c refer to the results of figure 5.8a.

exist to calculate the statistics e.g., for a 10 ns part of 10 000, 1 ps samples, a block size of 500 creates 20 blocks while a size of 2000 creates only 5 points. In total 5096 block size evaluations were needed for the total work presented in this dissertation (26 systems x 28 positions x 7 timeseries parts), which made manual judgement inefficient if not impossible. Unfortunately, setting an automatic converging criterion based on the derivative of the block size curve or simply on the absolute difference between standard deviations, did not work. The reason was that different systems behaved qualitatively similar but not identical which led to many misjudgements. To overcome the automation problem, it was decided to set a *de facto* block size for all cases.

In order to identify the default block size, the diffusion coefficients were calculated for the whole DOPC-water system for the first eight block sizes (25, 50, 100, 125, 250, 500, 1000 and 2000 ps). As it can be seen by figure 5.8a, after 100 ps the standard deviation reaches a plateau indicating that after that time, z-position points are no longer correlated. Figures 5.8b and 5.8c present the computed diffusion coefficients for each of the block size. For the small block sizes of 25, 50, 100 and 125 ns the results are qualitatively identical. However, in areas of higher diffusion such as close to the bilayer centre and above the polar/apolar interface, the size of the block alters the diffusion values e.g., the diffusion at the bilayer centre with the 25 ps block is almost double than the one from 125 ps. Another important observation is that from block size 250 ps (N=5) and larger, the calculation of the diffusion is very unpredictable and diverges in z positions above the polar/apolar interface where the diffusion of water is faster. These aforementioned inconsistencies are very problematic as they indicate a strong relationship of the method's robustness to a highly varying parameter such as the block size. For the test case presented here, the best results in terms of stability were obtained for the 100 or 125 ps (N=3 or N=4) block size.

5.1.3.3 Method selection

Figure 5.9 shows the diffusion coefficients for DOPC and DOPC:DOPE(1:3) for the water molecule and the most robust parameters of both methods. The Hummer method predicts the same water diffusion in the hydrophobic core of both membranes and apart from a peak in the z=2.3 nm for the DOPC membrane, the diffusion is also similar in the hydrophillic part of the membranes. The Zhu and Hummer method predicts for both membranes the same diffusion for the upper and lower part of the fatty acids, however deviations are larger in the bilayer centre (z=0) and in the water region (z=2.8 nm). Especially the latter is unexpected considering that the water permeant should behave with a similar way in the water region regardless of the membrane composition, which happens only for the Hummer method and not for the Zhu and Hummer. Furthermore, a huge discrepancy between the methods is observed on the computed local diffusion coefficient in the water region. The Hummer method predicts a local diffusion coefficient of approximately $3 \times 10^{-5}\,\mathrm{cm^2\,s^{-1}}$ for both membranes, while the Zhu and Hummer varies from $7 \times 10^{-5}\,\mathrm{cm^2\,s^{-1}}$ to $10 \times 10^{-5}\,\mathrm{cm^2\,s^{-1}}$. The experimental[259] self-diffusion coefficient of wa-

ter for 298 K and 1 atm is 2.3×10^{-5} cm^2 s^{-1} and for TIP3P[260] is 5.2×10^{-5} cm^2 s^{-1} due to the low viscosity of this particular water model[261].

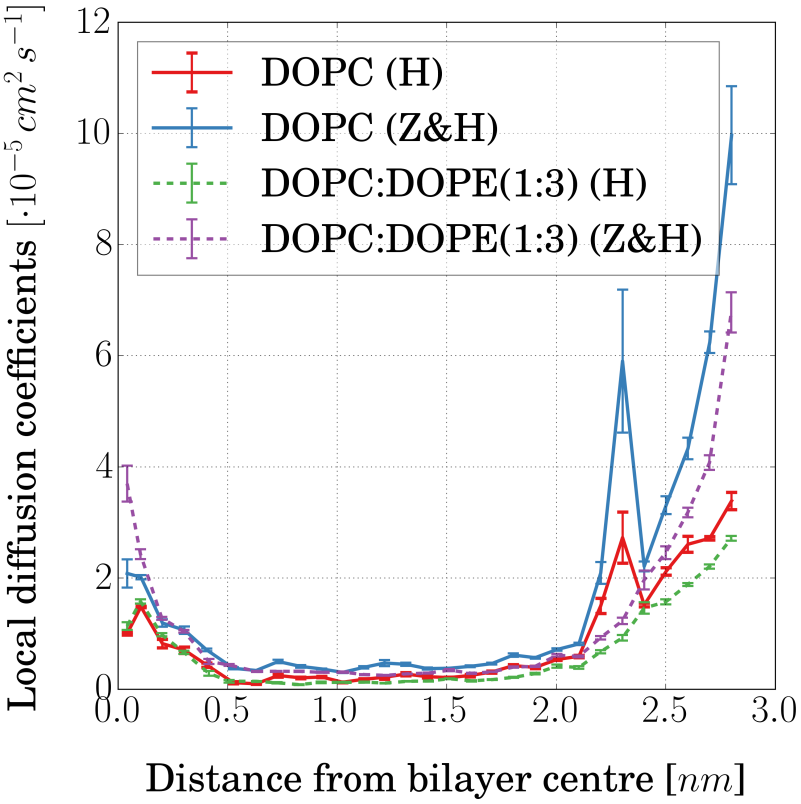

Figure 5.9: Local diffusion coefficients comparison for the two examined membranes and a water permeant. H refers to the Hummer method and Z&H refers to the Zhu and Hummer method.

In this dissertation a thorough analysis of both the Hummer method and the Zhu and Hummer technical sensitivities is presented for the first time. Especially in regards to the former, from the presented analysis it is clear that fitting of the ACF is a prone-to-failure technique due to the sensitivity to ACF decay rate and oscillatory behaviour, which anyway changes for each solute and position. Therefore, fitting of the ACF cannot be entirely automated and thus can not be part of a high throughput drug selection process. Even direct integration of the ACF is prone to error based on the selected integration domain as it was seen in this work and previous[23]. Considering the lack of robustness of the Zhu and Hummer method, as well as the larger deviation from experimental and simulation predictions for the water diffusion, the Hummer method with the integral domain up to the first zero crossing of the ACF was chosen as the methodology to compute the local diffusion coefficients for the rest of the systems.

5.2 Free-energy profiles

5.2.1 Free-energy profiles with the z-constraint

The z-constraint free-energy profiles for all molecules and both the pure DOPC and the DOPC-DOPE membranes are presented in figure 5.10. In regards to the comparison between the membranes, the results are very similar for the hydrophillic and upper hydrophobic regions of the bilayer. In the bilayer centre however, no clear trend can be observed due to the addition of DOPE lipids. For water, the free-energy curve of DOPC is higher, for ammonia is lower and for fluoromethane and carbon dioxide the results are the same since the standard errors (transparent regions) mostly overlap.

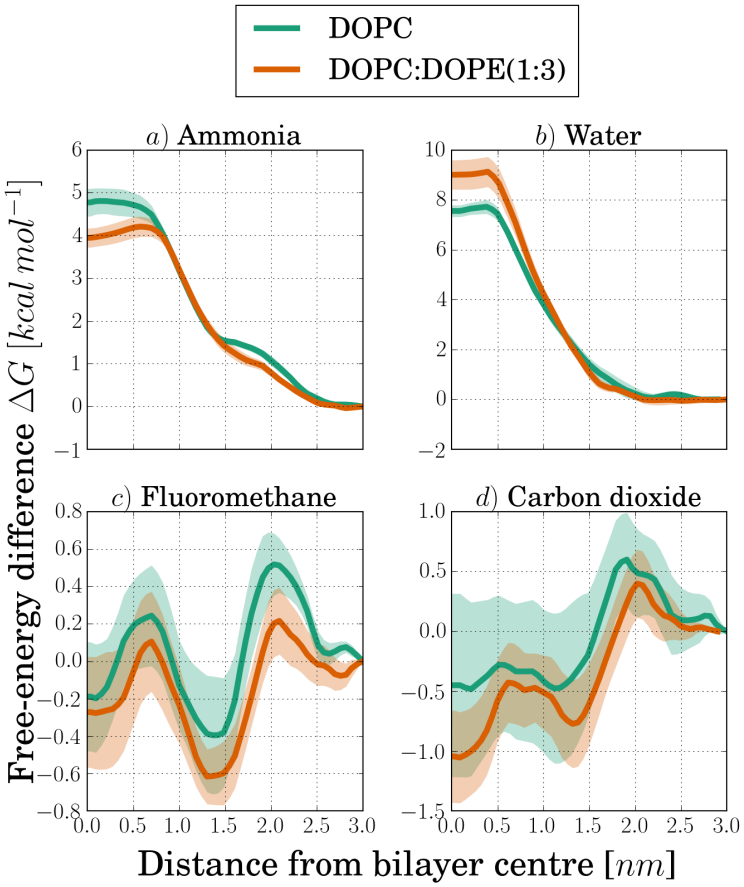

Figure 5.10: ΔG comparison between the pure DOPC membrane and DOPC:DOPE membrane for the z-constraint method.

Regarding the permeation behaviour, ammonia and water that are both hydrophillic molecules, experience an increase in the free-energy as they penetrate deeper in the hydrophobic part of the bilayer. As they reach closer to the bilayer centre the profiles form a plateau, for ammonia at 4 kcal mol^{-1} (DOPC) and 5 kcal mol^{-1} (DOPC:DOPE) and for water at 7.9 kcal mol^{-1} (DOPC) and 9 kcal mol^{-1} (DOPC:DOPE). Fluoro-methane and carbon dioxide have a small positive peak in the hydrophillic region and then their profiles oscillate around zero with the mean just in the negative side of the axis.

5.2.2 Free-energy profiles with the z-restraint

The z-restraint free-energy profiles $\Delta G(z)$ for the examined 13 molecules through the pure DOPC and DOPC:DOPE(1:3) bilayers are shown in figure 5.11. Initially, permeants can be separated in three distinct categories depending on where they exhibit the minimum of their free-energy difference. This minimum value shows the location where the molecules preferentially partition.

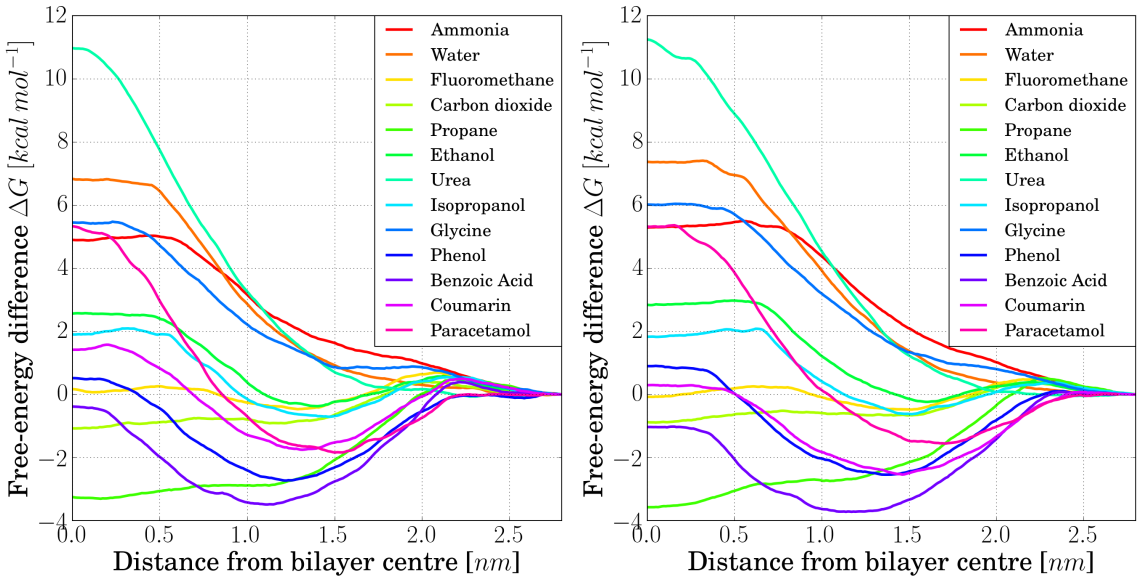

(a) DOPC membrane

(b) DOPC:DOPE(1:3) membrane

Figure 5.11: ΔG comparison of all permeants per membrane. Colours in legend are sorted by ascending molecular weight.

In the first category, the free-energy difference is always positive along the bilayer and the minimum position corresponds to the reference point for $\Delta G(z) = 0$ in the water phase. This is a typical characteristic of the polar hydrophilic ammonia, glycine, urea and water, indicating that their preferred location of accumulation is not inside the bilayer a behaviour that is expected given the hydrophobic nature of the bilayer core.

In the second category, the profiles have a small positive peak in the lipid head region, then exhibit a negative global minimum in the polar/apolar interface and finally a larger positive peak in the hydrophobic core. Coumarin for the DOPC membrane, ethanol and isopropanol, clearly belong to this category, with five more molecules exhibiting minor deviations from this behaviour. Benzoic acid has a peak in the hydrophobic core but is negative in value. Also, coumarin for the DOPC:DOPE(1:3) membrane, as well as paracetamol and phenol for both membranes, do not have a positive barrier in the head region. Fluoromethane has a positive peak in the head region, a global minimum in the interface, a second positive peak close to the hydrophobic core and then for the DOPC membrane the profile is marginally positive, while for the DOPC:DOPE(1:3) membrane the profile is marginally negative. All these molecules have an amphiphatic nature and under physiological conditions they would partition in the polar/apolar interface[262,263], therefore the free-energy profiles predict the

expected behaviour.

In the third category, carbon dioxide and propane, both hydrophobic, have a small positive peak in the lipid head region and then remain negative with the global minimum value located in the bilayer centre, corresponding to their preferred partitioning position.

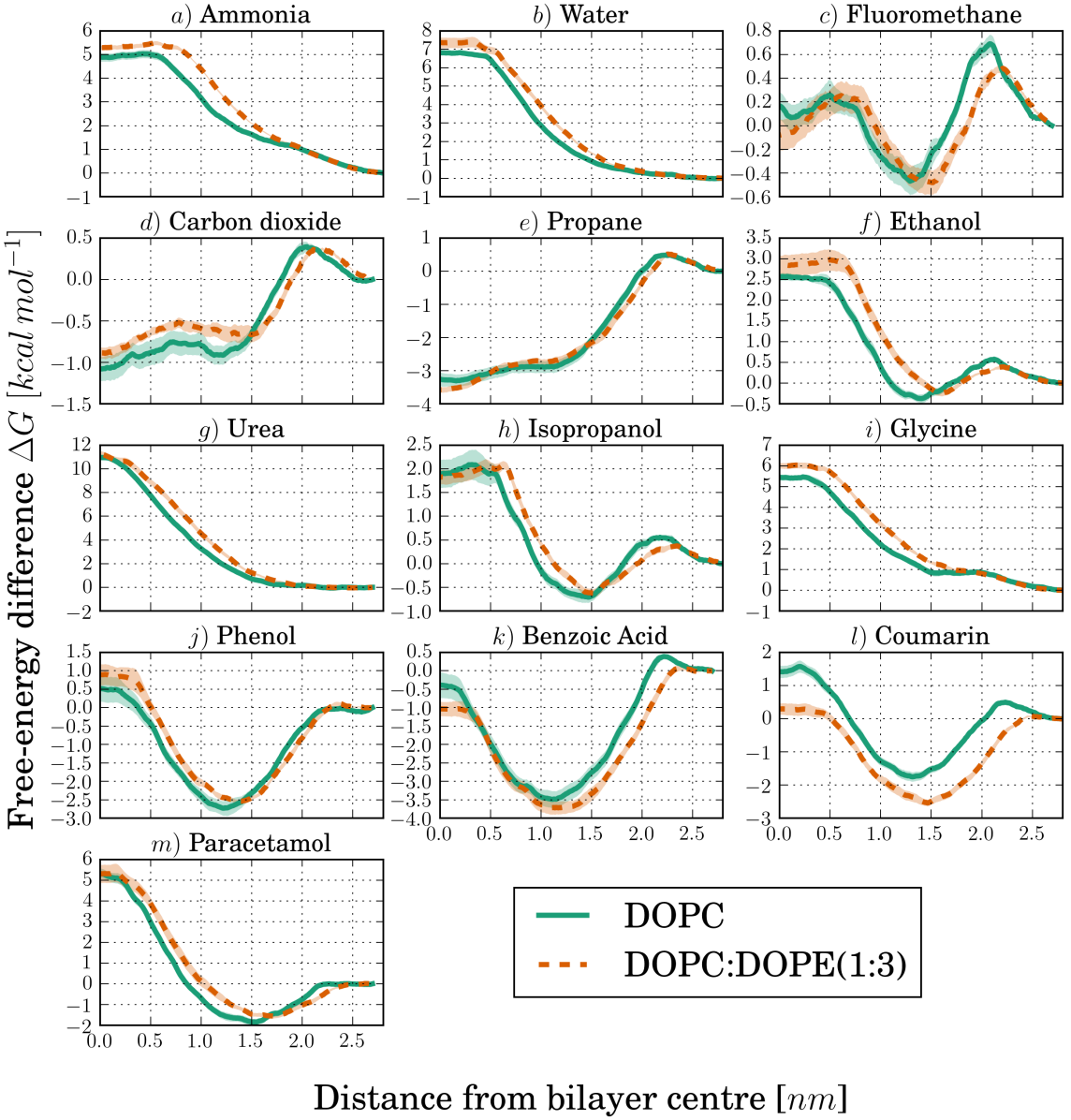

Figure 5.12: ΔG comparison between the DOPC and DOPC:DOPE membranes for the z-restraint method

Permeants can be further classified by examining the effect of DOPE lipids on the transfer process (figure 5.12). In the first group, comprising ammonia, glycine, urea and water, the free-energy profile of the PC:PE mixture is the same or higher than the DOPC profile, across the whole bilayer depth. This is an indication that the addition of DOPE lipids inhibits the permeation process, in parts or across the entire bilayer. For the second group of carbon dioxide, ethanol, paracetamol and phenol, a lower PC:PE mixture profile is observed in the head group area but a higher PC:PE profile is observed in the interface and hydrophobic

core area. Isopropanol and fluoromethane, have a slight deviation from this behaviour by having a marginally lower peak in the PC:PE bilayer core than in the pure PC membrane. Benzoic acid, coumarin and propane, form the third group where the PC:PE mixture profile is the same or lower than the DOPC profile all across the bilayer. Table 5.3 shows the summary of permeants classification depending on their free-energy difference profiles.

Table 5.3: Permeants classification based on their free-energy profile. "tails" refers to the lipid tails region and "head" refers to the lipid headgroups region.

	Partitioning area		
Observed ΔG	**Bulk water**	**Lipid headgroups**	**Lipid tails**
$\Delta G_{\text{PC:PE}} \geq \Delta G_{\text{PC}}$	Ammonia Glycine Urea Water		
$\Delta G_{\text{PC}}^{\text{tails}} \leq \Delta G_{\text{PC:PE}} \leq \Delta G_{\text{PC}}^{\text{head}}$		Ethanol Fluoromethane*† Isopropanol† Paracetamol* Phenol*	Carbon dioxide
$\Delta G_{\text{PC:PE}} \leq \Delta G_{\text{PC}}$		Benzoic acid* Coumarin*	Propane

$*$ permeant exhibits minor deviation from the definition of partitioning area category
† permeant exhibits minor deviation from the definition of PC:PE effect group

5.2.3 Validation and comparison between the methods

The free-energy profiles presented for both methods in the previous sections are in good qualitative agreement with previous studies of the same permeants and the same or different PC and PE lipids[139,210,218,248–250,254,264]. In particular, they all fit in the categories that were introduced by Neale et al.[151] who classified over 200 PMFs of more than 100 small molecules from the literature.

Direct comparison between the profiles of the two methods shows that while there are qualitatively the same, the are quantitative variations that lead to opposite interpretation. Ammonia in DOPC has an energy barrier in the bilayer centre of approximately 5 kcal mol^{-1} for both methods. The barrier however for the DOPC:DOPE membrane is lower with the z-constraint method and higher for the z-restraint. Water profiles are lower for both membranes in the z-restraint method but there is no discrepancy in terms of barrier height. For fluoromethane and carbon dioxide, the z-constraint profiles of the PC:PE membrane are lower than DOPC across the whole monolayer in disagreement to the z-restraint results. Previous comparative studies between the two methods[252,265] have suggested that the z-restraint and z-constraint methods should provide the same results, however the latter might be faster and more robust. In this work however, the z-restraint method not only produced

faster and more converged free-energy profiles (smaller error bars), but also results that can be explained by the physical properties of the bilayers (see section 5.8).

5.3 Local diffusion profiles

5.3.1 Local diffusion with the z-constraint

Figure 5.13 shows the local diffusion profiles calculated with equation 2.54. The results between the two membranes are the same both qualitatively and quantitatively. All permeants present a higher diffusion in the centre of the bilayer than in any other region and quantitatively the values for ammonia and water in that region are 2 times higher. In the rest of the bilayer, permeants reach a plateau between 0.2×10^{-5} and 0.45×10^{-5} $cm^2\ s^{-1}$.

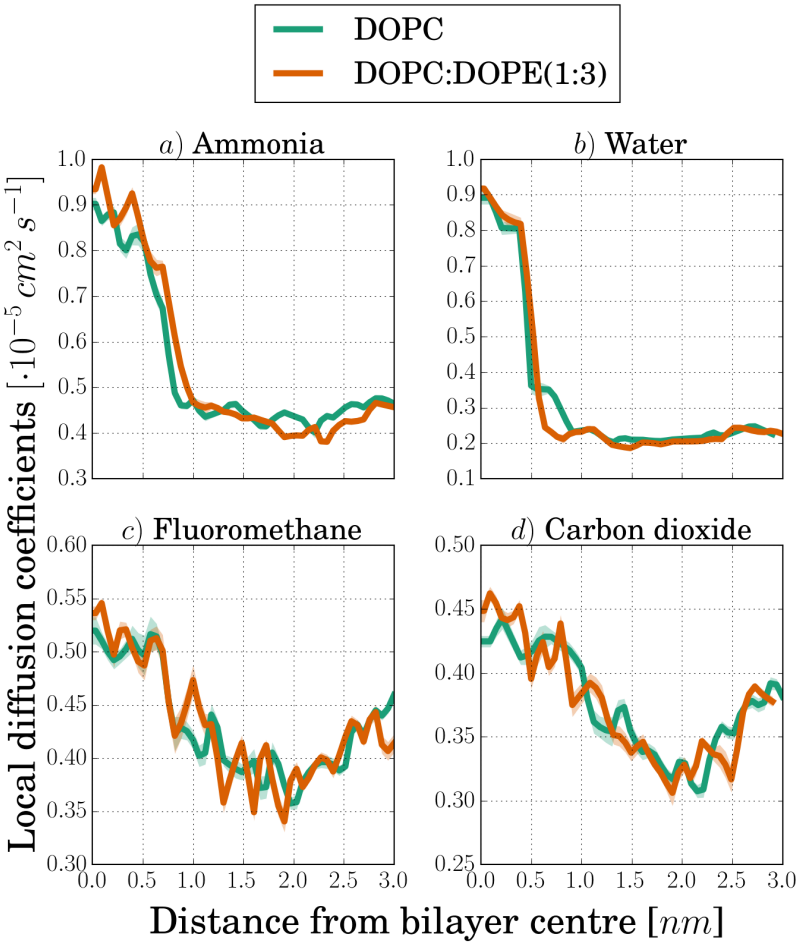

Figure 5.13: Local diffusion coefficients comparison between the pure DOPC membrane and DOPC:DOPE membrane for the z-constraint method.

5.3.2 Local diffusion with the z-restraint

Figure 5.14 shows the local diffusion coefficients of all permeants, sorted based on their molecular weight, for the DOPC (figure 5.14a) and the DOPC:DOPE(1:3) (figure 5.14b) membranes. In both membranes all permeants exhibit the same qualitative behaviour; in the water region the diffusion is the highest, then it drops quickly close to 0 as permeants

approach the hydrophobic lipid tails and finally increases again in the bilayer core, where the lipid chains of the two monolayers interact. Quantitatively, for both membranes, diffusion for heavier molecules, especially in the water region, is considerably slower e.g., paracetamol has 10 times slower diffusion in water than ammonia.

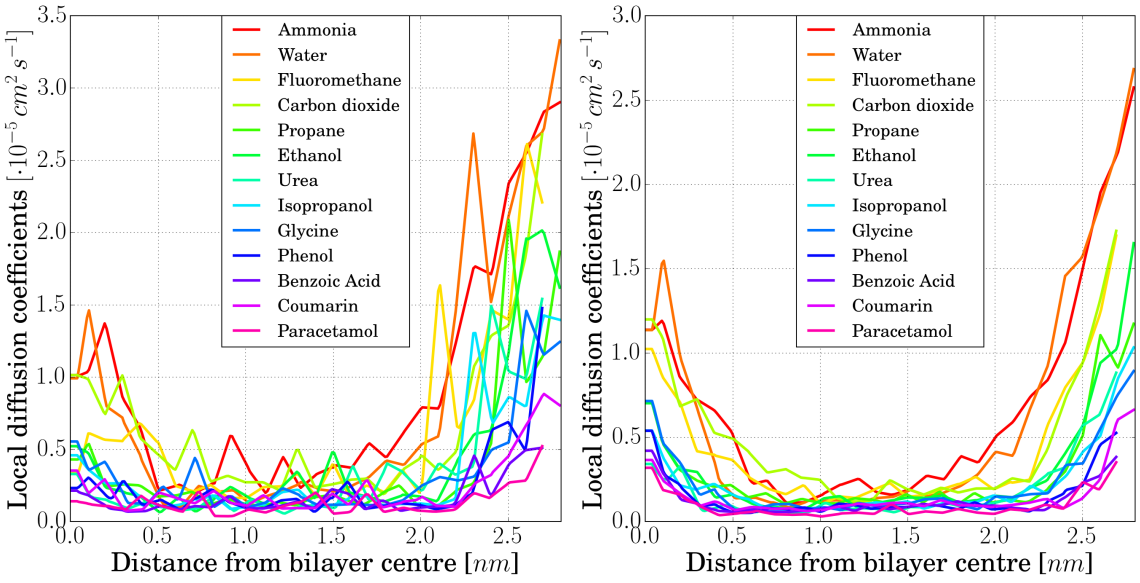

(a) DOPC (b) DOPC:DOPE (1:3)

Figure 5.14: Comparison of local diffusion coefficients between permeants. Error bars are omitted for clarity.

In regards to the effect of DOPE lipids, as can be seen by figure 5.15, there are no significant differences between the two examined membranes. For benzoic acid, fluoromethane, paracetamol and phenol, the peak in the bilayer core is marginally higher for the PC:PE mixture. Also, for all molecules, the PC profile is slightly higher in the head region than the PC:PE profile which tends to equalise towards the water region. This is counter-intuitive as generally choline is bulkier than ethanolamine and one would expect that the diffusion of permeants would be higher for the PC:PE bilayer. A possible explanation is that the PC:PE bilayer has higher thickness than the DOPC[22] ($\approx$ 4%), thus the permeant will leave the head group region a bit higher than in the DOPC and therefore the diffusion profile will be slightly shifted outwards (to the right side of the figures).

5.3.2.1 DOPC diffusion profiles oscillations

It has been noticed from previous studies[139,248,249,253,266,267] that local diffusion profiles are more noisy than the respective free-energy difference profiles. In this study, this behaviour is predominant in the DOPC rather than the PC:PE profiles. Especially for water, fluoromethane, propane, urea, isopropanol and benzoic acid there is an protruding peak at 2.3 nm away from bilayer centre, which has not been observed in past studies. Figure 5.16 shows the restrained z-position timeseries that the simulation for the DOPC-water system produced for two different positions, 1.8 nm and 2.3 nm. In the 2.3 nm timeseries (orange line) there is a highly oscillatory behaviour between 55 ns and 75 ns where the water perme-

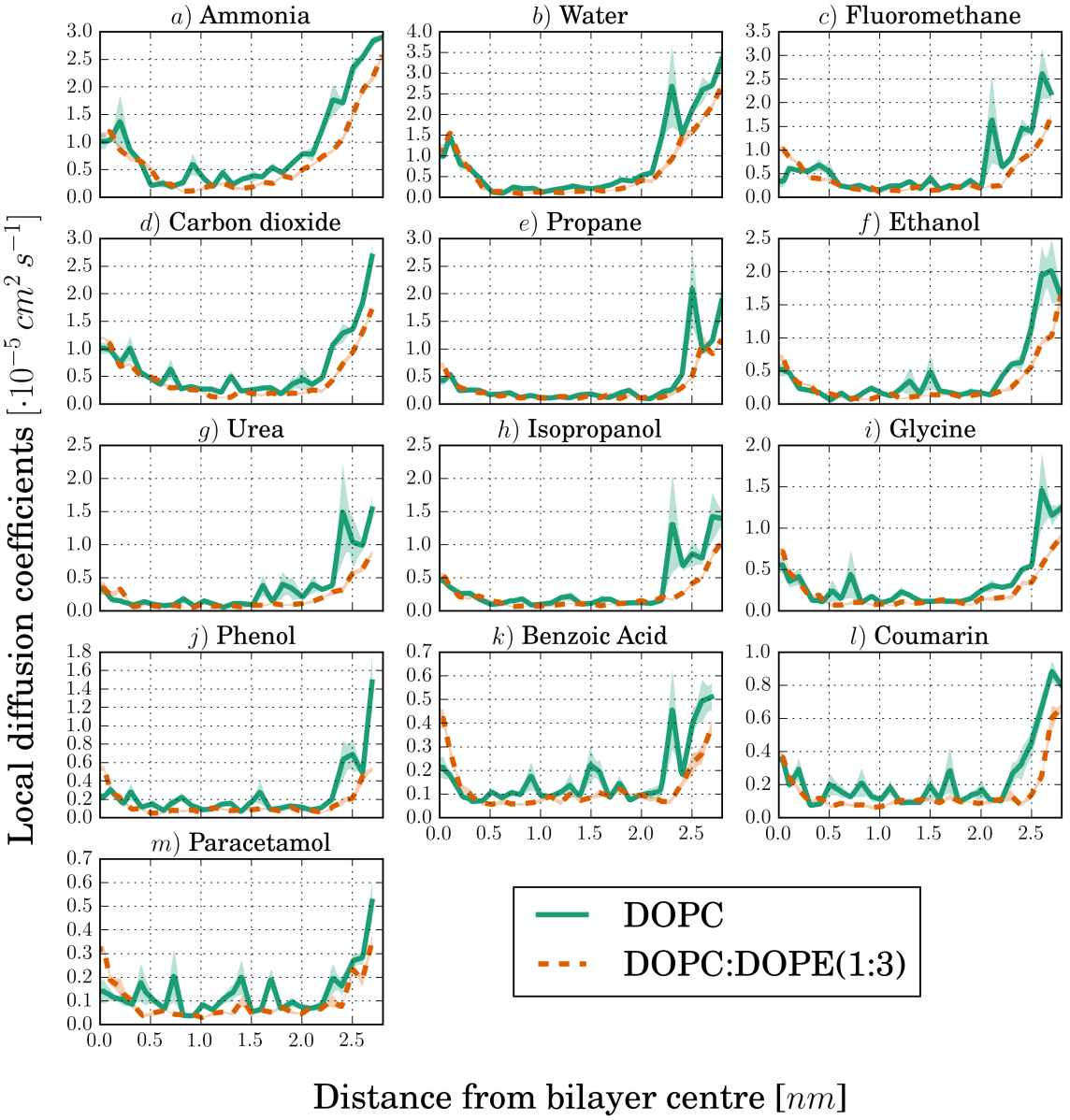

Figure 5.15: Comparison of local diffusion coefficients between membranes. The standard error is represented with a semi-transparent area above and below the line of the average. In most cases, the standard error is smaller than the thickness of the line.

ant moved further than the typical ±0.15 nm from the average position. Figure 5.17 shows 4 trajectory (sampling every 10 ps) snapshots from this time range. Apart from random crosses through the periodic boundary conditions (figure 5.17b), no obvious facilitators or bilayer structural irregularities were observed to explain this behaviour.

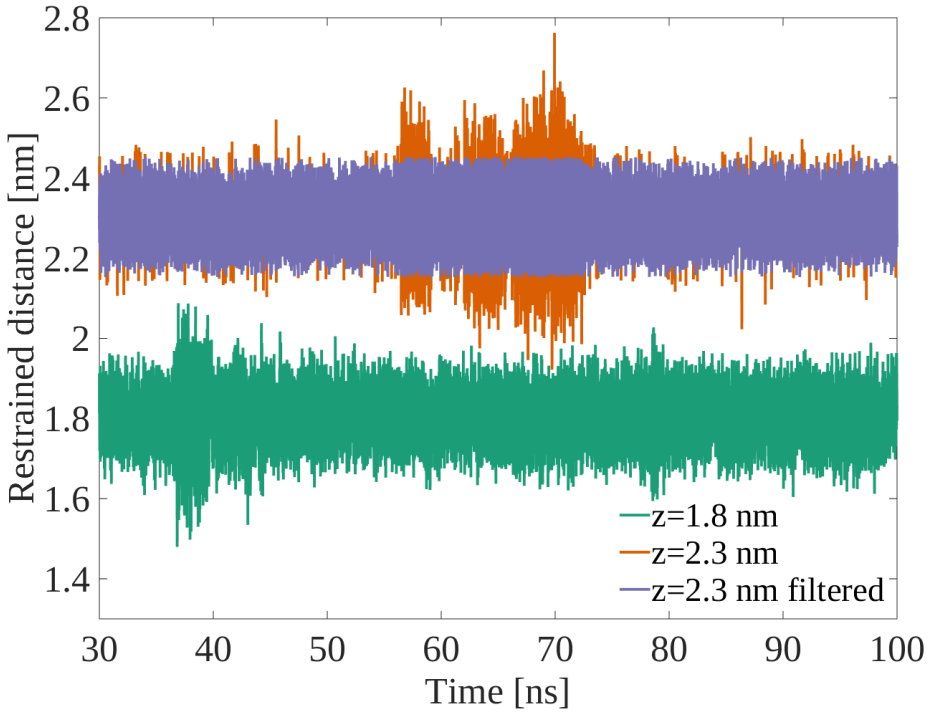

Figure 5.16: The restrained z-position timeseries for the z=1.8 nm and z=2.3 nm positions and the DOPC-water system. Also, the effect of applying an 'exclude-outliers' filter in the z=2.3 nm timeseries.

To examine whether manual removal of extreme outliers of the timeseries would improve the diffusion results, a filter was applied to the data to discard all z-restraint position that were deviating more than ±0.15 nm from the average position. Figure 5.16 shows the effect of the filter on the 2.3 nm timeseries and table 5.4 presents the diffusion coefficients and the percentage of timeseries that were outliers for three representative timeseries. Overall, for the cases that the rejection percentage was low, the effect on diffusion was marginal. In the case of z=2.3 nm, diffusion was reduced by $\approx$ 18%, however, even with the filter applied the diffusion value was still higher than in the neighbouring points. Considering that a filter can introduce other biases or artifacts on the results, it was decided not to implement filtering on the calculation of diffusion coefficients. For the rest of this dissertation, the results presented will be based on the unfiltered timeseries.

5.3.3 Comparison between the methods

Computing the local diffusion coefficients required for the calculation of the permeation coefficient was the most challenging part of the analysis process. In fact the determination of a robust and accurate method to calculate local diffusivity profiles is still a very active research field[268–271]. The results of the z-constraint method did not reproduce diffusion

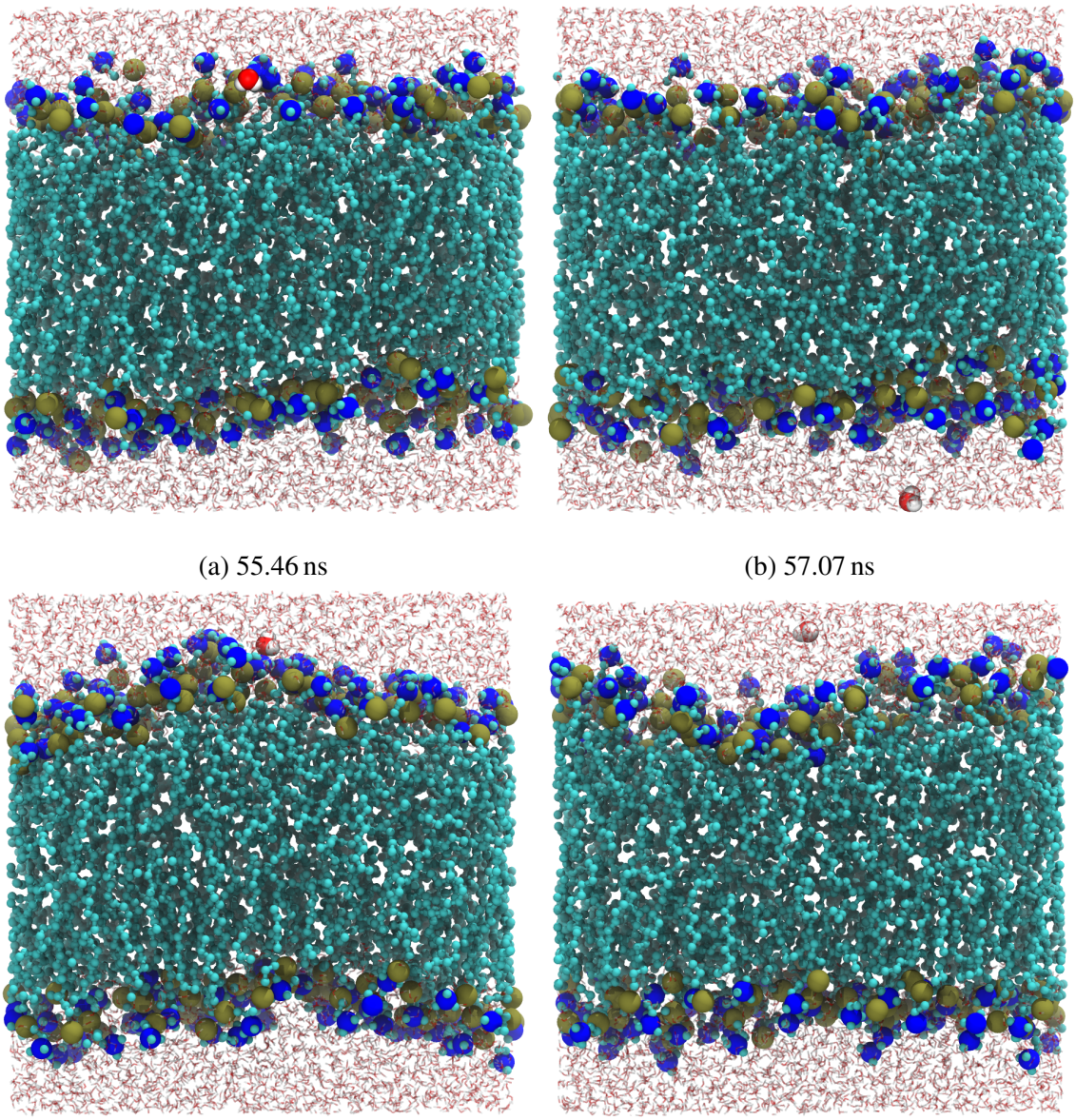

(a) 55.46 ns (b) 57.07 ns

(c) 62.49 ns (d) 70.00 ns

Figure 5.17: Trajectory snapshots of DOPC-water system during the time that high fluctuations of the permeant position were recorded. The water molecule is represented by the van der Waals red sphere representing oxygen. The rest of the water molecules are transparent lines.

Table 5.4: Effect of an 'exclude-outliers' filter in the diffusion coefficients. The outliers value shows the percentage of data that were discarded from the original timeseries.

	D [x10^{-5} cm^2/s]		
z [nm]	*Original*	*Filtered*	*Outliers*
1.8	0.4	0.4	0.6%
2.2	1.5	1.5	0.7%
2.3	2.7	2.2	1.7%
2.4	1.5	1.5	0.3%

profiles of previous studies neither quantitatively nor qualitatively. While the cause of this is not apparent, it can be attributed to the dependence of diffusion to the integral of the ACF of the extremely oscillatory constraint force. While the z-restraint, undergoes similar calculations, it was shown that apart from specific cases (section 5.3.2.1), the restraint position remains relatively stable. Overall, the z-restraint method achieved better and produced more accurate local diffusion coefficients.

5.4 Local resistance profiles

5.4.1 Local resistance with the z-constraint

According to the inhomogeneous solubility-diffusion model (equation 2.47), the local resistance is proportional to the exponential of the free-energy difference and inversely proportional to the local diffusion coefficient. Figure 5.18 shows the resistance profiles for the z-constraint method. It is clear that for hydrophillic molecules the higher resistance in permeation is in the bilayer centre, while for fluoromethane and carbon dioxide it is located in the headroup region.

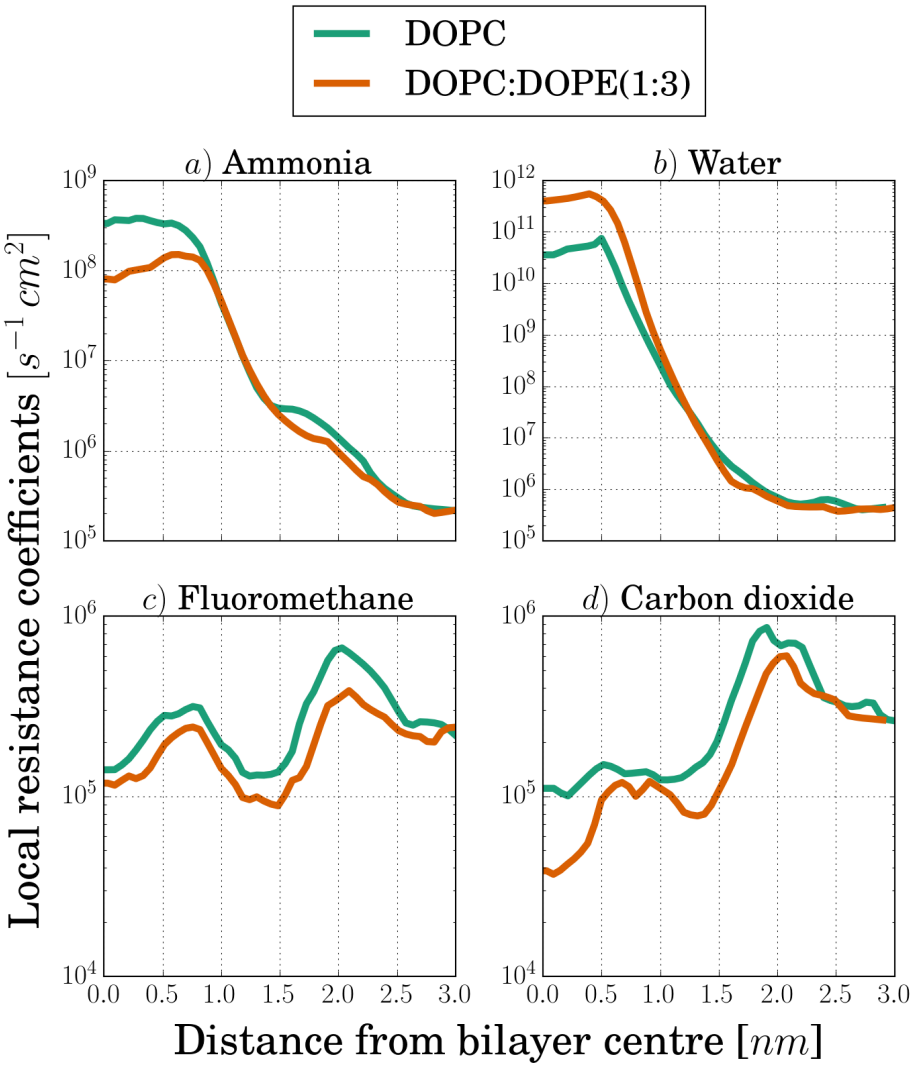

Figure 5.18: Local resistance profiles with the z-constraint method.

5.4.2 Local resistance with the z-restraint

Figure 5.19 displays the resistance profiles for both membranes and all permeants for the z-restraint method. Carbon dioxide and propane, both hydrophobic molecules, experience higher permeation resistance in the hydrophillic region of the bilayer. Hydrophillic molecules (ammonia, glycine, urea and water), experience the highest resistance in the bilayer core. Amphiphillic molecules are characterised by two peaks in their resistance profiles. The first exists in the hydrophillic area of the bilayer indicating a permeation barrier of the hydrophobic part of the permeant as it dissolves inside the hydrophillic region of the bilayer. The second exists in the lower chains region and the bilayer core indicating a resistance in permeation of the hydrophillic part of the permeant in the hydrophobic region of the bilayer.

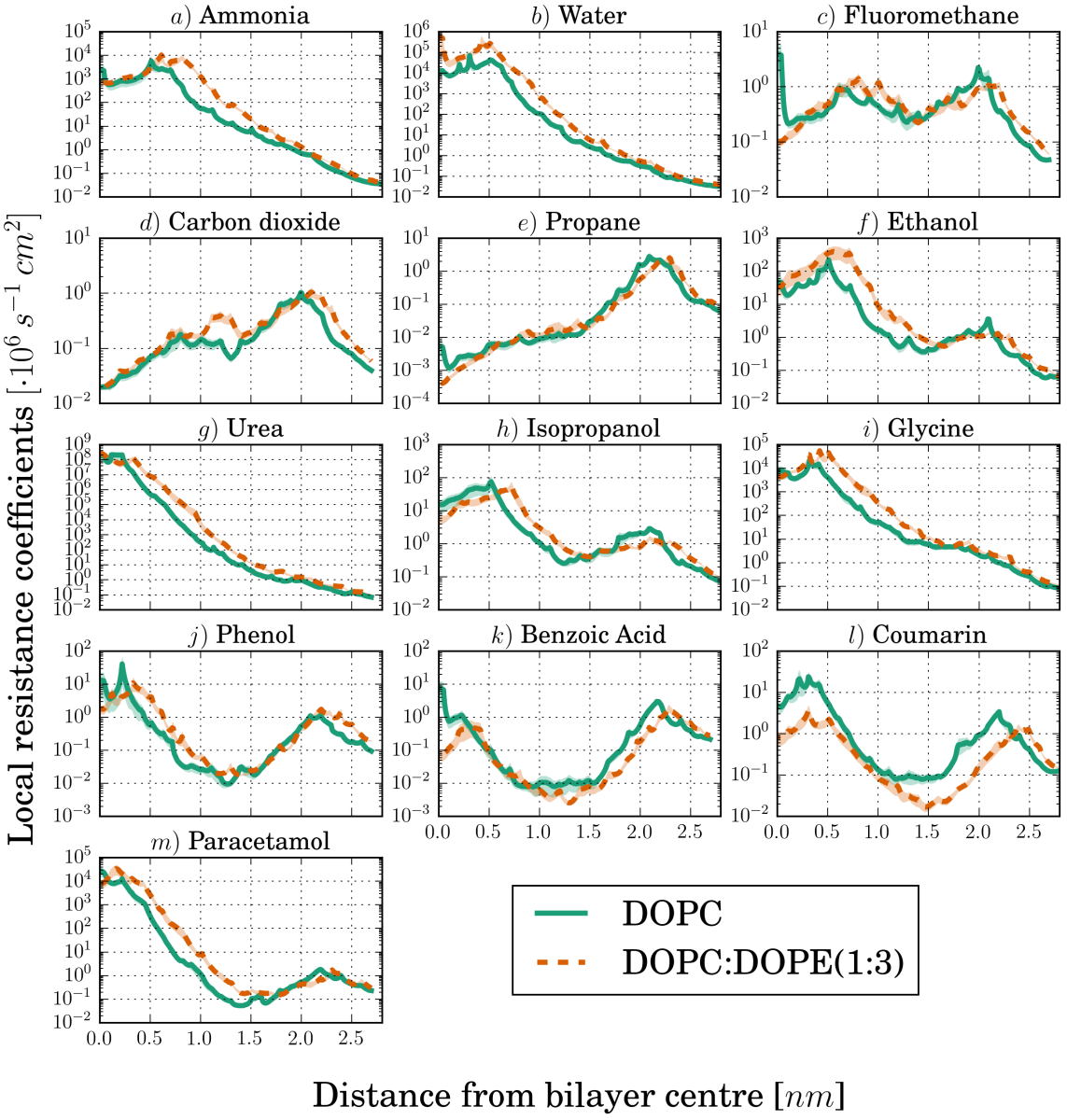

Figure 5.19: Local resistance profiles with the z-restraint method.

The effect of the lipid composition depends on the hydrophillicity of the permeants. The

DOPC:DOPE (1:3) bilayer profile has higher resistance profile for hydrophillic permeants, especially in the lipid chains region. For hydrophobic molecules the resistance is marginally higher in the polar region of the DOPC:DOPE (1:3) bilayer but it is unaffected in the rest. Finally, for the amphiphillic permeants, the DOPC:DOPE (1:3) membrane has lower resistance in the bilayer centre, higher resistance in the polar part and the 0.5 nm to 1.5 nm regions, and the same resistance in the other regions. Coumarin is an exception as the resistance is lower along the whole apolar part of the bilayer.

5.4.3 Free-energy and diffusion contributions on resistance

From figures 5.18 and 5.19 it is clear that both methods produced resistance profiles which despite some deviations are qualitatively similar to the free-energy profiles. These subtle deviations are due to the diffusion behaviour and are apparent in all profiles. For example, in the z-restraint method, ammonia has a monotonically increasing PMF which reaches a plateau in the bilayer centre. At the same time, diffusion is monotonically decreasing until 0.5 nm away from bilayer centre where it starts increasing. This enhanced diffusion is noticeable in the resistance profile with a drop in the bilayer centre region. These observations have been reported also in previous permeation studies [195,247].

Furthermore, the differences due to the subtle but important effect of diffusion manage to alter the relative resistance between the DOPC and DOPC:DOPE membrane for some permeants. In particular, resistance to permeation of both membranes to ammonia, urea, glycine and phenol becomes equal or higher for DOPC in the bilayer centre, although the PMF is clearly higher in the same region for the mixture. In other cases e.g., for water, fluoromethane and benzoic acid, the differences between the membranes are amplified. Also, comparison between the methods shows that the z-constraint results are generally in the same or 1-2 orders of magnitude higher than the z-restraint.

Overall, the observation of the resistance profile is important for the determination of the permeation mechanism. While the profile is predominantly affected by free-energy, diffusion can clearly affect the magnitude of the resistance to permeation.

5.5 Permeation coefficients

5.5.1 Permeation with the z-constraint

The permeation coefficients of the 4 small molecules are presented on table 5.5 together with their logarithm to base 10. First of all, these results are not in agreement to the initial hypothesis that due to the increase in the chain region of the lateral pressure profile, the permeation coefficient should reduce with the addition of nonlamellar DOPE lipids in the membrane. Comparison of the logP indicates that permeation was hindered through the DOPC:DOPE membrane only for water and was similar or faster for the rest, in contrast to the hypothesis expectations. Also, the computed P and logP values are orders of magnitude lower than previously reported experimentally and from simulation studies (see table 5.6).

Table 5.5: Permeation coefficients and their logarithm of base 10, through a DOPC and a DOPC:DOPE(1:3) membrane, at T=300 K, for the 4 examined molecules.

	DOPC		**DOPC:DOPE (1:3)**	
Permeant	**P** $\left[\mathbf{cm\,s^{-1}}\right]$	**logP**	**P** $\left[\mathbf{cm\,s^{-1}}\right]$	**logP**
Water	$(1.54 \pm 0.35) \times 10^{-11}$	-10.79 ± 0.40	$(1.79 \pm 0.34) \times 10^{-12}$	-11.74 ± 0.35
Ammonia	$(1.69 \pm 0.24) \times 10^{-9}$	-8.77 ± 0.09	$(4.23 \pm 0.55) \times 10^{-9}$	-8.37 ± 0.04
Fluoromethane	$(2.77 \pm 0.86) \times 10^{-7}$	-6.55 ± 0.31	$(3.27 \pm 0.92) \times 10^{-7}$	-6.48 ± 0.26
Carbon dioxide	$(5.45 \pm 0.49) \times 10^{-7}$	-6.26 ± 0.25	$(8.22 \pm 0.90) \times 10^{-7}$	-6.09 ± 0.17

The overall extremely low permeation coefficients of the z-constraint method can be explained by the combination of two factors, the overestimated free-energy profiles and the very low local diffusion coefficients. This combination leads to increased resistance coefficients and as a consequence, orders of magnitude lower permeation.

5.5.2 Permeation with the z-restraint

The permeation values of the molecules examined with the z-restraint method are presented in ascending permeability order in table 5.6 along with literature results for the same permeants. According to table 5.6 the permeation coefficients of the examined molecules can be separated in two main groups when comparing between the two examined membranes. The first group includes the molecules for which the permeation is slower through the DOPC:DOPE membrane, which are urea (-41%), water (-27%), glycine(-69%), ammonia (-71%), ethanol (-30%), isopropanol(-47%), phenol ($\approx -52\%$) and carbon dioxide ($\approx -30\%$). The second group includes the molecules with faster permeation through the DOPC:DOPE membrane, such as fluoromethane (6%), benzoic acid (31%), paracetamol (151%) and coumarin (219%). Finally, no difference in permeation was observed for propane ($\approx -0.6\%$).

In order to make comparisons between different molecules easier, the logarithms of base

10 of the permeation coefficients, logP, are also presented in table 5.6 and figure 5.20. As it can be seen from the latter, the majority of the permeants were on the right side of the equality line, indicating a higher logP value through the DOPC membrane, a result that was expected from the permeation coefficients. In fact, paracetamol and coumarin were the farthest to the left compared to the equality line. Furthermore, most permeants had a negative logP value with the most negative belonging to the 4 hydrophillic molecules (urea, water, glycine and ammonia). On the contrary, propane and carbon dioxide that are both hydrophobic, had the highest logP together with benzoic acid. The rest of the permeants were on the -1 to 0.7 logP range.

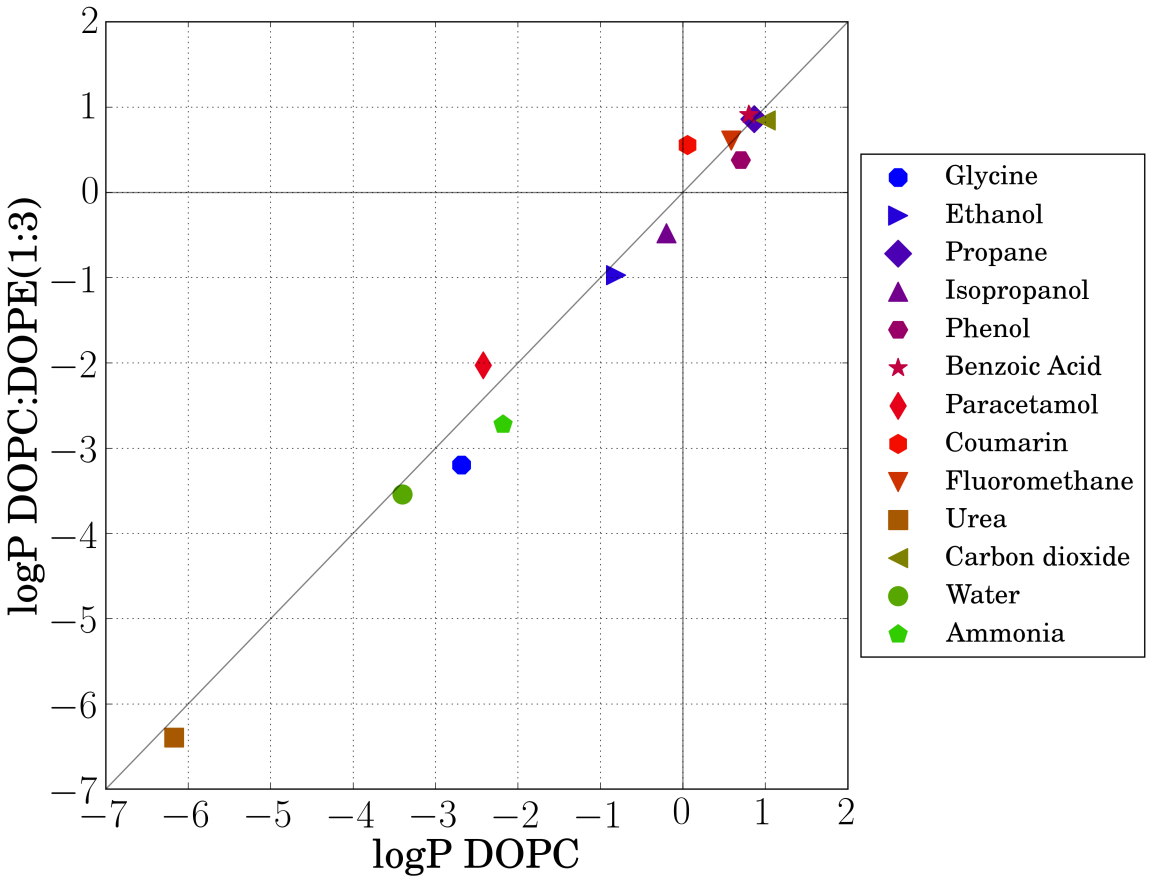

Figure 5.20: Comparison of logP values between membranes. For clarity, error bars are omitted.

Table 5.6: Permeation coefficients and their logarithm of base 10, for a DOPC and a DOPC:DOPE(1:3) membrane, at T=300 K. PC refers to DOPC and PC:PE refers to DOPC:DOPE(1:3).

This work			Previous studies		
P $\left[\mathrm{cm\,s^{-1}}\right]$	logP	Membrane	P $\left[\mathrm{cm\,s^{-1}}\right]$	logP	Membrane
Urea					
$(6.74 \pm 3.03) \times 10^{-7}$	-6.17 ± 0.23	PC	5.37×10^{-7}	−6.27	$\mathrm{DMPC}_{298\,\mathrm{K}}$ [α, 254]
$(4.01 \pm 1.95) \times 10^{-7}$	-6.40 ± 0.25	PC:PE(1:3)	1.95×10^{-8}	−7.71	Model $\mathrm{SC}_{310\,\mathrm{K}}$ [α, 258]
			1.41×10^{-6}	−5.85	$\mathrm{DOPC}_{303\,\mathrm{K}}$ [β, 121]
			4.00×10^{-6}	−5.40	DMPC [β, 272]
			4.56×10^{-6}	−5.34	Caco-$2_{310\,\mathrm{K}}$ [β, 273]

Continued on next page

α: MD simulation, β: Experimental study, γ: Theoretical model, δ: Monte Carlo simulation

Table 5.6 – continued from previous page

This work			Previous studies		
P $\left[\mathrm{cm\,s^{-1}}\right]$	logP	Membrane	P $\left[\mathrm{cm\,s^{-1}}\right]$	logP	Membrane
Water					
$(3.96 \pm 0.39) \times 10^{-4}$	-3.40 ± 0.05	PC	6.80×10^{-2}	-1.17	$\mathrm{DMPC}_{320\,\mathrm{K}}$ [α, 204]
$(2.89 \pm 1.50) \times 10^{-4}$	-3.54 ± 0.27	PC:PE(1:3)	4.00×10^{-2}	-1.40	$\mathrm{DPPC}_{320\,\mathrm{K}}$ [α, 204]
			1.30×10^{-2}	-1.89	$\mathrm{DPPC}_{310\,\mathrm{K}}$ [δ, 274]
			1.60×10^{-2}	-1.80	$\mathrm{DPPC}_{323\,\mathrm{K}}$ [α, 131]
			7.00×10^{-2}	-1.15	$\mathrm{DPPC}_{350\,\mathrm{K}}$ [α, 134]
			1.40×10^{-3}	-2.85	DMPC $\mathrm{CG}_{303\,\mathrm{K}}$ [α, 139]
			1.58×10^{-2}	-1.80	$\mathrm{DOPC}_{303\,\mathrm{K}}$ [β, 208]
			1.30×10^{-2}	-1.89	$\mathrm{POPC}_{303\,\mathrm{K}}$ [β, 208]
			6.47×10^{-3}	-2.19	$\mathrm{POPC}_{308\,\mathrm{K}}$ [α, 270]
			8.30×10^{-3}	-2.08	$\mathrm{DMPC}_{303\,\mathrm{K}}$ [γ, 275]
			2.40×10^{-2}	-1.62	$\mathrm{DMPC}_{303\,\mathrm{K}}$ [β, 121]
			1.90×10^{-2}	-1.72	$\mathrm{DPPC}_{303\,\mathrm{K}}$ [β, 121]
			1.50×10^{-2}	-1.82	$\mathrm{DOPC}_{303\,\mathrm{K}}$ [β, 121]
			1.22×10^{-2}	-1.91	$\mathrm{DOPC}_{298\,\mathrm{K}}$ [β, 115]
			7.40×10^{-3}	-2.13	$\mathrm{DOPC{:}DOPE}_{298\,\mathrm{K}}$ [β, 115]
			4.26×10^{-3}	-2.37	$\mathrm{DOPC}_{294\,\mathrm{K}}$ [β, 276]
			5.20×10^{-4}	-3.28	$\mathrm{DMPC}_{343\,\mathrm{K}}$ [β, 203]
			2.30×10^{-6}	-5.64	$\mathrm{DMPE}_{343\,\mathrm{K}}$ [β, 203]
			3.00×10^{-4}	-3.52	$\mathrm{DPPC}_{343\,\mathrm{K}}$ [β, 203]
			3.70×10^{-6}	-5.43	$\mathrm{DPPE}_{343\,\mathrm{K}}$ [β, 203]
			6.00×10^{-4}	-3.22	DMPC_{fluid} [β, 277]
			2.30×10^{-4}	-3.64	$\mathrm{DOPC}_{293\,\mathrm{K}}$ [β, 277]
			1.50×10^{-2}	-1.82	$\mathrm{DLPC}_{298\,\mathrm{K}}$ [β, 278]
			3.40×10^{-3}	-2.47	$\mathrm{EPC}_{298\,\mathrm{K}}$ [β, 279]
			2.20×10^{-3}	-2.66	$\mathrm{EPC}_{298\,\mathrm{K}}$ [β, 113]
			1.90×10^{-3}	-2.72	$\mathrm{EPC}_{298\,\mathrm{K}}$ [β, 280]
			1.36×10^{-2}	-1.87	$\mathrm{POPC}_{298\,\mathrm{K}}$ [β, 281]
Glycine					
$(2.05 \pm 0.80) \times 10^{-3}$	-2.69 ± 0.20	PC	5.70×10^{-12}	-11.24	EPC [β, 282]
$(6.38 \pm 1.67) \times 10^{-4}$	-3.20 ± 0.14	PC:PE(1:3)	2.00×10^{-11}	-10.70	DMPC [β, 282]
			3.00×10^{-7}	-6.52	SC [β, 283]
Paracetamol					
$(3.76 \pm 1.17) \times 10^{-3}$	-2.42 ± 0.16	PC	7.30×10^{-6}	-5.14	$\mathrm{Permeapad}_{310\,\mathrm{K}}$ [β, 284]
$(9.44 \pm 5.10) \times 10^{-3}$	-2.03 ± 0.28	PC:PE(1:3)			
Ammonia					
$(6.58 \pm 1.57) \times 10^{-3}$	-2.18 ± 0.12	PC	1.30×10^{-1}	-0.89	$\mathrm{POPC}_{300\,\mathrm{K}}$ [α, 210]
$(1.91 \pm 0.26) \times 10^{-3}$	-2.72 ± 0.07	PC:PE(1:3)	1.70×10^{-2}	-1.77	$\mathrm{POPE}_{300\,\mathrm{K}}$ [α, 210]
			1.30×10^{-1}	-0.89	$\mathrm{DOPC}_{300\,\mathrm{K}}$ [α, 218]
			9.00×10^{-1}	-0.05	$\mathrm{DPPC}_{350\,\mathrm{K}}$ [α, 264]
			1.30×10^{-1}	-0.89	$\mathrm{EPC}_{298\,\mathrm{K}}$ [β, 279]
			4.80×10^{-2}	-1.32	DPhPC [β, 285]
			3.70×10^{-2}	-1.43	EPC [β, 286]
Ethanol					
$(1.55 \pm 0.24) \times 10^{-1}$	-0.81 ± 0.08	PC	8.50×10^{-2}	-1.07	$\mathrm{POPC}_{323\,\mathrm{K}}$ [α, 287]
$(1.08 \pm 0.32) \times 10^{-1}$	-0.97 ± 0.15	PC:PE(1:3)	1.12×10^{-5}	-4.95	Model $\mathrm{SC}_{310\,\mathrm{K}}$ [α, 258]
			2.00	0.30	$\mathrm{POPC}_{308\,\mathrm{K}}$ [α, 269]
			3.80×10^{-5}	-4.42	$\mathrm{SOPC}_{298\,\mathrm{K}}$ [β, 288]
			2.75×10^{-7}	-6.56	SC [γ, 289]
Isopropanol					
$(6.27 \pm 1.75) \times 10^{-1}$	-0.20 ± 0.15	PC			
$(3.34 \pm 0.68) \times 10^{-1}$	-0.48 ± 0.11	PC:PE(1:3)			
Coumarin					
1.14 ± 0.31	0.06 ± 0.14	PC	1.50×10^{-4}	-3.82	$\mathrm{Caco\text{-}2}_{310\,\mathrm{K}}$ [β, 290]
3.62 ± 0.48	0.56 ± 0.07	PC:PE(1:3)	7.76×10^{-5}	-4.11	$\mathrm{Caco\text{-}2}_{310\,\mathrm{K}}$ [β, 291]
			3.58×10^{-6}	-5.45	$\mathrm{Pig\ skin}_{310\,\mathrm{K}}$ [β, 292]
Fluoromethane					
3.86 ± 0.45	0.59 ± 0.06	PC			

Continued on next page

α: MD simulation, β: Experimental study, γ: Theoretical model, δ: Monte Carlo simulation

Table 5.6 – continued from previous page

This work			Previous studies		
P $\left[\mathrm{cm\,s^{-1}}\right]$	logP	Membrane	P $\left[\mathrm{cm\,s^{-1}}\right]$	logP	Membrane
4.07 ± 0.53	0.61 ± 0.07	PC:PE(1:3)			
Phenol					
5.03 ± 1.04	0.70 ± 0.11	PC	2.57	0.41	Model $SC_{310\,K}$ [α, 258]
2.40 ± 0.59	0.38 ± 0.13	PC:PE(1:3)	5.42×10^{-6}	−5.27	$SC_{310\,K}$ [β, 293]
Benzoic Acid					
6.27 ± 1.57	0.80 ± 0.13	PC	2.82	0.45	$DMPC_{298\,K}$ [α, 254]
8.19 ± 0.85	0.91 ± 0.05	PC:PE(1:3)	4.40×10^{-5}	−4.36	DOPC [β, 154]
			1.20×10^{-7}	−6.92	$DOPC_{298\,K}$ [β, 220]
			1.11×10^{-6}	−5.95	$DOPE_{298\,K}$ [β, 220]
			5.50×10^{-1}	−0.26	$EPC_{298\,K}$ [β, 279]
Propane					
7.33 ± 1.49	0.86 ± 0.11	PC			
7.28 ± 0.86	0.86 ± 0.06	PC:PE(1:3)			
Carbon dioxide					
10.00 ± 1.2	1.00 ± 0.06	PC	3.00	0.48	$POPC:POPE_{300\,K}$ [α, 210]
7.02 ± 0.56	0.85 ± 0.04	PC:PE(1:3)	3.20	0.51	$DPhPC_{298\,K}$ [β, 294]
			3.20×10^{-1}	−0.49	$EPC_{296\,K}$ [β, 295]

α: MD simulation, β: Experimental study, γ: Theoretical model, δ: Monte Carlo simulation

5.5.2.1 Statistical significance of differences between membranes

In order to evaluate whether the predicted logP differences between the two membranes are statistically significant, a hypothesis test was performed in two different permeant groups, those with molecular weight smaller than $100\,\mathrm{g\,mol^{-1}}$ and those with molecular weight larger than $100\,\mathrm{g\,mol^{-1}}$. The null hypothesis stated that the difference of the logP values between the membranes was zero and the alternative hypothesis stated that the difference was negative, indicating smaller logP values for the DOPC:DOPE (1:3) membrane.

To perform the hypothesis test, a 1-tail paired t-test for each group was used. Table 5.7 shows the statistics of the test while the tables of the t-test analysis are presented in appendix B. For molecules with molecular weight lower than $100\,\mathrm{g\,mol^{-1}}$, the mixed DOPC:DOPE bilayer showed a statistically significant reduction in permeation (one-tailed paired t-test probability $p(x > 0) = 0.0019$, $x = \Delta\mathrm{logP}$), while the three drugs with molecular weight higher than $100\,\mathrm{g\,mol^{-1}}$ showed a statistically significant increase in permeability (one-tailed paired t-test probability $p(x < 0) = 0.0496$, $x = \Delta\mathrm{logP}$). The statistical significance is expected to be even higher (lower p value) for the permeation coefficients instead of the logP, which tends to "dampen" the differences. However, such a comparison is not possible because permeation coefficients vary orders of magnitude between molecules.

5.5.2.2 Validation of results

The results of this study are, in most cases, in agreement or within 1-2 order of magnitude with the permeation and logP values found in the literature. While for most cases permeation coefficients existed for similar lipid membranes, in some cases when data were

Table 5.7: Hypothesis test statistics for the comparison of ΔlogP for the two different permeant groups. $\Delta\log P = \log P_{DOPC:DOPE} - \log P_{DOPC}$. MW stands for molecular weight in $g\,mol^{-1}$.

Statistics	MW<100	MW>100
ΔlogP mean	-0.230	0.340
ΔlogP standard deviation	0.188	0.201
Hypothesised mean (h):	0	0
One-tailed probability p(h<x):	**0.0019**	0.950
One-tailed probability p(h>x):	0.998	**0.0496**

unavailable, free-energy profiles from the literature were used to assess the findings. In the following paragraphs, each permeant is discussed separately.

Urea. The computed logP value of −6.17 for the DOPC membrane is close to the −5.85 for DOPC[121] at 303 K and −6.27 for DMPC[254] at 298 K found in the literature.

Water. Studies of water permeation have reported a plethora of results that vary greatly, depending on the experimental and simulation protocols and lipid compositions. In general, logP values of water are between −1.15 to −5.64 and computed logP values of −3.40 for DOPC and −3.54 for DOPE belong to the lower end of this range. Generally values of this study are two orders of magnitude smaller than the DOPC and POPC permeation coefficients of Mathai et al.[208], Paula et al.[121], Huster et al.[115] and Koenig et al.[281], one order of magnitude smaller than those reported by Olbrich et al.[276] and Comer et al.[270] and very close to the values of DOPC from Carruthers et al.[277] and DMPC/DPPC of Jansen and Blume.[203]

Glycine. Chakrabarti et al.[282], reported a logP of −10.7 through large unilamellar vesicles of DMPC, which is much smaller than the computed logP of DOPC.

Ammonia. Present MD simulations underestimated the permeation coefficients of ammonia in comparison to the rest of the literature. In comparison to studies of similar lipid compositions, the values presented here are 1 to 2 orders of magnitude smaller than the POPC, POPE and DOPC MD simulations of Hub et al.[210] and Zocher et al.[218]. The discrepancy with both studies can be explained by the difference in the force fields used (Burger for lipids, OPLS for ammonia and TIP4P for water).

Ethanol. Literature values varied over 6 orders of magnitude and they were mostly negative apart from the simulation work of Comer et al.[269] that reported a logP value of 0.30 for POPC at T=308 K. Ghaemi et al.[287] computed a logP of −1.07 for POPC at T=323 K which is very similar to our values. The experimental work of Ly and Lango[288], with SOPC, returned a logP of −4.42 at room temperature. Further validation results were available from

the works of MacCallum et al.[296] and Carpenter et al.[253] that studied the free-energy of ethanol (Threonine,Thr, amino acid analog in the work of MacCallum et al.) permeating through a DOPC bilayer. In both cases current findings are almost identical to theirs, qualitatively and quantitatively, with the small differences attributed to the different force-fields used. Therefore it is expected that also the permeation coefficients would be very similar.

Benzoic Acid. Present results are in good agreement with the simulation work of Lee et al.[254] who computed a logP of 0.45 for DMPC at room temperature, similar to this work 0.80 for DOPC. These coefficients are both many orders of magnitude higher than the experimental findings for DOPC[154,220] and DOPE[220].

Carbon dioxide. The logP presented here is very similar to the one Hub et al.[210] found with MD simulations, for carbon dioxide permeation through a POPC:POPE bilayer.

Propane. While no reported permeation coefficients were found for propane, MacCallum et al.[296] have presented the free-energy profile of permeating propane, as an analog of the amino acid Valine (Val). As with ethanol, the findings here are in excellent agreement with theirs, observing the same $-3.2\,\mathrm{kcal\,mol^{-1}}$ free-energy trough in the bilayer centre and overall qualitative behaviour. Therefore, it is anticipated that the permeation coefficient would also be identical.

Isopropanol, Fluoromethane. No computational or experimental results were found regarding the permeation of isopropanol or fluoromethane. This is the first work reporting permeation coefficients for these two molecules.

Finally, for **phenol**, **paracetamol** and **coumarin** there are no literature permeation studies with similar lipid compositions, making a direct comparison inappropriate. However, Paloncỳovà et al.[252] have reported free-energy profiles of coumarin in a DOPC bilayer at 310 K that are qualitatively close to present findings, with a global minimum around 1.4 nm and an energy barrier in the centre of the bilayer. However quantitatively, the results differ considerably, possibly because of the difference in temperature and force field; they used the united atom Berger FF for lipids and custom parameters for coumarin based on GROMOS 53a6. In this study, the global minimum is $-1.5\,\mathrm{kcal\,mol^{-1}}$, while they report a global minimum of $-5.7\,\mathrm{kcal\,mol^{-1}}$ to $-6.7\,\mathrm{kcal\,mol^{-1}}$. Likewise, in the bilayer centre they report a $-3.5\,\mathrm{kcal\,mol^{-1}}$ to $-4.1\,\mathrm{kcal\,mol^{-1}}$ negative peak in contrast to the positive $1.2\,\mathrm{kcal\,mol^{-1}}$ barrier that was found in this work. Therefore, the permeation coefficient for coumarin from Paloncỳovà et al.[252] would be probably a few orders of magnitude higher than the one reported here.

5.6 Overall comparison of the methods

In this dissertation two of the most commonly used methods to study passive permeation with molecular dynamics simulations were used. In particular, both methods went under extensive testing of their parameters in order to ensure the production of the most robust and accurate options through the automated post-simulation analysis. Then, the methods were compared on six different simulation aspects and results for all permeating molecules, namely the computational efficiency, the convergence speed, the free-energy profiles, the local diffusion coefficients, the local resistance profiles and the most important, the permeation coefficients.

In regards to the computational efficiency, the z-restraint method in conjunction with the GROMACS software was almost six times faster due to the more purpose-optimised software but also the direct implementation of the tools to perform the permeation study. Convergence of free-energy profiles was also faster with the z-restraint method, possibly due to the same reasons, but also due to the fact that the main sampled variable for the z-restraint method (the z-position) is generally more stable than the highly oscillatory instant constraint force F_z.

In regards to the free-energy and local diffusion profiles, z-restraint also performed better. For the former, while the profiles were quantitatively similar, the values of the z-constraint were generally higher than the z-restraint and previously reported values in the literature indicating an overestimated barrier to permeation. In fact, for the latter, the profiles for the z-constraint were also qualitatively nonphysical and quantitatively very low. Due to these results, the produced resistance profiles were the same or higher for the z-constraint results, following the trend of the dominant free-energy profiles compensated by the lower diffusion.

Finally, as tables 5.5 and 5.6 show, the predicted values for the z-constraint are orders of magnitude lower than the corresponding z-restraint and literature data. Based on these, the z-restraint method is concluded to be the best of the two methods for these kind of permeation studies. In the next sections, the results of the z-restraint simulations will be further analysed to extract more useful information regarding the effect of DOPE lipids in permeation.

5.7 Further analysis of the z-restraint results

5.7.1 Hydrogen bonds

The average number of hydrogen bonds formed per frame (h.b.p.f.), is shown in figure 5.21 for all molecules and membranes. Each profile shows the total number of hydrogen bonds formed at each position, which is further decomposed to the number of hydrogen bonds formed between the permeant and either the bilayer or the solvent.

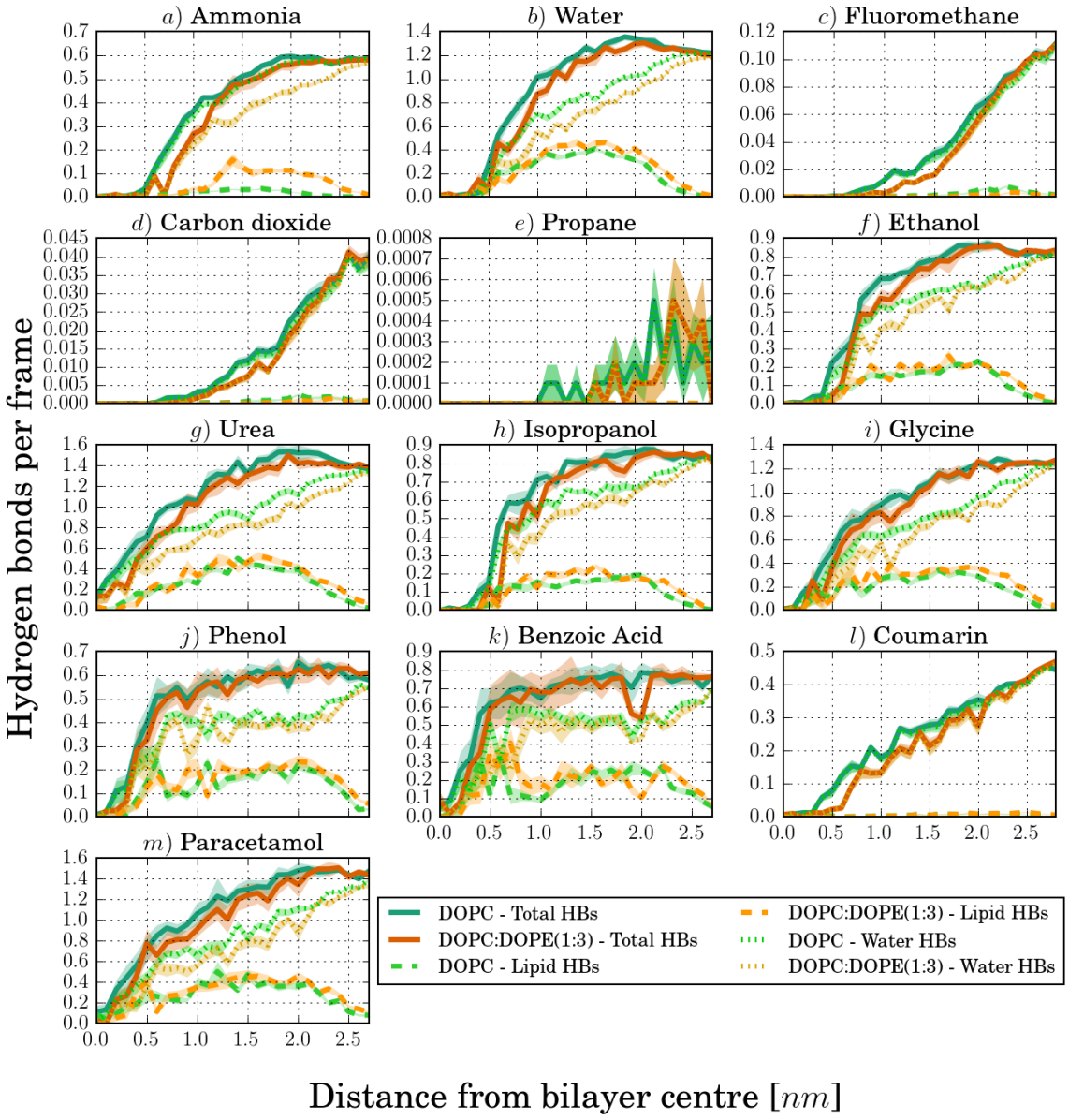

Figure 5.21: Comparison of hydrogen bonds formed per frame between membranes. The standard error is represented with a semi-transparent area above and below the line of the average.

Hydrogen bonds with the solvent are the predominant in comparison to the ones formed with the bilayer, and generally decrease with the increased proximity to the bilayer centre as also observed in previous studies [137,263]. It is noteworthy however, that hydrophillic and amphiphillic molecules form hydrogen bonds with water almost right down to the bilayer

core, showing the propensity of permeants to retain their hydration shell even deep into the hydrophobic region[297]. With regards to quantitative comparison, the average number of hydrogen bonds follows the expected pattern that arises from the ability of each permeant to form hydrogen bonds, hydrophillic molecules formed more hydrogen bonds with water.

Hydrogen bonds with the bilayer can be split in two profile categories. For fluoromethane, carbon dioxide, coumarin and ammonia/DOPC, they are very close to zero along the bilayer. For the rest, hydrogen bonds start to form around 0.1 nm to 0.5 nm, then reach a maximum at 1.5 nm to 2.0 nm (of 0.4 h.b.p.f. for water, urea, glycine and paracetamol, of 0.2 for ethanol, isopropanol, phenol and benzoic acid, of 0.1 for ammonia/DOPC:DOPE) and then fade back to zero in the solvent region.

In regards to the effect of DOPE, apart from ammonia, no significant difference was observed in the hydrogen bond formations of the molecules with the bilayer between the DOPC and DOPC:DOPE(1:3) membranes. In some cases, a marginal increase was observed in the head region of the PC:PE, but this could also be attributed to the 4% increase of thickness[22]. Furthermore, permeants formed marginally more hydrogen bonds with water in the DOPC membrane. Overall, the lipid composition did not affect the total number of hydrogen bonds formed between the permeants and their environment. The above observation is counter-intuitive because DOPE has an increased capability of hydrogen bond formations, although two possible factors could explain this behaviour. On one hand, it is possible that one permeant on its own per position is not enough to observe a significant difference in the total numbers of hydrogen bonds, and maybe alternative methods with more permeants per position could produce different numbers. On the other hand, it was observed in the past that the extra PE hydrogen bonds are mostly formed between the rest of the PC and PE headgroups or the solvent molecules and therefore the permeant could possibly remain unaffected[68].

It is important to mention that propane cannot form hydrogen bonds and is only presented here as a validation that it did not; although very low, the h.b.p.f. values are not entirely zero. This is due to the fact that the analysis code might have accidentally recognised a non existent hydrogen bond based on the defined criteria. Furthermore, carbon dioxide has been found to form weak hydrogen bonds despite the intuitive established opinion that it generally cannot[298], thus it is presented along the rest of the molecules. Finally, although it is still an open question, there are published data that fluoromethane can form hydrogen bonds[299].

5.7.2 Correlation of permeation to solute properties

The molecules examined in this work have a broad range of physicochemical properties which are summarised in table 3.2. A very common measure of permeability that has been used in the past and is also actively used in QSAR methods is the octanol/water partition coefficient $logP_{o/w}$ [300,301]. Figure 5.22 presents the correlations and linear regressions of 5 important properties of the permeants (the molecular weight, total number of hydrogen bonds acceptors and donors, the topological polar surface area and a QSAR and experimentally predicted $logP_{o/w}$ coefficients) to the logarithm of the computed permeation coefficients. Table 5.8 summarises the results of the correlation analysis where R represents Pearson's correlation coefficient and p the probability of the results not being correlated based on a two-tail hypothesis t-test. The significance level α for rejecting the null hypothesis ("there is no correlation") was considered 0.05 and based on this, the critical value of R above which correlation would exist was 0.553 for MW, HBAD, TPSA and CAxLogP (13 samples per membrane) and 0.602 for ExpLogP (11 samples per membrane)[302].

From figure 5.22 and table 5.8 it is clear that the molecular weight and number of hydrogen bonds donors and acceptors do not correlate with the logP value for neither membrane. On the contrary, TPSA and the octanol/water partition coefficients correlate with the permeation, with the experimental partition coefficient having the best correlation (R=0.824 and R=0.854). TPSA has a negative correlation meaning that as the polar surface increases, the permeation drops. QSAR and experimental $logP_{o/w}$ results indicate that the permeation increases almost linearly with the increase in lipophilicity, as it is expected from the literature[300]. Especially for the latter, the linear regression model is fairly accurate with an R^2 of $\approx$0.7. In regards to the composition of the membranes, while no major effect is observed, DOPC:DOPE results seem to correlate better with the experimental lipophilicity although the change is not significant. Overall, although these MD results correlate well with the $logP_{o/w}$ of the permeants, the use of the partition coefficient to assess permeation has been questioned in the past, especially for permeation through the blood brain barrier modelled as a DOPC bilayer[253] and descriptors such as the blood brain partitioning (logBB) and the permeability surface-area product (logPS) might be more accurate.

Table 5.8: Correlations between permeants physicochemical properties and the logarithm of permeability logP.

	MW		**HBAD**		**TPSA**		**CAxLogP**		**ExpLogP**	
	R	p	R	p	R	p	R	p	R	p
DOPC	0.136	0.659	-0.501	0.081	-0.662	0.014	0.653	0.016	0.824	0.002
DOPC:DOPE	0.222	0.465	-0.493	0.081	-0.642	0.018	0.716	0.006	0.854	0.001

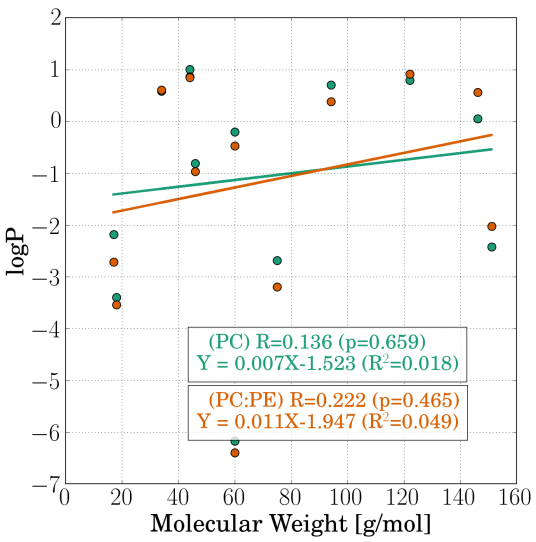

(a) Molecular weight

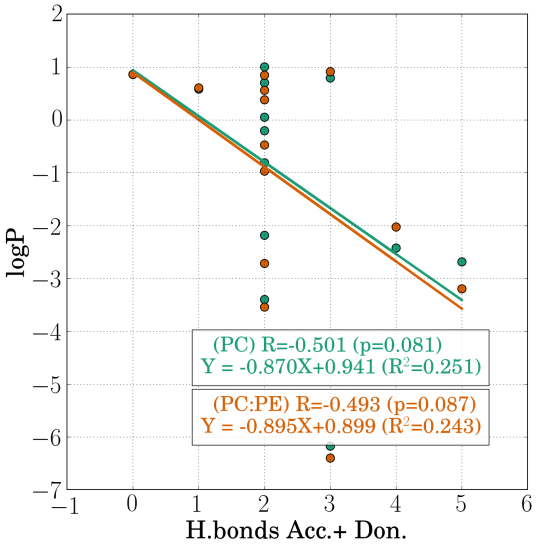

(b) Hydrogen bonds acceptors and donors

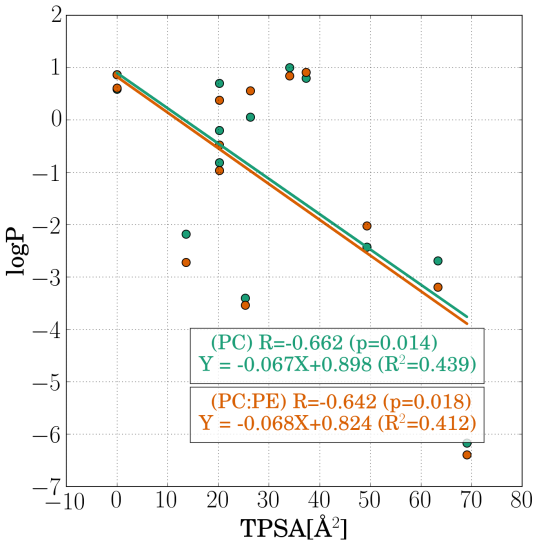

(c) Topological polar surface area

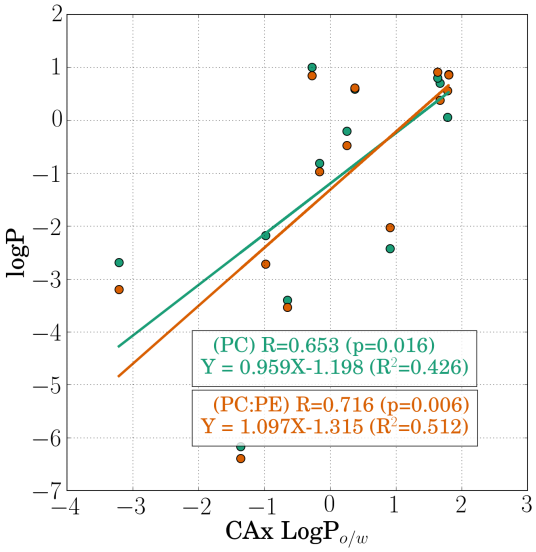

(d) QSAR logP$_{o/w}$

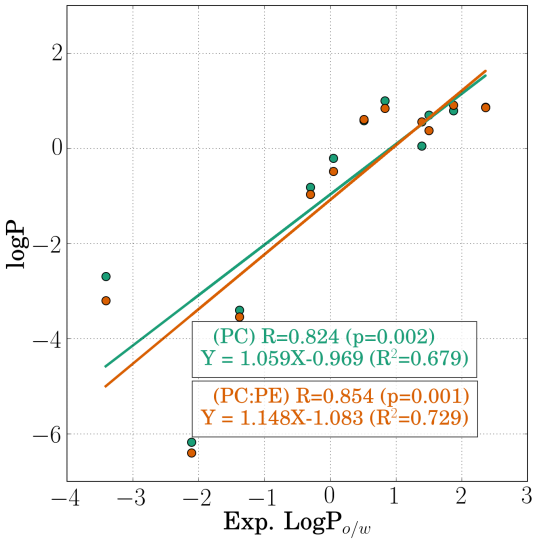

(e) Experimental logP$_{o/w}$

Figure 5.22: Correlation analysis and linear regression for 5 physicochemical properties and the logarithm of permeability logP.

5.7.3 Lateral mobility

The last analysis test examined the lateral mobility of both the lipid molecules and the permeant. For the former, a random lipid molecule was selected for each position and then the mean square displacement (MSD) of its lateral movement was calculated. The lateral diffusion coefficient was calculated then from the slope of the MSD and the average of the 28 positions. Figure 5.23 shows the average lateral diffusion for all permeant systems and for the DOPC and DOPE lipids in both membrane systems. The presented values for DOPC and DOPE which are approximately 17 $nm\,\mu s^{-1}$ are close to the higher end of the previously reported range of values in the literature[65,68,196,303–305] of 6 $nm\,\mu s^{-1}$ to 17 $nm\,\mu s^{-1}$.

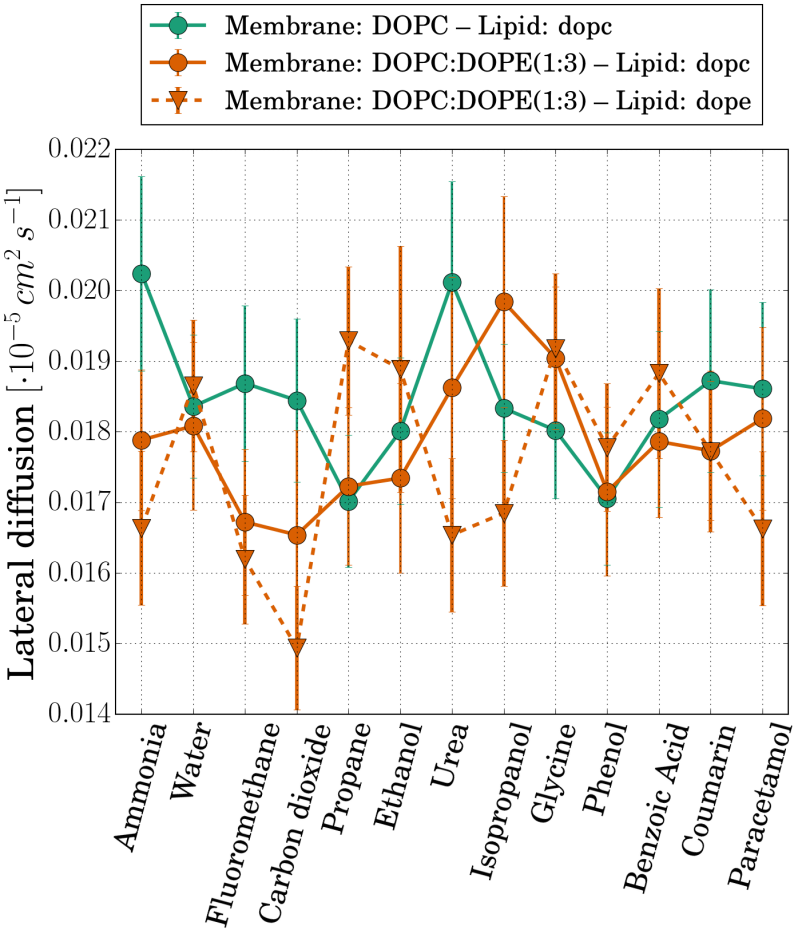

Figure 5.23: Lateral diffusion coefficients of the lipid molecules. Lines are plotted to guide the eye.

Figures 5.24, 5.25 and 5.26 display the trajectories of the permeants over the 100 ns simulations with the DOPC bilayer, in relation to the simulation box (dashed lines). Similarly, figures 5.27, 5.28 and 5.29 present the permeant lateral mobility for the DOPC:DOPE bilayer. Different columns indicate different positions inside the bilayer and the rows are sorted based on the molecular weight of the permeants starting from the lightest.

Regarding the mobility between different depths, it is generally observed that the permeant

diffuses faster in the water region (2.7 nm), then in the bilayer centre, then in the headgroup region (1.0 nm) and finally in the chain region (2.0 nm). These results are similar to the computed local diffusion profiles (figure 5.15). Furthermore, the lateral mobility exhibits a "rattle-in-a-cage" behaviour where the permeant is trapped locally in pockets of free volume accompanied by fast transitions to neighbouring pockets, in agreement with previous reports[266].

Finally, there is no significant difference in the plots in terms of membrane composition. There seems to be a small increase in movement in the centre of the mixed bilayer which could be rationalised by the small increase in thickness which could leave some more free-space, although that could be compensated by the more ordered lipid chains.

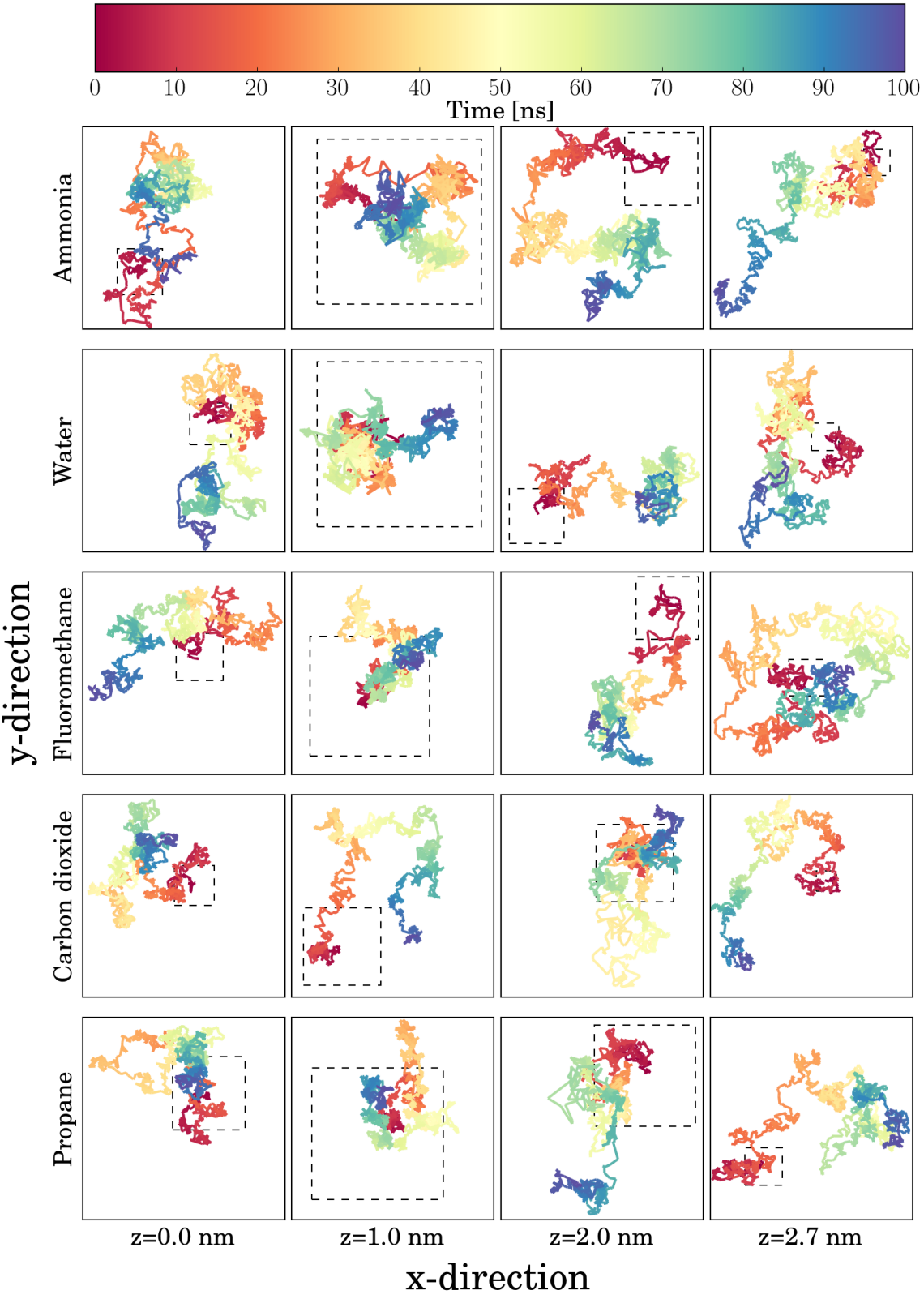

Figure 5.24: Lateral mobility of permeants in the DOPC membrane and in different depths; part A. Dashed lines indicate the simulation box (≈6 nm × 6 nm).

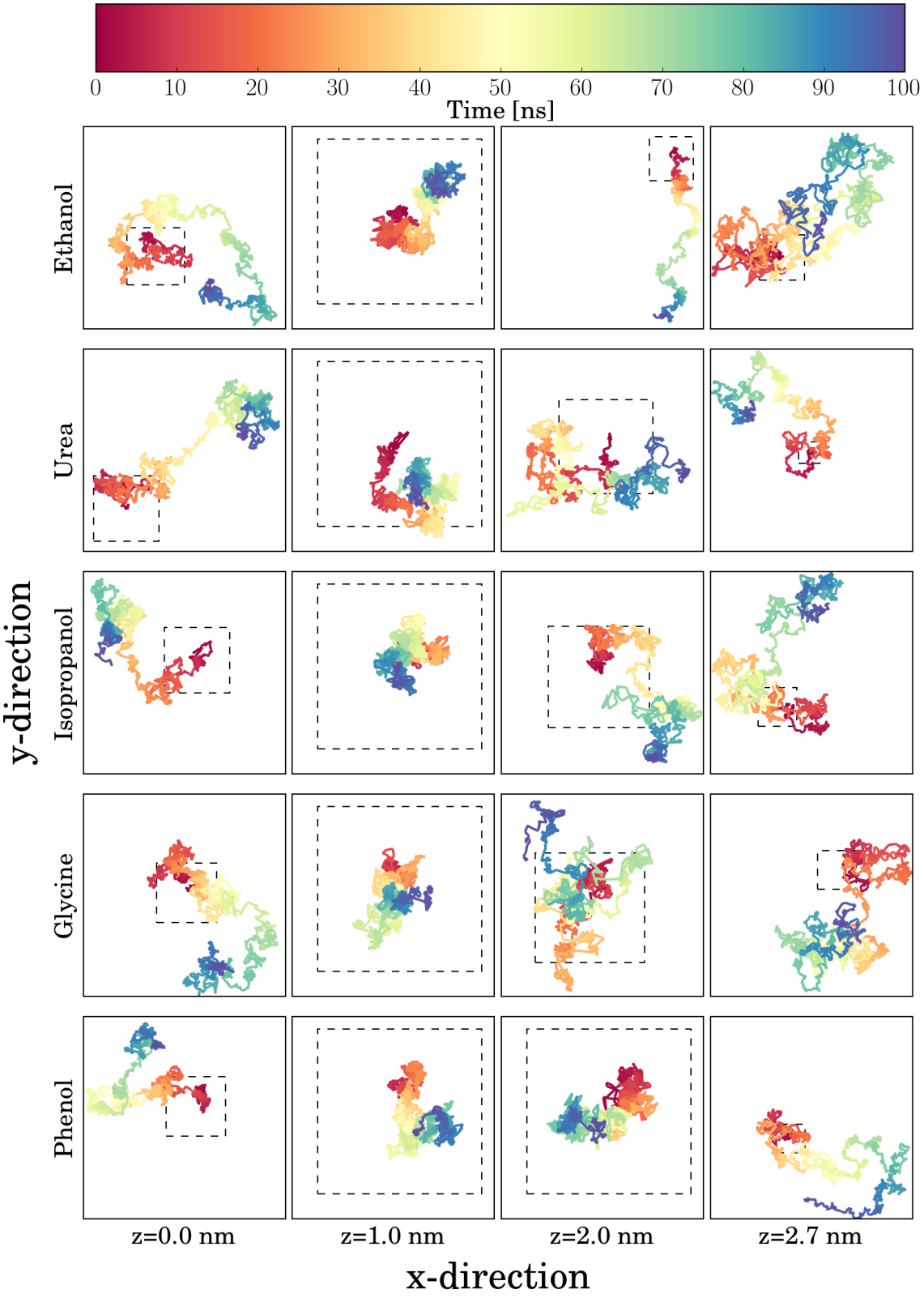

Figure 5.25: Lateral mobility of permeants in the DOPC membrane and in different depths; part B. Dashed lines indicate the simulation box (≈6 nm × 6 nm).

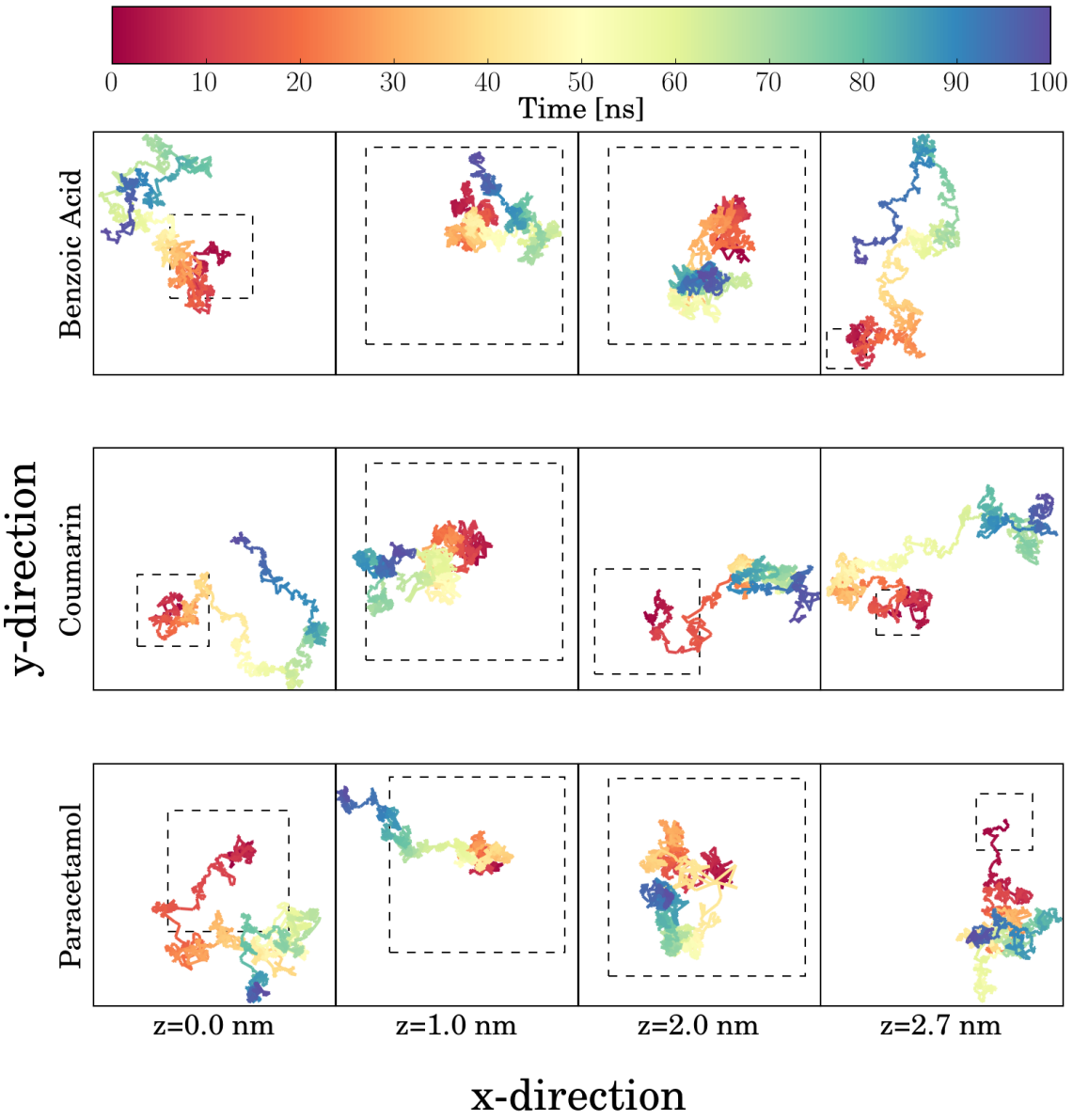

Figure 5.26: Lateral mobility of permeants in the DOPC membrane and in different depths; part C. Dashed lines indicate the simulation box (≈6 nm × 6 nm).

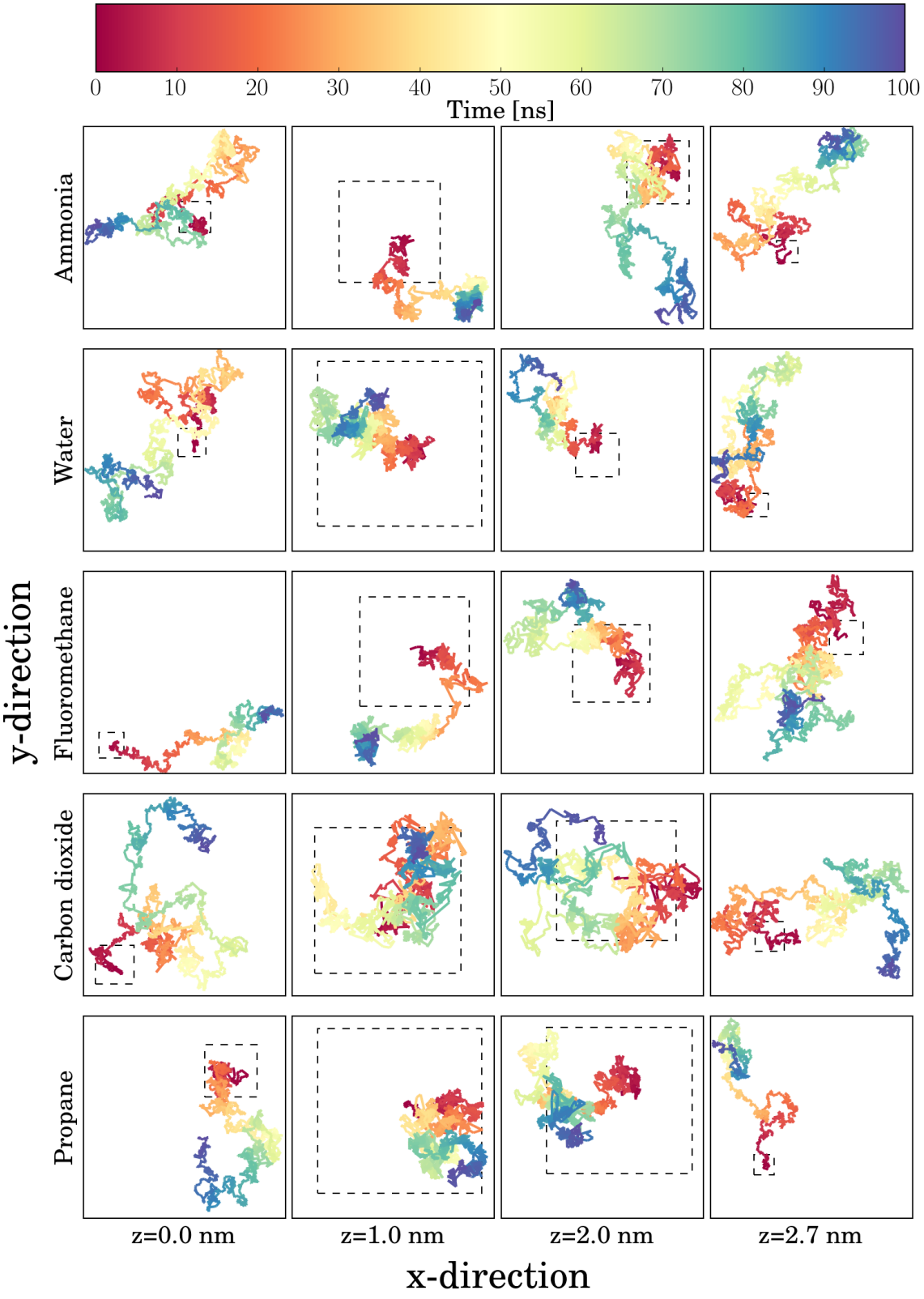

Figure 5.27: Lateral mobility of permeants in the DOPC:DOPE membrane and in different depths; part A. Dashed lines indicate the simulation box (≈6 nm × 6 nm).

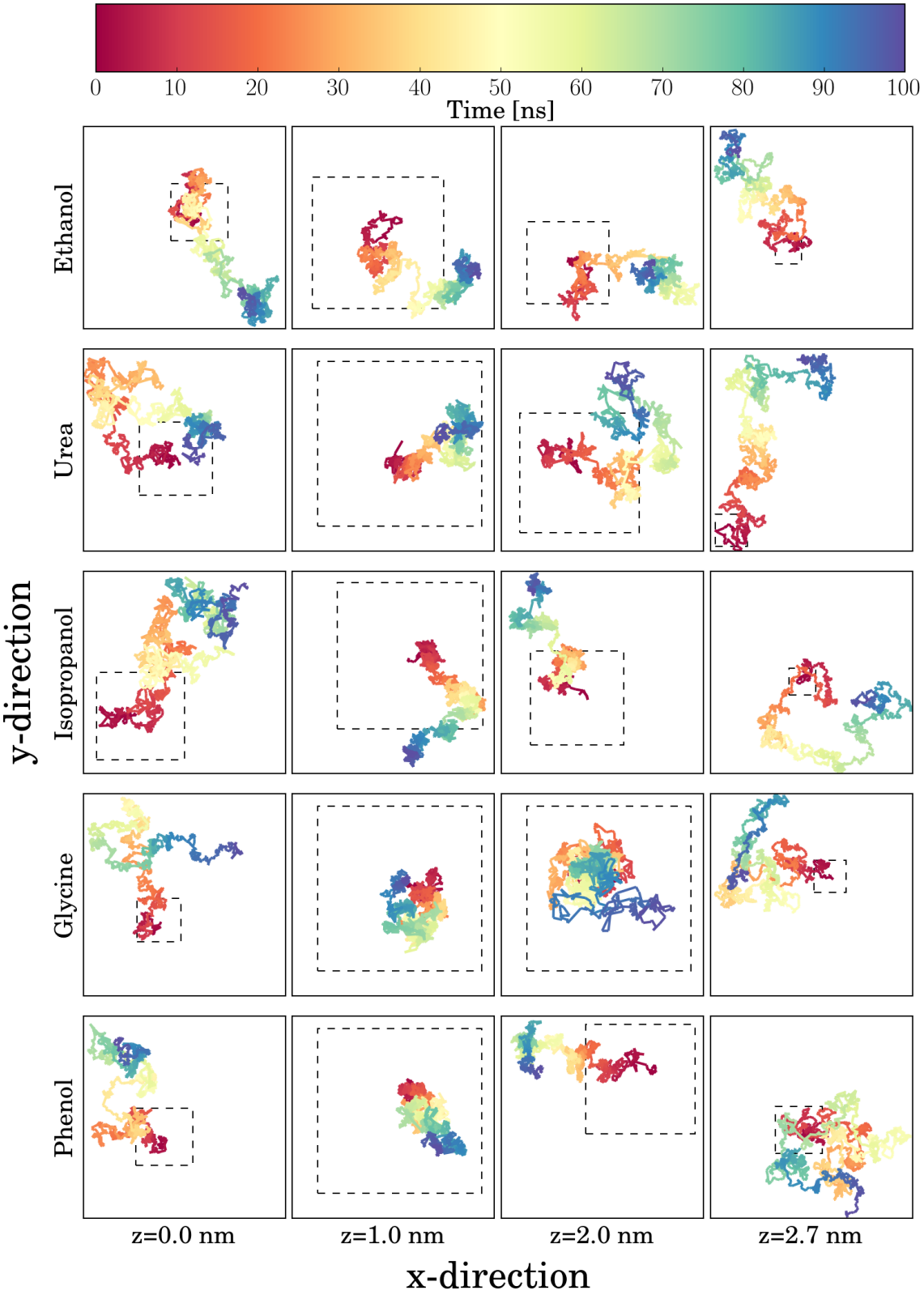

Figure 5.28: Lateral mobility of permeants in the DOPC:DOPE membrane and in different depths; part B. Dashed lines indicate the simulation box (≈6 nm × 6 nm).

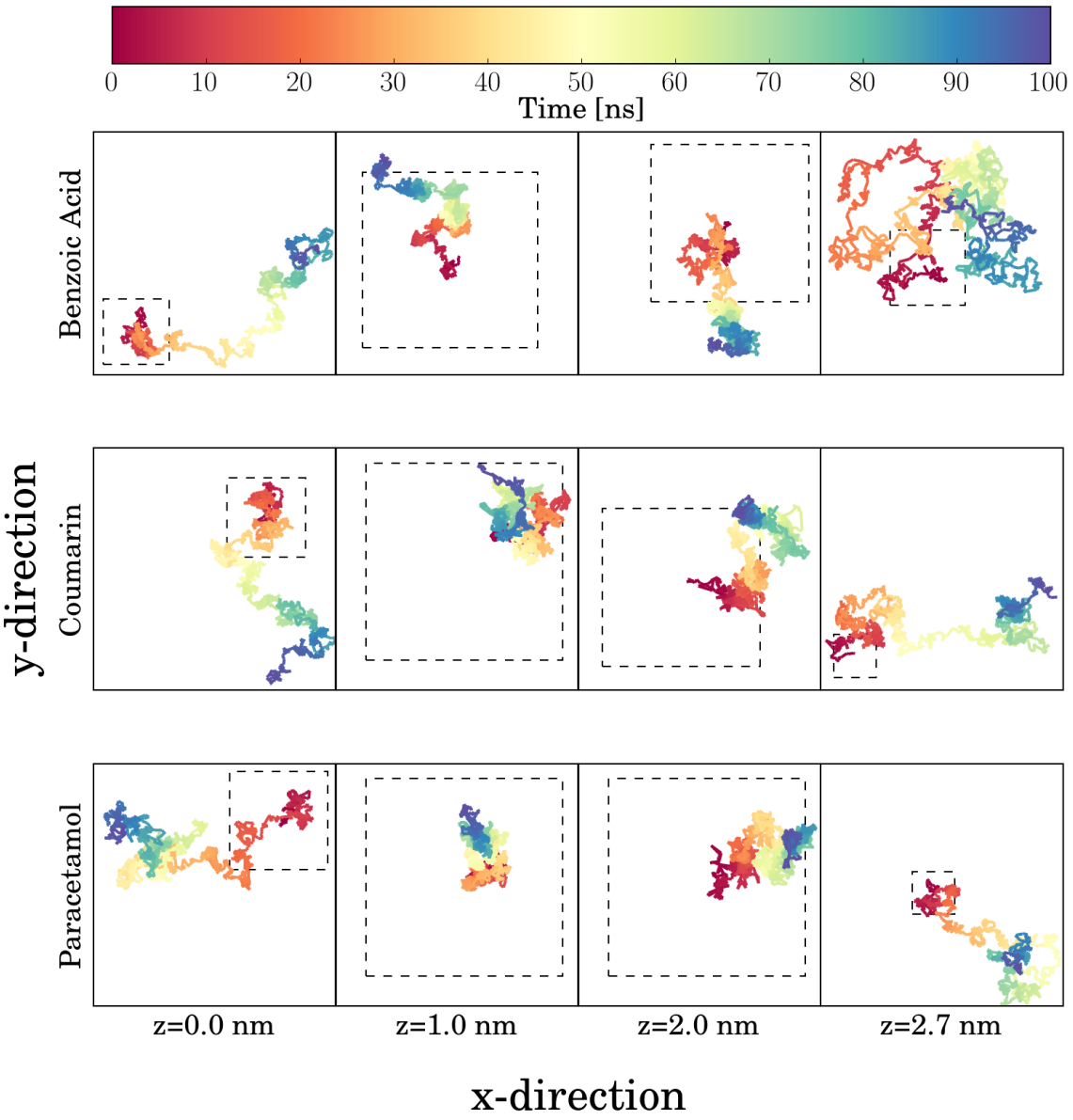

Figure 5.29: Lateral mobility of permeants in the DOPC:DOPE membrane and in different depths; part C. Dashed lines indicate the simulation box (≈6 nm × 6 nm).

5.8 Overall effect of DOPE lipids on permeation

Previous studies that examined lipid membranes of mixed lamellar/nonlamellar compositions have shown that the addition of DOPE lipids to DOPC bilayers did not significantly altered the bilayer structure and density[22]. However, while PC headgroups are bulky and introduce repulsive forces, the smaller size of PE headgroups which also introduce attractive forces due to the ability to form hydrogen bonds with their neighbouring headgroups and solvent, overall decreases the total area per lipid of the mixed bilayer[22,68]. These attractive forces and smaller headgroup size is also responsible for the propensity of the PE lipids to form inverse hexagonal phases which increases the spontaneous curvature of the monolayers. The aforementioned effects are expressed with a hundreds of atmospheres decrease of the lateral pressure profile in the headgroup region and a corresponding increase in the chain region of the bilayer which indicates an increase of the repulsive forces due to the frustrated situation of the DOPE lipid tails[22]. The main hypothesis of this dissertation is that this increase in lateral stresses should affect the passive permeation of molecules through the bilayer and in particular reduce it. Examination of the hydrogen bonds results (figure 5.21), shows that permeants do not form extra hydrogen bonds with DOPE lipids despite the enhanced capability of the latter to form them. This is a strong indication that the lateral pressure profile is the main source of the differences in the permeation coefficients.

All the comparisons in this section were performed with the logarithm of the permeation coefficient logP (which tends to "dampen" the differences), thus the statistical significance for the actual permeation coefficients is expected to be even higher. However, such a comparison was not possible because permeation coefficients varied orders of magnitude for such a diverse set of molecules.

The permeation coefficients reported in this work show that for molecules with molecular weight lower than $100\,\mathrm{g\,mol^{-1}}$, there was a statistically significant reduction in permeation through a mixed DOPC:DOPE bilayer compared to a pure DOPC. On the contrary the examined three drugs with molecular weight higher than $100\,\mathrm{g\,mol^{-1}}$ showed a statistically significant increase in permeability through the mixed membrane. That was a very interesting and counter-intuitive finding that went against the hypothesis of this work. With the available analysis results the cause of this behaviour is inconspicuous, although it is possible that the larger size of these drugs might in fact alter the lateral pressure profile. Remarkably, the limited experimental and computational data that are available in the literature validate in all cases our findings (table 5.6), even for the non-intuitive faster permeation of larger molecules through the DOPC:DOPE membrane.

Jansen and Blume[203] examined water permeation through several large unilamellar lipid vesicles. In particular, at T=343 K, DMPE and DPPE reduced permeation by $\approx$ 99% in comparison to pure DMPC and DPPC, respectively. The same behaviour was observed in

this study but the relative difference between the PC and PC:PE membrane was smaller (−27%).

Huster et al.[115] have also studied water permeation, with O^{17} nuclear magnetic resonance, through a pure DOPC and a DOPC:DOPE(1:1) bilayer, at T=303 K. They reported that for the latter, the permeation coefficient reduced by ≈ 39% , consistent with the present work.

Seo et al.[220] performed a study on the effect of lipid composition on the passive permeation of molecules through PAMPA assays, and observed an 825% increase on the permeation of benzoic acid through a DOPE bilayer, in comparison to a pure DOPC. While the two methodologies vary considerably and the size of lipid vesicles in PAMPA is greater than of the systems examined here, it is noteworthy that our simulations predicted the same relative increase in permeation (31%) through the mixed membrane. The experimental validation of this non-intuitive behaviour is reassuring for the accuracy of the findings of this study.

Hub et al.[210] examined the permeation of ammonia through a pure POPC and a pure POPE bilayer at T=300 K. They reported an ≈ 87% reduction in the permeation for the latter, which is very similar to the presented observation for DOPC:DOPE(1:3) (−71%).

Wennberg et al.[219] examined the partitioning of ammonia, ethanol and propane in a pure POPC and pure POPE bilayer and they saw that the transfer free-energy through the latter was increased for all solutes.

Finally, Zocher et al.[218] also observed a decrease on the permeation of ammonia through a pure DOPE membrane in comparison to a pure DOPC.

Table 5.9: Ranking of predicted logP values for both membranes. Permeation is in ascending order; bottom rows permeate faster.

DOPC	DOPC:DOPE
Urea	Urea
Water	Water
Glycine	Glycine
Paracetamol	Ammonia
Ammonia	Paracetamol
Ethanol	Ethanol
Isopropanol	Isopropanol
Coumarin	Phenol
Fluoromethane	Coumarin
Phenol	Fluoromethane
Benzoic acid	Carbon dioxide
Propane	Propane
Carbon dioxide	Benzoic acid

The aforementioned results and discussion enforces the established view that permeation

is a complicated process, affected by numerous parameters in an intricate way. The results presented in this work clearly indicate an effect of the lipid bilayer composition to the lateral pressure profile and thus in the passive permeation mechanism. However, this effect seems to be more subtle and play a secondary role in comparison to the individual characteristics of each permeant, such as the size, the shape or the polarity. The logP permeation ranking for the DOPC membrane and the DOPC:DOPE(1:3) is presented in table 5.9 and shows that permeation was mostly determined by the partitioning propensity, similar to past studies[248–250,306,307], rather than the changes in the lateral stresses. Furthermore, there are cases in which the permeants alter the lateral pressure profile of the membrane they permeate[81], which makes the understanding of the process even more challenging. To the knowledge of the authors, this is the first attempt to quantitatively connect the lateral pressure profile to the permeation through atomistic molecular dynamics simulations.

5.9 A critique on permeation simulations

Passive permeation is a crucial biological activity driven according to the corresponding concentration gradient. While this mechanism is theoretically explained by Fick's first law of diffusion, the numerous aspects that control real physiological systems remain mostly unexplored. Furthermore, experimental methods have important limitations on examining the underlying physics of passive permeation due to the small scales involved.

Molecular dynamics has revolutionised the research of passive permeation as it allowed for the first time an atomistic perspective on the interactions between the fluid membranes and the permeants. Molecular dynamic simulations however, do not come without disadvantages. The researcher that decides to simulate such a system has to keep in mind that a model is as accurate as the underlying force field parameters that describe it and numerical tools that is using. Furthermore, the single-lipid-type membranes that are used in passive permeation simulations are very far from the actual complexity of real cellular membranes. Even in the case of the more similar single-lipid *in vitro* methods like PAMPA, lipids form much larger and complex vesicles than the pseudo multi-lamellar systems examined with MD and thus results should be interpreted with these important aspects in mind.

Another drawback of MD permeation simulations is the large computational cost. While constant technological advances enable today's researchers to reach μs time-scales of MD simulations, more and more studies claim that true convergence of a permeant-membrane system might require up to hundreds of ns due to hidden barriers[149,150], which have even put into question the established inhomogeneous solubility diffusion model[308]. If this is taken into account along with the large number of positions that are required to explore the depth of monolayer or bilayer, it is without doubt that further steps towards more efficient methodologies are required. The final major drawback of the current established methodology is the lack of freely available analysis tools that are well tested for their accuracy and robustness.

In conclusion, although permeation simulations have undergone an impressive improvement the last 20 years, they still face problems of "immaturity" that prevent their wide adoption from the industry, in contrast to the established and "mature" QSAR[153]. Until the full potential of MD simulations can be exploited by non-academics, hybrid solutions of MD with QSAR as proposed by Lee et al.[254] might be the optimal solution for the near future. Alternatively, data from existing MD studies can be used to fine-tune the transfer free-energy or conformational free-energy values of enhanced physical models such as the one proposed by Leung et al.[155,156]. In fact, in the past 20 years there have been hundreds of permeation studies and the already published results could provide a substantial improvement on the transfer free-energy approximations.

Chapter 6

Conclusions and outlook

This dissertation investigated the biologically crucial process of passive permeation both methodologically and under the perspective of biophysics using MD simulations. Although previous passive permeation studies have utilised atomistic and coarse-grained molecular dynamics simulations, this is the first time that a software toolbox is created to assist the research community on streamlining the complicated pre- and post- processing, as well as HPC simulation management that is involved with these studies.

Additionally, for the first time, a systematic study of important methodological parameters and options are reported for the two mostly used methods, the z-constraint and the z-restraint. Such parameters included the sampling frequency of the constraint force, the PMF convergence analysis techniques and the establishing of a diffusion calculation method for the z-restraint method. In particular for the latter, a thorough comparison between the Hummer and the Zhu and Hummer techniques proved the robustness of the first. Several ways to compute the integral of the autocorrelation function of the restrained position were also tested.

Furthermore, the free-energy, local diffusion and local resistance profiles, as well as the final permeation coefficients are reported for thirteen small molecules and drugs. Eleven permeation coefficients are reported for the first time for transport through DOPC and DOPC:DOPE(1:3) membranes. Based on the results and a systematic comparison of the methods, the z-restraint method was found to be the best for robust, high-throughput MD simulations.

The effect of the nonlamellar DOPE lipids on passive permeation was also examined. According to the hypothesis of this work, the permeation through the mixed membrane should have been slower. The aforementioned findings showed that lamellar/nonlamellar mixtures hindered the permeation of molecules with molecular weight smaller than 100 g mol^{-1}

but facilitated permeation on small drugs with molecular weight larger than $100\,\mathrm{g\,mol^{-1}}$. The results of the small molecules validate the initial hypothesis. The results for the drug molecules are very interesting but also counter-intuitive as they do not follow the expected behaviour due to the increase of lateral pressure in the lipid tails region. Remarkably, all of the results were in agreement with previously reported coefficients, both hindered and facilitated. Hydrogen bonds analysis indicated no extra formations with DOPE lipids, isolating the lateral pressure profile as the predominant factor of effect. This is the first time that permeation through DOPC/DOPE compositions is systematically examined under the perspective of key membrane properties. Overall, although permeation is still predominantly dictated by the physicochemical properties of the solutes, this study showed that nonlamellar lipids also contribute to the passive permeation mechanism, in a complex fashion, through the lateral pressure profile. Therefore, they should be taken into account during the drug design process.

Considering the aforementioned conclusions, it is clear that there are numerous, potentially exciting research paths in the future. Increase of the compositional complexity of the membrane should be one of the research priorities. In particular, examination of how different lipids affect the lateral pressure profile and the elastic properties of a multi-component membrane, both individually and in synergy, should precede any permeation study through such a membrane. The addition of cholesterol is also crucial, as there is evidence of a significant effect on the stress distribution and membrane rigidity[77,94,184,218]. Furthermore, although most permeation studies consider membranes as symmetrical with regards to their composition, real cell membranes are asymmetrical between their internal and external monolayers[267,309,310] and thus future studies should examine the effect of this asymmetry on passive permeation in relation to the lateral pressure profile.

Future work should also include multiple reaction coordinates to ensure true convergence without any hidden barriers. Also, while computational demanding, an energetic analysis of the Gibbs free-energy components[135] of the permeating molecules would provide a better perspective of the forces acting inside the bilayer. The effect of larger molecules on the lateral pressure profile should also be further studied and taken into account on permeation simulations.

Finally, future work would also involve the improvement of the software toolbox created for this work. While already capable of automating the three main stages of the permeation study, it heavily relies on the side toolkits of other MD software packages. The modularisation of force field selection, the inclusion of more MD software suites for simulations, or the addition of extra methods for the study of permeation would certainly increase the outreach and user base of the toolbox.

References

[1] A. A. Ciociola, L. B. Cohen, P. Kulkarni, and FDA-Related Matters Committee of the American College of Gastroenterology, "How drugs are developed and approved by the FDA: current process and future directions," *Am. J. Gastroenterol.*, vol. 109, pp. 620–623, May 2014.

[2] D. Taylor, "The pharmaceutical industry and the future of drug development," in *Pharmaceuticals in the Environment*, pp. 1–33, The Royal Society of Chemistry, 27 Aug. 2015.

[3] M. Dickson and J. P. Gagnon, "The cost of new drug discovery and development," *Discov. Med.*, vol. 4, no. 22, pp. 172–179, 2009.

[4] E. A. Martis, R. Radhakrishnan, and R. R. Badve, "High-throughput screening: the hits and leads of drug discovery-an overview," *J. Basic Appl. Pharm. Sci.*, vol. 1, no. 1, pp. 2–10, 2011.

[5] R. P. Verma, C. Hansch, and C. D. Selassie, "Comparative QSAR studies on PAMPA/modified PAMPA for high throughput profiling of drug absorption potential with respect to caco-2 cells and human intestinal absorption," *J. Comput. Aided Mol. Des.*, vol. 21, pp. 3–22, Jan. 2007.

[6] H. van de Waterbee and E. Gifford, "ADMET in silico modelling: towards prediction paradise?," *Nat. Rev. Drug Discov.*, vol. 2, pp. 192–204, 1 Mar. 2003.

[7] A. Wadood, N. Ahmed, L. Shah, A. Ahmad, H. Hassan, and S. Shams, "In-silico drug design: An approach which revolutionarised the drug discovery process," *OA Drug Design & Delivery*, vol. 1, no. 1, p. 3, 2013.

[8] S. Ekins, J. Mestres, and B. Testa, "In silico pharmacology for drug discovery: methods for virtual ligand screening and profiling," *Br. J. Pharmacol.*, vol. 152, pp. 9–20, Sept. 2007.

[9] D. W. Borhani and D. E. Shaw, "The future of molecular dynamics simulations in drug discovery," *J. Comput. Aided Mol. Des.*, vol. 26, pp. 15–26, Jan. 2012.

[10] J. de Ruyck, G. Brysbaert, R. Blossey, and M. F. Lensink, "Molecular docking as a popular tool in drug design, an in silico travel," *Adv. Appl. Bioinform. Chem.*, vol. 9, pp. 1–11, 28 June 2016.

[11] X.-Y. Meng, H.-X. Zhang, M. Mezei, and M. Cui, "Molecular docking: a powerful approach for structure-based drug discovery," *Curr. Comput. Aided Drug Des.*, vol. 7, pp. 146–157, June 2011.

[12] Boghog, "Drug discovery cycle." https://commons.wikimedia.org/wiki/File:Drug_discovery_cycle.svg, 22 June 2015. [Online; accessed Jul 10, 2017].

[13] H. Zhao and A. Caflisch, "Molecular dynamics in drug design," *Eur. J. Med. Chem.*, vol. 91, pp. 4–14, 16 Feb. 2015.

[14] J. Mortier, C. Rakers, M. Bermudez, M. S. Murgueitio, S. Riniker, and G. Wolber, "The impact of molecular dynamics on drug design: applications for the characterization of ligand-macromolecule complexes," *Drug Discov. Today*, vol. 20, pp. 686–702, June 2015.

[15] J. D. Durrant and J. A. McCammon, "Molecular dynamics simulations and drug discovery," *BMC Biol.*, vol. 9, no. 1, p. 71, 2011.

[16] J. Dehairs, R. Derua, N. Rueda-Rincon, and J. V. Swinnen, "Lipidomics in drug development," *Drug Discov. Today Technol.*, vol. 13, pp. 33–38, June 2015.

[17] O. G. Mouritsen, *Life - As a Matter of Fat: The Emerging Science of Lipidomics*. The Frontiers Collection, Springer Science & Business Media, 30 Nov. 2004.

[18] D. Guinn, *Essentials of General, Organic, and Biochemistry*. W. H. Freeman, 1 Dec. 2013.

[19] Mariana Ruiz, "A detailed diagram of the cell membrane." https://en.wikipedia.org/wiki/Cell_membrane#/media/File:Cell_membrane_detailed_diagram_en.svg, 2007. [Online; accessed March 7, 2017].

[20] M. Orsi and J. W. Essex, "Chapter 4 passive permeation across lipid bilayers: a literature review," *Molecular Simulations and Biomembranes: From Biophysics to Function*, pp. 76–90, 2010.

[21] B. S. Perrin, Jr, A. J. Sodt, M. L. Cotten, and R. W. Pastor, "The curvature induction of Surface-Bound antimicrobial peptides piscidin 1 and piscidin 3 varies with lipid chain length," *J. Membr. Biol.*, vol. 248, pp. 455–467, June 2015.

[22] W. Ding, M. Palaiokostas, W. Wang, and M. Orsi, "Effects of lipid composition on bilayer membranes quantified by All-Atom molecular dynamics," *J. Phys. Chem. B*, vol. 119, pp. 15263–15274, 10 Dec. 2015.

[23] G. Hummer, "Position-dependent diffusion coefficients and free energies from bayesian analysis of equilibrium and replica molecular dynamics simulations," *New J. Phys.*, vol. 7, 2005.

[24] F. Zhu and G. Hummer, "Theory and simulation of ion conduction in the pentameric GLIC channel," *J. Chem. Theory Comput.*, vol. 8, pp. 3759–3768, 9 Oct. 2012.

[25] M. J. Abraham, D. van der Spoel, E. Lindahl, B. Hess, and and the GROMACS development team, *GROMACS User Manual version 2016.2*. Royal Institute of Technology and Uppsala University, 2017.

[26] A. D. MacKerell, D. Bashford, M. Bellott, R. L. Dunbrack, J. D. Evanseck, M. J. Field, S. Fischer, J. Gao, H. Guo, S. Ha, D. Joseph-McCarthy, L. Kuchnir, K. Kuczera, F. T. K. Lau, C. Mattos, S. Michnick, T. Ngo, D. T. Nguyen, B. Prodhom, W. E. Reiher, B. Roux, M. Schlenkrich, J. C. Smith, R. Stote, J. Straub, M. Watanabe,

J. Wiórkiewicz-Kuczera, D. Yin, and M. Karplus, "All-Atom empirical potential for molecular modeling and dynamics studies of proteins," *J. Phys. Chem. B*, vol. 102, no. 18, pp. 3586–3616, 1998.

[27] P. P. Ewald, "Die berechnung optischer und elektrostatischer gitterpotentiale," *Ann. Phys.*, vol. 369, pp. 253–287, 1 Jan. 1921.

[28] T. Darden, D. York, and L. Pedersen, "Particle mesh ewald: An N·log(N) method for ewald sums in large systems," *J. Chem. Phys.*, vol. 98, no. 12, pp. 10089–10092, 1993.

[29] O. Lenz, "Lennard-Jones potential." `https://en.wikipedia.org/wiki/Lennard-Jones_potential#/media/File:12-6-Lennard-Jones-Potential.svg`, 2007. [Online; accessed March 14, 2017].

[30] "What is the Maxwell-Boltzmann distribution?." [Online; Accessed: 2017-3-20].

[31] C. W. Gear, "The numerical integration of ordinary differential equations," *Math. Comput.*, vol. 21, no. 98, pp. 146–156, 1967.

[32] W. F. van Gunsteren and H. J. C. Berendsen, "Algorithms for macromolecular dynamics and constraint dynamics," *Mol. Phys.*, vol. 34, no. 5, pp. 1311–1327, 1977.

[33] H. Berendsen and W. F. Van Gunsteren, "Practical algorithms for dynamic simulations," *Molecular-dynamics simulation of statistical-mechanical systems*, pp. 43–65, 1986.

[34] L. Verlet, "Computer "experiments" on classical fluids. i. thermodynamical properties of Lennard-Jones molecules," *Phys. Rev.*, vol. 159, pp. 98–103, 5 July 1967.

[35] M. P. Allen and D. J. Tildesley, *Computer Simulation of Liquids*. Clarendon Press, 1989.

[36] W. C. Swope, H. C. Andersen, P. H. Berens, and K. R. Wilson, "A computer simulation method for the calculation of equilibrium constants for the formation of physical clusters of molecules: Application to small water clusters," *J. Chem. Phys.*, vol. 76, no. 1, pp. 637–649, 1982.

[37] F. Jensen, *Introduction to Computational Chemistry*. John Wiley & Sons, 2006.

[38] J.-P. Ryckaert, G. Ciccotti, and H. J. C. Berendsen, "Numerical integration of the cartesian equations of motion of a system with constraints: molecular dynamics of n-alkanes," *J. Comput. Phys.*, vol. 23, pp. 327–341, 1 Mar. 1977.

[39] H. C. Andersen, "Rattle: A "velocity" version of the shake algorithm for molecular dynamics calculations," *J. Comput. Phys.*, vol. 52, pp. 24–34, 1 Oct. 1983.

[40] B. Hess, H. Bekker, H. J. C. Berendsen, and J. G. E. M. Fraaije, "LINCS: A linear constraint solver for molecular simulations," *J. Comput. Chem.*, vol. 18, pp. 1463–1472, 1 Sept. 1997.

[41] B. Hess, "P-LINCS: A parallel linear constraint solver for molecular simulation," *J. Chem. Theory Comput.*, vol. 4, no. 1, pp. 116–122, 2008.

[42] H. J. C. Berendsen, J. P. M. Postma, W. F. van Gunsteren, A. DiNola, and J. R. Haak, "Molecular dynamics with coupling to an external bath," *J. Chem. Phys.*, vol. 81, pp. 3684–3690, 15 Oct. 1984.

[43] S. Nosé, "A molecular dynamics method for simulations in the canonical ensemble," *Mol. Phys.*, vol. 52, pp. 255–268, 1984.

[44] W. G. Hoover, "Canonical dynamics: Equilibrium phase-space distributions," *Phys. Rev. A Gen. Phys.*, vol. 31, pp. 1695–1697, Mar. 1985.

[45] G. Bussi, D. Donadio, and M. Parrinello, "Canonical sampling through velocity rescaling," *J. Chem. Phys.*, vol. 126, p. 014101, 7 Jan. 2007.

[46] M. Parrinello and A. Rahman, "Polymorphic transitions in single crystals: A new molecular dynamics method," *J. Appl. Phys.*, vol. 52, pp. 7182–7190, 1 Dec. 1981.

[47] X. Xu and E. London, "The effect of sterol structure on membrane lipid domains reveals how cholesterol can induce lipid domain formation," *Biochemistry*, vol. 39, pp. 843–849, 8 Feb. 2000.

[48] B. B. Issack and G. H. Peslherbe, "Effects of cholesterol on the thermodynamics and kinetics of passive transport of water through lipid membranes," *J. Phys. Chem. B*, vol. 119, p. 150213162609001, 23 July 2015.

[49] H. M. McConnell and A. Radhakrishnan, "Condensed complexes of cholesterol and phospholipids," *Biochim. Biophys. Acta*, vol. 1610, pp. 159–173, 10 Mar. 2003.

[50] "Glycolipids - latest research and news — nature." `http://www.nature.com/subjects/glycolipids`, 11 Oct. 2016. Accessed: 2017-3-27.

[51] I. W. Hamley, *Introduction to Soft Matter– Revised Edition*. Chichester, UK: John Wiley & Sons, Ltd, 7 Sept. 2007.

[52] D. Boal and D. H. Boal, *Mechanics of the Cell*. Cambridge University Press, 19 Jan. 2012.

[53] K. Gawrisch, V. A. Parsegian, D. A. Hajduk, M. W. Tate, S. M. Graner, N. L. Fuller, and R. P. Rand, "Energetics of a hexagonal-lamellar-hexagonal-phase transition sequence in dioleoylphosphatidylethanolamine membranes," *Biochemistry*, vol. 31, pp. 2856–2864, 24 Mar. 1992.

[54] D. Marsh, *Handbook of Lipid Bilayers, Second Edition*. CRC Press, 15 Feb. 2013.

[55] E. Gorter and F. Grendel, "ON BIMOLECULAR LAYERS OF LIPOIDS ON THE CHROMOCYTES OF THE BLOOD," *J. Exp. Med.*, vol. 41, pp. 439–443, 31 Mar. 1925.

[56] S. J. Singer and G. L. Nicolson, "The fluid mosaic model of the structure of cell membranes," *Science*, vol. 175, pp. 720–731, 18 Feb. 1972.

[57] J. N. Israelachvili, "The packing of lipids and proteins in membranes," *Light transducing membranes: structure, function and evolution. Academic Press, New York*, pp. 91–107, 1978.

[58] J. D. Robertson, "Membrane structure," *J. Cell Biol.*, vol. 91, pp. 189s–204s, Dec. 1981.

[59] K. Jacobson, E. D. Sheets, and R. Simson, "Revisiting the fluid mosaic model of membranes," *Science*, vol. 268, pp. 1441–1442, 9 June 1995.

[60] J. F. Nagle and S. Tristram-Nagle, "Structure of lipid bilayers," *Biochimica et Biophysica Acta (BBA) - Reviews on Biomembranes*, vol. 1469, pp. 159–195, Nov. 2000.

[61] B. W. Koenig, H. H. Strey, and K. Gawrisch, "Membrane lateral compressibility determined by NMR and x-ray diffraction: effect of acyl chain polyunsaturation," *Biophys. J.*, vol. 73, pp. 1954–1966, Oct. 1997.

[62] H. Berendsen and S. J. Marrink, "Molecular dynamics of water transport through membranes: Water from solvent to solute," *J. Macromol. Sci. Part A Pure Appl. Chem.*, vol. 65, no. 12, pp. 2513–2520, 1993.

[63] D. P. Tieleman, S. J. Marrink, and H. J. C. Berendsen, "A computer perspective of membranes: molecular dynamics studies of lipid bilayer systems," *Biochimica et Biophysica Acta (BBA) - Reviews on Biomembranes*, vol. 1331, pp. 235–270, 21 Nov. 1997.

[64] J. F. Nagle, "Introductory lecture: basic quantities in model biomembranes," *Faraday Discuss.*, vol. 161, pp. 11–29; discussion 113–50, 2013.

[65] M. Orsi and J. W. Essex, "Physical properties of mixed bilayers containing lamellar and nonlamellar lipids: insights from coarse-grain molecular dynamics simulations," *Faraday Discuss.*, pp. 249–272, 2013.

[66] Q. Waheed and O. Edholm, "Undulation contributions to the area compressibility in lipid bilayer simulations," *Biophys. J.*, vol. 97, pp. 2754–2760, 18 Nov. 2009.

[67] A. R. Braun, E. G. Brandt, O. Edholm, J. F. Nagle, and J. N. Sachs, "Determination of electron density profiles and area from simulations of undulating membranes," *Biophys. J.*, vol. 100, pp. 2112–2120, 4 May 2011.

[68] A. H. de Vries, A. E. Mark, and S. J. Marrink, "The binary mixing behavior of phospholipids in a bilayer: A molecular dynamics study," *J. Phys. Chem. B*, vol. 108, no. 7, pp. 2454–2463, 2004.

[69] K. Simons and E. Ikonen, "Functional rafts in cell membranes," *Nature*, vol. 387, pp. 569–572, 5 June 1997.

[70] P. S. Niemelä, S. Ollila, M. T. Hyvönen, M. Karttunen, and I. Vattulainen, "Assessing the nature of lipid raft membranes," *PLoS Comput. Biol.*, vol. 3, p. e34, 23 Feb. 2007.

[71] J. D. Nickels, S. Chatterjee, C. B. Stanley, S. Qian, X. Cheng, D. A. A. Myles, R. F. Standaert, J. G. Elkins, and J. Katsaras, "The in vivo structure of biological membranes and evidence for lipid domains," *PLoS Biol.*, vol. 15, p. e2002214, May 2017.

[72] R. H. Templer, S. J. Castle, A. R. Curran, G. Rumbles, and D. R. Klug, "Sensing isothermal changes in the lateral pressure in model membranes using di-pyrenyl phosphatidylcholine," *Faraday Discuss.*, no. 111, pp. 41–53; discussion 69–78, 1998.

[73] D. Marsh, "Lateral pressure in membranes," *Biochim. Biophys. Acta*, vol. 1286, pp. 183–223, 29 Oct. 1996.

[74] H. Saito, M. Iwayama, H. Takagi, M. Nishimura, T. Miyakawa, K. Kawaguchi, M. Takasu, T. Mizukami, and H. Nagao, "Molecular dynamics study of gramicidin a in lipid bilayer: Structure and lateral pressure profile," *Int. J. Quantum Chem.*, vol. 112, no. 24, pp. 3834–3839, 2012.

[75] A. Arouri, K. E. Lauritsen, H. L. Nielsen, and O. G. Mouritsen, "Effect of fatty acids on the permeability barrier of model and biological membranes," *Chem. Phys. Lipids*, vol. 200, pp. 139–146, Oct. 2016.

[76] S. Ollila, M. T. Hyvönen, and I. Vattulainen, "Polyunsaturation in lipid membranes: dynamic properties and lateral pressure profiles," *J. Phys. Chem. B*, vol. 111, pp. 3139–3150, 29 Mar. 2007.

[77] M. Patra, "Lateral pressure profiles in cholesterol-DPPC bilayers," *Eur. Biophys. J.*, vol. 35, pp. 79–88, Dec. 2005.

[78] M. Carrillo-Tripp and S. E. Feller, "Evidence for a mechanism by which omega-3 polyunsaturated lipids may affect membrane protein function," *Biochemistry*, vol. 44, pp. 10164–10169, 2 Aug. 2005.

[79] H. Binder and K. Gawrisch, "Effect of unsaturated lipid chains on dimensions, molecular order and hydration of membranes," *J. Phys. Chem. B*, vol. 105, no. 49, pp. 12378–12390, 2001.

[80] A. Polley and S. Vemparala, "Partitioning of ethanol in multi-component membranes: effects on membrane structure," *Chem. Phys. Lipids*, vol. 166, pp. 1–11, Jan. 2013.

[81] E. Terama, O. H. S. Ollila, E. Salonen, A. C. Rowat, C. Trandum, P. Westh, M. Patra, M. Karttunen, and I. Vattulainen, "Influence of ethanol on lipid membranes: from lateral pressure profiles to dynamics and partitioning," *J. Phys. Chem. B*, vol. 112, pp. 4131–4139, 3 Apr. 2008.

[82] A. L. Frischknecht and L. J. Douglas Frink, "Alcohols reduce lateral membrane pressures: Predictions from molecular theory," *Biophys. J.*, vol. 91, no. 11, pp. 4081–4090, 2006.

[83] L. Yang, L. Ding, and H. W. Huang, "New phases of phospholipids and implications to the membrane fusion problem," *Biochemistry*, vol. 42, pp. 6631–6635, 10 June 2003.

[84] G. C. Shearman, O. Ces, R. H. Templer, and J. M. Seddon, "Inverse lyotropic phases of lipids and membrane curvature," *J. Phys. Condens. Matter*, vol. 18, pp. S1105–24, 19 July 2006.

[85] T. Kamo, M. Nakano, Y. Kuroda, and T. Handa, "Effects of an amphipathic ??-helical peptide on lateral pressure and water penetration in phosphatidylcholine and monoolein mixed membranes," *J. Phys. Chem. B*, vol. 110, pp. 24987–24992, 2006.

[86] K. Charalambous, D. Miller, P. Curnow, and P. J. Booth, "Lipid bilayer composition influences small multidrug transporters," *BMC Biochem.*, vol. 9, no. 1, 2008.

[87] P. Curnow, M. Lorch, K. Charalambous, and P. J. Booth, "The reconstitution and activity of the small multidrug transporter EmrE is modulated by non-bilayer lipid composition," *J. Mol. Biol.*, vol. 343, pp. 213–222, 8 Oct. 2004.

[88] R. S. Cantor, "The lateral pressure profile in membranes: a physical mechanism of general anesthesia," *Biochemistry*, vol. 36, pp. 2339–2344, 4 Mar. 1997.

[89] R. S. Cantor, "The lateral pressure profile in membranes: a physical mechanism of general anesthesia," *Toxicol. Lett.*, vol. 100-101, pp. 451–458, 23 Nov. 1998.

[90] B. Fábián, M. Sega, V. P. Voloshin, N. N. Medvedev, and P. Jedlovszky, "Lateral pressure profile and free volume properties in phospholipid membranes containing anesthetics," *J. Phys. Chem. B*, 27 Mar. 2017.

[91] J. T. Mohr, G. W. Gribble, S. S. Lin, R. G. Eckenhoff, and R. S. Cantor, "Anesthetic potency of two novel synthetic polyhydric alkanols longer than the n-alkanol cutoff: evidence for a bilayer-mediated mechanism of anesthesia?," *J. Med. Chem.*, vol. 48, pp. 4172–4176, 16 June 2005.

[92] R. S. Cantor, "Lateral pressures in cell membranes: A mechanism for modulation of protein function," *J. Phys. Chem. B*, vol. 101, no. 10, pp. 1723–1725, 1997.

[93] D. Marsh, "Lateral pressure profile, spontaneous curvature frustration, and the incorporation and conformation of proteins in membranes," *Biophys. J.*, vol. 93, pp. 3884–3899, 1 Dec. 2007.

[94] S. Ollila, T. Róg, M. Karttunen, and I. Vattulainen, "Role of sterol type on lateral pressure profiles of lipid membranes affecting membrane protein functionality: Comparison between cholesterol, desmosterol, 7-dehydrocholesterol and ketosterol," *J. Struct. Biol.*, vol. 159, pp. 311–323, Aug. 2007.

[95] J. Gullingsrud, A. Babakhani, and J. A. McCammon, "Computational investigation of pressure profiles in lipid bilayers with embedded proteins," *Mol. Simul.*, vol. 32, no. 10-11, pp. 831–838, 2006.

[96] E. Van Den Brink-Van Der Laan, J. Antoinette Killian, and B. De Kruijff, "Nonbilayer lipids affect peripheral and integral membrane proteins via changes in the lateral pressure profile," *Biochimica et Biophysica Acta - Biomembranes*, vol. 1666, no. 1-2, pp. 275–288, 2004.

[97] J. Gullingsrud and K. Schulten, "Lipid bilayer pressure profiles and mechanosensitive channel gating," *Biophys. J.*, vol. 86, no. 6, pp. 3496–3509, 2004.

[98] R. S. Cantor, "Solute modulation of conformational equilibria in intrinsic membrane proteins: Apparent 'cooperativity' without binding," *Biophys. J.*, vol. 77, no. 5, pp. 2643–2647, 1999.

[99] S. J. Cowsley, R. H. Templer, and D. R. Klug, "Dipyrenylphosphatidylcholine as a probe of bilayer pressures," *J. Fluoresc.*, vol. 3, pp. 149–152, Sept. 1993.

[100] M. Dékány Fraňová, I. Vattulainen, and O. H. Samuli Ollila, "Can pyrene probes be used to measure lateral pressure profiles of lipid membranes? perspective through atomistic simulations," *Biochim. Biophys. Acta*, vol. 1838, pp. 1406–1411, May 2014.

[101] S. I. Mukhin and S. Baoukina, "Analytical derivation of thermodynamic characteristics of lipid bilayer from a flexible string model," *Phys. Rev. E Stat. Nonlin. Soft Matter Phys.*, vol. 71, p. 061918, June 2005.

[102] O. H. S. Ollila and I. Vattulainen, "Lateral pressure profiles in lipid membranes: Dependence on molecular composition," in *Molecular Simulations and Biomembranes*, pp. 26–55, pubs.rsc.org, 2010.

[103] J. H. Irving and J. G. Kirkwood, "The statistical mechanical theory of transport processes. IV. the equations of hydrodynamics," *J. Chem. Phys.*, vol. 18, pp. 817–829, 1 June 1950.

[104] A. Harasima, "Molecular theory of surface tension," *Adv. Chem. Phys.*, vol. 1, pp. 203–237, 1958.

[105] W. Helfrich, "Elastic properties of lipid bilayers: theory and possible experiments," *Z. Naturforsch. C*, vol. 28, pp. 693–703, Nov. 1973.

[106] J. M. Seddon and R. H. Templer, "Polymorphism of lipid-water systems," in *Structure and Dynamics of Membranes: I. From Cells to Vesicles / II. Generic and Specific Interactions* (R. Lipowsky and E. Sackmann, eds.), vol. 1, pp. 97–160, Elsevier Science: Amsterdam, 1995.

[107] A. K. Mandagere, T. N. Thompson, and K.-K. Hwang, "Graphical model for estimating oral bioavailability of drugs in humans and other species from their caco-2 permeability and in vitro liver enzyme metabolic stability rates," *J. Med. Chem.*, vol. 45, pp. 304–311, 17 Jan. 2002.

[108] M. R. Villarreal, "Simple diffusion in cell membrane." `https://en.wikipedia.org/wiki/Passive_transport#/media/File:Scheme_simple_diffusion_in_cell_membrane-en.svg`, Feb. 2007. [Online; accessed Apr 04, 2017].

[109] G. Camenisch, G. Folkers, and H. van de Waterbeemd, "Review of theoretical passive drug absorption models: historical background, recent developments and limitations," *Pharm. Acta Helv.*, vol. 71, pp. 309–327, Nov. 1996.

[110] T.-X. Xiang and B. D. Anderson, "Liposomal drug transport: a molecular perspective from molecular dynamics simulations in lipid bilayers," *Adv. Drug Deliv. Rev.*, vol. 58, pp. 1357–1378, 30 Nov. 2006.

[111] H. Meyer, "Zur theorie der alkoholnarkose," *Archiv f. experiment. Pathol. u. Pharmakol*, vol. 42, pp. 109–118, 1 Mar. 1899.

[112] C. E. Overton, *Studien über die Narkose zugleich ein Beitrag zur Allgemeinen Pharmakologie*. Fischer, 1901.

[113] A. Finkelstein, "Water and nonelectrolyte permeability of lipid bilayer membranes," *J. Gen. Physiol.*, vol. 68, no. 1971, pp. 127–135, 1976.

[114] J. M. Diamond and Y. Katz, "Interpretation of nonelectrolyte partition coefficients between dimyristoyl lecithin and water," *J. Membrain Biol.*, vol. 17, pp. 121–154, 1 Dec. 1974.

[115] D. Huster, a. J. Jin, K. Arnold, and K. Gawrisch, "Water permeability of polyunsaturated lipid membranes measured by 17O NMR," *Biophys. J.*, vol. 73, pp. 855–864, Aug. 1997.

[116] Y. Sambuy, I. De Angelis, G. Ranaldi, M. L. Scarino, A. Stammati, and F. Zucco, "The caco-2 cell line as a model of the intestinal barrier: Influence of cell and culture-related factors on caco-2 cell functional characteristics," *Cell Biol. Toxicol.*, vol. 21, no. 1, pp. 1–26, 2005.

[117] T. X. Xiang, X. Chen, and B. D. Anderson, "Transport methods for probing the barrier domain of lipid bilayer membranes," *Biophys. J.*, vol. 63, pp. 78–88, July 1992.

[118] E. Orbach and A. Finkelstein, "The nonelectrolyte permeability of planar lipid bilayer membranes," *J. Gen. Physiol.*, vol. 75, pp. 427–436, Apr. 1980.

[119] A. Walter and J. Gutknecht, "Monocarboxylic acid permeation through lipid bilayer membranes," *J. Membr. Biol.*, vol. 77, no. 3, pp. 255–264, 1984.

[120] T. X. Xiang and B. D. Anderson, "Phospholipid surface density determines the partitioning and permeability of acetic acid in DMPC:cholesterol bilayers," *J. Membr. Biol.*, vol. 148, pp. 157–167, Nov. 1995.

[121] S. Paula, A. G. Volkov, A. N. Van Hoek, T. H. Haines, and D. W. Deamer, "Permeation of protons, potassium ions, and small polar molecules through phospholipid bilayers as a function of membrane thickness," *Biophys. J.*, vol. 70, pp. 339–348, Jan. 1996.

[122] "Caco-2 permeability assay." `http://www.cyprotex.com/admepk/in-vitro-permeability/caco-2-permeability`. Accessed: 2017-5-11.

[123] I. Hubatsch, E. G. E. Ragnarsson, and P. Artursson, "Determination of drug permeability and prediction of drug absorption in caco-2 monolayers," *Nat. Protoc.*, vol. 2, no. 9, pp. 2111–2119, 2007.

[124] J. Fogh and G. Trempe, "New human tumor cell lines," in *Human Tumor Cells in Vitro* (J. Fogh, ed.), pp. 115–159, Springer US, 1975.

[125] P. Artursson and J. Karlsson, "Correlation between oral drug absorption in humans and apparent drug permeability coefficients in human intestinal epithelial (caco-2) cells," *Biochem. Biophys. Res. Commun.*, vol. 175, pp. 880–885, 29 Mar. 1991.

[126] J. Ruell, "Membrane-based drug assays," *Mod. Drug Discovery*, vol. 6, pp. 28–30, 2003.

[127] M. Kansy, F. Senner, and K. Gubernator, "Physicochemical high throughput screening: parallel artificial membrane permeation assay in the description of passive absorption processes," *J. Med. Chem.*, vol. 41, pp. 1007–1010, 26 Mar. 1998.

[128] M. Bermejo, A. Avdeef, A. Ruiz, R. Nalda, J. A. Ruell, O. Tsinman, I. González, C. Fernández, G. Sánchez, T. M. Garrigues, and V. Merino, "PAMPA–a drug absorption in vitro model 7. comparing rat in situ, caco-2, and PAMPA permeability of fluoroquinolones," *Eur. J. Pharm. Sci.*, vol. 21, pp. 429–441, Mar. 2004.

[129] A. Avdeef, P. Artursson, S. Neuhoff, L. Lazorova, J. Gråsjö, and S. Tavelin, "Caco-2 permeability of weakly basic drugs predicted with the double-sink PAMPA pka(flux) method," *Eur. J. Pharm. Sci.*, vol. 24, pp. 333–349, Mar. 2005.

[130] C. Dagenais, A. Avdeef, O. Tsinman, A. Dudley, and R. Beliveau, "P-glycoprotein deficient mouse in situ blood-brain barrier permeability and its prediction using an in combo PAMPA model," *Eur. J. Pharm. Sci.*, vol. 38, pp. 121–137, 10 Sept. 2009.

[131] W. Shinoda, M. Mikami, T. Baba, and M. Hato, "Molecular dynamics study on the effects of chain branching on the physical properties of lipid bilayers: 2. permeability," *J. Phys. Chem. B*, vol. 108, pp. 9346–9356, July 2004.

[132] J. Haorah, D. Heilman, B. Knipe, J. Chrastil, J. Leibhart, A. Ghorpade, D. W. Miller, and Y. Persidsky, "Ethanol-induced activation of myosin light chain kinase leads to dysfunction of tight junctions and blood-brain barrier compromise," *Alcohol. Clin. Exp. Res.*, vol. 29, pp. 999–1009, June 2005.

[133] L. Koubi, M. Tarek, M. L. Klein, and D. Scharf, "Distribution of halothane in a dipalmitoylphosphatidylcholine bilayer from molecular dynamics calculations," *Biophys. J.*, vol. 78, pp. 800–811, Feb. 2000.

[134] S.-J. Marrink and H. J. C. Berendsen, "Simulation of water transport through a lipid membrane," *J. Phys. Chem.*, vol. 98, pp. 4155–4168, Apr. 1994.

[135] J. L. MacCallum and D. P. Tieleman, "Computer simulation of the distribution of hexane in a lipid bilayer: spatially resolved free energy, entropy, and enthalpy profiles," *J. Am. Chem. Soc.*, vol. 128, pp. 125–130, 11 Jan. 2006.

[136] E. Awoonor-Williams and C. N. Rowley, "Molecular simulation of nonfacilitated membrane permeation," *Biochimica et Biophysica Acta (BBA) - Biomembranes*, vol. 1858, pp. 1672–1687, July 2016.

[137] W. Shinoda, "Permeability across lipid membranes," *Biochim. Biophys. Acta*, vol. 1858, pp. 2254–2265, Oct. 2016.

[138] B. L. Lee, K. Kuczera, C. R. Middaugh, and G. S. Jas, "Permeation of the three aromatic dipeptides through lipid bilayers: Experimental and computational study," *J. Chem. Phys.*, vol. 144, p. 245103, 28 June 2016.

[139] M. Orsi, W. E. Sanderson, and J. W. Essex, "Permeability of small molecules through a lipid bilayer: a multiscale simulation study," *J. Phys. Chem. B*, vol. 113, pp. 12019–12029, 3 Sept. 2009.

[140] G. M. Torrie and J. P. Valleau, "Nonphysical sampling distributions in monte carlo free-energy estimation - umbrella sampling," *J. Comput. Phys.*, vol. 23, pp. 187–199, 1977.

[141] S. Kumar, J. M. Rosenberg, D. Bouzida, R. H. Swendsen, and P. A. Kollman, "THE weighted histogram analysis method for free-energy calculations on biomolecules. i. the method," *J. Comput. Chem.*, vol. 13, pp. 1011–1021, 1 Oct. 1992.

[142] S. Kumar, J. M. Rosenberg, D. Bouzida, R. H. Swendsen, and P. A. Kollman, "Multidimensional free-energy calculations using the weighted histogram analysis method," *J. Comput. Chem.*, vol. 16, pp. 1339–1350, 1 Nov. 1995.

[143] J. Lemkul, "Umbrella sampling."

[144] B. J. Berne, M. Borkovec, and J. E. Straub, "Classical and modern methods in reaction rate theory," *J. Phys. Chem.*, vol. 92, pp. 3711–3725, 1 June 1988.

[145] T. B. Woolf and B. Roux, "Conformational flexibility of o-phosphorylcholine and o-phosphorylethanolamine: A molecular dynamics study of solvation effects," *J. Am. Chem. Soc.*, vol. 116, pp. 5916–5926, 1 June 1994.

[146] H. Flyvbjerg and H. G. G. Petersen, "Error estimates on averages of correlated data," *J. Chem. Phys.*, vol. 91, no. 1, p. 461, 1989.

[147] H. J. C. Berendsen, *A Student's Guide to Data and Error Analysis*. Cambridge: Cambridge University Press, 2011.

[148] K. Shinoda, W. Shinoda, and M. Mikami, "Efficient free energy calculation of water across lipid membranes," *J. Comput. Chem.*, vol. 29, pp. 1912–1918, 2008.

[149] C. Neale, W. F. D. Bennett, D. P. Tieleman, and R. Pomès, "Statistical convergence of equilibrium properties in simulations of molecular solutes embedded in lipid bilayers," *J. Chem. Theory Comput.*, vol. 7, pp. 4175–4188, 13 Dec. 2011.

[150] C. Neale, C. Madill, S. Rauscher, and R. Pomès, "Accelerating convergence in molecular dynamics simulations of solutes in lipid membranes by conducting a random walk along the bilayer normal," *J. Chem. Theory Comput.*, vol. 9, pp. 3686–3703, 13 Aug. 2013.

[151] C. Neale and R. Pomès, "Sampling errors in free energy simulations of small molecules in lipid bilayers," *Biochim. Biophys. Acta*, vol. 1858, pp. 2539–2548, Oct. 2016.

[152] V. N. Viswanadhan, A. K. Ghose, G. R. Revankar, and R. K. Robins, "Atomic physicochemical parameters for three dimensional structure directed quantitative structure-activity relationships. 4. additional parameters for hydrophobic and dispersive interactions and their application for an automated superposition of certain naturally occurring nucleoside antibiotics," *J. Chem. Inf. Comput. Sci.*, vol. 29, no. 3, pp. 163–172, 1989.

[153] R. V. Swift and R. E. Amaro, "Back to the future: can physical models of passive membrane permeability help reduce drug candidate attrition and move us beyond QSPR?," *Chem. Biol. Drug Des.*, vol. 81, pp. 61–71, Jan. 2013.

[154] J. A. Ruell, K. L. Tsinman, and A. Avdeef, "PAMPA–a drug absorption in vitro model. 5. unstirred water layer in iso-ph mapping assays and pka(flux)–optimized design (pOD-PAMPA)," *Eur. J. Pharm. Sci.*, vol. 20, pp. 393–402, Dec. 2003.

[155] S. S. F. Leung, J. Mijalkovic, K. Borrelli, and M. P. Jacobson, "Testing physical models of passive membrane permeation," *J. Chem. Inf. Model.*, vol. 52, pp. 1621–1636, June 2012.

[156] S. S. F. Leung, D. Sindhikara, and M. P. Jacobson, "Simple predictive models of passive membrane permeability incorporating Size-Dependent Membrane-Water partition," *J. Chem. Inf. Model.*, vol. 56, pp. 924–929, May 2016.

[157] S. L. Keller, S. M. Bezrukov, S. M. Gruner, M. W. Tate, I. Vodyanoy, and V. A. Parsegian, "Probability of alamethicin conductance states varies with nonlamellar tendency of bilayer phospholipids," *Biophys. J.*, vol. 65, pp. 23–27, July 1993.

[158] B. Chu, A. M. Dopico, J. R. Lemos, and S. N. Treistman, "Ethanol potentiation of calcium-activated potassium channels reconstituted into planar lipid bilayers," *Mol. Pharmacol.*, vol. 54, pp. 397–406, Aug. 1998.

[159] M. F. Brown, "Chapter 8 influence of Nonlamellar-Forming lipids on rhodopsin," *Curr. Top. Membr.*, vol. 44, pp. 285–356, 1 Jan. 1997.

[160] S. E. Rankin, G. H. Addona, M. A. Kloczewiak, B. Bugge, and K. W. Miller, "The cholesterol dependence of activation and fast desensitization of the nicotinic acetylcholine receptor," *Biophys. J.*, vol. 73, pp. 2446–2455, Nov. 1997.

[161] D. C. Mitchell, J. T. Lawrence, and B. J. Litman, "Primary alcohols modulate the activation of the G protein-coupled receptor rhodopsin by a lipid-mediated mechanism," *J. Biol. Chem.*, vol. 271, pp. 19033–19036, 9 Aug. 1996.

[162] D. C. Mitchell, M. Straume, and B. J. Litman, "Role of sn-1-saturated,sn-2-polyunsaturated phospholipids in control of membrane receptor conformational equilibrium: effects of cholesterol and acyl chain unsaturation on the metarhodopsin I in equilibrium with metarhodopsin II equilibrium," *Biochemistry*, vol. 31, pp. 662–670, 28 Jan. 1992.

[163] B. J. Litman and D. C. Mitchell, "A role for phospholipid polyunsaturation in modulating membrane protein function," *Lipids*, vol. 31 Suppl, pp. S193–7, Mar. 1996.

[164] V. S. Markin and F. Sachs, "Thermodynamics of mechanosensitivity," *Phys. Biol.*, vol. 1, pp. 110–124, June 2004.

[165] A. Pohorille, M. A. Wilson, C. Chipot, M. H. New, and K. Schweighofer, "Interactions of small molecules and peptides with membranes," in *Computational Molecular Biology*, vol. 8 of *Theoretical and Computational Chemistry*, pp. 485–535, Elsevier, 1999.

[166] J. L. MacCallum and D. P. Tieleman, "Chapter 8 interactions between small molecules and lipid bilayers," in *Current Topics in Membranes* (Scott E. Feller, ed.), vol. 60, pp. 227–256, Academic Press, 2008.

[167] C. G. Mayne, M. J. Arcario, P. Mahinthichaichan, J. L. Baylon, J. V. Vermaas, L. Navidpour, P.-C. Wen, S. Thangapandian, and E. Tajkhorshid, "The cellular membrane as a mediator for small molecule interaction with membrane proteins," *Biochim. Biophys. Acta*, vol. 1858, pp. 2290–2304, Oct. 2016.

[168] H. Jerabek, G. Pabst, M. Rappolt, and T. Stockner, "Membrane-mediated effect on ion channels induced by the anesthetic drug ketamine," *J. Am. Chem. Soc.*, vol. 132, pp. 7990–7997, 16 June 2010.

[169] M. Kranenburg and B. Smit, "Simulating the effect of alcohol on the structure of a membrane," *FEBS Lett.*, vol. 568, pp. 15–18, 18 June 2004.

[170] M. Patra, E. Salonen, E. Terama, I. Vattulainen, R. Faller, B. W. Lee, J. Holopainen, and M. Karttunen, "Under the influence of alcohol: the effect of ethanol and methanol on lipid bilayers," *Biophys. J.*, vol. 90, pp. 1121–1135, 15 Feb. 2006.

[171] J. Chanda and S. Bandyopadhyay, "Perturbation of phospholipid bilayer properties by ethanol at a high concentration," *Langmuir*, vol. 22, pp. 3775–3781, 11 Apr. 2006.

[172] R. Thind, D. W. O'Neill, A. Del Regno, and R. Notman, "Ethanol induces the formation of water-permeable defects in model bilayers of skin lipids," *Chem. Commun.*, vol. 51, pp. 5406–5409, 23 Dec. 2014.

[173] H. I. Ingólfsson and O. S. Andersen, "Alcohol's effects on lipid bilayer properties," *Biophys. J.*, vol. 101, pp. 847–855, 17 Aug. 2011.

[174] B. W. Lee, R. Faller, A. K. Sum, I. Vattulainen, M. Patra, and M. Karttunen, "Structural effects of small molecules on phospholipid bilayers investigated by molecular simulations," *Fluid Phase Equilib.*, vol. 225, pp. 63–68, 9 Nov. 2004.

[175] M. E. Haque, T. J. McIntosh, and B. R. Lentz, "Influence of lipid composition on physical properties and peg-mediated fusion of curved and uncurved model membrane vesicles: "nature's own" fusogenic lipid bilayer," *Biochemistry*, vol. 40, pp. 4340–4348, 10 Apr. 2001.

[176] A. G. Lee, "How lipids affect the activities of integral membrane proteins," *Biochim. Biophys. Acta*, vol. 1666, pp. 62–87, 3 Nov. 2004.

[177] S. M. Gruner, "Intrinsic curvature hypothesis for biomembrane lipid composition: a role for nonbilayer lipids," *Proc. Natl. Acad. Sci. U. S. A.*, vol. 82, pp. 3665–3669, June 1985.

[178] J. R. Lewis and D. S. Cafiso, "Correlation between the free energy of a channel-forming voltage-gated peptide and the spontaneous curvature of bilayer lipids," *Biochemistry*, vol. 38, pp. 5932–5938, 4 May 1999.

[179] H. Hong and L. K. Tamm, "Elastic coupling of integral membrane protein stability to lipid bilayer forces," *Proc. Natl. Acad. Sci. U. S. A.*, vol. 101, pp. 4065–4070, 23 Mar. 2004.

[180] G. S. Attard, R. H. Templer, W. S. Smith, A. N. Hunt, and S. Jackowski, "Modulation of CTP:phosphocholine cytidylyltransferase by membrane curvature elastic stress," *Proc. Natl. Acad. Sci. U. S. A.*, vol. 97, pp. 9032–9036, 1 Aug. 2000.

[181] A. R. Curran, R. H. Templer, and P. J. Booth, "Modulation of folding and assembly of the membrane protein bacteriorhodopsin by intermolecular forces within the lipid bilayer," *Biochemistry*, vol. 38, pp. 9328–9336, 20 July 1999.

[182] A. V. Botelho, N. J. Gibson, R. L. Thurmond, Y. Wang, and M. F. Brown, "Conformational energetics of rhodopsin modulated by nonlamellar-forming lipids," *Biochemistry*, vol. 41, pp. 6354–6368, 21 May 2002.

[183] R. S. Cantor, "The influence of membrane lateral pressures on simple geometric models of protein conformational equilibria," *Chem. Phys. Lipids*, vol. 101, pp. 45–56, Aug. 1999.

[184] R. S. Cantor, "Lipid composition and the lateral pressure profile in bilayers," *Biophys. J.*, vol. 76, pp. 2625–2639, May 1999.

[185] S. Ollila, *Lateral Pressure in Lipid Membranes and Its Role in Function of Membrane Proteins*. PhD thesis, Tampere University of Technology, 2010.

[186] D. Marsh, "Protein modulation of lipids, and vice-versa, in membranes," *Biochim. Biophys. Acta*, vol. 1778, pp. 1545–1575, July 2008.

[187] O. G. Mouritsen, "Lipids, curvature, and nano-medicine," *Eur. J. Lipid Sci. Technol.*, vol. 113, pp. 1174–1187, Oct. 2011.

[188] R. P. Rand and V. A. Parsegian, "Hydration forces between phospholipid bilayers," *Biochimica et Biophysica Acta (BBA) - Reviews on Biomembranes*, vol. 988, pp. 351–376, 6 Dec. 1989.

[189] M. W. Tate and S. M. Gruner, "Temperature dependence of the structural dimensions of the inverted hexagonal (HII) phase of phosphatidylethanolamine-containing membranes," *Biochemistry*, vol. 28, pp. 4245–4253, 16 May 1989.

[190] R. P. Rand, N. L. Fuller, S. M. Gruner, and V. A. Parsegian, "Membrane curvature, lipid segregation, and structural transitions for phospholipids under dual-solvent stress," *Biochemistry*, vol. 29, pp. 76–87, 9 Jan. 1990.

[191] T. J. McIntosh, "Hydration properties of lamellar and non-lamellar phases of phosphatidylcholine and phosphatidylethanolamine," *Chem. Phys. Lipids*, vol. 81, pp. 117–131, 15 July 1996.

[192] L. Lu and G. A. Voth, "Systematic coarse-graining of a multicomponent lipid bilayer," *J. Phys. Chem. B*, vol. 113, pp. 1501–1510, 5 Feb. 2009.

[193] G. L. Kirk and S. M. Gruner, "Lyotropic effects of alkanes and headgroup composition on the lα -hii lipid liquid crystal phase transition : hydrocarbon packing versus intrinsic curvature," *Journal de Physique*, vol. 46, pp. 761–769, 1 May 1985.

[194] C. P. Tilcock, M. B. Bally, S. B. Farren, and P. R. Cullis, "Influence of cholesterol on the structural preferences of dioleoylphosphatidylethanolamine-dioleoylphosphatidylcholine systems: a phosphorus-31 and deuterium nuclear magnetic resonance study," *Biochemistry*, vol. 21, pp. 4596–4601, 14 Sept. 1982.

[195] M. Orsi, *The development of a coarse-grain biomembrane model and its use in multiscale simulations of solute permeability*. PhD thesis, University of Southampton, 2008.

[196] M. Orsi, J. Michel, and J. W. Essex, "Coarse-grain modelling of DMPC and DOPC lipid bilayers," *J. Phys. Condens. Matter*, vol. 22, p. 155106, 2010.

[197] M. Orsi and J. W. Essex, "The ELBA force field for coarse-grain modeling of lipid membranes," *PLoS One*, vol. 6, no. 12, 2011.

[198] Z. Chen and R. P. Rand, "The influence of cholesterol on phospholipid membrane curvature and bending elasticity," *Biophys. J.*, vol. 73, no. 1, pp. 267–276, 1997.

[199] A. M. Seddon, D. Casey, R. V. Law, A. Gee, R. H. Templer, and O. Ces, "Drug interactions with lipid membranes," *Chem. Soc. Rev.*, vol. 38, pp. 2509–2519, 23 June 2009.

[200] H. L. Casal, "Infrared spectroscopic determination of water penetration in lipid bilayer membranes'," *J. Phys. Chem.*, vol. 93, pp. 4328–4330, 1989.

[201] A. Finkelstein, *Water movement through lipid bilayers, pores, and plasma membranes: theory and reality*. Wiley, 12 Mar. 1987.

[202] B. A. Lewis and D. M. Engelman, "Lipid bilayer thickness varies linearly with acyl chain length in fluid phosphatidylcholine vesicles," *J. Mol. Biol.*, vol. 166, pp. 211–217, 15 May 1983.

[203] M. Jansen and A. Blume, "A comparative study of diffusive and osmotic water permeation across bilayers composed of phospholipids with different head groups and fatty acyl chains," *Biophys. J.*, vol. 68, pp. 997–1008, Mar. 1995.

[204] T. Sugii, S. Takagi, and Y. Matsumoto, "A molecular-dynamics study of lipid bilayers: effects of the hydrocarbon chain length on permeability," *J. Chem. Phys.*, vol. 123, p. 184714, 8 Nov. 2005.

[205] M. H. Lee, B. Lim, J. W. Kim, E. J. An, and D. Lee, "Effect of composition on water permeability of model stratum corneum lipid membranes," *Soft Matter*, vol. 8, no. 5, p. 1539, 2012.

[206] D. R. Carl and S. E. Feller, "Free energy of water transfer into a hydrophobic medium: Effect of polyunsaturation," *Langmuir*, vol. 19, pp. 8560–8564, 1 Sept. 2003.

[207] A. L. Rabinovich, N. K. Balabaev, M. G. Alinchenko, V. P. Voloshin, N. N. Medvedev, and P. Jedlovszky, "Computer simulation study of intermolecular voids in unsaturated phosphatidylcholine lipid bilayers," *J. Chem. Phys.*, vol. 122, p. 84906, 22 Feb. 2005.

[208] J. C. Mathai, S. Tristram-Nagle, J. F. Nagle, and M. L. Zeidel, "Structural determinants of water permeability through the lipid membrane," *J. Gen. Physiol.*, vol. 131, no. 1, pp. 69–76, 2008.

[209] A. C. V. Johansson and E. Lindahl, "The role of lipid composition for insertion and stabilization of amino acids in membranes," *J. Chem. Phys.*, vol. 130, p. 185101, 14 May 2009.

[210] J. S. Hub, F. K. Winkler, M. Merrick, and B. L. De Groot, "Potentials of mean force and permeabilities for carbon dioxide, ammonia, and water flux across a rhesus protein channel and lipid membranes," *J. Am. Chem. Soc.*, vol. 132, no. 10, pp. 13251–13263, 2010.

[211] S. Purushothaman, J. Cama, and U. F. Keyser, "Dependence of norfloxacin diffusion across bilayers on lipid composition," *Soft Matter*, vol. 12, pp. 2135–2144, 21 Feb. 2016.

[212] T. Róg and I. Vattulainen, "Cholesterol, sphingolipids, and glycolipids: what do we know about their role in raft-like membranes?," *Chem. Phys. Lipids*, vol. 184, pp. 82–104, Dec. 2014.

[213] H. Saito and W. Shinoda, "Cholesterol effect on water permeability through DPPC and PSM lipid bilayers: a molecular dynamics study," *J. Phys. Chem. B*, vol. 115, pp. 15241–15250, 29 Dec. 2011.

[214] W. K. Subczynski, J. S. Hyde, and A. Kusumi, "Oxygen permeability of phosphatidylcholine-cholesterol membranes," *Proc. Natl. Acad. Sci. U. S. A.*, vol. 86, no. 12, pp. 4474–4478, 1989.

[215] S. J. McKinnon, S. L. Whittenburg, and B. Brooks, "Nonequilibrium molecular dynamics simulation of oxygen diffusion through hexadecane monolayers with varying concentrations of cholesterol," *J. Phys. Chem.*, vol. 96, pp. 10497–10506, Dec. 1992.

[216] J. Widomska, M. Raguz, and W. K. Subczynski, "Oxygen permeability of the lipid bilayer membrane made of calf lens lipids," *Biochim. Biophys. Acta*, vol. 1768, pp. 2635–2645, Oct. 2007.

[217] P. Jedlovszky and M. Mezei, "Effect of cholesterol on the properties of phospholipid membranes. 2. free energy profile of small molecules," *J. Phys. Chem. B*, vol. 107, pp. 5322–5332, 2003.

[218] F. Zocher, D. Van Der Spoel, P. Pohl, and J. S. Hub, "Local partition coefficients govern solute permeability of cholesterol-containing membranes," *Biophys. J.*, vol. 105, no. 12, pp. 2760–2770, 2013.

[219] C. L. Wennberg, D. van der Spoel, and J. S. Hub, "Large influence of cholesterol on solute partitioning into lipid membranes," *J. Am. Chem. Soc.*, vol. 134, pp. 5351–5361, 21 Mar. 2012.

[220] P. R. Seo, Z. S. Teksin, J. P. Y. Kao, and J. E. Polli, "Lipid composition effect on permeability across PAMPA," *Eur. J. Pharm. Sci.*, vol. 29, pp. 259–268, Nov. 2006.

[221] T. J. McIntosh and S. A. Simon, "Area per molecule and distribution of water in fully hydrated dilauroylphosphatidylethanolamine bilayers," *Biochemistry*, vol. 25, pp. 4948–4952, 26 Aug. 1986.

[222] E. Y. Shalaev and P. L. Steponkus, "Phase diagram of 1,2-dioleoylphosphatidylethanolamine (DOPE): Water system at subzero temperatures and at low water contents," *Biochimica et Biophysica Acta - Biomembranes*, vol. 1419, no. 2, pp. 229–247, 1999.

[223] R. P. Rand and N. L. Fuller, "Structural dimensions and their changes in a reentrant hexagonal-lamellar transition of phospholipids," *Biophys. J.*, vol. 66, no. 6, pp. 2127–2138, 1994.

[224] J. Sangster, "Octanol water partition coefficients of simple organic compounds," *J. Phys. Chem. Ref. Data*, vol. 18, pp. 1111–1229, 1 July 1989.

[225] C. Hansch, *Exploring QSAR*. American Chemical Society, 1 edition ed., 1995.

[226] S. Plimpton, "Fast parallel algorithms for Short-Range molecular dynamics," *J. Comput. Phys.*, vol. 117, pp. 1–19, 1 Mar. 1995.

[227] J. B. Klauda, R. M. Venable, J. A. Freites, J. W. O'Connor, D. J. Tobias, C. Mondragon-Ramirez, I. Vorobyov, A. D. MacKerell, and R. W. Pastor, "Update of the CHARMM all-atom additive force field for lipids: validation on six lipid types," *J. Phys. Chem. B*, vol. 114, pp. 7830–7843, 17 June 2010.

[228] R. W. Pastor and A. D. Mackerell, Jr, "Development of the CHARMM force field for lipids," *J. Phys. Chem. Lett.*, vol. 2, no. 13, pp. 1526–1532, 2011.

[229] K. Vanommeslaeghe, E. Hatcher, C. Acharya, S. Kundu, S. Zhong, J. Shim, E. Darian, O. Guvench, P. Lopes, I. Vorobyov, a. D. Mackerell, and A. Manuscript, "CHARMM general force field: A force field for drug-like molecules compatible with the CHARMM all-atom additive biological force fields," *J. Comput. Chem.*, vol. 31, pp. 671–690, Mar. 2010.

[230] W. Yu, X. He, K. Vanommeslaeghe, and A. D. MacKerell, Jr, "Extension of the CHARMM general force field to sulfonyl-containing compounds and its utility in biomolecular simulations," *J. Comput. Chem.*, vol. 33, pp. 2451–2468, 5 Dec. 2012.

[231] R. W. Hockney and J. W. Eastwood, "Computer simulation using particles," *Bristol: Hilger, 1988*, 1988.

[232] E. L. Pollock and J. Glosli, "Comments on P3M, FMM, and the ewald method for large periodic coulombic systems," *Comput. Phys. Commun.*, vol. 95, pp. 93–110, 1 June 1996.

[233] M. J. Abraham, T. Murtola, R. Schulz, S. Páll, J. C. Smith, B. Hess, and E. Lindahl, "GROMACS: High performance molecular simulations through multi-level parallelism from laptops to supercomputers," *SoftwareX*, vol. 1–2, pp. 19–25, 2015.

[234] S. Pronk, S. Páll, R. Schulz, P. Larsson, P. Bjelkmar, R. Apostolov, M. R. Shirts, J. C. Smith, P. M. Kasson, D. van der Spoel, B. Hess, and E. Lindahl, "GROMACS 4.5: a high-throughput and highly parallel open source molecular simulation toolkit," *Bioinformatics*, vol. 29, pp. 845–854, 1 Apr. 2013.

[235] B. Hess, C. Kutzner, D. v. der Spoel, and E. Lindahl, "GROMACS 4: Algorithms for highly efficient, Load-Balanced, and scalable molecular simulation," *J. Chem. Theory Comput.*, vol. 4, no. 3, pp. 435–447, 2008.

[236] D. Van Der Spoel, E. Lindahl, B. Hess, G. Groenhof, A. E. Mark, and H. J. C. Berendsen, "GROMACS: fast, flexible, and free," *J. Comput. Chem.*, vol. 26, pp. 1701–1718, Dec. 2005.

[237] E. Lindahl, B. Hess, and D. van der Spoel, "GROMACS 3.0: a package for molecular simulation and trajectory analysis," *J. Mol. Model.*, vol. 7, pp. 306–317, 1 Aug. 2001.

[238] H. J. C. Berendsen, D. van der Spoel, and R. van Drunen, "GROMACS: A message-passing parallel molecular dynamics implementation," *Comput. Phys. Commun.*, vol. 91, pp. 43–56, 2 Sept. 1995.

[239] U. Essmann, L. Perera, M. L. Berkowitz, T. Darden, H. Lee, and L. G. Pedersen, "A smooth particle mesh ewald method," *J. Chem. Phys.*, vol. 103, pp. 8577–8593, 15 Nov. 1995.

[240] W. L. Jorgensen, J. Chandrasekhar, J. D. Madura, R. W. Impey, and M. L. Klein, "Comparison of simple potential functions for simulating liquid water," *J. Chem. Phys.*, vol. 79, no. 2, p. 926, 1983.

[241] M. Parrinello and A. Rahman, "Crystal structure and pair potentials: A Molecular-Dynamics study," *Phys. Rev. Lett.*, vol. 45, pp. 1196–1199, 6 Oct. 1980.

[242] M. Parrinello and A. Rahman, "Strain fluctuations and elastic constants," *J. Chem. Phys.*, vol. 76, pp. 2662–2666, 1 Mar. 1982.

[243] S. Miyamoto and P. A. Kollman, "Settle: An analytical version of the SHAKE and RATTLE algorithm for rigid water models," *J. Comput. Chem.*, vol. 13, pp. 952–962, 1 Oct. 1992.

[244] J. S. Hub, B. L. de Groot, and D. v. der Spoel, "g_wham—a free weighted histogram analysis implementation including robust error and autocorrelation estimates," *J. Chem. Theory Comput.*, vol. 6, no. 12, pp. 3713–3720, 2010.

[245] B. Roux, "The calculation of the potential of mean force using computer simulations," *Comput. Phys. Commun.*, vol. 91, pp. 275–282, 2 Sept. 1995.

[246] A. Grossfield and D. M. Zuckerman, "Chapter 2 quantifying uncertainty and sampling quality in biomolecular simulations," 2009.

[247] D. Bemporad, *Computer Simulation of Biological Membranes and Small Molecule Permeation*. PhD thesis, University of Southampton, 2003.

[248] D. Bemporad, C. Luttmann, and J. W. Essex, "Computer simulation of small moleculle permeation across a lipid bilayer: Dependence on bilayer properties and solute volume, size, and cross-sectional area," *Biophys. J.*, vol. 87, no. 1, pp. 1–13, 2004.

[249] D. Bemporad, J. W. Essex, and C. Luttmann, "Permeation of small molecules through a lipid bilayer: A computer simulation study," *J. Phys. Chem. B*, vol. 108, pp. 4875–4884, Apr. 2004.

[250] D. Bemporad, C. Luttmann, and J. W. Essex, "Behaviour of small solutes and large drugs in a lipid bilayer from computer simulations," *Biochim. Biophys. Acta*, vol. 1718, pp. 1–21, 10 Dec. 2005.

[251] N. Nitschke, K. Atkovska, and J. S. Hub, "Accelerating potential of mean force calculations for lipid membrane permeation: System size, reaction coordinate, solute-solute distance, and cutoffs," *J. Chem. Phys.*, vol. 145, p. 125101, 28 Sept. 2016.

[252] M. Paloncýová, K. Berka, and M. Otyepka, "Convergence of free energy profile of coumarin in lipid bilayer," *J. Chem. Theory Comput.*, vol. 8, no. 4, pp. 1200–1211, 2012.

[253] T. S. Carpenter, D. A. Kirshner, E. Y. Lau, S. E. Wong, J. P. Nilmeier, and F. C. Lightstone, "A method to predict Blood-Brain barrier permeability of Drug-Like compounds using molecular dynamics simulations," *Biophys. J.*, vol. 107, pp. 630–641, Aug. 2014.

[254] C. T. Lee, J. Comer, C. Herndon, N. Leung, A. Pavlova, R. V. Swift, C. Tung, C. N. Rowley, R. E. Amaro, C. Chipot, Y. Wang, and J. C. Gumbart, "Simulation-Based approaches for determining membrane permeability of small compounds," *J. Chem. Inf. Model.*, vol. 56, pp. 721–733, 25 Apr. 2016.

[255] C. Hong, D. P. Tieleman, and Y. Wang, "Microsecond molecular dynamics simulations of lipid mixing," *Langmuir*, vol. 30, pp. 11993–12001, 14 Oct. 2014.

[256] J. P. M. Jämbeck and A. P. Lyubartsev, "Exploring the free energy landscape of solutes embedded in lipid bilayers," *J. Phys. Chem. Lett.*, vol. 4, pp. 1781–1787, 6 June 2013.

[257] P. L. O'neill, D. Nicolaides, D. Honnery, J. Soria, and Others, "Autocorrelation functions and the determination of integral length with reference to experimental and numerical data," in *15th Australasian Fluid Mechanics Conference The University of Sydney, Sydney, Australia*, pp. 13–17, 2004.

[258] R. Gupta, D. B. Sridhar, and B. Rai, "Molecular dynamics simulation study of permeation of molecules through skin lipid bilayer," *J. Phys. Chem. B*, vol. 120, pp. 8987–8996, 1 Sept. 2016.

[259] M. Holz, S. R. Heil, and A. Sacco, "Temperature-dependent self-diffusion coefficients of water and six selected molecular liquids for calibration in accurate 1H NMR PFG measurements," *Phys. Chem. Chem. Phys.*, vol. 2, pp. 4740–4742, 1 Jan. 2000.

[260] M. W. Mahoney and W. L. Jorgensen, "Diffusion constant of the TIP5P model of liquid water," *J. Chem. Phys.*, vol. 114, no. 1, pp. 363–366, 2001.

[261] Y. Mao and Y. Zhang, "Thermal conductivity, shear viscosity and specific heat of rigid water models," *Chem. Phys. Lett.*, vol. 542, pp. 37–41, 2012.

[262] R. W. Tejwani, M. E. Davis, B. D. Anderson, and T. R. Stouch, "Functional group dependence of solute partitioning to various locations within a DOPC bilayer: a comparison of molecular dynamics simulations with experiment," *J. Pharm. Sci.*, vol. 100, pp. 2136–2146, June 2011.

[263] R. W. Tejwani, M. E. Davis, B. D. Anderson, and T. R. Stouch, "An atomic and molecular view of the depth dependence of the free energies of solute transfer from water into lipid bilayers," *Mol. Pharm.*, vol. 8, no. 6, pp. 2204–2215, 2011.

[264] S. J. Marrink and H. J. C. Berendsen, "Permeation process of small molecules across lipid membranes studied by molecular dynamics simulations," *J. Phys. Chem.*, vol. 100, pp. 16729–16738, Jan. 1996.

[265] D. Trzesniak, A.-P. E. Kunz, and W. F. van Gunsteren, "A comparison of methods to compute the potential of mean force," *Chemphyschem*, vol. 8, pp. 162–169, 8 Jan. 2007.

[266] M. Orsi and J. W. Essex, "Permeability of drugs and hormones through a lipid bilayer: insights from dual-resolution molecular dynamics," *Soft Matter*, vol. 6, no. 16, p. 3797, 2010.

[267] T. S. Carpenter, J. Parkin, and S. Khalid, "The free energy of small solute permeation through the e. coli outer membrane has a distinctly asymmetric profile," *J. Phys. Chem. Lett.*, vol. 0, p. null, 12 Aug. 2016.

[268] J. Comer, C. Chipot, and F. D. González-Nilo, "Calculating Position-Dependent diffusivity in biased molecular dynamics simulations," *J. Chem. Theory Comput.*, vol. 9, pp. 876–882, 12 Feb. 2013.

[269] J. Comer, K. Schulten, and C. Chipot, "Diffusive models of membrane permeation with explicit orientational freedom," *J. Chem. Theory Comput.*, vol. 10, pp. 2710–2718, 8 July 2014.

[270] J. Comer, K. Schulten, and C. Chipot, "Calculation of Lipid-Bilayer permeabilities using an average force," *J. Chem. Theory Comput.*, vol. 10, pp. 554–564, 11 Feb. 2014.

[271] M. L. Mugnai and R. Elber, "Extracting the diffusion tensor from molecular dynamics simulation with milestoning," *J. Chem. Phys.*, vol. 142, p. 014105, 7 Jan. 2015.

[272] E. Gallucci, S. Micelli, and C. Lippe, "Non-electrolyte permeability across thin lipid membranes," *Arch. Int. Physiol. Biochim.*, vol. 79, pp. 881–887, Dec. 1971.

[273] M. Yazdanian, S. L. Glynn, J. L. Wright, and A. Hawi, "Correlating partitioning and caco-2 cell permeability of structurally diverse small molecular weight compounds," *Pharm. Res.*, vol. 15, pp. 1490–1494, Sept. 1998.

[274] P. Jedlovszky and M. Mezei, "Calculation of the free energy profile of H2O, o2, CO, CO2, NO, and CHCl3 in a lipid bilayer with a cavity insertion variant of the widom method," *J. Am. Chem. Soc.*, vol. 122, no. 21, pp. 5125–5131, 2000.

[275] J. F. Nagle, J. C. Mathai, M. L. Zeidel, and S. Tristram-Nagle, "Theory of passive permeability through lipid bilayers," *J. Gen. Physiol.*, vol. 131, no. 1, pp. 77–85, 2008.

[276] K. Olbrich, W. Rawicz, D. Needham, and E. Evans, "Water permeability and mechanical strength of polyunsaturated lipid bilayers," *Biophys. J.*, vol. 79, pp. 321–327, July 2000.

[277] A. Carruthers and D. L. Melchior, "Studies of the relationship between bilayer water permeability and bilayer physical state?," *Biochemistry*, vol. 22, pp. 5797–5807, 1983.

[278] M. B. Lande, J. M. Donovan, and M. L. Zeidel, "The relationship between membrane fluidity and permeabilities to water, solutes, ammonia, and protons," *J. Gen. Physiol.*, vol. 106, pp. 67–84, July 1995.

[279] A. Walter and J. Gutknecht, "Permeability of small nonelectrolytes through lipid bilayer membranes," *J. Membr. Biol.*, vol. 90, no. 3, pp. 207–217, 1986.

[280] T. X. Xiang and B. D. Anderson, "The relationship between permeant size and permeability in lipid bilayer membranes," *J. Membr. Biol.*, vol. 140, pp. 111–122, June 1994.

[281] S. H. Koenig, Q. F. Ahkong, R. D. Brown, 3rd, M. Lafleur, M. Spiller, E. Unger, and C. Tilcock, "Permeability of liposomal membranes to water: results from the magnetic field dependence of T1 of solvent protons in suspensions of vesicles with entrapped paramagnetic ions," *Magn. Reson. Med.*, vol. 23, pp. 275–286, Feb. 1992.

[282] A. C. Chakrabarti and D. W. Deamer, "Permeability of lipid bilayers to amino acids and phosphate," *Biochim. Biophys. Acta*, vol. 1111, pp. 171–177, 9 Nov. 1992.

[283] J. Arct, M. Chelkowska, K. Kasiura, and P. Pietrzykowski, "The fatty acids as penetration enhancers of amino acids by ion pairing," *Int.J.Cosmet.Sci.*, vol. 24, no. 1467-2494 (Electronic), pp. 313–322, 2002.

[284] M. di Cagno, H. A. Bibi, and A. Bauer-Brandl, "New biomimetic barrier permeapad^{TM} for efficient investigation of passive permeability of drugs," *Eur. J. Pharm. Sci.*, vol. 73, pp. 29–34, 20 June 2015.

[285] Y. N. Antonenko, P. Pohl, and G. A. Denisov, "Permeation of ammonia across bilayer lipid membranes studied by ammonium ion selective microelectrodes," *Biophys. J.*, vol. 72, pp. 2187–2195, May 1997.

[286] Y. N. Antonenko and L. S. Yaguzhinsky, "The role of ph gradient in the unstirred layers in the transport of weak acids and bases through bilayer lipid membranes," *Bioelectrochem. Bioenerg.*, vol. 13, pp. 85–91, Nov. 1984.

[287] Z. Ghaemi, M. Minozzi, P. Carloni, and A. Laio, "A novel approach to the investigation of passive molecular permeation through lipid bilayers from atomistic simulations," *J. Phys. Chem. B*, vol. 116, pp. 8714–8721, 26 July 2012.

[288] H. V. Ly and M. L. Longo, "The influence of short-chain alcohols on interfacial tension, mechanical properties, area/molecule, and permeability of fluid lipid bilayers," *Biophys. J.*, vol. 87, pp. 1013–1033, Aug. 2004.

[289] M. H. Abraham, F. Martins, and R. C. Mitchell, "Algorithms for skin permeability using hydrogen bond descriptors: the problem of steroids*," *J. Pharm. Pharmacol.*, vol. 49, pp. 858–865, 1 Sept. 1997.

[290] A. Galkin, A. Fallarero, and P. M. Vuorela, "Coumarins permeability in caco-2 cell model," *J. Pharm. Pharmacol.*, vol. 61, pp. 177–184, 8 Feb. 2009.

[291] G. Camenisch, J. Alsenz, H. van de Waterbeemd, and G. Folkers, "Estimation of permeability by passive diffusion through caco-2 cell monolayers using the drugs' lipophilicity and molecular weight," *Eur. J. Pharm. Sci.*, vol. 6, pp. 317–324, Oct. 1998.

[292] T.-L. Pan, P.-W. Wang, I. A. Aljuffali, Y.-L. Leu, Y.-Y. Hung, and J.-Y. Fang, "Coumarin derivatives, but not coumarin itself, cause skin irritation via topical delivery," *Toxicol. Lett.*, vol. 226, pp. 173–181, 21 Apr. 2014.

[293] P. Singh and M. S. Roberts, "Skin permeability and local tissue concentrations of nonsteroidal anti-inflammatory drugs after topical application," *J. Pharmacol. Exp. Ther.*, vol. 268, pp. 144–151, Jan. 1994.

[294] A. Missner, P. Kügler, S. M. Saparov, K. Sommer, J. C. Mathai, M. L. Zeidel, and P. Pohl, "Carbon dioxide transport through membranes," *J. Biol. Chem.*, vol. 283, pp. 25340–25347, 2008.

[295] J. Gutknecht, M. A. Bisson, and F. C. Tosteson, "Diffusion of carbon dioxide through lipid bilayer membranes: effects of carbonic anhydrase, bicarbonate, and unstirred layers," *J. Gen. Physiol.*, vol. 69, pp. 779–794, June 1977.

[296] J. L. MacCallum, W. F. D. Bennett, and D. P. Tieleman, "Distribution of amino acids in a lipid bilayer from computer simulations," *Biophys. J.*, vol. 94, pp. 3393–3404, 1 May 2008.

[297] A. C. V. Johansson and E. Lindahl, "Position-resolved free energy of solvation for amino acids in lipid membranes from molecular dynamics simulations," *Proteins*, vol. 70, pp. 1332–1344, 14 Mar. 2008.

[298] H. Sato, N. Matubayasi, M. Nakahara, and F. Hirata, "Which carbon oxide is more soluble? ab initio study on carbon monoxide and dioxide in aqueous solution," *Chem. Phys. Lett.*, vol. 323, pp. 257–262, 16 June 2000.

[299] R. E. Rosenberg, "Does fluoromethane form a hydrogen bond with water?," *J. Phys. Chem. A*, vol. 116, no. 44, pp. 10842–10849, 2012.

[300] A. Mälkiä, L. Murtomäki, A. Urtti, and K. Kontturi, "Drug permeation in biomembranes: in vitro and in silico prediction and influence of physicochemical properties," *Eur. J. Pharm. Sci.*, vol. 23, pp. 13–47, Sept. 2004.

[301] J. M. Nitsche and G. B. Kasting, "Permeability of fluid-phase phospholipid bilayers: assessment and useful correlations for permeability screening and other applications," *J. Pharm. Sci.*, vol. 102, pp. 2005–2032, June 2013.

[302] G. Currell and A. Dowman, *Essential Mathematics and Statistics for Science*. Wiley, 30 Mar. 2009.

[303] J. Kuśba, L. Li, I. Gryczynski, G. Piszczek, M. Johnson, and J. R. Lakowicz, "Lateral diffusion coefficients in membranes measured by resonance energy transfer and a new algorithm for diffusion in two dimensions," *Biophys. J.*, vol. 82, pp. 1358–1372, Mar. 2002.

[304] N. Kahya, D. Scherfeld, K. Bacia, B. Poolman, and P. Schwille, "Probing lipid mobility of raft-exhibiting model membranes by fluorescence correlation spectroscopy," *J. Biol. Chem.*, vol. 278, pp. 28109–28115, 25 July 2003.

[305] A. Filippov, G. Orädd, and G. Lindblom, "Influence of cholesterol and water content on phospholipid lateral diffusion in bilayers," *Langmuir*, vol. 19, pp. 6397–6400, 1 Aug. 2003.

[306] T. X. Xiang and B. D. Anderson, "Influence of chain ordering on the selectivity of dipalmitoylphosphatidylcholine bilayer membranes for permeant size and shape," *Biophys. J.*, vol. 75, pp. 2658–2671, Dec. 1998.

[307] M. Orsi, M. G. Noro, and J. W. Essex, "Dual-resolution molecular dynamics simulation of antimicrobials in biomembranes," *J. R. Soc. Interface*, vol. 8, pp. 826–841, 6 June 2011.

[308] G. Parisio, M. Stocchero, and A. Ferrarini, "Passive membrane permeability: Beyond the standard Solubility-Diffusion model," *J. Chem. Theory Comput.*, vol. 9, pp. 5236–5246, 10 Dec. 2013.

[309] S. Manno, Y. Takakuwa, and N. Mohandas, "Identification of a functional role for lipid asymmetry in biological membranes: Phosphatidylserine-skeletal protein interactions modulate membrane stability," *Proc. Natl. Acad. Sci. U. S. A.*, vol. 99, pp. 1943–1948, 19 Feb. 2002.

[310] A. A. Gurtovenko and I. Vattulainen, "Membrane potential and electrostatics of phospholipid bilayers with asymmetric transmembrane distribution of anionic lipids," *J. Phys. Chem. B*, vol. 112, pp. 4629–4634, 17 Apr. 2008.

Appendix A

constraint force sampling frequency

In order to calculate the permeation coefficient of each molecule with the z-constraint method, the free-energy profile has to be computed (equation 2.53), thus is necessary to sample the force applied to the permeant in order to constrain its distance from the membrane centre. The constraint force is a widely fluctuating property as the permeating molecule experiences different membrane conformations in each timestep. To identify whether the sampling frequency affects the final results, a comparison study between three different sampling options was performed. The three options were:

1. to use the instant force value of the timestep on every 10 ps sample
2. to use a local average of the last 10 timesteps before every 10 ps sample
3. to use an average of 25 timesteps, evenly distributed between every 10 ps sample.

Figure A.1 shows the free-energy profile, for the water molecule permeating through the pure DOPC membrane, produced with the three different sampling choices. Qualitatively, all curves exhibit the same characteristics where the free-energy profile gradually increases to a maximum barrier in the core region of the bilayer. Quantitatively, the third "10 ps barrier" is slightly lower than the other two and also is closer to the barrier values that have been reported in the literature (see the results and discussion chapter). In addition, due to the fact that each 10 ps sample is computed as an average of 25 timesteps, evenly distributed between each sampling point, the third option provides a better representation of the constraint forces that the permeant "feels" and therefore, all of the z-constraint results were produced based on it.

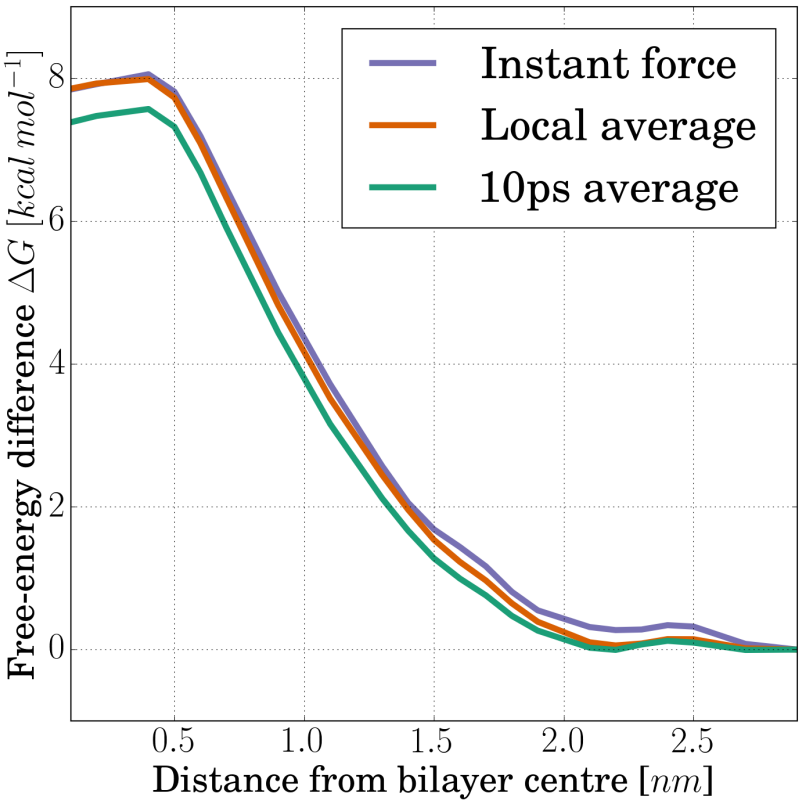

Figure A.1: Comparison of constraint force sampling on ΔG profiles.

Appendix B

Hypothesis testing tables

Table B.1: The logP values that were used for the hypothesis t-test

Permeant	**logP**		**ΔlogP**
	DOPC	**DOPC:DOPE**	
Ammonia	-2.18	-2.72	-0.54
Water	-3.40	-3.54	-0.14
Fluoromethane	0.59	0.61	0.02
Carbon dioxide	1.00	0.85	-0.16
Propane	0.86	0.86	0.00
Ethanol	-0.81	-0.97	-0.16
Urea	-6.17	-6.40	-0.23
Isopropanol	-0.20	-0.48	-0.27
Glycine	-2.69	-3.20	-0.51
Phenol	0.70	0.38	-0.32
Benzoic Acid	0.80	0.91	0.12
Coumarin	0.06	0.56	0.50
Paracetamol	-2.42	-2.03	0.40

Table B.2: The analysis of the t-test.

	MW<100	MW>100	All
Mean:	-0.230	0.340	-0.098
Standard deviation:	0.188	0.201	0.309
Hypothesised mean (h):	0	0	0
t-statistic:	3.862	-2.933	1.144
Degrees of freedom:	9	2	12
Critical t-value (one-tailed):	1.833	2.920	1.782
Critical t-value (two-tailed) +-:	2.262	4.303	2.179
One-tailed probability P(h <x):	0.0019	0.950	0.137
One-tailed probability P(h >x):	0.998	0.0496	0.863
Two-tailed probability P(h = x):	0.004	0.099	0.275
Two-tailed probability P(h ≠ x):	0.996	0.901	0.725